

Copyright is owned by the Author of the thesis. Permission is given for a copy to be downloaded by an individual for the purpose of research and private study only. The thesis may not be reproduced elsewhere without the permission of the Author.

A Study into the Use of Ion Beam Analysis for the Quantitative and Qualitative Analysis of Conducting Polymers

Giovanna Lucia Moretto

July 2004

A Study into the Use of Ion Beam Analysis for the Quantitative and Qualitative Analysis of Conducting Polymers

A thesis presented in partial fulfilment of the
requirements for the degree of
Doctor of Philosophy

In

Chemistry

at Massey University, Palmerston North
New Zealand

Giovanna Lucia Moretto

July 2004

Abstract

Since their discovery in the late 1970s conducting polymers have become increasingly used materials in many applications. They are utilised for their conductivity and/or their electroactive properties. These applications include sensor technologies, actuators, and battery materials.

The properties of conducting polymers rely on the extent of the reduction / oxidation or redox state, and hence the dopant levels, of the materials. The aim of this work was to investigate the use of the Ion Beam Analysis (IBA) techniques Rutherford Backscattering Spectroscopy (RBS), and Proton Induced X-ray Emission (PIXE) for the analysis of 'soft' organic materials, in particular, conducting polymers. These IBA techniques are not new, as they have been extensively used for the characterisation of many inorganic, 'hard', materials such as aluminium oxide and silicon oxynitride. While they have been used to alter the molecular structure, and hence the properties of conducting polymers in the past, little to no research has explored the use of ion beams as a tool for the characterisation of these materials.

Conducting polymers can either be prepared chemically or electrochemically. They are predominantly prepared in an oxidised state and this charge is balanced by negatively charged counter ions. In this work, the conducting polymers were formed electrochemically by deposition onto support materials at constant electrode potential. The number of counter ions required to balance the polymer chain depends on the type of conducting polymer formed and extent of oxidation. Issues such as the influence of the support material and extent of polymer oxidation on the extent of counter ions through the polymer films are of importance. Gaining knowledge of the dispersion of counter ions may provide new insights into the redox mechanisms for conductive polymers.

Complex bis terthiophene porphyrin conducting polymers were prepared and investigated for the uptake of zinc into the freebase porphyrin unit after polymerisation by acquiring elemental depth profiles using RBS analysis. Issues such as the influence of the support material and extent of polymer oxidation on the extent of counter ions through the polymer films were found to be of importance. Gaining knowledge of the

extent of counter ions provides new insights into the redox mechanisms for conductive polymers. The results were compared to those obtained for a sample where zinc was coordinated to the porphyrin prior to the polymerisation process. Unexpected high concentrations of both nitrogen and oxygen were found, which were interpreted to be due to entrapped cations originating from the electrolyte $((\text{Bu})_4\text{N}^+)$, together with trapped water molecules, within the polymer films. The chlorine depth profiling assisted with understanding the extent of the perchlorate counter ion throughout the polymer films. The combination of both RBS and PIXE demonstrated that trace element impurities can be detected using ion beam analysis, which other analytical techniques are unable to do.

A series of polypyrrole films incorporating a range of counter ions were prepared as model compounds for study in the second section of this work. RBS and PIXE techniques were used to evaluate film homogeneity with respect to depth and to infer the counter ion / pyrrole unit ratio for each of the six PPy film formed.

RBS was also used to characterise a series of terthiophene-ferrocene based conducting co-polymers. The ratio of co-polymer monomer to terthiophene-ferrocene monomers and the dopant levels for the polymers were determined using a RBS deconvolution method developed in this study. This new method can be extended for characterization of a wide range of organic polymers.

The limitations of RBS for the analysis of these soft materials were identified. The advantage that RBS offers over other analytical techniques is that it provides a means for low atomic number element depth profiling in these materials.



CANDIDATES'S DECLARATION

This is to certify that the research carried out for my Doctoral thesis entitled "A study into the use of Ion Beam Analysis for the Quantitative and Qualitative analysis of conducting polymers" in the Institute of Fundamental Sciences, Massey University, Turitea, New Zealand is my own work and that the thesis material has not been used in part or in whole for any other qualification.

Candidate's Name: Giovanna L. Moretto

Signature:

Date: 8 Dec 2004



Massey University

COLLEGE OF SCIENCES

INSTITUTE OF
FUNDAMENTAL SCIENCES
Private Bag 11 222
Palmerston North
New Zealand
T 64 6 356 9099
F 64 6 350 5682
ifs@massey.ac.nz
www.massey.ac.nz

SUPERVISOR'S DECLARATION

This is to certify that the research carried out for the Doctoral thesis entitled "A study into the use of Ion Beam Analysis for the Quantitative and Qualitative analysis of conducting polymers" was done by Giovanna Lucia Moretto in the Institute of Fundamental Sciences, Massey University, Turitea, New Zealand. The thesis material has not been used in part or in whole for any other qualification, and I confirm that the candidate has pursued the course of study in accordance with the requirements of the Massey University regulations.

Supervisor's Name: Simon B. Hall

Signature:

Date: 8 Dec 2004



CERTIFICATE OF REGULATORY COMPLIANCE

This is to certify that the research carried out in the Doctoral thesis entitled “A study into the use of Ion Beam Analysis for the Quantitative and Qualitative analysis of conducting polymers” in the Institute of Fundamental Sciences, Massey University, Turitea, New Zealand:

- (a) is the original work of the candidate, except as indicated by appropriate attribution in the text and/or in the acknowledgements;
- (b) that the text, excluding appendices/annexes, does not exceed 100,000 words;
- (c) all the ethical requirements applicable to this study have been complied with as required by Massey University, other organisations and/or committees which had a particular association with this study, and relevant legislation.

Candidate's Name: Giovanna L. Masetto

Supervisor's Name: Simon B. Hall

Signature:

Signature:

Date: 8 Dec. 2004

Date: 8 Dec. 2004

Acknowledgements

The only part of this thesis where I get to write whatever I want and I can't figure out where to start!

To all of my supervisors I would like to give a huge thanks to. David and Tony, without the two of you I would never have been in a financial position to do this, so thank you very much. To Andreas, big thanks, for giving me the opportunity to work with you and your group, and for all the things you have taught and helped me with over the last few years. Simon, where to start? Thank you for everything over the last however many years. All of your guidance, support, time, and much more, has been most appreciated.

I would like to thank the New Zealand Foundation for Research and Technology for providing the grant from which I received my Stipend.

I would also like to thank the Institute of Fundamental Sciences Graduate Research Fund for the support I have received throughout my PhD and to all the staff in IFS - chemistry for the help each of them has given me over the years.

Thanks to Bill, John, Chris, Steven, and all the other people at GNS which have helped me over the time of my PhD and made moving somewhere where I didn't know anyone an easy and fun time.

Thanks to all my friends from Palmerston North, past and present, each of which has helped me in some way over the 10 years I have been at Massey. Of all those friends a special super big thanks must go to a few, Justin, Carol, Karen, Jo, Karen, Amy. You have all made my time here at Massey not just bearable, but memorable and fun filled. A big special thanks to Warwick you made everything ok even when I thought it was time to quit, love you.

All my friends in Wellington can't go unmentioned, so a big thanks to Dave, Claire, Annie, Brain, Susan, Brendan, and Gemma. Thanks for everything!

Lastly I would like to thank my family. To Gino, thanks for being the best brother anyone could have, just knowing you are always there for me means more than I can ever tell you. To Mum and Dad, thank you isn't enough. Because of your love and support, and everything thing else, the two of you have made me who I am today. You both mean the world to me and I love you both so much. And Dad, this means I have finally finished being at school *grin*.

Table of Contents

Abstract	i
Declarations	iii
Acknowledgements	vi
Table of Contents	viii
List of Figures	xii
List of Tables	xxi
List of Schemes	xxvi
List of Symbols	xxviii
List of Abbreviations	xxix

Chapter 1	Introduction	1-14
------------------	---------------------	-------------

1.1	Introduction	1
1.2	Conducting polymers	2
1.2.1	<i>Polyacetylene</i>	2
1.3	Polyhetrocycles as conducting polymers	4
1.4	Mechanisms of conducting	6
1.5	Copolymers	10
1.6	Applications	10
1.6.1	<i>Rechargeable batteries</i>	12
1.7	Scope of this study	14

Chapter 2	Experimental Methods	15-65
------------------	-----------------------------	--------------

2.1	Introduction	15
2.2	Electrochemistry	15
2.2.1	<i>Potentiostatic and Galvanostatic Instrumentation</i>	16
2.2.2	<i>Electrodes</i>	16
2.2.2.1	Counter Electrode	18
2.2.2.2	Reference Electrode	18
2.2.3	<i>Electrochemical Cells</i>	18
2.2.3.1	Scoping study electrochemical cell	18

2.2.3.2	Electrochemical cell for polypyrrole preparation	20
2.2.3.3	Electrochemical cell for terthiophene-ferrocene films	22
2.3	Electrochemical Techniques	22
2.3.1	<i>Cyclic Voltammetry</i>	22
2.3.2	<i>Chronoamperometry</i>	24
2.4	Ion Beam Analysis	25
2.4.1	<i>Introduction – Rutherford's experiment</i>	25
2.4.2	<i>Incident particles used in Ion Beam Analysis</i>	26
2.5	Ion Beam Analysis at Geological and Nuclear Sciences, NZ	27
2.5.1	<i>Introduction</i>	27
2.5.2	<i>The Van de Graaff Accelerator</i>	28
2.5.3	<i>Beam Lines</i>	31
2.5.4	<i>Detectors</i>	36
2.5.4.1	RBS detectors	36
2.5.4.2	PIXE detectors	36
2.6	Rutherford Backscattering – RBS	38
2.6.1	<i>Collection of spectra</i>	38
2.6.2	<i>Idealised simple spectrum</i>	40
2.6.3	<i>Scattering cross sections</i>	46
2.6.4	<i>Stopping powers and depth profiling</i>	49
2.6.5	<i>Scattering angle</i>	53
2.6.6	<i>Multi-element spectra</i>	53
2.6.7	<i>Analysis methods for RBS</i>	55
2.6.7.1	RUMP	55
2.6.7.2	SIMNRA	58
2.7	Particle Induced X-ray Emission (PIXE)	59
2.7.1	<i>Introduction</i>	59
2.7.2	<i>Calibration and Qualitative Analysis</i>	63
2.7.3	<i>Quantitative Analysis</i>	65
Chapter 3	Scoping Study	66-87
3.1	Introduction	66
3.2	Electrochemistry	66

3.2.1	<i>Monomers</i>	66
3.2.2	<i>Electrochemical deposition</i>	68
3.2.3	<i>Post-polymerisation</i>	68
3.3	Ion Beam Analysis	71
3.3.1	<i>Film durability</i>	71
3.3.2	<i>Rutherford Backscattering – RBS</i>	74
3.3.3	<i>Proton Induced X-ray Emission – PIXE</i>	85
3.4	Conclusions	85

Chapter 4 88-118

4.1	Introduction	88
4.2	Experimental Conditions	88
4.2.1	<i>Reagents</i>	88
4.2.2	<i>Electrochemistry</i>	90
4.2.3	<i>Ion Beam Analysis Techniques</i>	91
4.2.3.1	PIXE	91
4.2.3.2	RBS	91
4.2.4	<i>Combustion analysis</i>	91
4.3	Ion beam analysis	91
4.3.1	<i>Film durability</i>	91
4.3.2	<i>PIXE – trace elements</i>	93
4.3.3	<i>RBS – monomer to counter ion ratios</i>	104
4.3.4	<i>Comparison with combustion analysis</i>	115
4.4	Conclusions	117

Chapter 5 Electrochemical preparation of terthiophene-ferrocene copolymers 119-137

5.1	Introduction	119
5.2	Deposition of terthiophene-ferrocene	119
5.3	Electrochemistry	123
5.3.1	<i>Stepping potential</i>	125
5.3.2	<i>Post polymerisation analysis</i>	133

5.3.3 *Ion beam analysis and scanning electron microscope images of films* 133

Chapter 6	SIMNRA modelling	138-155
6.1	Introduction	138
6.2	Model I	139
6.3	Model II	143
6.4	Model III	146
6.5	Model IV	151
Chapter 7	Analysis of TTh-Fc copolymers	156-260
7.1	Introduction	156
7.2	Low energy tailing of spectra	156
7.3	Roughness Factors	158
7.4	Other parameters used in RBS simulation	159
7.5	Ion Beam durability	160
7.6	Conclusions and significant features	160
7.7	TTh-Fc copolymers	165
7.7.1	Pyrrole copolymers	165
7.7.2	Bithiophene copolymers	169
7.7.3	EDOT copolymers	172
7.7.4	TTh-Por-TTh copolymers	178
7.7.5	Bridging TTh copolymers	183
7.8	Variation of film thickness	187
Chapter 8	Conclusions	261-267
References		268-278
Appendix		279-311

List of Figures

<u>Number</u>	<u>Description</u>	<u>Page</u>
1.1	Chemical structure of polyacetylene isomers	3
1.2	The two degenerate (<i>E</i>)-structures of polyacetylene, and a soliton at a phase boundary	7
1.3	Aromatic, quinoid, a polaron and bipolaron defect in polypyrrole	9
1.4	Schematic diagram of four main types of copolymers	11
2.1	Schematic diagram of the circuits of a three electrode cell	17
2.2	Schematic diagram of the electrochemical cell from scoping study	19
2.3	Schematic diagram of the electrochemical cell used for the polypyrrole study	21
2.4	Schematic diagram of the electrochemical cell used for the formation of the terthiophene-ferrocene copolymers	23
2.5	Schematic of the IBA processes which can occur	29
2.6	Schematic diagram of the 3 MV Van de Graaff accelerator	30
2.7	Photograph of the general IBA line at GNS	32
2.8	Photograph of the general IBA chamber at GNS	33
2.9	General sample holder	34
2.10	Sample holder designed for terthiophene-ferrocene copolymers	35
2.11	Silicon surface barrier detector	37
2.12	RBS spectrum of Si/N on Si substrate	39
2.13	Idealised spectrum of three elements of infinite thickness	41
2.14	<i>k</i> -factors at $\theta = 170^\circ$ with $^4\text{He}^+$ beam for isotopes of elements with $Z < 90$ with natural abundance greater than 0.5 %	44
2.15	Graph showing <i>k</i> -factor independence from E_0	45
2.16	Scattering cross section of isotopes for elements with $Z < 80$ with naturally occurring isotopes above 0.5%	48
2.17	Schematic diagram of an incident ion backscattering from surface and depth of sample	50
2.18	Schematic of the relationship of nuclear and electronic stopping power with energy for an element	51

2.19	Schematic RBS spectrum of Na samples with varying thickness	52
2.20	<i>k</i> -factor dependence on detector angle	54
2.21	Schematic RBS of N and Na film with finite thickness	56
2.22	Schematic RBS of sample containing C, O, and Na with a thickness of 6000 al/cm ²	57
2.23	Schematic diagram of X-ray production	60
2.24	Comparison of electron and proton induced X-ray emission	62
2.25	PIXE spectrum of Si/N on Si substrate	64
3.1	Structure of freebase and Zn coordinated TTh-Por-TTh	67
3.2	CV of TTh-Por-TTh on GC	69
3.3	CV of TTh-ZnPor-TTh on GC	69
3.4	Post growth CV of TTh-Por-TTh, first cycle	70
3.5	Post growth CVs of TTh-Por-TTh, cycles 1-5	70
3.6	Post growth CV of TTh-ZnPor-TTh, first cycle	72
3.7	Post growth CVs of TTh-ZnPor-TTh, cycles 1-5	72
3.8	RBS spectrum showing regions of interest for film durability test	73
3.9	Plot of film durability, accumulated charge vs counts	75
3.10	RBS of TTh-Por-TTh	76
3.11	RBS of TTh-Por-TTh cycled in ZnOAc	77
3.12	RBS of TTh-Por-TTh soaked in ZnOAc	78
3.13	RBS of TTh-ZnPor-TTh	79
3.14	Flow diagram of steps to obtain elemental results for TTh-Por-TTh and TTh-ZnPor-TTh samples	80
3.15	PIXE spectrum of TTh-Por-TTh	86
4.1	Accumulated charge for polymer durability of PPy-DBS film	92
4.2	PIXE spectrum for PPy-DBS, solution side	94
4.3	PIXE spectrum for PPy-NBS, solution side	94
4.4	PIXE spectrum for PPy-HBS, solution side	95
4.5	PIXE spectrum for PPy-MS, solution side	95
4.6	PIXE spectrum for PPy-SB, solution side	96
4.7	PIXE spectrum for PPy-PTS, solution side	96
4.8	Overlaid PIXE spectra for PPy-DBS film, solution and electrode sides	98
4.9	Expanded PIXE spectrum pf PPy-DBS	99

4.10	Overlaid high energy region RBS spectra for solution and electrode sides of PPy-DBS film	102
4.11	Simulation of high energy region of PPy-DBS film, electrode side	103
4.12	RBS simulation and data for PPy-DBS film, solution side	105
4.13	RBS simulation and data for PPy-NBS film, solution side	106
4.14	RBS simulation and data for PPy-HBS film, solution side	107
4.15	RBS simulation and data for PPy-MS film, solution side	108
4.16	RBS simulation and data for PPy-SB film, solution side	109
4.17	RBS simulation and data for PPy-PTS film, solution side	110
4.18	Flow diagram of steps undertaken to obtain monomer to counter ion ratios and layer thicknesses of PPy films	112
4.19	Pictorial figure of monomer to counter ion ratios for solution sides of PPy films	114
4.20	Example from spreadsheet of monomer to counter ion ratios for the combustion analysis	116
5.1	Chemical structure of TTh-Fc monomer	120
5.2	Chemical structures of Bridging TTh, bithiophene and EDOT	124
5.3	Overlaid CVs of 1:20 TTh-Fc / Py solution	126
5.4	Overlaid CVs of 1:20 TTh-Fc / Bithiophene solution	126
5.5	Overlaid CVs of 1:20 TTh-Fc / EDOT solution	128
5.6	Overlaid CVs of 1:20 TTh-Fc / TTh-Por-TTh solution	128
5.7	Overlaid CVs of 1:20 TTh-Fc / Bridging TTh solution	130
5.8	Three overlaid CVs of TTh-Fc monomer	130
5.9	Two overlaid CVs of Py monomer	131
5.10	Three overlaid CVs of bithiophene monomer	131
5.11	Three overlaid CVs of EDOT monomer	132
5.12	Post polymerisation CVs for 1:20 TTh-Fc / Py film, first five cycles	132
5.13	Post polymerisation CVs for 1:20 TTh-Fc / bithiophene film, first five cycles	135
5.14	Post polymerisation CVs for 1:20 TTh-Fc / EDOT film, first five cycles	135
5.15	Post polymerisation CVs for 1:20 TTh-Fc / TTh-Por-TTh film, first five cycles	136

5.16	Post polymerisation CVs for 1:20 TTh-Fc / Bridging TTh film, first five cycles	136
6.1	Flow diagram of Model I	140
6.2	Four 1:10 TTh-Fc / Py RBS spectra with varying thicknesses	142
6.3	Flow diagram of Model II	144
6.4	Schematic RBS spectra displaying roughness factor effects	145
6.5	SEM images of 1:100 TTh-Fc / Py copolymer	147
6.6	Schematic diagram showing which layer in simulation would have roughness associated with it	148
6.7	Overlaid RBS showing roughness effects	149
6.8	Flow diagram of Model III	150
6.9	Three RBS simulations for a bithiophene copolymer with varying elemental composition	152
6.10	Flow diagram of Model IV	155
7.1	Schematic RBS of a Type 1 spectrum	190
7.2	Schematic RBS of a Type 2 spectrum	191
7.3	Schematic RBS of a Type 3 spectrum	192
7.4	Schematic sample structural diagram and Type 1 spectrum	193
7.5	Schematic sample structural diagram and Type 2 spectrum	194
7.6	Schematic sample structural diagram and Type 3 spectrum	195
7.7	Schematic diagram indicating which layer requires roughness	196
7.8	Accumulated charge for polymer durability of 1:10 TTh-Fc / Py film, solution side	197
7.9	RBS experimental and simulated spectra for the solution side of a TTh-Fc / Py copolymer (1:10) using a 2.5 MeV proton beam, as simulated by Matej Mayer	199
7.10	Experimental and simulated RBS spectra for electrode side of 1:10 TTh-Fc / Py copolymer	200
7.11	Experimental and simulated RBS spectra for solution side of 1:20 TTh-Fc / Py copolymer	201
7.12	Experimental and simulated RBS spectra for electrode side of 1:20 TTh-Fc / Py copolymer	201
7.13	Experimental and simulated RBS spectra for solution side of 1:50 TTh-Fc / Py copolymer	202

7.14	Experimental and simulated RBS spectra for electrode side of 1:50 TTh-Fc / Py copolymer	202
7.15	Experimental and simulated RBS spectra for solution side of 1:100 TTh-Fc / Py copolymer	203
7.16	Experimental and simulated RBS spectra for electrode side of 1:100 TTh-Fc / Py copolymer	203
7.17	SEM images of solution and electrode sides of 1:10 TTh-Fc / Py copolymer	204
7.18	SEM images of solution and electrode sides of 1:20 TTh-Fc / Py copolymer	205
7.19	SEM images of solution and electrode sides of 1:50 TTh-Fc / Py copolymer	206
7.20	SEM images of solution and electrode sides of 1:100 TTh-Fc / Py copolymer	207
7.21	Plot of Py / TTh-Fc ratios with depth into the solution side of TTh-Fc / Py copolymers	210
7.22	Plot of counter ion / TTh-Fc ratios with depth into the solution sides of the TTh-Fc / Py copolymers	210
7.23	Plot of Py / TTh-Fc ratios with depth into the electrode side of TTh-Fc / Py copolymers	211
7.24	Plot of counter ion / TTh-Fc ratios with depth into the electrode sides of the TTh-Fc / Py copolymers	211
7.25	Experimental and simulated RBS spectra for solution side of 1:10 TTh-Fc / Bithiophene copolymer	212
7.26	Experimental and simulated RBS spectra for electrode side of 1:10 TTh-Fc / Bithiophene copolymer	212
7.27	SEM images of solution and electrode sides of 1:10 TTh-Fc / Bithiophene copolymer	213
7.28	Experimental and simulated RBS spectra for solution side of 1:20 TTh-Fc / Bithiophene copolymer	214
7.29	Experimental and simulated RBS spectra for electrode side of 1:20 TTh-Fc / Bithiophene copolymer	214
7.30	SEM images of solution and electrode sides of 1:20 TTh-Fc / Bithiophene copolymer	215

7.31	Experimental and simulated RBS spectra for solution side of 1:50 TTh-Fc / Bithiophene copolymer	216
7.32	Experimental and simulated RBS spectra for electrode side of 1:50 TTh-Fc / Bithiophene copolymer	216
7.33	SEM images of solution and electrode sides of 1:50 TTh-Fc / Bithiophene copolymer	217
7.34	Experimental and simulated RBS spectra for solution side of 1:100 TTh-Fc / Bithiophene copolymer	218
7.35	Experimental and simulated RBS spectra for electrode side of 1:100 TTh-Fc / Bithiophene copolymer	218
7.36	SEM images of solution and electrode sides of 1:100 TTh-Fc / Bithiophene copolymer	219
7.37	Plot of Bithiophene / TTh-Fc ratios with depth into the solution side of TTh-Fc / Bithiophene copolymers	222
7.38	Plot of counter ion / TTh-Fc ratios with depth into the solution sides of the TTh-Fc / Bithiophene copolymers	222
7.39	Plot of Bithiophene / TTh-Fc ratios with depth into the electrode side of TTh-Fc / Bithiophene copolymers	223
7.40	Plot of counter ion / TTh-Fc ratios with depth into the electrode sides of the TTh-Fc / Bithiophene copolymers	223
7.41	Experimental and simulated RBS spectra for solution side of 1:10 TTh-Fc / EDOT copolymer	224
7.42	Experimental and simulated RBS spectra for electrode side of 1:10 TTh-Fc / EDOT copolymer	224
7.43	SEM images of solution and electrode sides of 1:10 TTh-Fc / EDOT copolymer	225
7.44	Experimental and simulated RBS spectra for solution side of 1:20 TTh-Fc / EDOT copolymer	226
7.45	SEM images of solution and electrode sides of 1:20 TTh-Fc / EDOT copolymer	227
7.46	Experimental and simulated RBS spectra for solution side of 1:50 TTh-Fc / EDOT copolymer	228
7.47	Experimental and simulated RBS spectra for electrode side of 1:50 TTh-Fc / EDOT copolymer	228

7.48	SEM images of solution and electrode sides of 1:50 TTh-Fc / EDOT copolymer	229
7.49	Experimental and simulated RBS spectra for solution side of 1:100 TTh-Fc / EDOT copolymer	230
7.50	SEM images of solution and electrode sides of 1:100 TTh-Fc / EDOT copolymer	231
7.51	Plot of EDOT / TTh-Fc ratios with depth into the solution side of TTh-Fc / EDOT copolymers	234
7.52	Plot of counter ion / TTh-Fc ratios with depth into the solution sides of the TTh-Fc / EDOT copolymers	234
7.53	Plot of EDOT / TTh-Fc ratios with depth into the electrode side of TTh-Fc / EDOT copolymers	235
7.54	Plot of counter ion / TTh-Fc ratios with depth into the electrode sides of the TTh-Fc / EDOT copolymers	235
7.55	Experimental and simulated RBS spectra for electrode side of 2:1 TTh-Fc / TTh-Por-TTh copolymer	236
7.56	Experimental and simulated RBS spectra for solution side of 2:1 TTh-Fc / TTh-Por-TTh copolymer	236
7.57	SEM images of solution and electrode sides of 2:1 TTh-Fc / TTh-Por-TTh copolymer	237
7.58	Experimental and simulated RBS spectra for electrode side of 1:5 TTh-Fc / TTh-Por-TTh copolymer	238
7.59	Experimental and simulated RBS spectra for solution side of 1:5 TTh-Fc / TTh-Por-TTh copolymer	238
7.60	SEM images of solution and electrode sides of 1:5 TTh-Fc / TTh-Por-TTh copolymer	239
7.61	Experimental and simulated RBS spectra for solution side of 2:5 TTh-Fc / TTh-Por-TTh copolymer	240
7.62	Experimental and simulated RBS spectra for electrode side of 2:5 TTh-Fc / TTh-Por-TTh copolymer	240
7.63	SEM images of solution and electrode sides of 2:5 TTh-Fc / TTh-Por-TTh copolymer	241
7.64	Experimental and simulated RBS spectra for solution side of 1:1 TTh-Fc / TTh-Por-TTh copolymer	242

7.65	Experimental and simulated RBS spectra for electrode side of 1:1 TTh-Fc / TTh-Por-TTh copolymer	242
7.66	SEM images of solution and electrode sides of 1:1 TTh-Fc / TTh-Por-TTh copolymer	243
7.67	Plot of TTh-Por-TTh / TTh-Fc ratios with depth into the solution side of TTh-Fc / TTh-Por-TTh copolymers	246
7.68	Plot of counter ion / TTh-Fc ratios with depth into the solution sides of the TTh-Fc / TTh-Por-TTh copolymers	246
7.69	Plot of TTh-Por-TTh / TTh-Fc ratios with depth into the electrode side of TTh-Fc / TTh-Por-TTh copolymers	247
7.70	Plot of counter ion / TTh-Fc ratios with depth into the electrode sides of the TTh-Fc / TTh-Por-TTh copolymers	247
7.71	Experimental and simulated RBS spectra for electrode side of 1:10 TTh-Fc / Bridging TTh copolymer	248
7.72	Experimental and simulated RBS spectra for solution side of 1:10 TTh-Fc / Bridging TTh copolymer	248
7.73	SEM images of solution and electrode sides of 1:10 TTh-Fc / Bridging TTh copolymer	249
7.74	Experimental and simulated RBS spectra for electrode side of 1:1 TTh-Fc / Bridging TTh copolymer	250
7.75	Experimental and simulated RBS spectra for solution side of 1:1 TTh-Fc / Bridging TTh copolymer	250
7.76	SEM images of solution and electrode sides of 1:1 TTh-Fc / Bridging TTh copolymer	251
7.77	Experimental and simulated RBS spectra for electrode side of 10:1 TTh-Fc / Bridging TTh copolymer	252
7.78	Experimental and simulated RBS spectra for solution side of 10:1 TTh-Fc / Bridging TTh copolymer	252
7.79	SEM images of solution and electrode sides of 10:1 TTh-Fc / Bridging TTh copolymer	253
7.80	Plot of Bridging TTh / TTh-Fc ratios with depth into the solution side of TTh-Fc / Bridging TTh copolymers	256
7.81	Plot of counter ion / TTh-Fc ratios with depth into the solution sides of the TTh-Fc / Bridging TTh copolymers	256

7.82	Plot of Bridging TTh / TTh-Fc ratios with depth into the electrode side of TTh-Fc / Bridging TTh copolymers	257
7.83	Plot of counter ion / TTh-Fc ratios with depth into the electrode sides of the TTh-Fc / Bridging TTh copolymers	257
7.84	Schematic diagrams of cell set up with Pt wire and gauze counter electrodes	258
7.85	Schematic diagram showing film variation experiment beam spot positions	259
7.86	Overlaid experimental RBS 1:10 TTh-Fc / Bridging TTh film with Pt wire counter electrode	260
7.87	Overlaid experimental RBS 1:10 TTh-Fc / Bridging TTh film with Pt gauze counter electrode	260
A.1	RBS experimental spectrum for the solution side of a TTh-Fc / Py copolymer (1:10)	290
A.2	RBS experimental spectrum for the electrode side of a TTh-Fc / EDOT copolymer (1:20)	291
A.3	RBS experimental spectrum for the solution side of a TTh-Fc / EDOT copolymer (1:100)	291

List of Tables

<u>Number</u>	<u>Description</u>	<u>Page</u>
1.1	Names and idealised structures of some widely studied conducting polymers	5
1.2	Conductive and electroactive applications of conducting polymers	13
2.1	The five main IBA techniques used at GNS	29
2.2	k -factor and E_1 energies for a selection of elements for a 2.5 MeV $^4\text{He}^+$ beam, $\theta = 170^\circ$	43
3.1	A list of elements in TTh-Por-TTh sample as expected from chemical stoichiometry	82
3.2	A list of common unexpected elements found from TTh-Por-TTh RBS spectra	82
4.1	Qualitative and quantitative results for solution and electrode sides of PPy-DBS film	101
4.2	Monomer to counter ion ratios with depth into PPy polymer films	113
5.1	Copolymer monomers and their associated deposition potentials and growth times	134
5.2	Copolymer monomers and their associated deposition potentials and the number of cycles required to produce films for post polymerisation CV analysis	137
7.1	A list of some examples of other parameters used in the simulation of 1:10 TTh-Fc / Bridging TTh copolymer	167
7.2	Layer thickness, roughness factors, and total analysis depth of all TTh-Fc / Py copolymers	180
7.3	Py / TTh-Fc monomer ratios and counter ion / TTh-Fc ratios for all TTh-Fc / Py copolymers	181
7.4	Layer thickness, roughness factors, and total analysis depth of all TTh-Fc / Bithiophene copolymers	195
7.5	Bithiophene / TTh-Fc monomer ratios and counter ion / TTh-Fc ratios for all TTh-Fc / Bithiophene copolymers	197

7.6	Layer thickness, roughness factors, and total analysis depth of all TTh-Fc / EDOT copolymers	213
7.7	EDOT / TTh-Fc monomer ratios and counter ion / TTh-Fc ratios for all TTh-Fc / EDOT copolymers	214
7.8	Layer thickness, roughness factors, and total analysis depth of all TTh-Fc / TTh-Por-TTh copolymers	230
7.9	TTh-Por-TTh / TTh-Fc monomer ratios and counter ion / TTh-Fc ratios for all TTh-Fc / TTh-Por-TTh copolymers	232
7.10	Layer thickness, roughness factors, and total analysis depth of all TTh-Fc / Bridging TTh copolymers	245
7.11	Bridging TTh / TTh-Fc monomer ratios and counter ion / TTh-Fc ratios for all TTh-Fc / Bridging TTh copolymers	246
A.1	RBS simulation data for TTh-Por-TTh spectrum in Chapter 3	280
A.2	RBS simulation data for cycled TTh-Por-TTh spectrum in Chapter 3	280
A.3	RBS simulation data for soaked TTh-Por-TTh spectrum in Chapter 3	281
A.4	RBS simulation data for the TTh-ZnPor-TTh sample from Chapter 3	281
A.5	RBS simulation data for the solution side PPy-DBS film from Chapter 4	282
A.6	RBS simulation data for the solution side PPy-NBS film from Chapter 4	282
A.7	RBS simulation data for the solution side PPy-HBS film from Chapter 4	283
A.8	RBS simulation data for the solution side PPy-MS film from Chapter 4	283
A.9	RBS simulation data for the solution side PPy-SB film from Chapter 4	284
A.10	RBS simulation data for the solution side PPy-PTS film from Chapter 4	284
A.10	Parameters other than copolymer monomers and ClO_4^- used in the calculations of copolymer to TTh-Fc ratios and counter ion to TTh-Fc ratios.	285

A.12	Un-simulated copolymer films and their spectrum type	292
A.13	RBS simulation data for the solution side 1:10 TTh-Fc / Py copolymer film from Chapter 7	293
A.14	RBS simulation data for the solution side 1:20 TTh-Fc / Py copolymer film from Chapter 7	293
A.15	RBS simulation data for the electrode side 1:20 TTh-Fc / Py copolymer film from Chapter 7	294
A.16	RBS simulation data for the solution side 1:50 TTh-Fc / Py copolymer film from Chapter 7	294
A.17	RBS simulation data for the solution side 1:100 TTh-Fc / Py copolymer film from Chapter 7	295
A.18	RBS simulation data for the solution side 1:100 TTh-Fc / Py copolymer film from Chapter 7	295
A.19	RBS simulation data for the electrode side 1:100 TTh-Fc / Py copolymer film from Chapter 7	296
A.20	RBS simulation data for the solution side 1:10 TTh-Fc / bithiophene copolymer film from Chapter 7	297
A.21	RBS simulation data for the electrode side 1:10 TTh-Fc / bithiophene copolymer film from Chapter 7	297
A.22	RBS simulation data for the solution side 1:20 TTh-Fc / bithiophene copolymer film from Chapter 7	298
A.23	RBS simulation data for the electrode side 1:20 TTh-Fc / bithiophene copolymer film from Chapter 7	298
A.24	RBS simulation data for the solution side 1:50 TTh-Fc / bithiophene copolymer film from Chapter 7	299
A.25	RBS simulation data for the electrode side 1:50 TTh-Fc / bithiophene copolymer film from Chapter 7	299
A.26	RBS simulation data for the solution side 1:100 TTh-Fc / bithiophene copolymer film from Chapter 7	300
A.27	RBS simulation data for the electrode side 1:100 TTh-Fc / bithiophene copolymer film from Chapter 7	300
A.28	RBS simulation data for the solution side 1:10 TTh-Fc / EDOT copolymer film from Chapter 7	301

A.29	RBS simulation data for the electrode side 1:10 TTh-Fc / EDOT copolymer film from Chapter 7	301
A.30	RBS simulation data for the solution side 1:20 TTh-Fc / EDOT copolymer film from Chapter 7	302
A.31	RBS simulation data for the solution side 1:50 TTh-Fc / EDOT copolymer film from Chapter 7	303
A.32	RBS simulation data for the electrode side 1:50 TTh-Fc / EDOT copolymer film from Chapter 7	303
A.33	RBS simulation data for the electrode side 1:100 TTh-Fc / EDOT copolymer film from Chapter 7	304
A.34	RBS simulation data for the solution side 2:1 TTh-Fc / TTh-Por-TTh copolymer film from Chapter 7	305
A.35	RBS simulation data for the electrode side 2:1 TTh-Fc / TTh-Por-TTh copolymer film from Chapter 7	305
A.36	RBS simulation data for the solution side 1:5 TTh-Fc / TTh-Por-TTh copolymer film from Chapter 7	306
A.37	RBS simulation data for the electrode side 1:5 TTh-Fc / TTh-Por-TTh copolymer film from Chapter 7	306
A.38	RBS simulation data for the solution side 2:5 TTh-Fc / TTh-Por-TTh copolymer film from Chapter 7	307
A.39	RBS simulation data for the electrode side 2:5 TTh-Fc / TTh-Por-TTh copolymer film from Chapter 7	307
A.40	RBS simulation data for the solution side 1:1 TTh-Fc / TTh-Por-TTh copolymer film from Chapter 7	308
A.41	RBS simulation data for the electrode side 1:1 TTh-Fc / TTh-Por-TTh copolymer film from Chapter 7	308
A.42	RBS simulation data for the solution side 1:10 TTh-Fc / Bridging TTh copolymer film from Chapter 7	309
A.43	RBS simulation data for the electrode side 1:10 TTh-Fc / Bridging TTh copolymer film from Chapter 7	309
A.44	RBS simulation data for the solution side 1:1 TTh-Fc / Bridging TTh copolymer film from Chapter 7	310
A.45	RBS simulation data for the electrode side 1:1 TTh-Fc / Bridging TTh copolymer film from Chapter 7	310

A.46	RBS simulation data for the solution side	
	10:1 TTh-Fc / Bridging TTh copolymer film from Chapter 7	311
A.47	RBS simulation data for the electrode side	
	10:1 TTh-Fc / Bridging TTh copolymer film from Chapter 7	311

List of Schemes

<u>Number</u>	<u>Description</u>	<u>Page</u>
4.1	Chemical scheme of the production of polypyrrole electrochemically	89
5.1	Chemical scheme of the production of terthiophene-ferrocene copolymer films electrochemically	121, 189

List of symbols

<u>Symbol</u>	<u>Description</u>	<u>Unit</u>
c	calibration off set	keV
dQ	number of particles recorded by the detector	
$dQ/d\Omega_i$	differential cross section	mb sr ⁻¹
$d\sigma/d\Omega$	differential scattering cross section	
D	diffusion coefficient	m ² s ⁻¹
e	electron charge, charge on a proton	μC
E	potential (electrochemistry), energy of incident ion (RBS)	mV MeV
E_0	initial potential (electrochemistry), energy of incident particle (RBS)	mV MeV
E_1	upper potential limit (electrochemistry), kinematic energy of incident particle (RBS)	mV MeV
E_2	final potential	mV
E_K	kinetic energy of incident alpha particle	keV
f_r	roughness factor	at cm ⁻²
F	Faraday constant	C mol ⁻¹
i	current density (electrochemistry) current density (IBA)	mA cm ⁻² nA cm ⁻²
I	element	
j	flux	m ⁻² s ⁻¹
k	Coulomb's constant, kinematic factor (RBS)	N m ² C ⁻²
K_α	X-ray produced from L-K shell	keV
K_β	X-ray produced from M-K shell	keV
l	depth	at cm ⁻²
L	thickness of target	cm
m	energy per channel	keV
M_0	mass of projectile ion	amu

M_1	mass of target atom	amu
n	linear response across all channels, number of electrons transferred (Fick's Law), number of atoms per unit volume in target (Scattering)	
N_i	number of incident alpha particles	counts
$(Nt)_i$	areal density	at cm ⁻²
$N(\theta)$	number of alpha particles scattered at angle θ	counts.msr
Q	total number of particles striking the target	
r	target to detector distance	cm
t	time	s
x	distance	m
Z	atomic number of target	
Z_1	atomic number of incident ion	
Z_2	atomic number of target atom	
$\delta c_{(x, t)} / \delta x$	concentration gradient	cm ⁻⁴
Δk	difference in k -factor	
ΔE_1	energy separation between particles scattered by two different target elements	MeV
ΔM_1	mass difference	amu
$\Delta \Omega$	solid angle	sr
ε	stopping cross section factor	
$\varepsilon(E_{K,1}), \varepsilon(E_0)$	stopping cross section incident energies	keV / micron
θ	scattering angle	°
θ_{out}	angle detector is set at	°
γ	gamma	keV
%	percent	

List of abbreviations

amu	atomic mass units
Bridging TTh	Bridging terthiophene
Bu_4N^+	tetrabutylammonium ion
CA	chronoamperometry
ClO_4^-	perchlorate ion
CRI	Crown Research Institute
CV	Cyclic voltammetry
DBS	dodecylbenzenesulfonate
DCM	dichloromethane
DMSO	dimethyl sulfoxide
DSRI	Department of Scientific and Industrial Research
EDOT	3,4-Ethylenedioxythiophene
ERD	Elastic recoil detection
GC	Glassy carbon
GNS	Geological and Nuclear Sciences
HBS	4-hydroxybenzenesulfonate
IBA	Ion beam analysis
ICP	intrinsically conducting polymers
INS	Institute of Nuclear Sciences
ITO	Indium tin oxide
LOD	limit of detection
MS	methane sulfonate
NBS	3-nitrobenzenesulfonate
NMR	nuclear magnetic resonance
NRA	Nuclear reaction analysis
PIGE	Proton induced gamma-ray emission
PIXE	Proton induced X-ray emission
PTS	4-toluenesulfonate
Py	pyrrole
PPy	Polypyrrole

RBS	Rutherford backscattering spectrometry
RHS	right hand side
SB	4-sulfobenzoate
SEM	Scanning electron microscope
SHE	Standard hydrogen electrode
Si(Li)	Lithium drifted silicon
SIM	simulation mode
TaO	Tantalum oxide
TBAHFP	tetrabutylammonium hexafluoro-phosphate
TBAP	tetrabutylammonium perchlorate
TBATFB	tetrabutylammonium tetrafluoroborate
TTh-Fc	terthiophene-ferrocene
TTh-Por-TTh	bis terthiophene porphyrin
TTh-ZnPor-TTh	zinc coordinated bis terthiophene porphyrin

CHAPTER 1

General Introduction

1.1 Introduction

Polymers and organic materials have been known and utilised for many years, although only recently have people been finding out about the intrinsic properties of semi-conductors that these polymers hold in some cases. Until the 1970's all carbon based polymers were rigidly regarded as insulators. Indeed, plastics have been extensively utilised by the electronics industry for their insulating properties. The idea that plastics could be made to conduct electricity would have been considered absurd [1].

The properties of conducting polymers which have made them very appealing are that they are lightweight, possess high tensile strength, are easy to chemically modify and customise, and that they have low temperature processability [2]. These properties have led to the replacement of many metals in applications, and the creation of original materials [2]. Over the last few decades conventional insulating polymer systems have increasingly been used as substitutes for structural materials as wood, ceramics, and metals [3].

This narrow perspective has been changing as a new class of polymers, known as intrinsically conducting polymers (ICP), or electroactive polymers, were discovered in 1977 by Alan MacDiarmid, Alan Heeger, and Hideki Shirakawa^[4-7] (this discovery led to their jointly awarded Noble Prize in Chemistry in 2000^[8-13]). ICPs have the potential of combining the high conductivities close to that of pure metals with the possibility, corrosion resistance, and low density of organic polymers^[14] and are beginning to find applications in the fields such as battery materials^[15-18], electrochemical drug-delivery systems^[19], electrochemical displays^[20], electromagnetic shielding^[21], sensor technology^[22], electrochemical actuators^[15, 23], and anti-corrosion agents^[24].

1.2 Conducting polymers

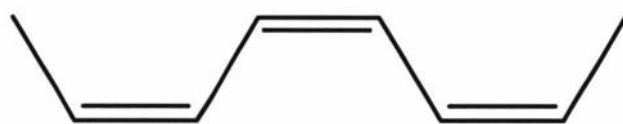
The conjugate π system which conducting polymers possess, similar to that of semi-conductors, extends over a large number of recurrent monomer units. However, unlike semi-conductors which are atomic solids, organic π -electron materials are typically amorphous polymeric materials. Comprising generally of only C, H, and simple heteroatoms such as N and S, the intrinsic conductivity of these organic materials arises uniquely from π -conjugation [25].

The conductivity of conducting polymers is achieved through either simple chemical or electrochemical oxidation, or in some cases reduction, by a number of anionic or cationic dopants [26]. The polymeric backbone of these materials needs to be oxidised or reduced to introduce charge centres before conductivity is observed [12, 19, 26].

In the case of many conducting polymers, their non-conducting forms were well known before properties such as their conductivities were discovered, while others were known in their conductive forms, but not much interest had been paid to their conductivity and they had not been well characterised. For example the history of pyrrole dates back to 1916 when it was first prepared by the oxidation of pyrrole as powder called 'pyrrole black' [27]. However, not until 1968 was it noted that pyrrole could be electrochemically polymerised, using a variety of oxidation agents, to give a black conducting powder [28].

1.2.1 Polyacetylene

Although there have been materials which might be considered electrically conductive polymers, such as filled polymers and aniline black, which were known at the beginning of the last century, large scale interest in conducting polymers is a relatively recent occurrence. The current interest in conducting polymers began in the 1970s when it was found that the electrical conductivity of polyacetylene could be increased by 12 orders of magnitude by treatment with oxidising agents such as iodine [4]. Owing to its simplistic conjugated structure and high conductivity (10^4 - 10^6 S cm⁻¹) polyacetylene has become the most theoretically and experimentally studied conducting polymer [28]. Most research on polyacetylene has been performed on the 'Shirakawa' type, which is synthesised via the Ziegler-Natta polymerisation of acetylene [29, 30]. Polyacetylene is formed as two isomers, (*E*) and (*Z*) (Fig. 1.1), of



(*Z*)-isomer



(*E*)-isomer

Fig. 1.1 Chemical structures (*Z*)-isomer (above) and of (*E*)-isomer (below) of polyacetylene.

which the (*E*)-form is the more conducting and thermodynamically stable. The relative proportion of the two isomers depends upon the reaction temperature, solvent, and the nature of the catalyst. It is possible to obtain polyacetylene as a gel, powder, or thin film by varying the catalyst concentration in the solvent ^[31].

Polyacetylene produced by this method has two main disadvantages. First, the electrical conductivity decreases rapidly upon exposure to air and secondly, the polymer is entirely intractable. The exposure to air results in the formation of carbonyl, hydroxyl, and epoxide groups, these all leading to the destruction of the conjugated structure. A modified version of the Shirakawa process, the Naarman process, results in a product which is much more environmentally stable ^[32].

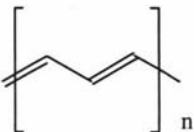
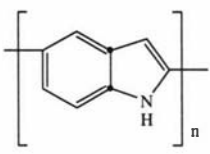
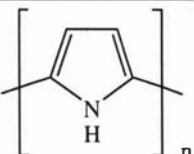
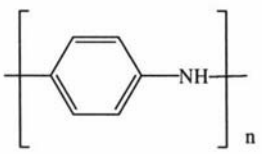
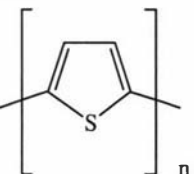
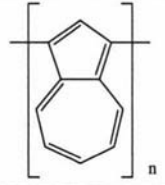
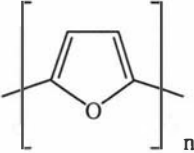
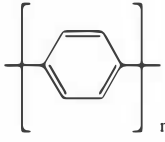
1.2 Polyheterocycles as conducting polymers

The synthesis of polyacetylene in the highly conducting doped form was the starting point for several studies, even though studies of the electrochemical oxidation of aromatic monomers had been reported since 1957 under various descriptions such as “electro-organic preparations” and “electro-oxidations” ^[33]. It was the electrochemical deposition of free standing polypyrrole from organic media ^[34] which opened the door to the intensive research into the use of heterocyclic and aromatic compounds to form conducting polymers ^[35].

The electrochemical oxidation of these resonance-stabilised aromatic molecules has become one of the principal methods of preparing conjugated, electronically conducting polymers. Since the first reports of the oxidation of pyrrole, many other aromatic systems have been found to undergo electrochemical polymerisation to produce conducting polymers. Some of these molecules include thiophene ^[36-39], furan ^[36], aniline ^[40-42], as well as many substituted multi-ring and polynuclear aromatic hydrocarbon systems. The structures of some of these aromatic systems and polyacetylene are displayed in Table 1.1.

All resulting polymers have a conjugated backbone which is required for electroactivity. In addition, the polymers are electrochemically oxidised to their doped states as they are formed. This oxidation necessitates the incorporation of charge the

Table 1.1 Names and idealised structures of some of the most widely studied conducting polymers.

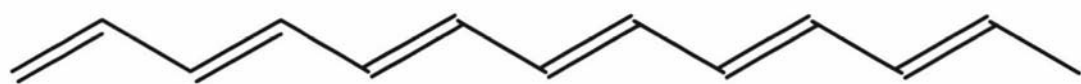
POLYMER	STRUCTURE	POLYMER	STRUCTURE
Polyacetylene		Polyindole	
Polypyrrole		Polyaniline	
Polythiophene		Polyazulene	
Polyfuran		Poly-para-phenylene	

compensating anions, also known as dopants, or counter ions, in the oxidised film to maintain electroneutrality.

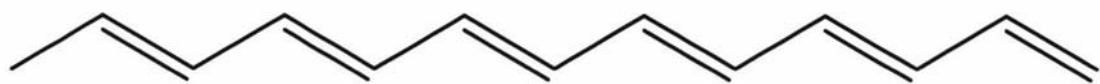
1.2 Mechanisms of conduction

Mechanisms for the electronic conductivity and nature of charge carries in conjugated polymers are still a subject of debate. There are various theoretical models for the electronic conductivity of conjugated polymers.

Conjugated polymers with a degenerate ground state, for example (*E*)-polyacetylene (Fig. 1.2 (a) and (b)), produce structural defects in polymer chains, causing a bond alternation (Fig. 1.2 (c)). At the defect site, a single unpaired electron is thought to exist, although the overall charge remains zero, creating a new energy level (a non-bonding orbital). Since the ground state structure of such polymers are two-fold degenerate, the charged cations are not bound to each other by a higher energy bonding configuration and can freely separate along the chain. The effect of this is that the charged defects are independent of one another and can form domain walls that separate two phases of opposite orientation and identical energy. This neutral defect state, known as a 'soliton', is singly occupied, possessing a spin of $1/2$, and is delocalised over about fifteen carbon atoms ^[11, 43]. The energy level of the soliton can accommodate zero, one, or two electrons, which means the soliton may be positively or negatively charged, giving the unusual property of separating spin and charge, with neutral solitons possessing spin, but no charge, and charged solitons having no spin. In a doped polymer, charge is located in the mid-gap states, since these provide the HOMO for charge removal and the LUMO for charge injection. Since a defect can occur anywhere along the chain, there is translational symmetry in the system, providing mobility of the soliton along the chain, offering a mechanism for electronic conductivity. Two neutral solitons usually recombine eliminating structural defects, although single solitons can arise on chains with imperfections ^[44]. In contrast, charged solitons repel each other and lead to isolated defects ^[43]. A neutral and a charged soliton can however achieve a minimum energy configuration by pairing ^[45] producing a 'polaron', which is essentially a radical cation, and gives rise to two states in the band gap, a bonding and anti bonding orbital, with symmetry placed about the mid-gap energy. At higher doping levels, the charged solitons interact with



(a)



(b)



(c)

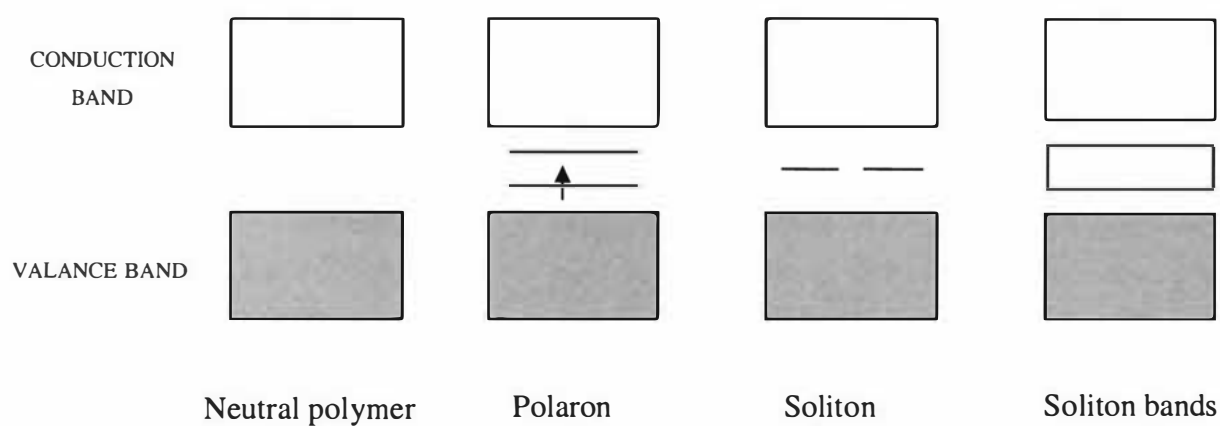


Fig. 1.2 The two degenerate (*E*)-structures of polyacetylene (a) and (b); (c) shows a soliton at a phase boundary between the two degenerate (*E*)-phases of polyacetylene, where the bond alternation is reversed.

each other to form a soliton band which eventually merges with the band edges to create metallic-like conductivity.

Of all the conjugated polymers (*E*)-Polyacetylene is the only polymer which possesses a degenerate ground-state. All other conjugated polymers possess non-degenerate ground states, and this affects the nature of charges which they can support^[46]. In these polymers where two non-degenerate regions are separated by a defect, the formation of single solitons is energetically unfavourable^[43] and paired sites are formed^[45]. This is the case for polypyrrole, which can be represented by either aromatic or quinoid structures (Fig. 1.3 (a) and (b) respectively) of which the latter possess a higher energy configuration. In the oxidative doping of polypyrrole an electron is removed from the π -system backbone producing a free radical and a spinless positive charge^[25]. The radical and cation are coupled to each other via local resonance of the charge and the radical. In this case, the consideration of quinoid-like rings is appropriate. The distortion produced by this is of higher energy than the remaining portion of the chain. The creation and separation of these defects costs a considerable amount of energy. This limits the number of quinoid-like rings that can link together. Two neutral radicals on a single chain will recombine to eliminate a structural defect and in the case of polypyrrole it is believed that this is delocalised over four pyrrole rings^[43] (Fig. 1.3 (c)). This could be either a radical cation or radical anion. This creates a new localised electronic state in the band gap, with the lower energy states located about 0.5 eV from the band edges. Upon further oxidation the free radical of the polaron is removed, creating a new spinless defect called a 'bipolaron'^[43] (Fig. 1.3 (d)). This is of lower energy than the creation of two distinct polarons. At higher doping levels it becomes possible that two polarons combine to form a bipolaron, thus at higher doping level the polarons are replaced with bipolarons^[26]. The bipolarons are located symmetrically with a band gap of 0.75 eV for polypyrrole. With continued doping these eventually form into continuous bipolaron bands. Their band gap also increases as new bipolarons are made at the expense of the band edges. For a very heavily doped polymer it is conceivable that the upper and lower conduction and valence bands respectively to produce partially filled bands and metallic like conductivity.

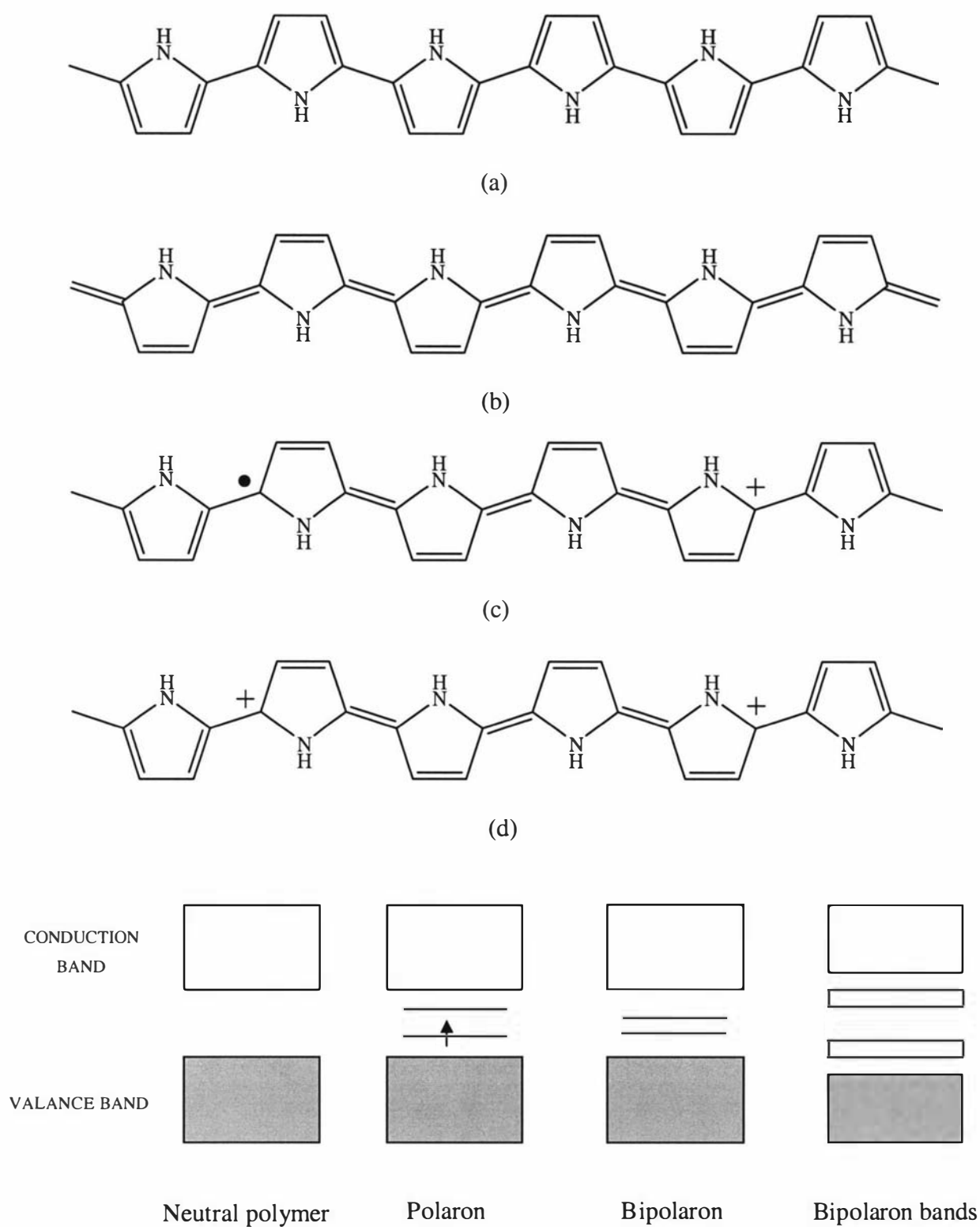


Fig. 1.3 Possible structures of polypyrrole showing the non-degenerate aromatic (a) and quinoid (b) configurations, and a polaron defect (c), and a bipolaron defect (d).

1.5 Copolymers

When two different monomer units are combined into polymer chains, these materials are known as copolymers. Two means of forming copolymers are through chemical or electrochemical polymerisation. The copolymers formed in this work were achieved so by electrochemical polymerisation.

There are four main types of copolymers which may be formed. The first type is grafted copolymers^[47]. If chains of a homopolymer are attached onto a backbone of polymer chains consisting of a different monomer one forms grafted copolymers^[47, 48] (Fig. 1.4 (a)). One example of a graft copolymer is high-impact polystyrene. This copolymer has a polystyrene backbone with chains of polybutadiene grafted onto the backbone. The polystyrene provides the material strength, but the incorporation of polybutadiene chains affords material resilience, and makes the resulting copolymer less brittle. The second type of copolymers are block copolymers, where one type of monomers are grouped together, and the other monomers are grouped together in discrete sequences^[49, 50] (Fig 1.4 (b)). A block copolymer can be thought of as two short chains of homopolymers joined together. Using the same monomers as in the high-impact polystyrene example, provides an example of a block copolymer. The rubber used for soles of shoes and tire treads are both examples of block copolymers of poly(styrene-butadiene-styrene). The third type of copolymer are those which are arranged in an alternating fashion, and these are referred to as alternating copolymers (Fig. 1.4 (c))^[51, 53]. The last types of copolymers are random copolymers^[54]. As the name suggests, the two monomers may be arranged in any fashion (Fig. 1.4 (d)).

The main disadvantage of using chemical or electrochemical polymerisation techniques to form copolymers is that the composition of the copolymer materials produced in this way does not always correspond to the composition of the solution from which the material was polymerised^[55]. It would be difficult to know if the copolymer had formed as a alternating, random, or block copolymer.

1.6 Applications

The extended π -systems of conjugated polymers are highly susceptible to chemical or electrochemical oxidation or reduction. These alter the electrical and optical

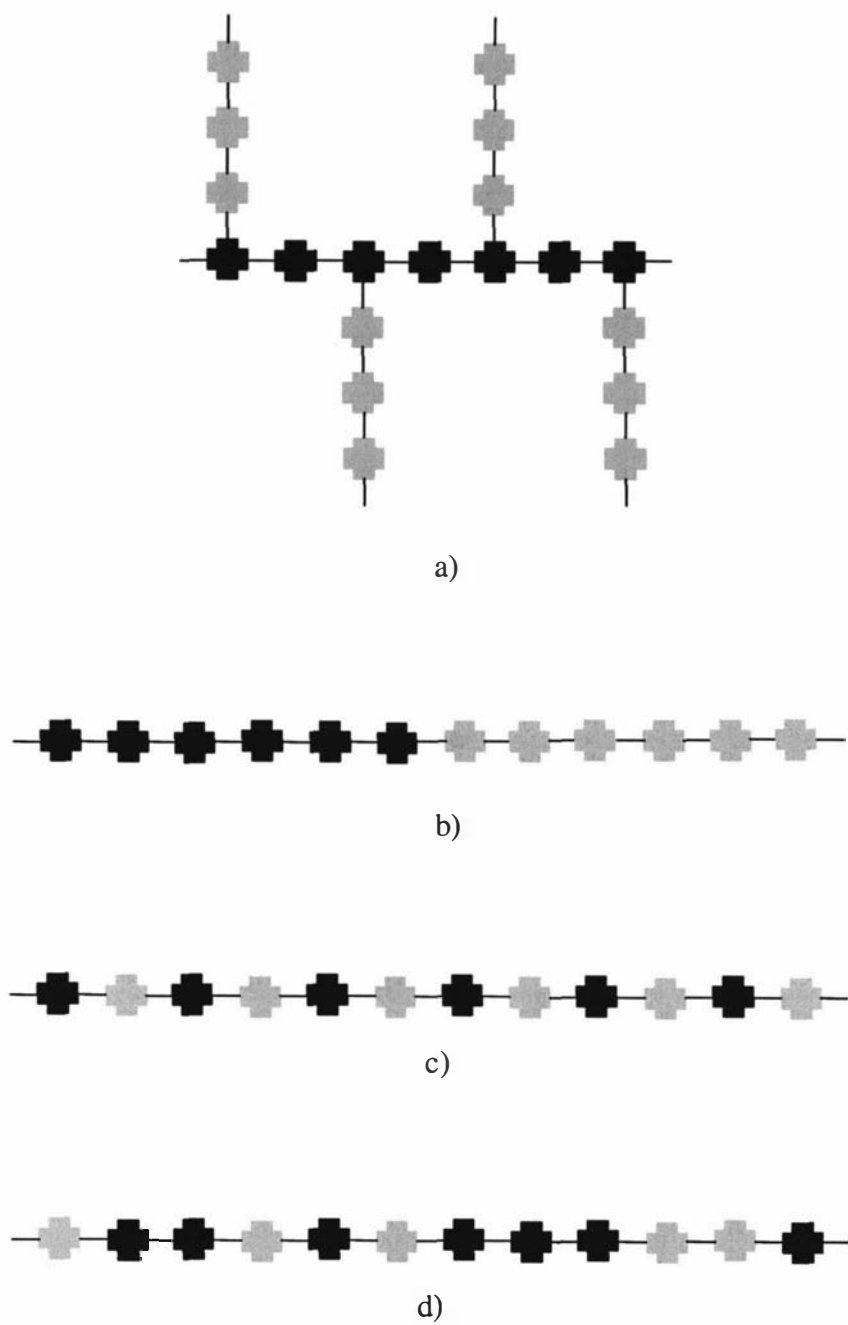


Fig. 1.4 Schamatic diagram of the four main types of copolymers, a) grafted, b) block, c) alternating, d) random copolymers.

properties of the polymer, and by controlling this oxidation and reduction, it is possible to precisely control the electrical and optical properties with a great deal of precision. It is even possible to switch from a conducting to insulating state.

There are two main groups for the applications of conducting polymers. Firstly, those whose conductivities are mainly utilised, and secondly, those whose electrochemical functionalities are utilised. Some examples of different applications of each of these two groups can be seen in Table 1.2.

1.6.1 *Rechargeable batteries*

Over the last 15 years or so many different research groups have been working on the development of lithium polymer batteries. Up until 1987 all the billions of batteries in all the variety of shapes and sizes had one common feature, to make electricity they depended exclusively upon chemical reactions involving the metal components of the battery.

Using polypyrrole, polythiophene, polyaniline, and derivatives of these polymers, as cathodes in “plastic batteries”, rechargeable batteries based on conducting polymers were one of the first commercial products to be released using conducting polymers^[83]. The anodes of the batteries are usually lithium or some lithium alloy, such as lithium-aluminium^[84, 85], but other metals can be used, such as zinc^[86].

During discharge, electrons flow from the anode to the cathode through the external circuit. This reduces the p-doped polymer cathode, and as reduction takes place the dopant anions are ejected from the polymer into the electrolyte. The lithium at the anode dissolves into the electrolyte as lithium ions, simultaneously as the dopants are ejected into the electrolyte.

Once the entire polymer has reached the neutral state the cell is fully discharged. To recharge, an opposite current is applied to the electrodes. During recharging the polymer cathode is oxidised and removes dopant ions from the electrolyte, while lithium ions deposit at the anode as lithium metal.

Table 1.2 A list of possible uses of conducting polymers under the headings of conductivity and electroactivity.

CONDUCTIVITY	ELECTROACTIVITY
Electrostatic materials ^[56, 57]	Molecular electronic ^[68, 69]
Conducting adhesives ^[58, 59]	Electrical displays ^[60, 70]
Electromagnetic shielding ^[60, 61]	Chemical/ biochemical sensors ^[71-74]
Printed circuit boards ^[60, 62-64]	Rechargeable batteries ^[75, 76]
Antistatic clothing ^[65, 66]	Ion exchange membranes ^[77, 78]
Piezoceramics ^[67]	Electromechanical actuators ^[79-82]

These electrodes have poor performance due to the lithium anode. During charging when the lithium is plated onto the anode, dendrites tend to form. These dendrites can grow to a considerable length and eventually can short-circuit cells internally ^[75].

1.7 Scope of this study

The principle objective of this research was to investigate the possibility and utility of using Ion Beam Analysis (IBA) techniques for the characterisation of soft, organic based materials, predominantly focusing on organic conducting polymers. IBA has been extensively used in the past for the modification of polymers through ion implantation ^[87-93], but the use in characterisation has not been reported.

A range of varying organic materials and conducting polymers were examined using IBA techniques and a novel method developed to interpret the resulting data.

- i) electrochemically deposited bis terthiophene porphyrin materials was examined to establish if useful information could be obtained from these IBA techniques (Chapter 3)
- ii) monomer to counter ion ratios were established for a range of polypyrrole (PPy) films electrochemically deposited with a variety of counter ions (Chapter 4)
- iii) new terthiophene-ferrocene based copolymers were electrochemically formed (Chapter 5) and examined using IBA
- iv) a novel approach to obtaining copolymer to terthiophene-ferrocene and counter ion to terthiophene-ferrocene ratios were developed (Chapter 6)
- v) this new approach was used to obtain depth profiling of these ratios for the terthiophene-ferrocene based copolymers

The electrochemical methods used in this work have predominantly been cyclic voltammetry and chronoamperometry, and the IBA techniques predominantly used have been Rutherford Backscattering Spectrometry (RBS) and Proton Induced X-ray Emission (PIXE).

CHAPTER 2

Experimental Methods

2.1 Introduction

The focus of this chapter is to provide an overview of

- the electrochemical methods and experimental conditions used for the deposition of organic materials onto electrode surfaces, and
- the use of ion beam analysis (IBA) techniques for the analysis of these electrochemically prepared materials.

This chapter does not attempt to provide an overview of all IBA techniques – rather it describes those techniques and their development at Geological and Nuclear Sciences (GNS), Lower Hutt, New Zealand.

Since these two areas do not overlap, this chapter will be divided into two distinct sections – those of electrochemical and IBA techniques.

Three types of films were prepared:

- a bis-terthiophene porphyrin film for the purposes of a scoping study;
- a range of polypyrrole (PPy) films; and
- terthiophene-ferrocene (TTh-Fc) copolymerised with PPy, bithiophene, 3,4-Ethylenedioxythiophene (EDOT), bridging terthiophene (Bridging TTh), and bis-terthiophene porphyrin (TTh-Por-TTh).

2.2 Electrochemistry

The electrochemistry was carried out in both aqueous and non-aqueous solvents, depending on monomer, at room temperature (20°C), in a range of electrolytes, concentrations, and working electrodes. Hydrodynamic control was not employed and static electrodes in quiescent solutions were employed in all cases.

2.2.1 *Potentiostatic and Galvanostatic Instrumentation*

Three different potentiostats were used for the deposition of organic materials onto electrode substrates during this work. The primary potentiostat used was a digital BAS 100B/W Electrochemical Analyzer and accompanying BAS 100 B/W Version 2.0 software (Bioanalytical Systems Inc., West Lafayette, Indiana, USA). The second was an analog CV-27 Cyclic Voltammograph (Bioanalytical Systems Inc., West Lafayette, Indiana, USA) in combination with a MacLab/2e, 12 bit analog-to-digital analyser to record electrode response (ADInstruments, Colorado Springs, Colorado, USA). Both the BAS100B/W and CV-27 were potentiostatic devices. The third instrument was used on those occasions when galvanostatic control was required. The device was an analog Model 362 Scanning Potentiostat (EG & G Instruments Inc., Princeton Applied Research, Oakridge, Tennessee, USA), the output of which was monitored with the MacLab/2e, 12 bit analog-to-digital analyser.

2.2.2 *Electrodes*

The potential of the working electrode in an electrochemical system is determined by the use of a potentiostat that controls the potential difference between the working electrode and the reference electrode by altering the current flowing through the working electrode and counter electrode (Fig. 2.1) ^[94]. The reference electrode serves purely as a reference potential and does not pass current ^[94].

The electrochemical reactions of interest occur at the working electrode with the generation of a faradaic current due to electron transfer processes with accompanying chemical change. The processes at the counter electrode are usually of no interest since they are merely required to balance the faradaic process at the working electrode. The reference electrode provides a means to monitor the potential change in the working electrode. In this work, the potential of the working electrode is quoted with respect to the reference electrode unless otherwise stated.

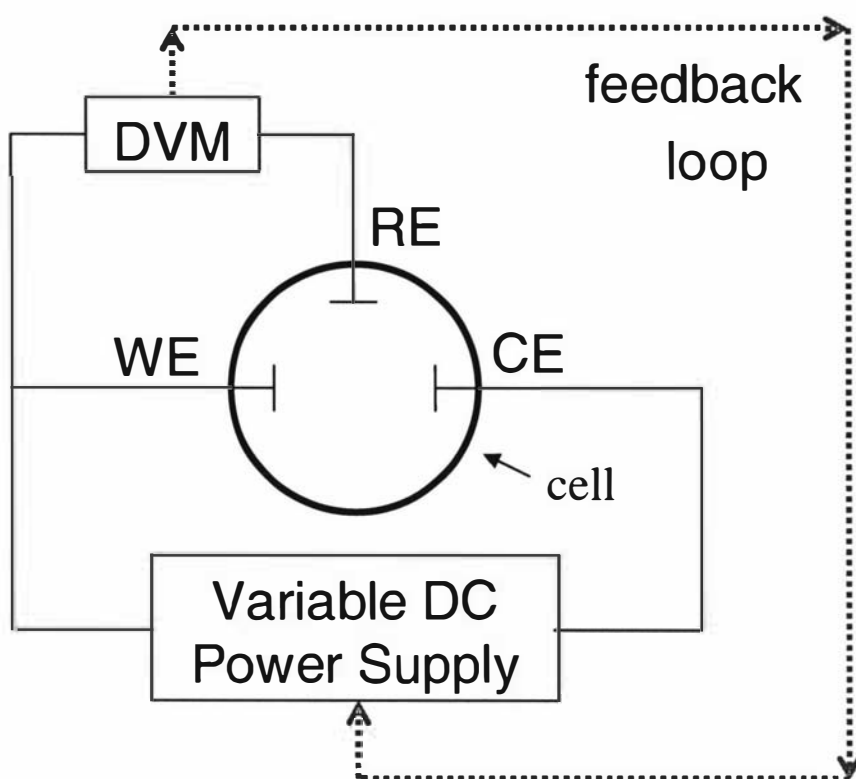


Fig. 2.1 Schematic diagram of the circuits of a three electrode system with Digital voltage meter (DVM), counter electrode (CE), reference electrode (RE), and working electrode (WE).

2.2.2.1 Counter Electrode

For the most part, platinum wire was used as the counter electrode, although stainless steel plates were employed in the polypyrrole study (Chapter 4). The counter electrode is driven by the potentiostatic circuit to balance the faradaic process at the working electrode but in the opposite direction (i.e. when oxidation occurs at the working electrode, then an equal amount of reduction will occur at the counter electrode).

2.2.2.2 Reference Electrode

Silver wire with a potential of 274 mV vs the standard hydrogen electrode (SHE) was used as a pseudo-reference electrode in the electrochemical cells unless otherwise stated ^[95].

2.2.3 *Electrochemical Cells*

Each of the film types formed in this study had differing preparation requirements. These included:

- aqueous vs non-aqueous solvents;
- electrode substrate differences; or
- low cell volume requirements (due to scarcity of monomer material) vs no volume restrictions.

Consequently three types of electrochemical cells were used in this work to accommodate these requirements.

2.2.3.1 Scoping study electrochemical cell

A low internal volume electrochemical cell was designed for the scoping study (Chapter 3) due to the restraints on the amount of monomer material available. This cell was designed so that the working electrode formed one end of the cylindrical cell and could be readily removed and submitted to IBA analysis. A schematic of this cell is shown in Fig. 2.2. Further, the working electrode discs were designed to permit ready fixing in the IBA sample holders.

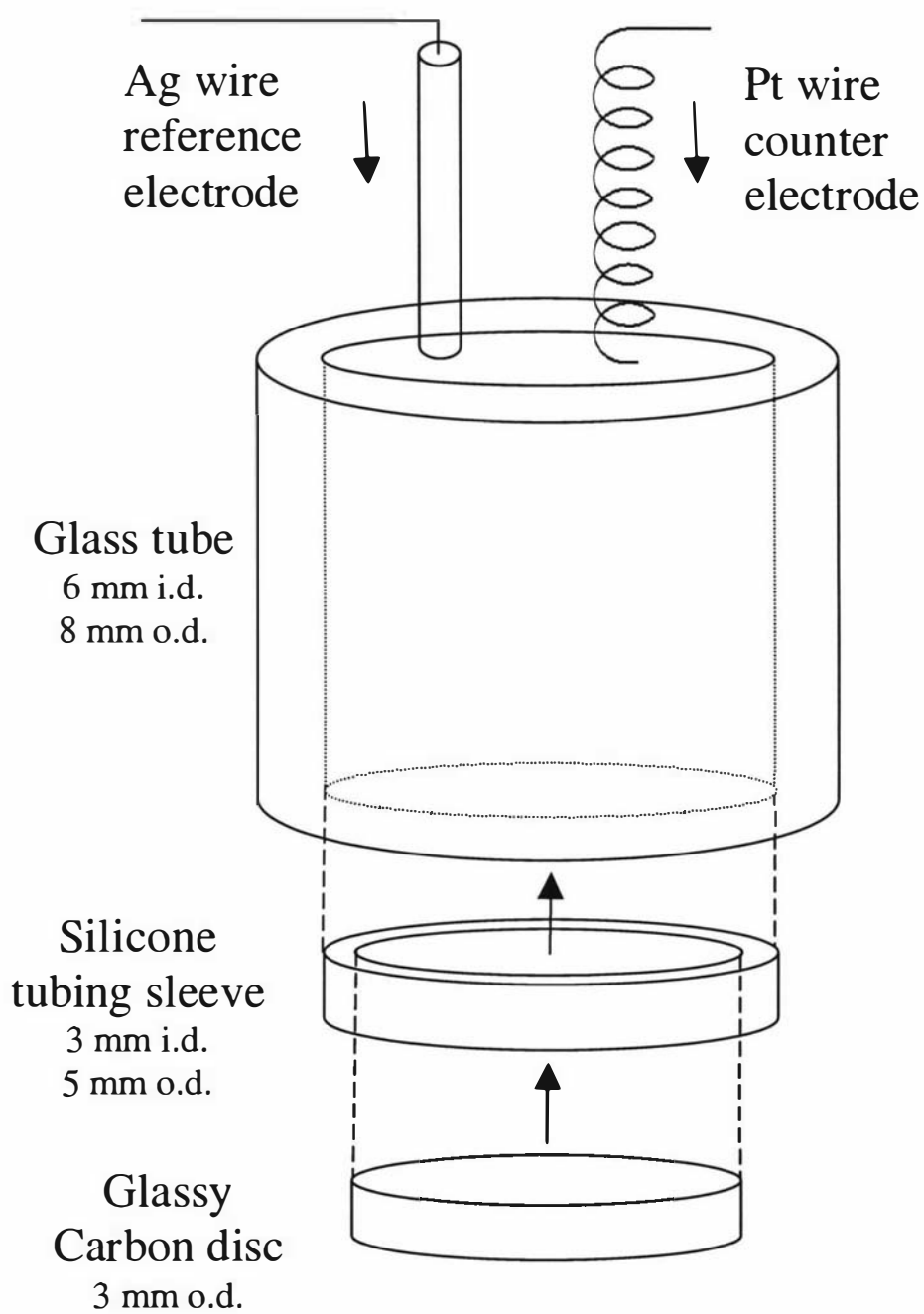


Fig. 2.2 Schematic diagram of the electrochemical cell used throughout the scoping study (Chapter 3).

A glass tube with a 6 mm i.d. and an 8 mm o.d. was cut to 30 mm length to form the body of the cell. The working electrodes in this cell were glassy carbon (GC) discs (5 mm diameter, 3 mm thick). These discs were inserted into one end of the glass tube using a silicone tubing connector sleeve. The silicone tubing had an i.d. of 3 mm and an o.d. of 5 mm (Nalgene). Insertion of the GC disc into the silicone sleeve and then insertion of this combination into the glass tube formed a tight seal.

The reference electrode and counter electrode for this cell were a length of Ag wire (1.5 mm diameter) and a piece of Pt wire (0.5 mm diameter) respectively. Both of these electrodes were placed in the solution through the open end of the electrochemical cell.

2.2.3.2 Electrochemical cell for polypyrrole preparation

A schematic of the cell used for the electrochemical deposition of polypyrrole (Chapter 4) is shown in Fig. 2.3. This is a larger volume cell than that for the Scoping study and produced films with width and height dimensions of centimetres. The use of the pyrrole monomer, which is available in high quantity, enabled this approach. This cell was a 2-electrode system with a working electrode and a counter electrode (that also acted as a pseudo-reference electrode) (IRL, Lower Hutt, NZ). A separate reference electrode was not used as film growth was controlled galvanostatically and the potential between the working and counter electrodes was not required to be monitored. Both electrodes were planar and manufactured from stainless steel sheet (Grade 316).

The cell was constructed of Perspex and consisted of two hollow pieces that when held together formed a cavity for the aqueous electrolyte. These pieces were held together through the use of a clamp. The inside edges of each piece were lined with foam rubber to form a water-proof seal. The cell was constructed in this way so that a piece of filter paper could be placed between the two halves to form a porous separator. This separator prevented hydrogen bubbles formed at the counter electrode from adhering to the growing polypyrrole film on the working electrode, while still permitting flow of ions between the two halves of the cell. Such bubble adherence leads to macroscopic imperfections in the film ^[96].

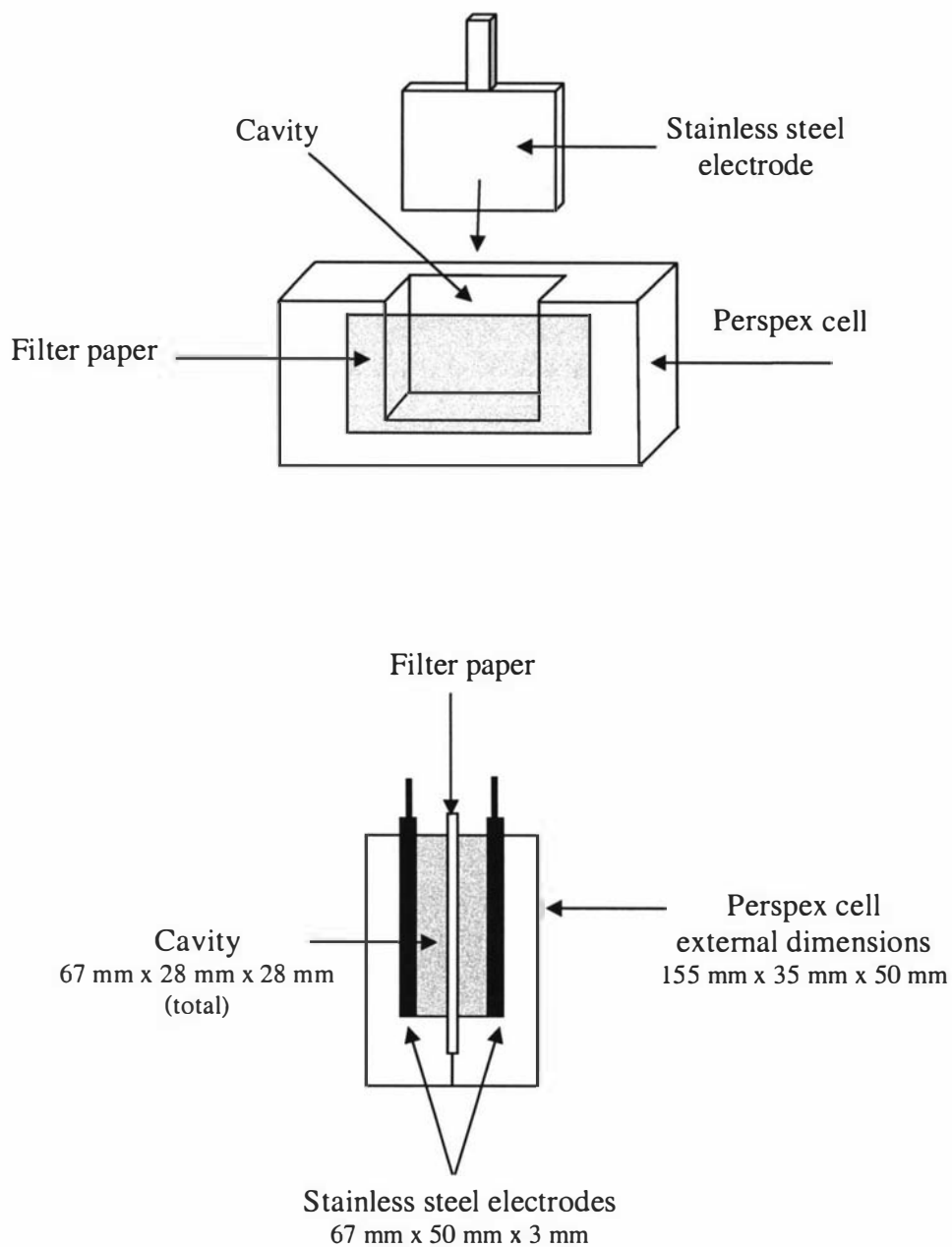


Fig. 2.3 Schematic diagrams of the electrochemical cell used for the polypyrrole study (Chapter 4), (a) half view of cell, and (b) end view of cell.

The cell had outside dimensions of 115 mm × 35 mm × 95 mm and inside cavity dimensions of 67 mm × 28 mm × 70 mm when assembled. The two stainless steel electrodes were placed parallel along the long walls of this cavity.

2.2.3.3 Electrochemical cell for terthiophene-ferrocene film preparation

A wide range of substrates for film growth were assessed for the terthiophene film preparation. These substrates included stainless steel, GC, Pt, and ITO coated glass. It was found that of all the substrates, only on ITO coated glass were suitable films (films which could be removed from the electrode substrate intact) produced and therefore this was the substrate used as the working electrode for this work (Chapter 5). A new electrochemical cell was required for this work, not because of the restrictions from the amount of monomer available, but that of the working electrode. A new piece of ITO glass was required for each procedure since these are not readily cleaned without damaging the thin conductive ITO layer. Due to the non-aqueous solvent required for the monomer, a glass cell was preferable. A schematic of this cell is shown in Fig. 2.4.

A cylindrical glass cell, 40 mm in height, with an i.d. of 20 mm and an o.d. of 24 mm was used with a 3-electrode system. The pseudo reference electrode was a length of Ag wire (274 mV *vs* SHE). The counter electrode was a length of coiled Pt wire unless otherwise stated. The working electrodes in this section of work were 10 mm × 25 mm × 1 mm pieces of glass coated on one side with ITO.

2.3 Electrochemical Techniques

2.3.1 *Cyclic Voltammetry*

Cyclic Voltammetry (CV) is a potential-controlled technique where a triangular-wave potential is applied to the cell so that the working electrode (WE) potential is swept linearly and continuously between two potential limits^[97]. The number of cycles may be varied to investigate long term changes in the electrochemical behaviour of a system^[97]. The observed faradaic current is dependent on the kinetics and transportation of the electroactive species to the electrode and is reported as a function of applied potential. The resulting plot of *i vs E* is termed a voltammogram. Important parameters for a CV are the initial potential, the initial sweep direction, scan rate,

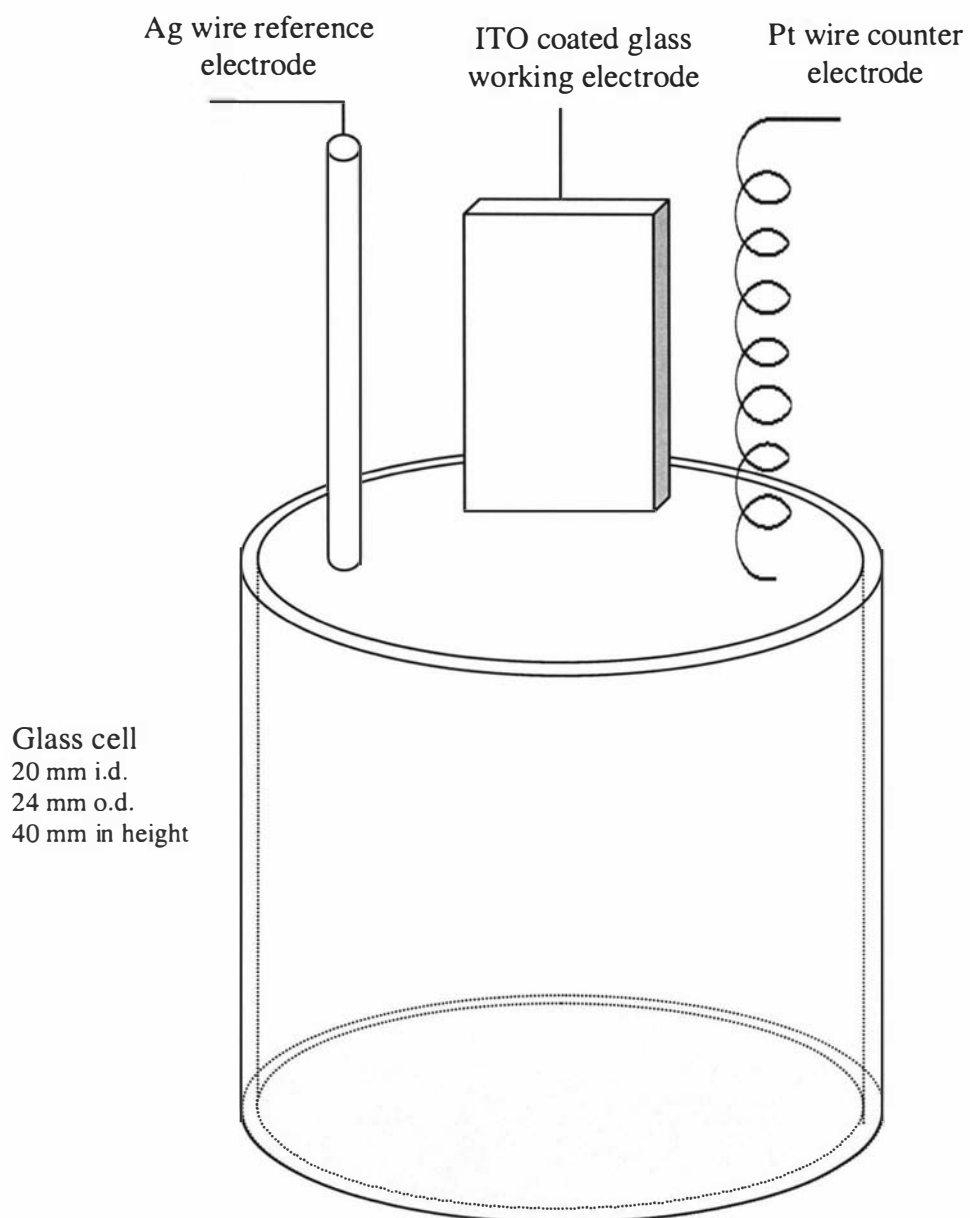


Fig. 2.4 Schematic of the electrochemical cell used for the formation of terthiophene-ferrocene films (Chapter 5).

the maximum potential, the minimum potential, and the final potential ^[97].

The primary use of CV is as a diagnostic tool to provide information about electrochemical processes under various conditions. While CV is not used for routine quantitative analysis it has become an important tool for the study of mechanisms and rates of oxidation/reduction processes ^[97].

The convention adopted in the thesis is that employed in the Bioanalytical System Inc. BAS 100 B/W software, positive currents denote net reduction processes and negative currents denote net oxidation processes. Cyclic voltammograms of i vs E are plotted with increasingly more negative potentials to the right side of the x -axis and increasingly positive currents up the y -axis. In this study, all CVs commence and terminate at the lower potential limit in the reduction region unless otherwise stated. The statement 'forward sweep' refers to scanning to more positive (oxidising) potentials.

2.3.2 Chronoamperometry

In potential step experiments the potential of the working electrode is changed instantaneously, from one value to another ^[98]. Either the current-time response or the charge-time response is recorded. The variation of the current response with time under such potentiostatic control is called chronoamperometry (CA). An experiment is usually performed by stepping the potential applied to a working electrode from a value where there is little to no electron reaction, E_1 , to a potential, E_2 , at which a current response, in this case the oxidation of monomers, may be recorded.

Fick's First Law for the rate of diffusion or flux is directly proportional to the concentration gradient

$$j(x,t) = -D \frac{\partial c(x,t)}{\partial x} \quad (2.1)$$

where D is the diffusion coefficient of monomer in $\text{m}^2 \text{s}^{-1}$, and $\partial c_{(x,t)} / \partial x$ is the concentration gradient at time t at distance x from the electrode. The flux, j , is the rate

of molar mass transport at a fixed point and is defined as the number of molecules passing through a unit area of an imaginary plane perpendicular to the direction of movement per unit time, and has units $\text{mol m}^{-2} \text{s}^{-1}$.

The current density is directly proportional to the flux, given by,

$$i = -nFj \quad (2.2)$$

where n is the number of electrons per molecule and F is the faraday constant. The combination of Eqns. 2.1 and 2.2 provides a general expression for the current that is dependent on the concentration gradient of the electroactive species.

$$i = -nFD \frac{\partial c(x,t)}{\partial x} \quad (2.3)$$

2.4 Ion Beam Analysis

2.4.1 Introduction – Rutherford’s experiment

In 1909 Hans Geiger and Ernest Marsden, while working in Ernest Rutherford’s laboratory, observed that alpha particles arising from radioactive decay, after hitting metal foils, occasionally scattered at angles greater than 90° from the incident path^[99]. This was impossible unless the particles were scattering from something more massive than themselves. This observation led Rutherford to deduce that the positive charge in an atom was concentrated into a small compact nucleus. From 1911-1913 they bombarded foils with high energy alpha particles and observed the number of scattered alpha particles as a function of angle. All of the alpha particles should have been found within a small fraction of a degree from the beam according to the Thomson model of the atom, but Geiger and Marsden found a few scattered alpha particles at angles over 140° from the incident beam. Rutherford’s remark to this information was “*It was quite the most incredible event that ever happened to me in my life. It was almost as incredible as if you had fired a 15 inch shell at a piece of tissue paper and it came back and hit you*”^[100]. The scattering data was consistent with a small positive nucleus, which repelled the incoming positively charged alpha

particles. Rutherford developed a relationship (Eqn. 2.4) for the scattering that matched the data collected by Geiger and Marsden

$$N(\theta) = \frac{N_i n L Z^2 k^2 e^4}{4 r^2 E_K^2 \sin^4(\theta/2)} \quad (2.4)$$

where

$N(\theta)$ is the number of alpha particles scattered at angle θ

N_i is the number of incident alpha particles

n is the number of atoms per unit volume in target

L is the thickness of target

Z is the atomic number of target

e is the electron charge

k is Coulomb's constant

r is the target – to – detector distance

E_K is the kinetic energy of the incident alpha particle

θ is the scattering angle

2.4.2 *Incident particles used in Ion Beam Analysis*

Four different incident particles are typically employed in 3 MV Van de Graaff accelerators; protons, deuterons, ^3He , and ^4He .

The main type of incident ion used in RBS studies is the $^4\text{He}^+$ ion. The energy for these $^4\text{He}^+$ ions is generally in the range 1.5-2.0 MeV. This energy range is significantly lower than those Rutherford, Geiger, and Marsden employed in 1911. The only ready source of alpha particles for these workers were those from the nuclear decay of radium. These alpha particles have energies of 7.7 MeV.

The reason alpha particles are predominantly used for RBS is due to alpha particles undergoing only 'Rutherford' cross sections at incident beam energies below *ca.* 2.5 MeV (first non-Rutherford interaction for carbon), whereas protons also undergo 'non-Rutherford' cross sections at these low incident beam energies. As the

incident beam energy range for $^4\text{He}^+$ ion beams is typically 1.5 – 2.0 MeV, non-Rutherford cross sections are not an issue. The term cross section refers to the probability that an interaction between an incident particle and a nucleus will occur at a given scattering angle. The Rutherford cross sections describe the interaction probability in the Coulombic collisions between the ion and the target. Non-Rutherford elastic scattering cross sections arise when the ion energy is sufficiently high that the ion penetrates the Coulomb barrier of the target atom. When the ion penetrates the Coulomb barrier of the target atom, the scattering is from the target atom's nuclear potential and the effect of the nuclear forces for the scattering become significant. When the ion energy is sufficiently low the screening of the electrons around the target nucleus alters the cross section ^[101]. The ion does not fully interact with the whole charge of the target nucleus and the cross section is smaller than the Rutherford cross section. The screening effect decreases the cross section only some ten percent while the ion scattering from the target nucleus and the resonances may increase or decrease the scattering cross sections by several orders of magnitude ^[102].

2.5 Ion Beam Analysis at Geological and Nuclear Sciences, NZ

2.5.1 Introduction

At the end of World War II, a small research team in the New Zealand Department of Scientific and Industrial Research (DSIR) was established to explore the fast growing field of atomic science. This small group was attached to the Dominion Physical Laboratory and formed the beginning of the Isotope Laboratory. In 1957 the Isotope Laboratory was made into a separate division of the DSIR on a new site, eventually becoming the Institute of Nuclear Sciences (INS) in 1959. In the early 1960s a 3 MV Van de Graaff Accelerator was installed at the Isotope Laboratory, INS. In 1991 the DSIR was dissolved and the various divisions were organised into ten Crown Research Institutes (CRI). In this process, INS was merged with the earth science components of the DSIR and became the Institute of Geological and Nuclear Sciences, Ltd. (GNS).

It was not until 1994 that any significant ion beam analysis commenced at these facilities. Indeed, over the last five years this laboratory has undergone alterations and reconfigurations to meet new analytical challenges. These challenges are rapidly evolving and wide ranging, from environmental sciences to nanotechnology. Over the

term of this present study the IBA team at the Rafter Research Centre has consisted of a team of 5 personnel involved in research activities ranging from trace element analysis, pollution measurements, nanotechnology research, to analysis of industrial materials. Both new and novel research and commercial work is carried out at this laboratory. The present study has presented a further challenge to these facilities given that this work represents the first IBA of soft organic based materials undertaken at these facilities.

The five main types of IBA techniques that are undertaken at the Rafter Research Centre are summarised in Table 2.1 and Fig. 2.5 and include RBS, PIXE, Particle Induced Gamma-ray Emission (PIGE), and Nuclear Reaction Analysis (NRA), Elastic Recoil Detection (ERD), on the general and microprobe lines. The techniques used in this study were confined to RBS and PIXE.

All IBA work presented in this thesis was performed at the Rafter Research Centre at GNS (Geological and Nuclear Sciences), Lower Hutt, NZ.

2.5.2 *The Van de Graaff Accelerator*

The 3 MV single-ended Van de Graaff accelerator can produce deuterium, $^3\text{He}^+$, $^4\text{He}^+$, and proton ions, with energies ranging from a few hundreds of keV to 3 MeV. The accelerator is housed behind one metre thick concrete walls to protect staff from extraneous radiation produced by thermal neutrons. The beam lines extend through this wall into the main laboratory. The position of the analysing magnet may be moved so that the one accelerator may be used for all three beam lines. A schematic diagram of the beam line at the Rafter laboratory is shown in Fig. 2.6.

In the Van de Graaff accelerator electric charge is sprayed on to a moving insulated belt and transported to a terminal. A high voltage develops and this is used for

Table 2.1

The five main IBA techniques used at GNS.

Process	Acronym	Description
Rutherford Backscattering	RBS	Elastic backscattering of the incident beam from the target nuclei.
Particle Induced X-ray Emission	PIXE	Characteristic X-rays produced by particle-atom interaction.
Particle Induced Gamma-ray Emission	PIGE	Specific gamma rays produced by particle-nucleus interaction.
Nuclear Reaction Analysis	NRA	Specific high energy particle emitted by nuclear reaction.
Elastic Recoil Detection	ERD	Light elements from sample are scattered in forward directions.

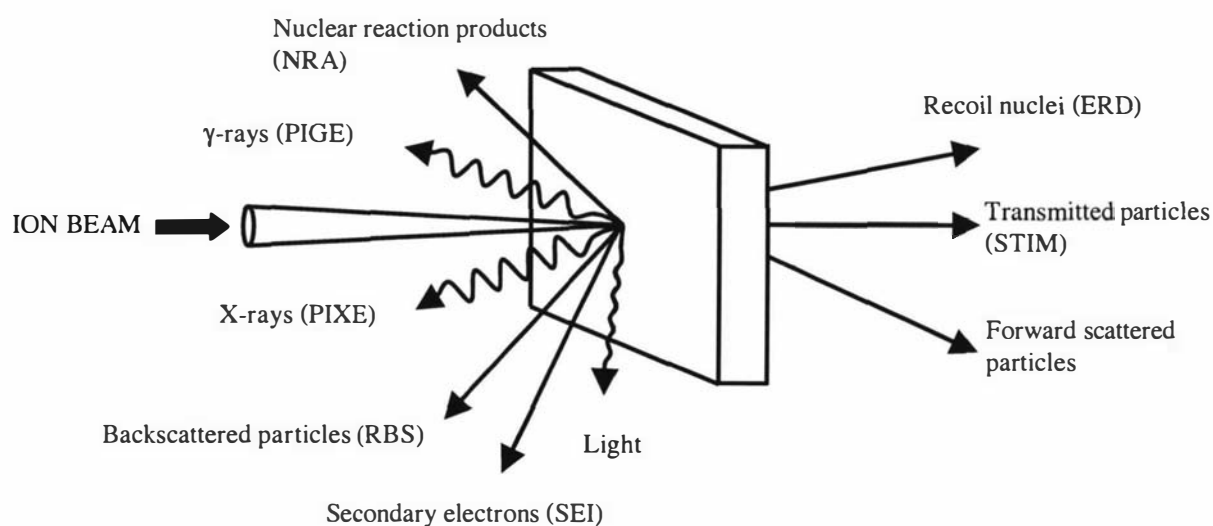


Figure 2.5 Schematic of the IBA processes that can occur when an ion beam hits a target.

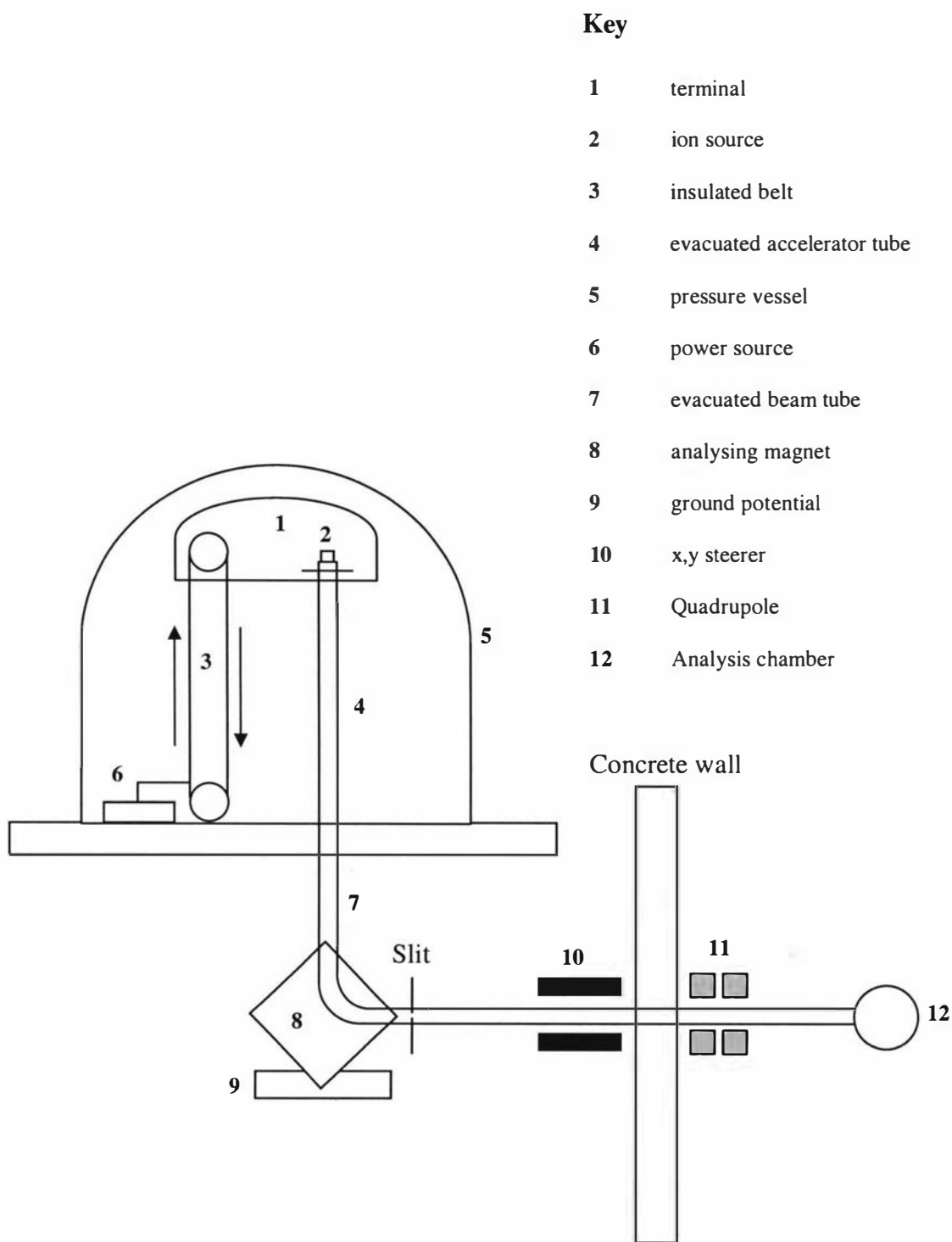


Fig. 2.6 Schematic of the basic aspects of the 3 MV Van de Graaff accelerator, beam line, and detection systems at the Rafter Research Centre, GNS, Lower Hutt, NZ.

accelerating charged particles produced in the ion source, down an evacuated accelerator tube towards ground potential. The analysing magnet selects for ions of appropriate energy and changes their pathway by 90°. The analysing magnet can rotate around the axis of incoming ions so that three different beam lines can be selected. The selected ions continue along the evacuated beam tube, maintaining their momentum, towards the target. Once the ions hit the sample target then a number of different analysis techniques may be employed to investigate the sample.

2.5.3 *Beam Line*

There are two beam lines at the Rafter laboratory, the general IBA line, and the microprobe line. All the work undertaken in this thesis was performed using the general IBA beam line.

The general IBA beam line (Fig. 2.7) has two evacuated analysis chambers and the ability to produce an external beam that may be extended into the atmosphere. This external beam is typically used for the analysis of geological core samples and is located at the end of the beam line. The first of the two sample chambers, the general IBA chamber, is used for more specialised analysis. It was in this chamber that all the data described in this thesis was collected. The second chamber is used predominantly for the routine analysis of air particulates, and is positioned further down the beam line than the general IBA chamber.

The general IBA chamber can be equipped with a remotely controlled sample holder so that up to 18 samples may be loaded into the vacuum chamber at a time (Fig. 2.8). This system was used in the present work. The samples referred to in Chapters 3 and 4 were fixed on standard aluminium SEM stubs, 12.6 mm diameter (ProSciTech, Thuringowa, Australia) and mounted in the sample holder (Fig. 2.9). A further sample holder was designed (Fig. 2.10) to hold the terthiophene-ferrocene polymers (Chapter 5). This sample holder permitted the mounting of free-standing TTh-Fc films. An advantage of this new holder is that these films could be mounted with no metal stubs or structure behind the film. This removes any possibility of IBA response from the sample holder material.

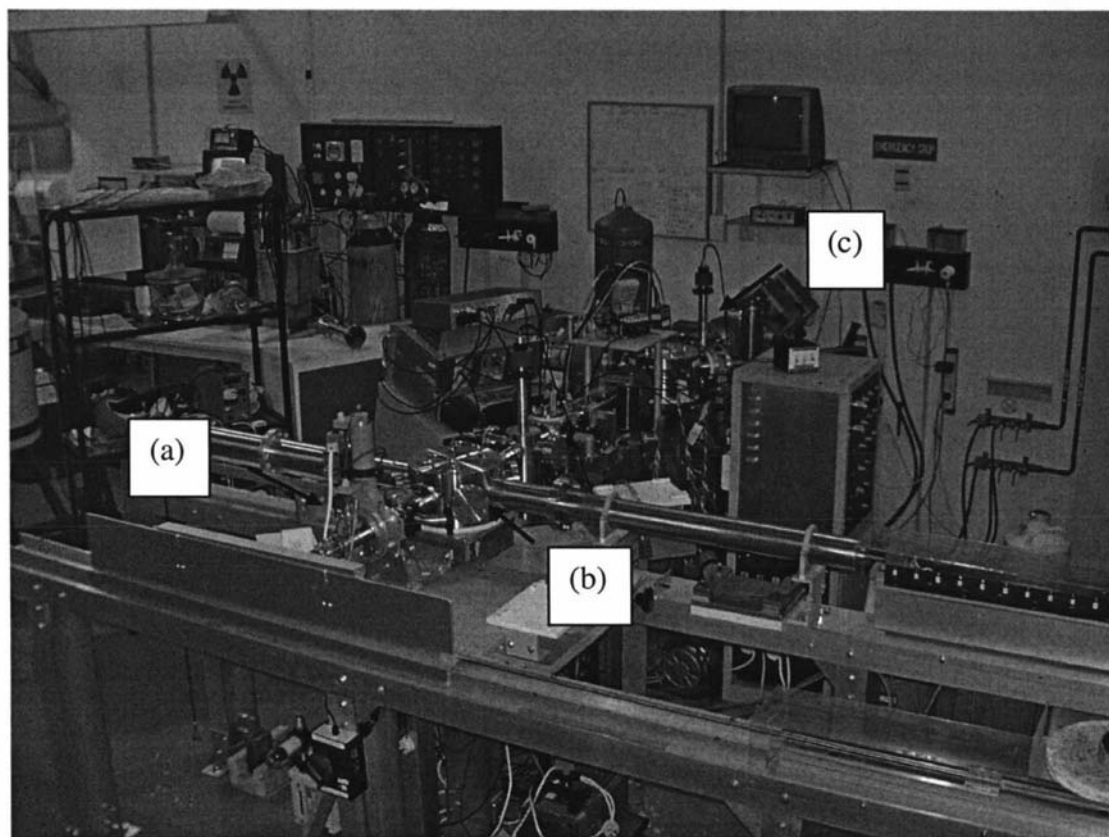


Fig. 2.7 Photograph of the general IBA beam line at the Rafter Research Centre, GNS, Lower Hutt, NZ; (a) external beam, (b) second analysis chamber, (c) first analysis chamber (general IBA chamber).

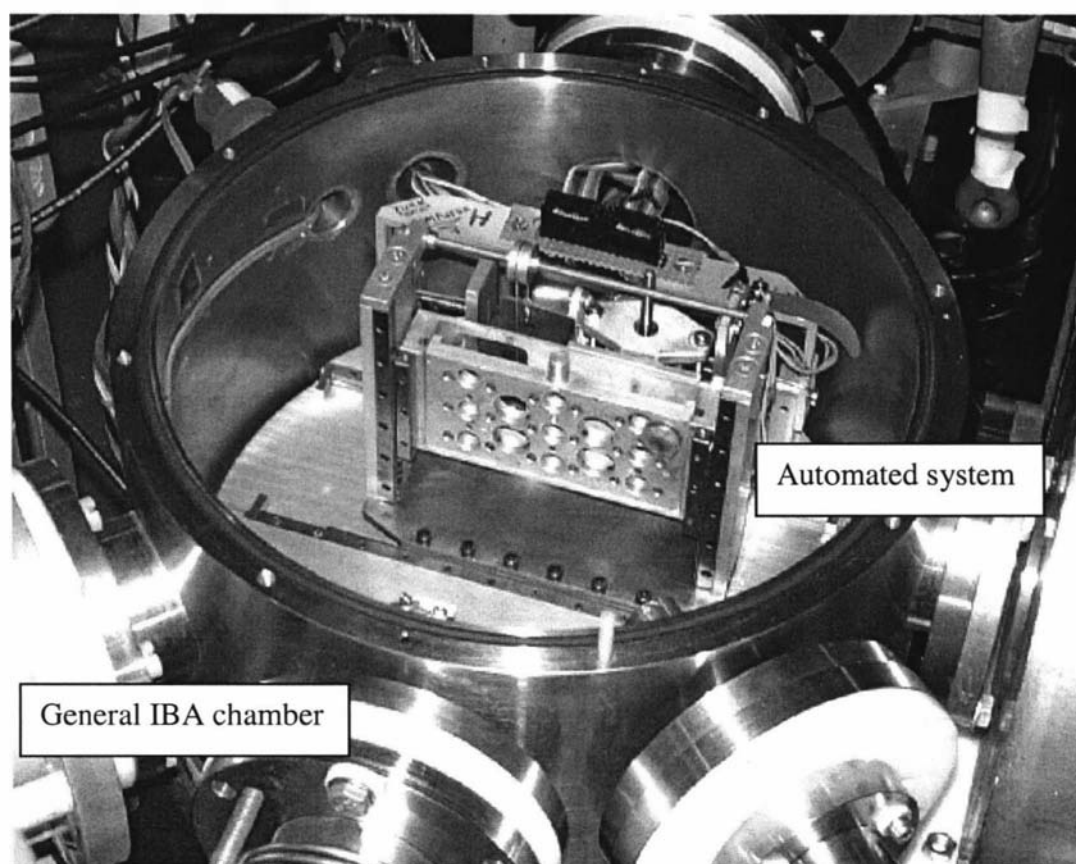
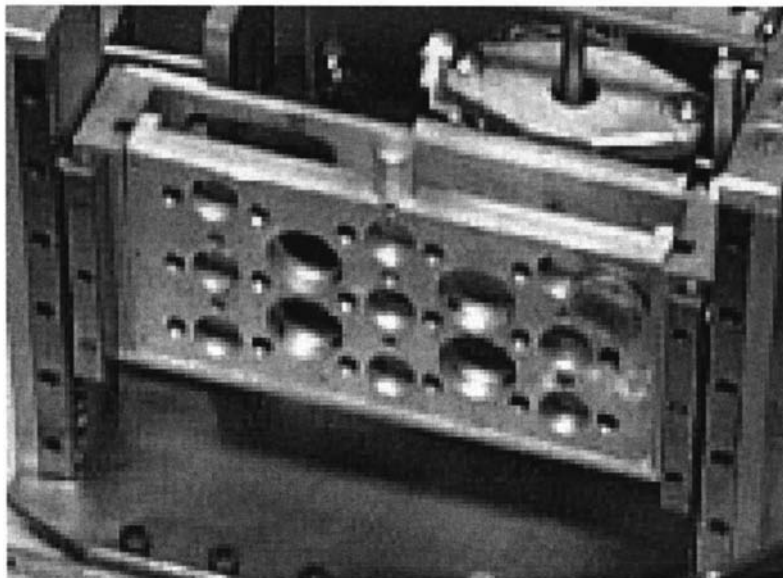
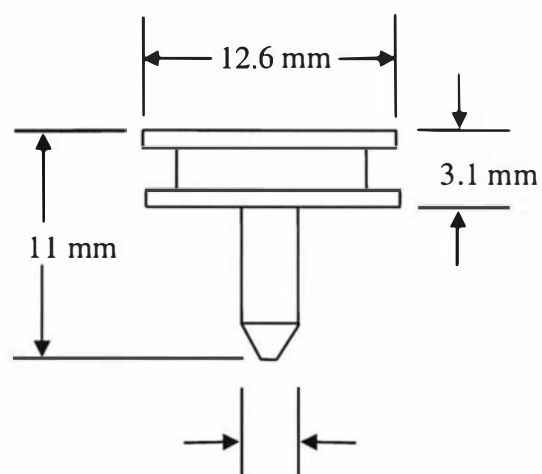


Fig. 2.8 Photograph of the general IBA chamber and automated system on general IBA line at Rafter Research Centre, GNS, Lower Hutt, NZ (i.d. 35 cm).



(a)



(b)

Fig. 2.9 Above, a picture of the general sample holder (a), and below, a schematic of an aluminium stub.

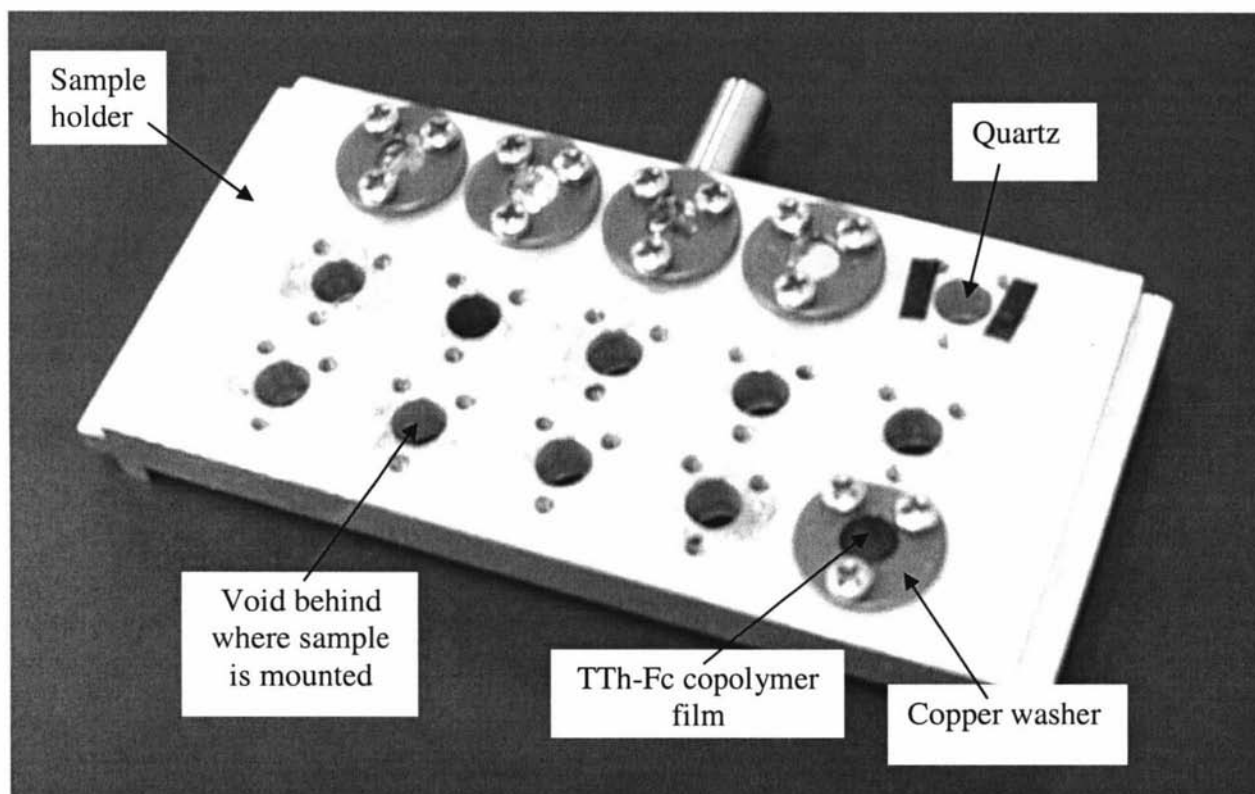


Fig. 2.10 Picture of the newly designed sample holder constructed for the terthiophene-ferrocene copolymer work (Chapter 5).

2.5.4 Detectors

2.5.4.1 RBS detectors

Silicon surface barrier detectors are used in RBS experiments to measure the relatively few particles that recoil from the target (Fig. 2.11). These devices are often called semiconductor diode detectors, since they are essentially diodes. The high energy charged particles produce electron-hole pairs in the semiconducting material. The average energy expended by alpha particles in each electron-hole pair production is 3.7 eV so that each 1 MeV particle will yield 2700 electron-hole pairs. The creation of each electron-hole pairs forms two oppositely charged carriers – an electron and a positive hole. The detector is operated with an electrical potential (typically 4 kV) between the front and back surfaces. In this electric field, the movement of the electrons and holes to the *n*- and *p*- regions respectively produces an electric current. It is the magnitude of this current that provides information on the incident ion energy.

Particle arrival times at the detector are randomly spaced in time, leading to the possibility of interference between measurements when particles arrive at nearly the same time. This phenomenon, termed pulse pile-up, becomes a serious problem at high arrival rates. There are two distinct types of pile-up. Tail pile-up involves the superposition of pulses on the long duration tail or undershoots from a preceding pulse, leading to reduced spectral resolution. High quality electronic circuits minimise tail pile-up. The second type of pile-up is where two pulses arrive sufficiently close together to be detected as a single pulse producing peak pile-up. Detector dead time is the minimum time between successive ion arrivals if they are to be measured separately. Peak pile-up ultimately limits the rate at which RBS data collection can occur.

The inclusion of a collimator to the RBS detector can decrease the amount of pile-up and hence increase the rate of data collection.

2.5.4.2 PIXE detectors

To utilise PIXE as an analytical technique, the detection of the characteristic X-ray must be such that individual and adjacent X-ray energy peaks can be resolved. A

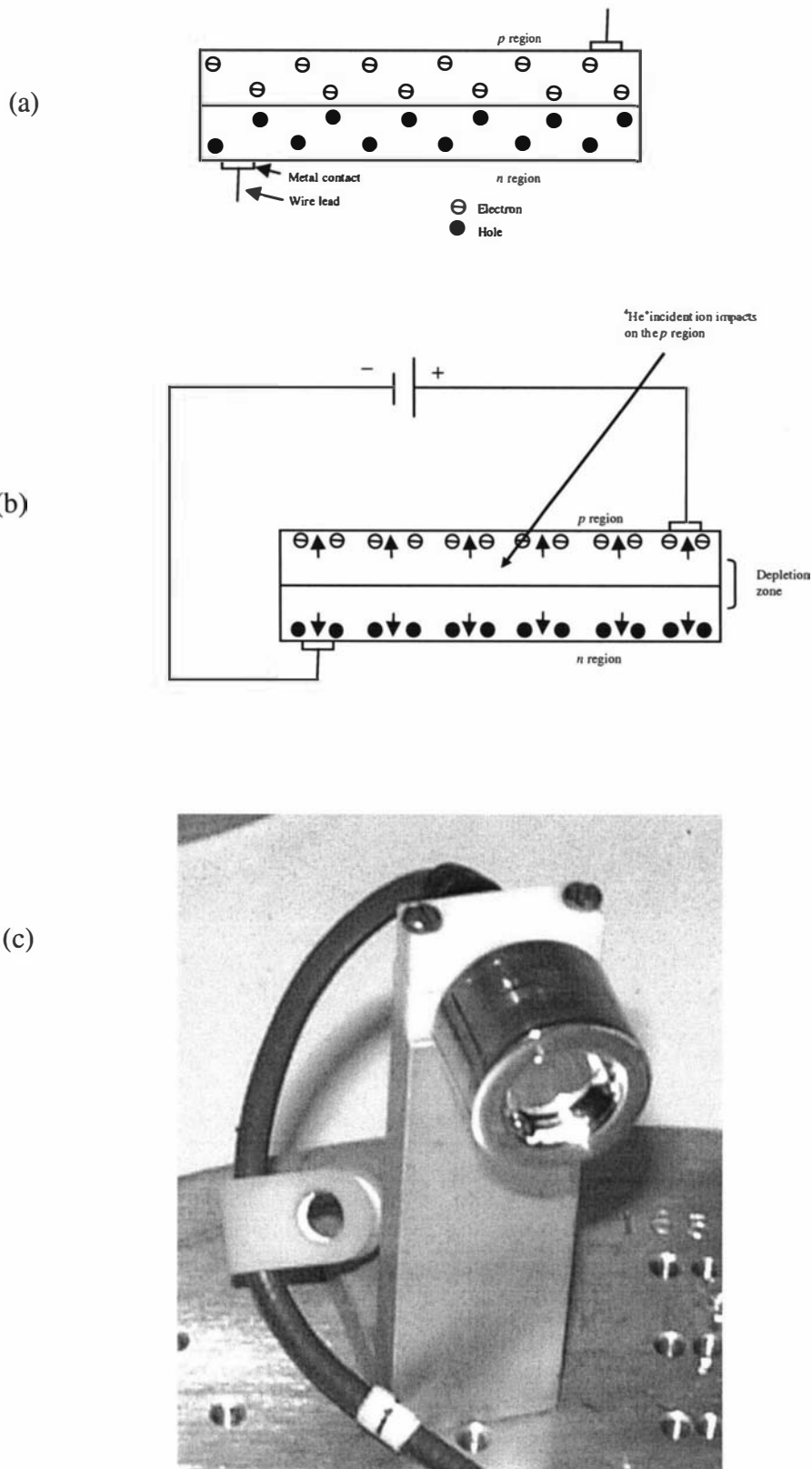


Fig. 2.11 Schematic diagram of (a) RBS silicon surface barrier detectors, (b) the formation of depletion layer that courses a small current flow, and (c) a photograph of RBS surface barrier silicon detectors.

detector that fulfils this criterion, with a high efficiency of detection, is the solid state lithium drifted silicon, Si(Li), detector. When an X-ray passes through this detector it produces electron-ion pairs which are collected by a low noise charge amplifier to produce a voltage pulse which is proportional to the X-ray energy. The detector and pre-amplification stages are cooled to liquid nitrogen temperature in order to reduce background detector noise. A good quality Si(Li) detector will have an energy resolution of 150 eV, sufficient to separate X-ray pulses for each element above sodium in the periodic table.

This type of detector employs a Si(Li) crystal which should be maintained at liquid nitrogen temperatures. The environment around the crystal is usually protected by a thin beryllium window. This window, depending upon its thickness, absorbs X-rays of energies up to *ca.* 1 keV (i.e. Na in the periodic table). Consequently only elements with atomic numbers greater than that for Na are detected with such systems. The detector can be used without a beryllium window being present. When not employed, elements below Na in the periodic table can be detected with PIXE, but the background noise increases greatly without the beryllium window present.

Pulses from the Si(Li) detector are subsequently analysed by an analog-to-digital converter and a multi-channel analyser.

2.6 Rutherford Backscattering - RBS

2.6.1 *Collection of spectra*

The procedure for the collection of data has already been discussed in Section 2.5.4.1, but the resulting spectra have not yet been considered. The data collected by the RBS detectors is typically displayed as counts vs channel number where channel number relates to a series of fixed bandwidth energy windows for the detector system. An example of a RBS spectrum of Si/N on a Si substrate is shown in Fig. 2.12. The conversion of channel number to energy is performed by calibrating the collected spectra and determining an energy/channel ratio. This calibration of RBS spectra will be discussed in relation to each of the two software packages used to interpret the data in later sections (2.6.7.1, 2.6.7.2).

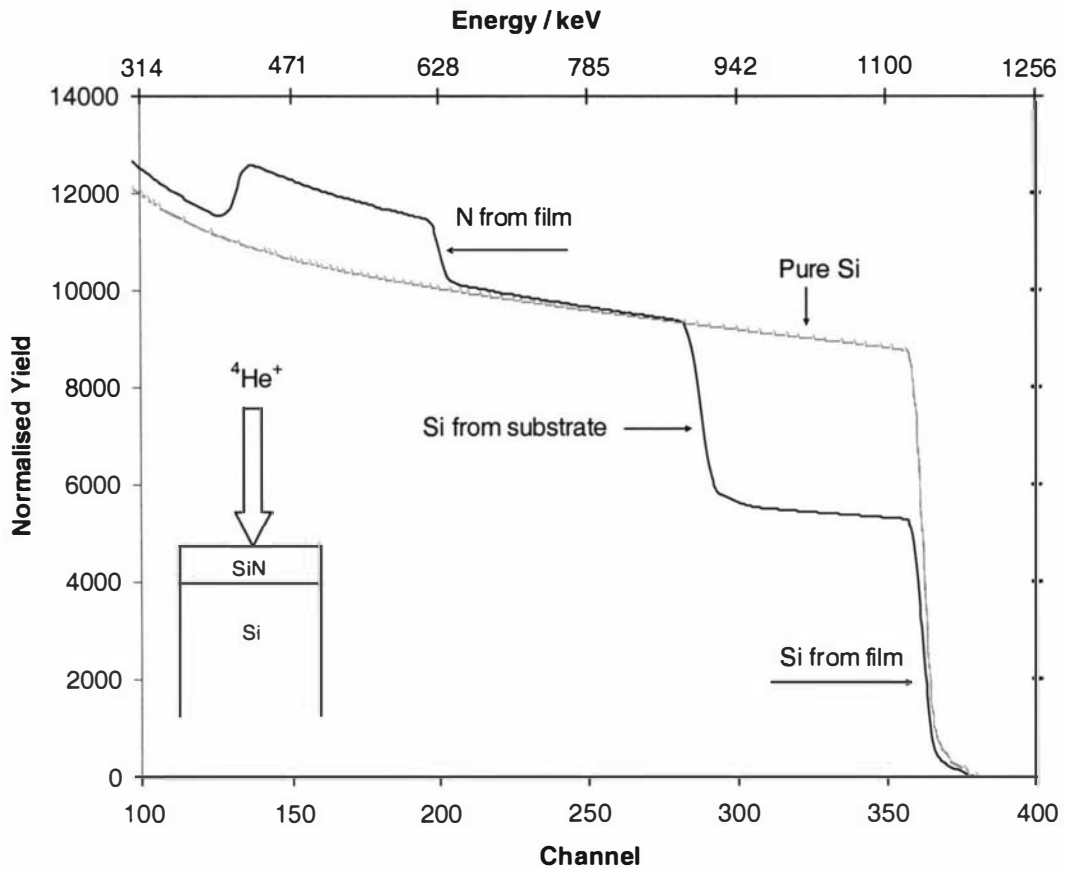


Fig. 2.12 A RBS spectrum for a Si/N on Si substrate, 1.5 MeV $^4\text{He}^+$ beam, $\theta - 165^\circ$, 7 nA, 20 keV FWHM.

2.6.2 *Idealised simple spectrum*

Figure 2.13 shows idealised spectra for a series of different elements (Na, O, and C). The y-axis here records the counts for each channel number (lower x-axis). It is usual to record the corresponding energy scale on the upper x-axis. The feature to note in this schematic spectrum is that of the surface edge. The energy for the surface edge is defined by the half height of the plateau of the element. This is the point at which energy is invariant of backscattering rate (discerned by a constant count rate). The heights of the backscattered plateau in Fig. 2.13 are described in section 2.6.3. The only energy loss mechanism for scattering at a sample surface is that of momentum transfer to the target atom. The ratio of the projectile energy after a collision is defined as the kinematic factor, k . This kinematic factor, k -factor, determines the energy of the surface for each element and accounts for each element having a different surface edge energy position for a fixed ion beam energy. Heavier elements have surface edges closer to the ion beam energy compared to lighter elements as shown in Fig. 2.13.

There is much greater separation between the energies of particles backscattered from light elements than from heavy elements, since a significant proportion of momentum is transferred from the incident particle to a light target atom. Equation 2.5 together with Eqns. 2.6 and 2.7 describe this relationship ^[103].

$$E_1 = E_0 k \quad (2.5)$$

where E_0 is the kinematic energy of the incident particle ion, E_1 is the kinematic energy of the incident particle ion after scattering, and k is a number between zero and unity.

The k -factor for an element may be predicted on the basis of the masses of projectile and target species, and the backscattering angle using Eqn. 2.6,

$$k = \left(\alpha + \sqrt{\alpha^2 + \frac{M_1 - M_0}{M_1 + M_0}} \right)^2 \quad (2.6)$$

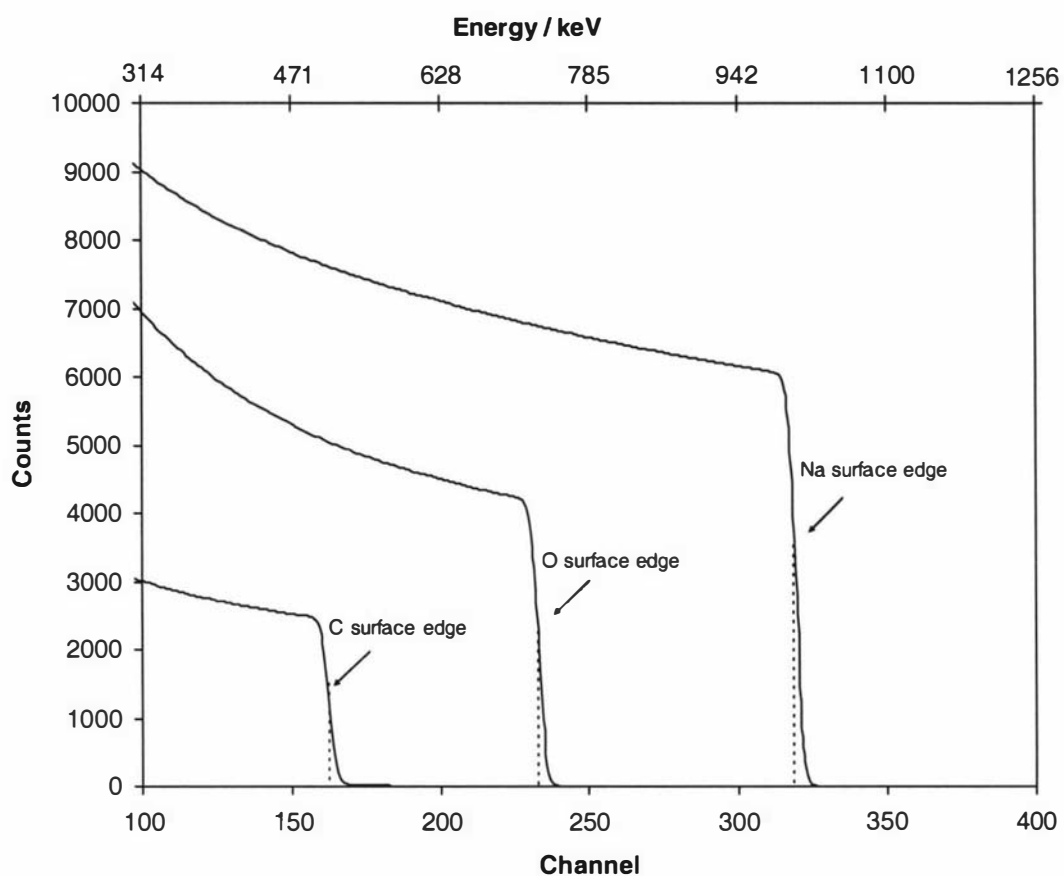


Fig. 2.13 Idealised spectra for three different elements of infinite film thickness and their surface edge for a 1.5 MeV $^4\text{He}^+$ incident beam.

$$\text{where } \alpha = \left(\frac{M_0}{M_0 + M_1} \right) \cos \theta \quad (2.7)$$

and M_0 is the mass of the projectile ion, M_1 is the mass of the target atom, and θ is the scattering angle.

Since E_1 is the energy measured by the detector and E_0 , M_0 , and θ are known, then M_1 can be determined. Consequently, the RBS energy spectrum provides a mass spectrum.

As the mass of the target atom increases, the k -factor values also increases (Eqn. 2.5 and 2.6) and asymptotically approaches the incident particle energy as listed in Table 2.2 and shown in Fig. 2.14.

These factors dictate that RBS is more useful for distinguishing between two light elements than it is for distinguishing between two heavy elements. Consequently, RBS has good mass resolution for light elements. Further, it has long been established that the k -factor is independent of the energy of the incident particle consistent with Eqns. 2.6 and 2.7 (Fig. 2.15) ^[103].

In most situations, the target sample comprises of more than one element. It can be shown that for a fixed scattering angle the energy separation, ΔE_1 , between particles scattered by two different target elements of mass difference, ΔM_1 , is given by

$$\Delta E_1 = E_0 \left(\frac{\Delta k}{\Delta M_1} \right) \Delta M_1 \quad (2.8)$$

where Δk is the difference in k -factor for the two elements.

For example, when $^4\text{He}^+$ ions impact upon light elements such as C, N, and O, a significant fraction of the projectiles energy is transferred to the target atom and the energy recorded for that backscattered ion is much lower than the energy of the beam as stated by Eqn. 2.8. It is usually possible to resolve C from N, and P from Si, even

Table 2.2 k -factor and E_1 energies are show for a selection of elements for a 1.5 MeV ${}^4\text{He}^+$ beam at a scattering angle of 170° .

Element	k -factor	E_1
C	0.2526	0.63
N	0.3113	0.78
O	0.3625	0.91
Fe	0.7520	1.88

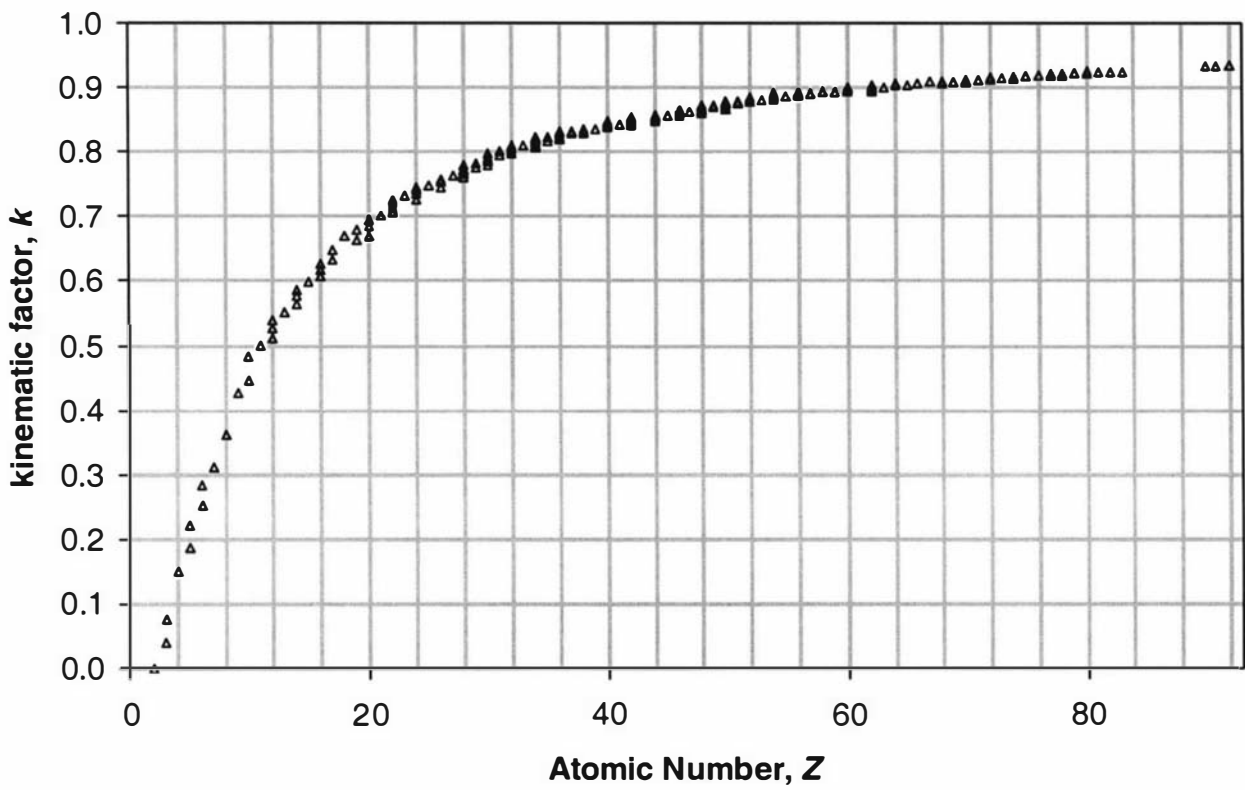


Fig. 2.14 k -factor at θ 170° with a $^4\text{He}^+$ incident beam, for isotopes of elements with $Z < 90$ with a natural abundance greater than 0.5 %.

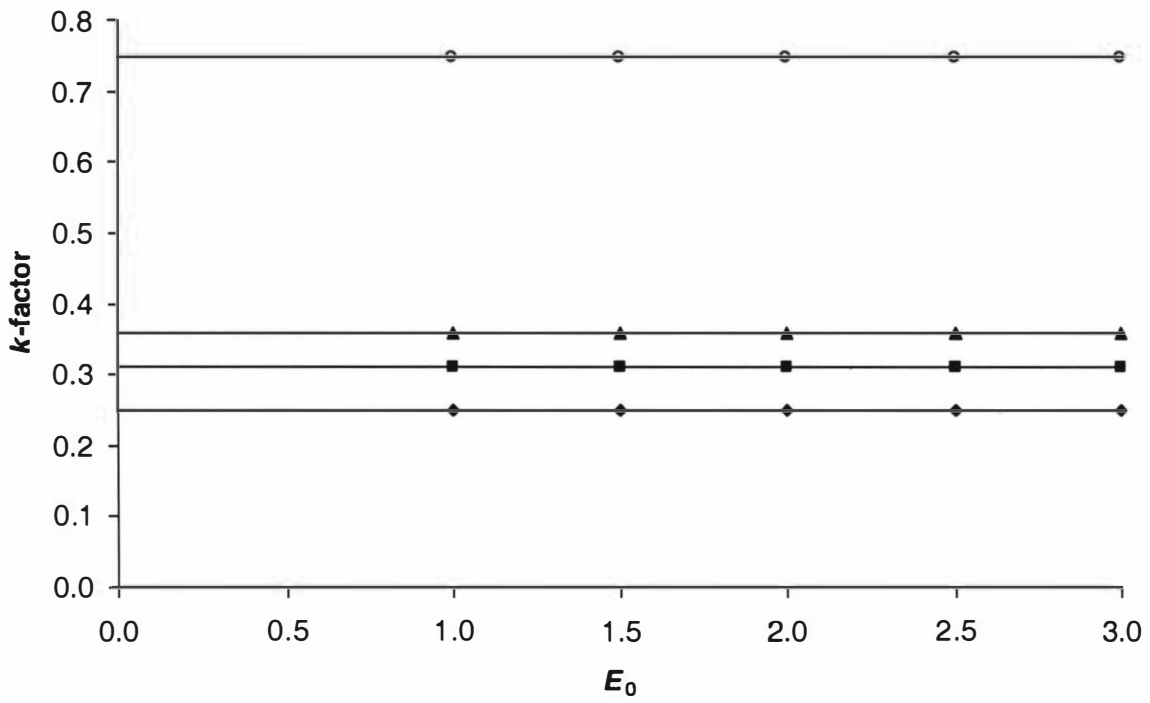


Figure 2.15 Graph showing the independence of the kinematic factor on E_0 .

Carbon - ♦, nitrogen - ■, oxygen - ▲, iron - ○.

though these elements only differ in mass by one atomic number. However, as the mass of the target atom increases, an increasingly smaller portion of the projectile energy is transferred to the target atom during collision, and the energy of the incident backscattered atom asymptotically approaches the energy of the beam. As a result, it is not usually possible to resolve W from Ta, or Fe from Co, when these elements are present at the same depth in a sample, even though these heavier elements also only differ in mass by one atomic number^[104, 105].

An important related issue is that $^4\text{He}^+$ will not backscatter from H or He atoms in a sample. Elements as light as, or lighter than, the projectile element will instead scatter at forward trajectories with significant retention of energy. The technique used to probe for H in a sample using $^4\text{He}^+$ ions is Elastic Recoil Detection (ERD)^[106]. This capability does exist at GNS but is not used in the present study due to hydrogen being one of the major elements present in organic compounds and not of great interest as the hydrogen content can be calculated once other elements have been detected.

2.6.3 Scattering Cross Sections

The relative number of particles backscattered from a target atom into a given solid angle for a given number of incident particles is related to the differential scattering cross section $d\sigma/d\Omega$. This scattering cross section is predominately the factor that determines the heights of the surface edge of the target element peaks within a spectrum. Equation 2.9 provides the relationship for scattering cross section in terms of the probability that a projectile ion will be scattered into a detector at a given solid angle.

$$\frac{d\sigma}{d\Omega} = \left[\frac{Z_1 Z_2 e^2}{4E} \right]^2 \frac{4}{\sin^4 \theta} \frac{\left[\sqrt{1 - \left[\frac{M_0 \sin \theta}{M_1} \right]^2} + \cos \theta \right]^2}{\sqrt{1 - \left[\frac{M_0 \sin \theta}{M_1} \right]^2}} \quad (2.9)$$

where

- Z_1 is the atomic number of incident ion
 Z_2 is the atomic number of target atom
 E is the energy of incident ion
 M_0 is the mass of incident ion
 M_1 is the mass of target atom
 θ is the scattering angle
 e is the charge on a proton

Figure 2.16 shows a relation plot of this probability of backscattering occurring increasing with atomic number. This indicates that RBS is more sensitive quantitatively for heavy elements than for light elements, due to the larger scattering cross section of the heavier elements.

This leads to the ability to determine the number of atoms of an element in a sample. If Q is the total number of particles striking the target and n_Q the number of particles recorded by the detector, then the areal density, denoted $(Nt)_i$, can be calculated for an element i by ^[106]

$$(Nt)_i = \frac{n_Q}{Q \left(\frac{dQ}{d\Omega} \right)_i \Delta\Omega} \quad (2.10)$$

where $\Delta\Omega$ is the solid angle of the detector and $(dQ/d\Omega)_i$ is the differential cross section for collision with element i .

The ion energy in RBS experiments is applied in an energy window where Coulomb interaction between ion and atom dominates. Consequently, the areal density of an element in the sample can be found using Eqn. 2.10. When the energy of the incident ion beam exceeds the energy window for RBS, non-Rutherford scattering occurs (e.g. 2.50 MeV for C, 3.50 MeV for ^{14}N , and 3.05 MeV for ^{16}O).

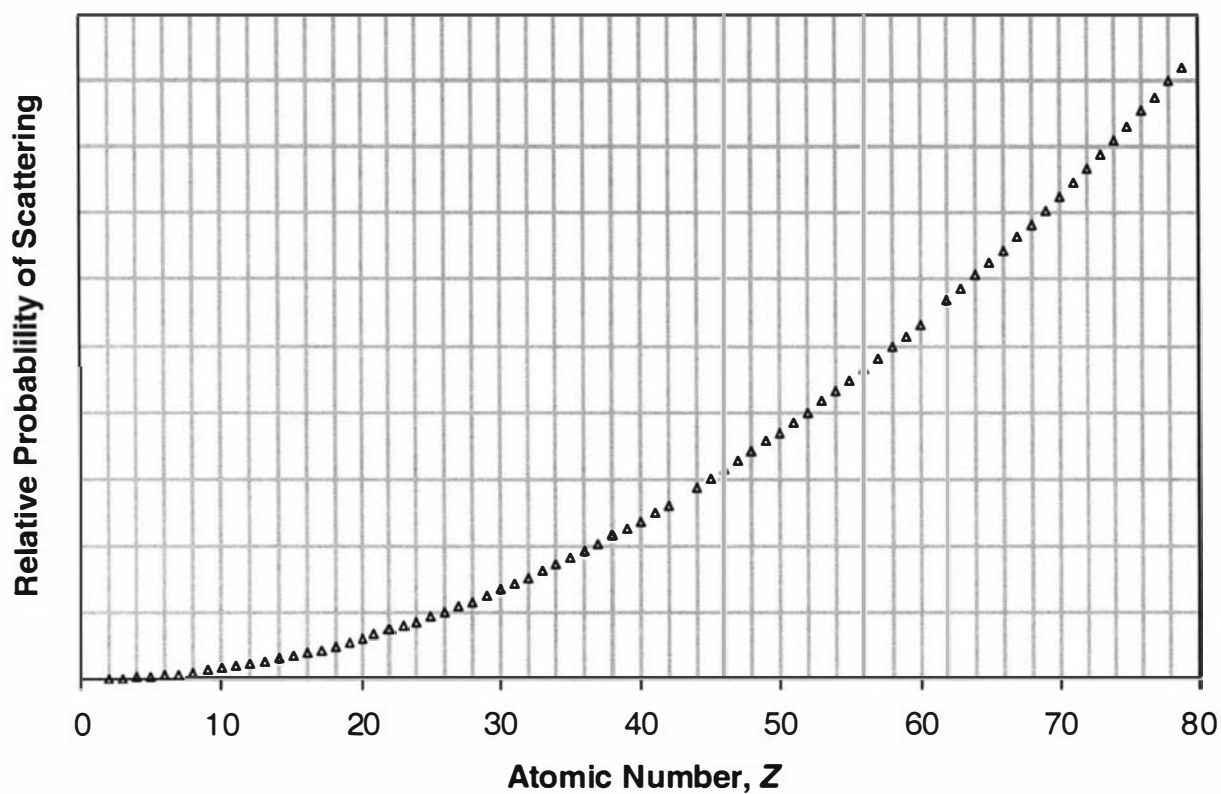


Fig. 2.16 Scattering cross section of isotopes for elements with $Z < 80$ with naturally occurring isotopes above 0.5 %. The differences in scattering cross section for each isotope of an element (typically less than 0.01 %) are not discernable.

2.6.4 Stopping powers and depth profiling

RBS can also reveal at what depth in a sample the atoms of a certain element are situated. Some projectile ions scatter from atoms at the surface while others penetrate deeper into the sample before interacting with an atom and scattering out of the sample (Fig. 2.17).

The energy difference between an ion scattered at the surface and one at depth l is,

$$\Delta = kE_0 - E_2 \quad (2.11)$$

where

$$\Delta = \varepsilon l \quad (2.12)$$

and

$$\varepsilon = \left[\frac{k\varepsilon(E_0)}{1} + \frac{\varepsilon(E_{K,1})}{\cos \theta_{out}} \right] \quad (2.13)$$

where ε is the stopping cross section factor, $\varepsilon(E_0)$, and $\varepsilon(E_{K,1})$ are the stopping cross section incident energies which are previously reported ^[106, 107], θ_{out} is the angle at which the detector is set. Δ can be measured from the spectrum, so layer thickness, l , can be determined. In this way an energy interval in a spectrum can be converted to a depth interval.

There are two contributions to stopping power (Fig. 2.18). The first is the electronic stopping power and the majority of energy loss is through this type. As ions travel through a sample they interact with a succession of electrons with progressive transfer of energy, much in the way a moving object transfers energy to its surroundings through friction. This dictates that a particle which backscatters from an element at some depth in a sample will have lower energy than a particle which backscatters from the surface. In Fig. 2.19, five schematic RBS spectra for a series of Na samples

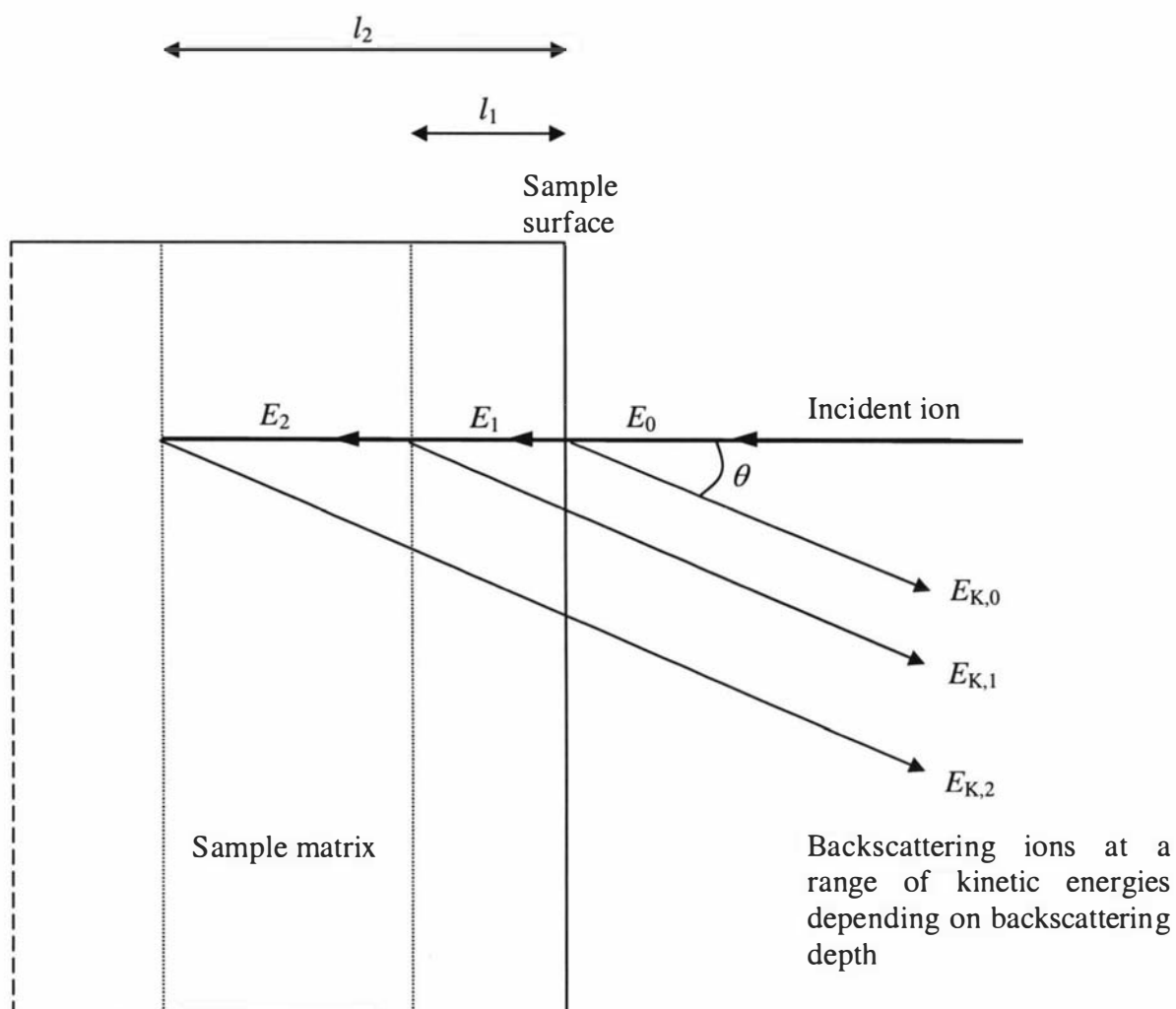


Fig. 2.17 Schematic drawing of an incident ion backscattering, at an angle θ , from the surface and from distances l_1 and l_2 into the sample matrix.

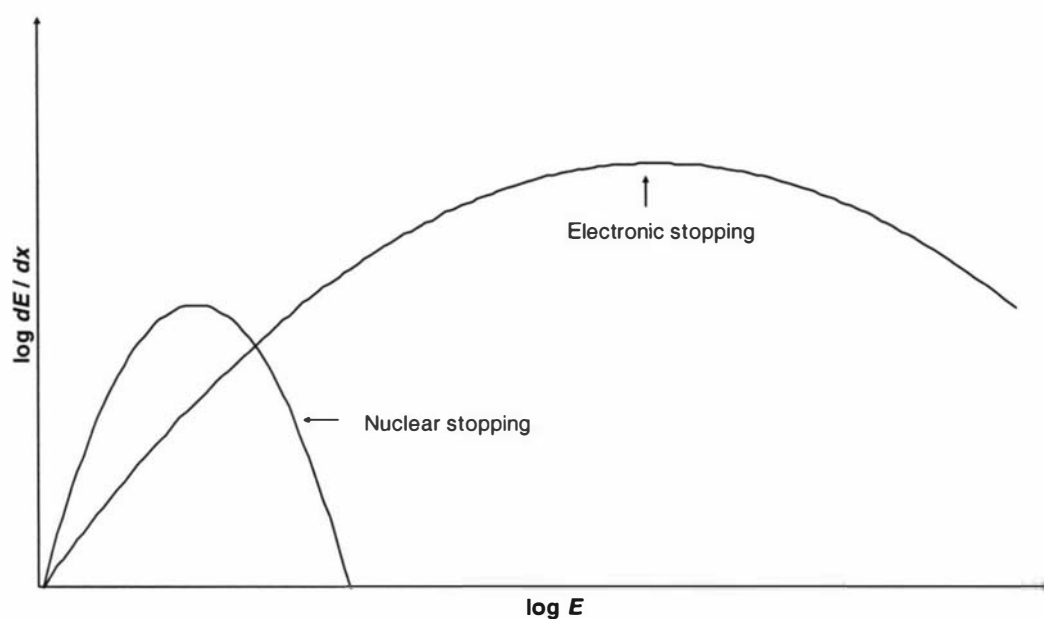


Fig. 2.18 Schematic of the relationship of nuclear and electronic stopping power with energy for an element. The maximum of the nuclear stopping curve typically occurs at an energy around 1 keV/amu and the maximum of the electronic stopping power at about 100 keV/amu energies. For very light ions decelerating in heavy materials, the nuclear stopping is weaker than the electronic stopping power at all energies.

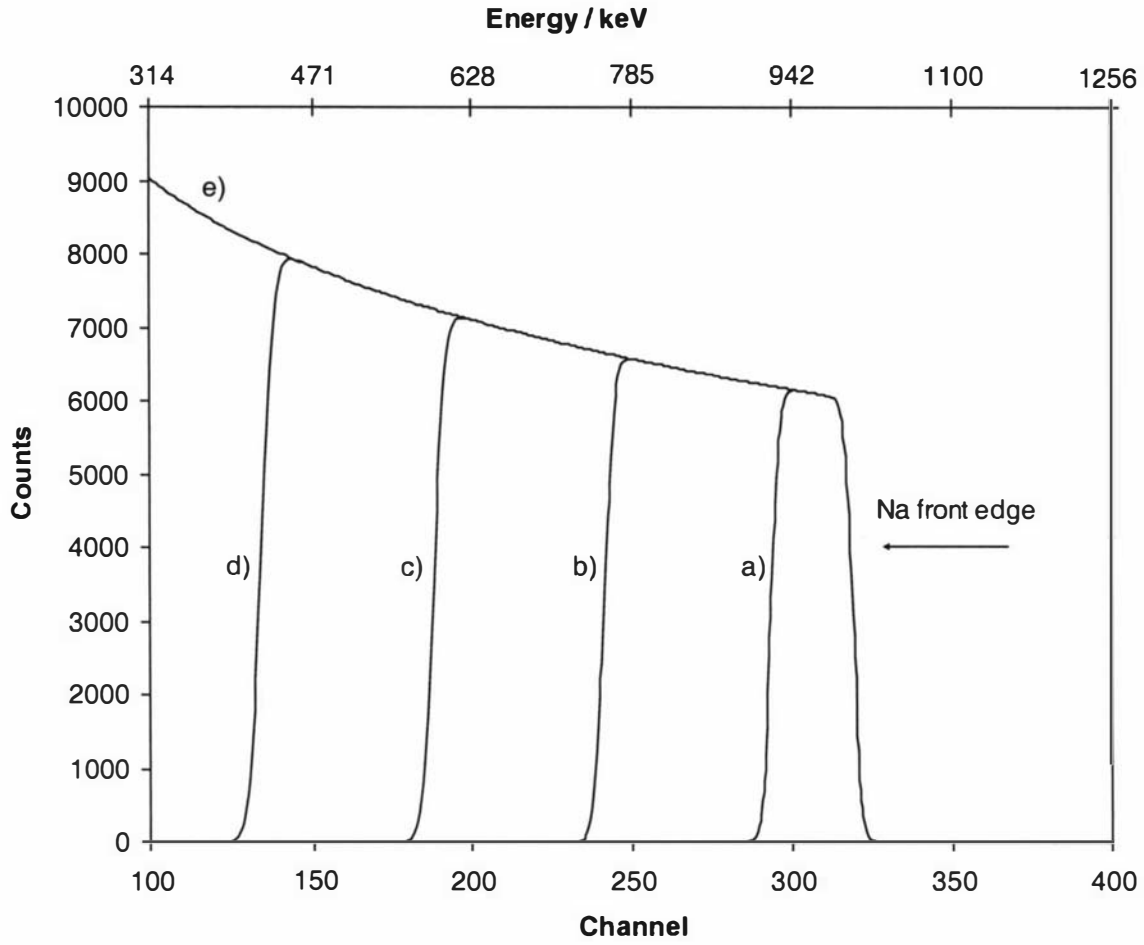


Fig. 2.19 Schematic RBS spectra of five Na samples with varying thicknesses, from a) 1000 at/cm^2 , b) 3000 at/cm^2 , c) 5000 at/cm^2 , d) 7000 at/cm^2 , and e) infinitely thick.

with increasing thicknesses (expressed as total atoms per projected area of sample, at/cm²) of films are shown. All samples have the same surface edge on the high energy side of the continuum, corresponding to ions scattered at the surface (Section 2.6.2). As ions penetrate deeper into the progressively thicker samples they lose more energy due to electronic stopping. As a consequence, their backscattered energy is decreased and shifted to the left in the spectrum. A RBS spectrum of an infinitely thick film will show a maximum level of backscattering for all energies below that of the surface edge to zero energy as projectile ions backscatter with diminishing energies further and further into the sample. Thinner films will exhibit no RBS counts beyond the maximum energy loss through the thickness of the film, so that the backscattering count drops to zero, and hence provides a measure of film thickness.

The second contribution to stopping power is nuclear stopping. This is caused by the large number of glancing collisions which occur along the path of the probing atom. Nuclear stopping contributes significant energy losses only at low particle energies. Since the majority of energy loss is caused by interactions with electrons, the electronic structure of the target material has a significant affect upon its stopping power.

2.6.5 *Scattering angle*

The detector position is set within the IBA chamber to select for a desired backscattering angle θ . Depending on the value of θ , different responses are recorded from a given sample. Figure 2.20 shows the dependence of the k -factor upon this selected scattering angle according to Eqn. 2.6. Each of the four curves show the same general trend, with the energy of the backscattered particles asymptotically approaching the incident particle energy. This asymptotic approach is more pronounced at lower scattering angles. The most common value for θ using ⁴He⁺ RBS is 165°^[107] and this was the angle used in this work.

2.6.6 *Multi-element spectra*

The above principles in Sections 2.6.2 – 2.6.5 also apply to RBS in the presence of more than one element. The overall RBS response is additive for each element. If there are two or more elements in a sample, and these elements are separated by large

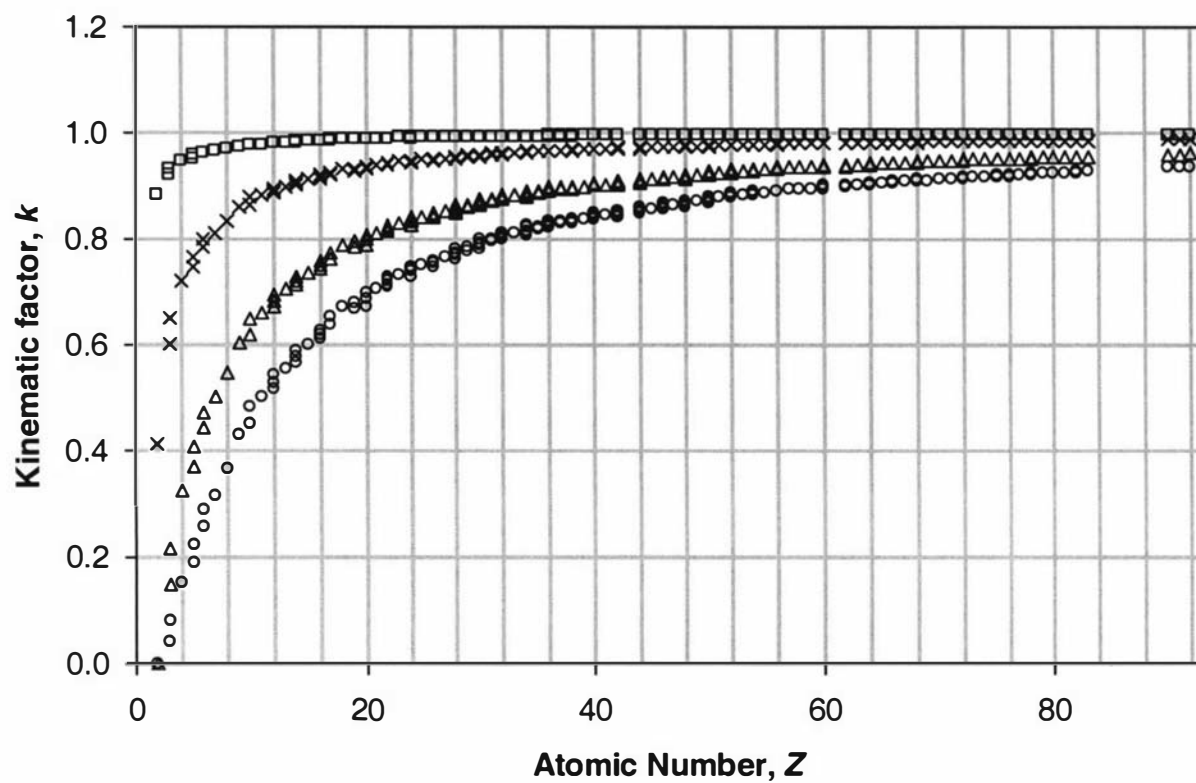


Fig. 2.20 Dependence of k -factor on detector angle selected (o - 165° , Δ - 80° , \times - 50° , \times - 20°).

atomic numbers, or the sample thickness is sufficiently thin so that element peaks do not overlap, a spectrum would be of the form shown in Fig. 2.21.

When the atomic numbers for the elements in a sample do not differ greatly, and/or the sample is thick, a more complex overall response is observed. The solid line in Fig. 2.22 represents the experimental RBS spectrum that would be seen from a multi-element sample containing C, O, and Na, in a thick sample. Each of the elements are detectable to different depths within the sample, and concentrations of each element also varies.

If the concentrations for a multi element sample were constant throughout the sample there would only be the need to determine the element concentration for a single homogenous layer. If, however, the elemental composition varied with depth the elements concentrations would have to be determined by consideration of a series of discrete and differing layers.

2.6.7 *Analysis methods for RBS*

Two analysis programs were used to fit additive simulation curves to the data in this work, RUMP and SIMNRA. These two different analysis programs were used throughout this work for both $^4\text{He}^+$ and proton RBS to determine the element composition of sample films: $^4\text{He}^+$ RBS for the work undertaken in Chapters 3 and 4 (RUMP); and proton RBS for the work in Chapter 5 (SIMNRA).

2.6.7.1 RUMP

RUMP is a program developed by, the then graduate students, Michael Thompson and Larry Doolittle in 1987 when at Cornell University, NY, USA, and is now marketed by Computer Graphic Service Ltd. (El Paso, TX, USA) ^[108]. A number of the experimental parameters must be loaded when using RUMP. These experimental parameters include beam energy, beam type, scattering angle, geometry, and beam current. The next step is to perform an energy calibration using a selection of standard samples analysed together with the samples. These standards are samples of known element composition and concentration. This process involves loading the standard spectra and allocating channel numbers at energies with fixed energy bandwidths to

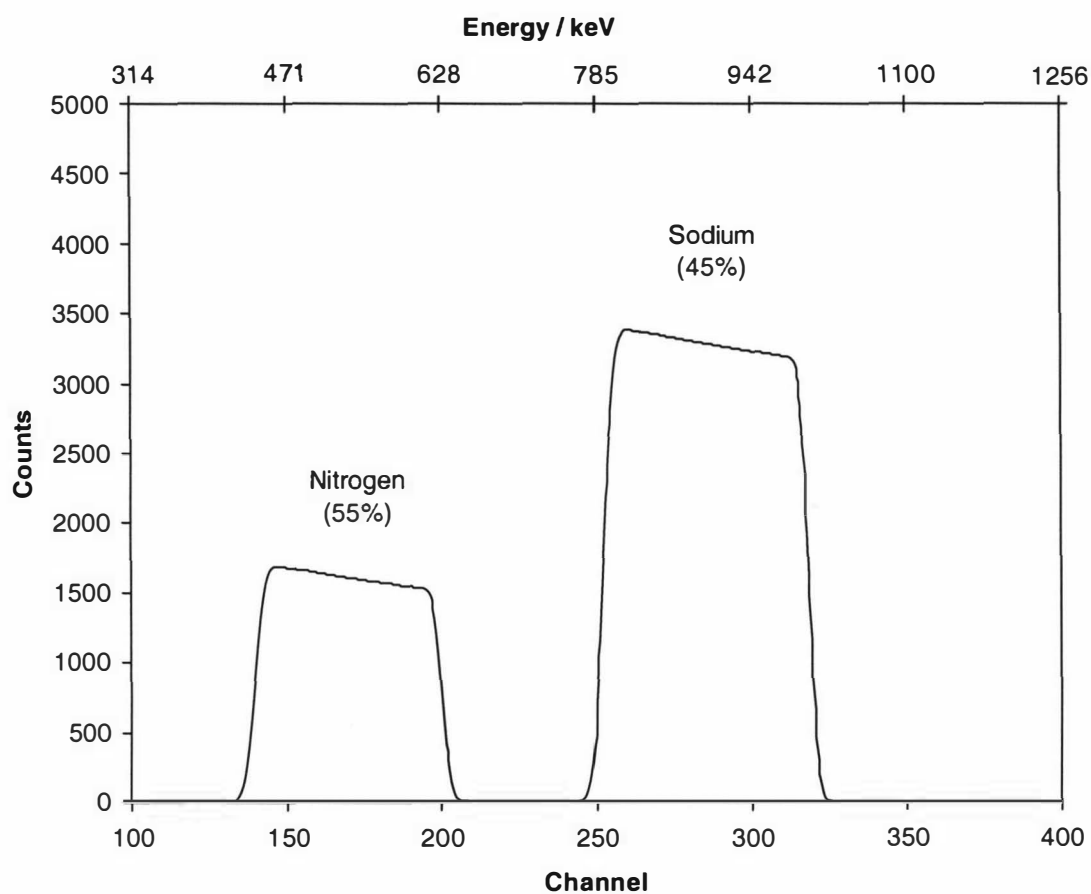


Fig. 2.21 A schematic RBS spectrum of a sample containing two elements, N and Na, with a sample thickness of 3000 at/cm^2 , whose backscattered energies are such that they do not overlap in the spectrum ($^4\text{He}^+$ 2.0 MeV beam, $\theta = 165^\circ$)

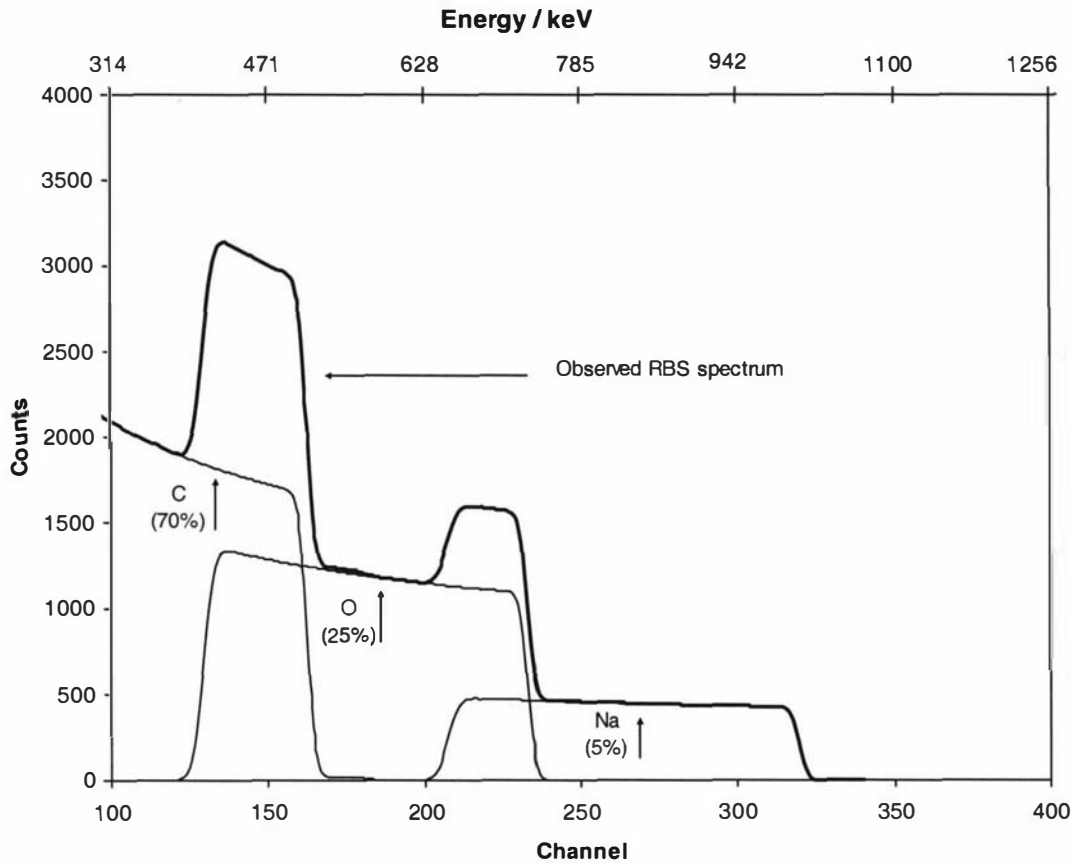


Fig. 2.22 A schematic RBS spectrum (bold solid line) of a sample containing three elements (C, O, and Na) (each thin line), with a sample thickness of 6000 at/cm^2 , whose backscattered energies do overlap in the spectrum, resulting in an observed overall response curve ($^4\text{He}^+$ 2.0 MeV beam, $\theta = 165^\circ$).

these well-characterised samples. This energy conversion information is linked to the experimental data sets to permit subsequent data analysis involving iterative determination of elemental composition and depth profiling of the sample. This is achieved in RUMP by using a simulation mode (SIM). In this mode the predicted RBS spectrum for the elemental composition and individual element concentrations are set for each discrete layer deemed necessary, to obtain a satisfactory fit to the experimental spectrum. In the present study it was not atypical to include consideration of up to four layers with differing elemental composition to afford a satisfactory fit between observed and predicted RBS.

2.6.7.2 SIMNRA

SIMNRA was developed by Matej Mayer in 1997 at the Max Planck Institute for Plasma Physics (Garching, Germany) ^[109] as a Microsoft Windows program for the simulation of backscattering spectra for ion beam analysis with MeV ions. It is mainly intended for the simulation of RBS non-Rutherford backscattering, nuclear reactions, and ERD. This program was used in this study for interpretation of the TTh-Fc co-polymers as a proton beam was used for this section of work. RUMP has the capability to take into account RBS non-Rutherford backscattering but it is challenging to adequately include this data into simulations.

Experimental parameter entry and calibration is required with SIMNRA. This program requires two calibration values to be set before any of the samples can be analysed. These are the calibration offset and energy per channel. This is achieved by identifying the channel number location of the half-height surface edges for two standard element samples. Ideally, the two elements should be of high and low energy (i.e. Au and C). These known elements and channel numbers are then linked to another program written by a member of the Wellington IBA group called 'Kinematics' ^[110]. In this program, the ion species of the beam, the beam energy, and the target element's mass are identified, and under the conditions of an elastic collision, the energy of the rebounding ions from the beam are calculated and reported. This is performed for the two standard elements whose surface edge channel numbers have been located. These values are then used together with Eqn. 2.14 to calculate the energy per channel value, m , where

$$m = \frac{\Delta E}{\Delta channel} = \text{keV/channel} \quad (2.14)$$

Once a value for m has been determined, this value is then inserted into Eqn. 2.15 to determine the calibration offset (keV) (assuming a linear response across all channels, n).

$$E = mn + c \quad (2.15)$$

where c is the calibration offset value in keV.

These calibration values are linked to each of the experimental spectra for subsequent analysis.

The extent of non-Rutherford scattering is then determined. SIMNRA incorporates a database of non-Rutherford behaviour. For each of the anticipated elements in the sample non-Rutherford data is required. This data must cover the energy range up to the energy of the incident beam, and appropriate for the scattering angle used in data collection. It is not unusual to interpolate these parameters for non-tabulated θ ^[111].

2.7 Particle Induced X-ray Emission (PIXE)

2.7.1 Introduction

When an inner core electron from an atom is removed a vacancy occurs which is subsequently filled by an electron from one of the outer electron shells (Fig. 2.23). With this transition from an outer electron shell to an inner core shell a quantum of energy is simultaneously released, equal to the energy spacing between the two electron shells. The energy of this quantum of radiation, which is in the X-ray region of the electromagnetic spectrum, is characteristic of the parent atom and its measurement can therefore be used to identify the parent atom. The main characteristic X-rays are labelled as K, L, or M to denote the shells they originated from. A further designation, alpha (α), beta (β), or gamma (γ), is made to mark the X-rays that originated from the transitions of electrons from higher shells. Hence, a K_α X-ray is produced from a transition of an electron from the M to a K shell, and a

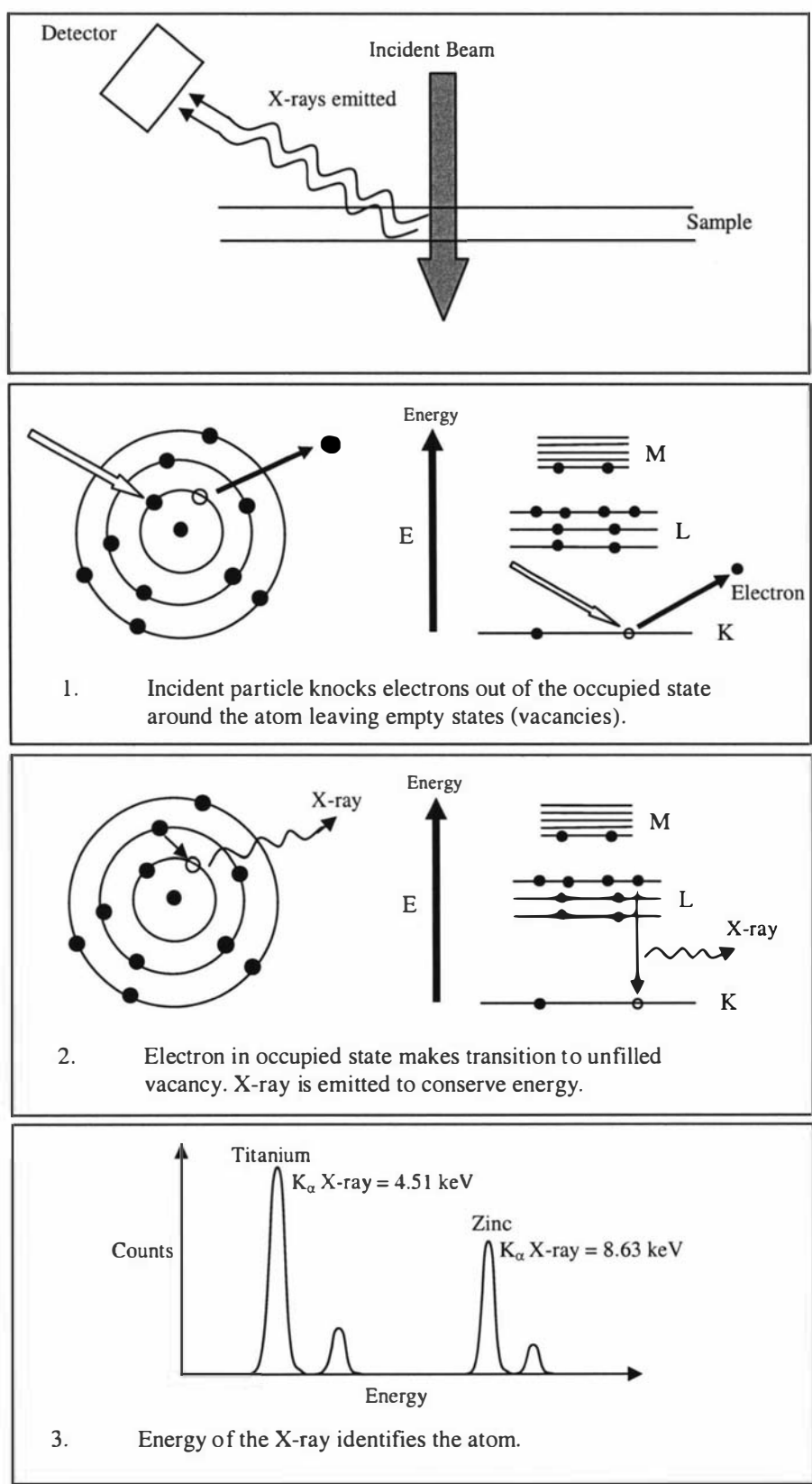


Fig. 2.23 Schematic diagrams of the production of X-rays.

K_{β} X-ray is produced from a transition of an electron from the M to a K shell, and so on. α -lines have the highest intensity of the three sub-groups, but the lowest energy. β -lines have a higher energy but a lower intensity compared to α -lines. γ -lines have the highest energies but the lowest intensity of the three sub-groups.

There are a variety of possible collision processes which can be used to remove an inner core electron to facilitate the emission of a characteristic X-ray.

- i)* the use of another incident X-ray of slightly higher energy (X-ray fluorescence)
- ii)* a high kinetic energy electron (Electron Induced X-ray Emission)
- iii)* a fast moving proton with energy *ca.* 2 MeV (Particle (or proton) Induced X-ray Emission, (PIXE)).

The most easily arranged method for inducing characteristic X-rays would seem to be by electron bombardment, since electron microscopes are relatively common instruments. However, the problem with employing electron induced X-ray emission is that prior to a primary electron colliding with an inner core electron, the primary electron suffers a large deceleration, either by loss of energy or change in direction (large angle scattering). Accompanying this change in velocity is a “bremsstrahlung” (German for ‘deceleration radiation’) and this radiation causes a large X-ray background which limits the sensitivity of the electron induced X-ray emission technique^[107].

PIXE does exhibit bremsstrahlung background, but to much lower intensity than electron induced X-ray emission produces, since protons are 1800 times more massive than electrons and do not change their velocities significantly when colliding with an electron. A comparison of X-ray spectra obtained from electron induced X-ray emission and PIXE are displayed in Fig. 2.24. In general, the X-ray background with PIXE is 100 to 1000 times lower than that for electron induced X-ray emission, and

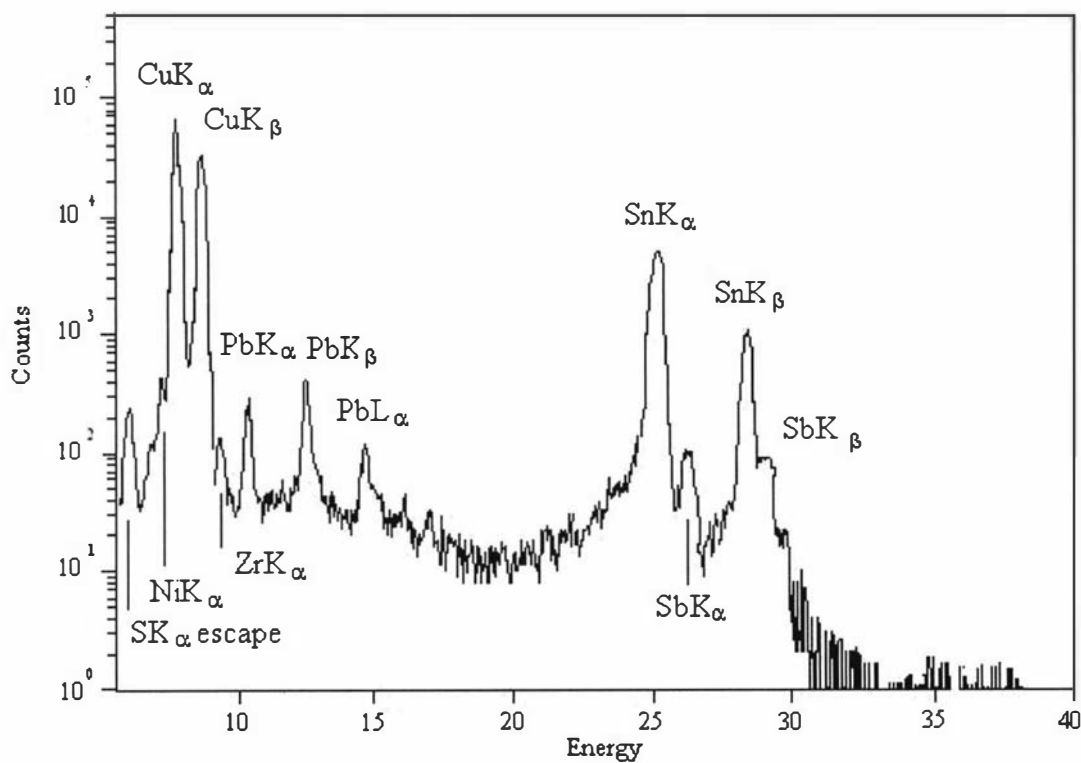
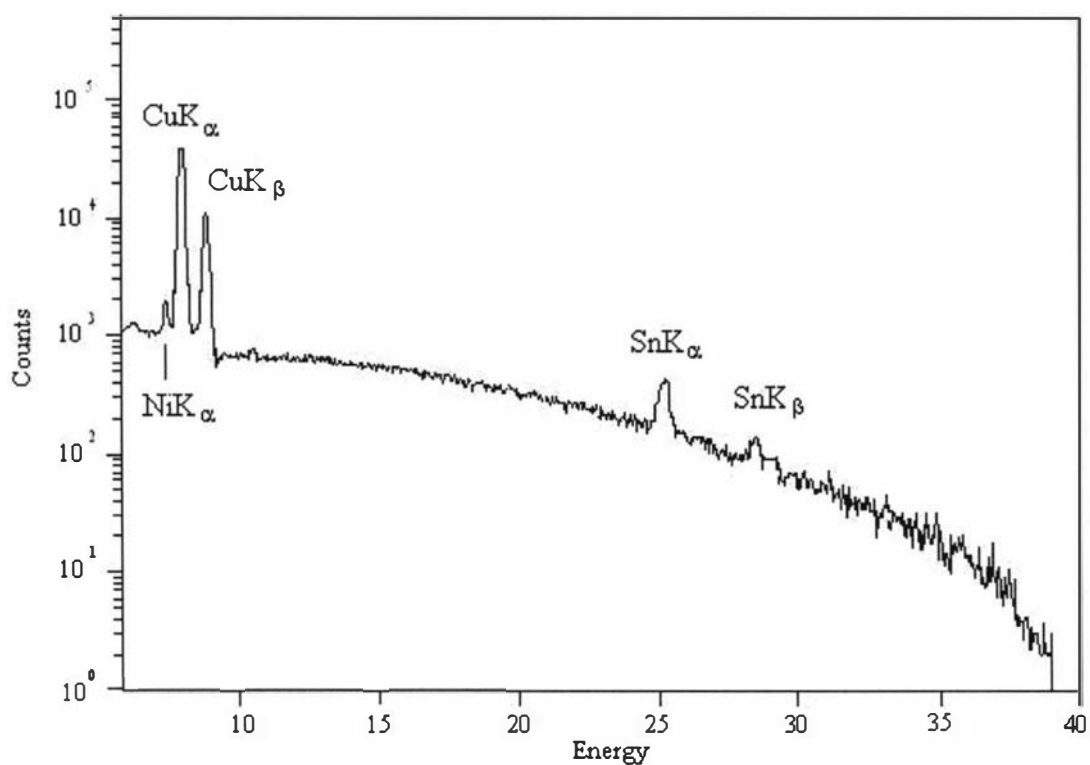


Fig. 2.24 Composite schematic spectra showing the main features when comparing Electron Induced X-ray Emission (above) to PIXE (below)

this is reflected by improved sensitivities for PIXE which can be in the parts per million range.

The contributing effects to background in X-ray spectra arise from the following:

- i) Secondary electron bremsstrahlung, where electrons are ejected from target atoms during irradiation;
- ii) Projective bremsstrahlung, which is caused by decelerating ions;
- iii) Compton scattering; and
- iv) Insulating targets, which can have localised high-voltage which can accelerate free electrons.

The further advantage of protons over X-rays for inner core electron removal is that protons can be focused to smaller spot sizes, and can therefore analyse much smaller samples with a greater flux of X-ray emission.

2.7.2 *Calibration and Qualitative Analysis*

Before any analytical information can be extracted from a PIXE spectrum it must first be calibrated in terms of energy. This is performed using X-rays from at least two known elements. Standards are run (e.g. Au, Fe, Mylar) before collecting data for the unknown samples. During calibration, the energy of the first and final channels are determined and these two values are used to calibrate each of the unknown sample spectra. Once the energies of the unknown peaks for a sample are determined, the associated element can be identified using charts which list elements and their X-ray production energies^[107].

Figure 2.24 shows a typical PIXE spectrum. All PIXE spectra in this thesis are plotted with one y-axis (log Counts), and two x-axes (lower – channels, upper – energy (keV)). The broad increase in response increasing with decreasing channel number seen from channel 60 – 260 in Fig. 2.25 is the contribution from bremsstrahlung.

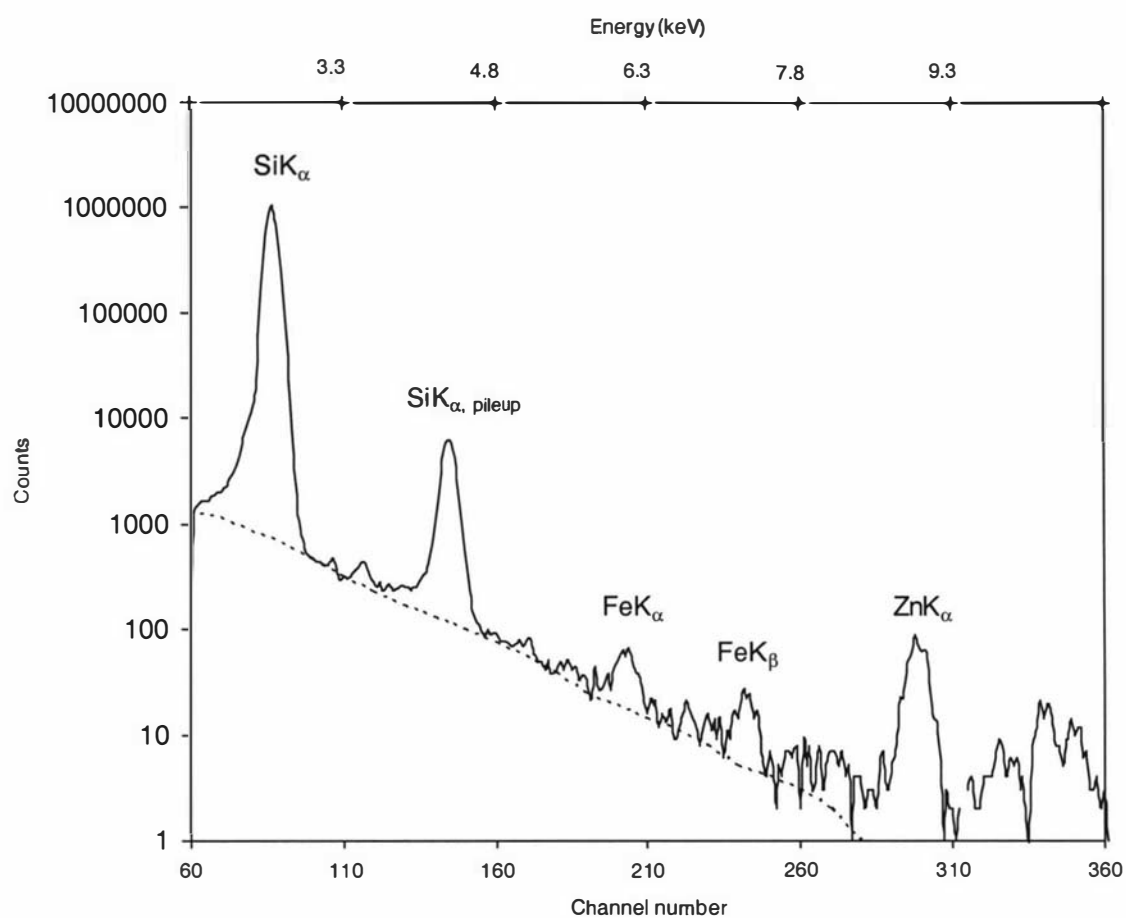


Fig. 2.25 A PIXE spectrum for a Si/N on Si substrate, the dashed line is indicates the bremsstrahlung background.

Nevertheless this is sufficiently low that it does not interfere significantly with peak detection.

2.7.3 *Quantitative Analysis*

GUPIX is a versatile software package for fitting PIXE spectra, extracting peak intensities and converting to atom concentrations. GUPIX was developed by J. L. (Iain) Campbell and John Maxwell at the University of Guelph, Ontario, Canada in 1995 ^[112].

GUPIX uses a non-linear least-square procedure to fit the PIXE data spectrum. The least-squares technique used in Chapter 4 for this thesis was that developed by Marquardt (Bevington, *Data Reduction and Error Analysis for the Physical Sciences*, McGraw-Hill, New York, 1969).

A theoretical spectrum is generated by using Gaussian peaks for each of the main X-ray lines for the anticipated sample element (including escape peaks, radiative Auger peaks, double ionization satellite peaks and pile-up peaks). This theoretical spectrum is then compared with that of the data and tested via the chi-square criterion for goodness of fit on the basis of the channel weighting. The program also takes into account contributions from bremsstrahlung background.

CHAPTER 3

Scoping study

3.1 Introduction

The aim of the work carried out in this Chapter was to first determine whether the IBA techniques (RBS and PIXE) could be used to analyse soft organic material that had been electrochemically deposited onto Glassy Carbon (GC) electrodes, and if they could differentiate between four differently prepared bis terthiophene porphyrin (TTh-Por-TTh) based samples. The monomer of the material is complex, but was used because of their affinity of coordinating metal to the four pyrrole ring centre in porphyrins. Three different depositions of the TTh-Por-TTh were undertaken, and one deposition of a zinc coordinated bis terthiophene porphyrin (TTh-ZnPor-TTh) monomer. Of the three TTh-Por-TTh samples one was left as it was, one was cycled using CV in zinc acetate (cycled TTh-Por-TTh), and the other was left to soak in zinc acetate (soaked TTh-Por-TTh). This was performed to determine if any difference between the amount of zinc found from IBA analysis could be discerned between a sample with no prior contact with zinc, one which had been electrochemically cycled in zinc, one which had been soaked in zinc, and one which had had zinc already coordinated into the sample.

3.2 Electrochemistry

3.2.1 *Monomers*

The organic material was electrochemically deposited onto GC discs from two related monomers. The two monomers used were TTh-Por-TTh and TTh-ZnPor-TTh and are shown in Fig. 3.1

Solutions of both the TTh-Por-TTh and the TTh-ZnPor-TTh monomers (4 mg) were prepared in dichloromethane (DCM) (2 mL) with 0.1 M tetrabutylammonium perchlorate (TBAP) as supporting electrolyte. The material was electrochemically

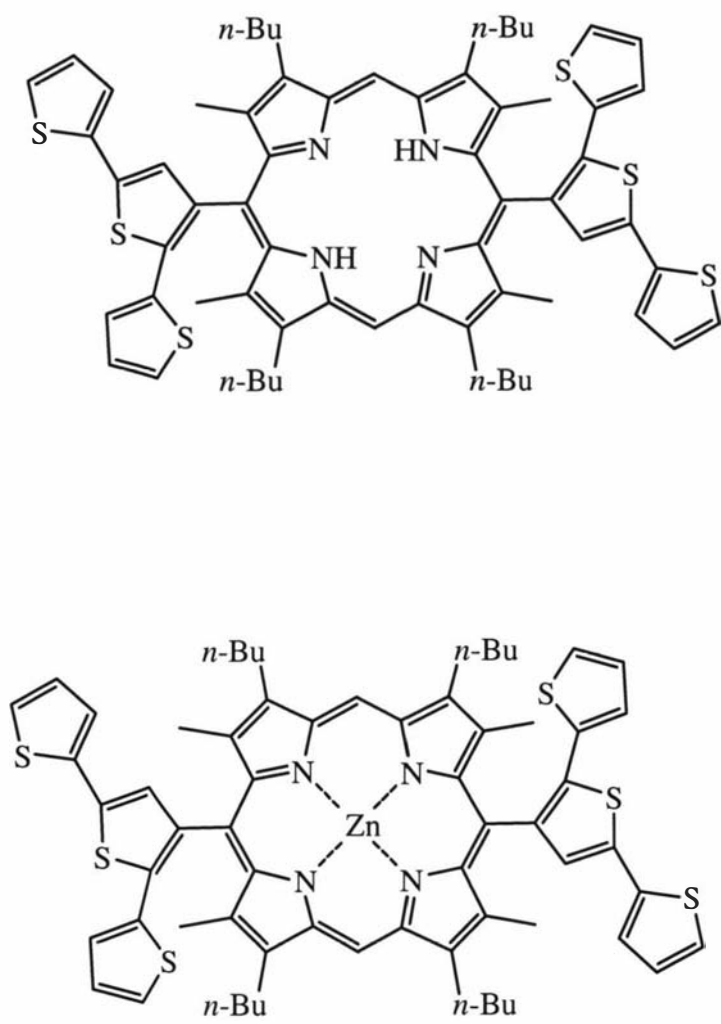


Fig. 3.1 Structure of freebase bis terthiophene porphyrin, TTh-Por-TTh, (above), and Zn coordinated bis terthiophene porphyrin, TTh-ZnPor-TTh (below).

deposited onto GC working electrodes (6 mm diameter) with a silver wire and platinum wire as the reference electrode and counter electrode respectively.

3.2.2 *Electrochemical deposition*

Single cycle CVs were carried out on both the TTh-Por-TTh and TTh-ZnPor-TTh solutions on polished GC electrodes. These are shown in Fig. 3.2 and Fig. 3.3 respectively. In the forward sweep in Fig. 3.2 there is an onset of oxidation at 275 mV. This appears to reach a steady state until a potential of *ca.* 650 mV where a pronounced oxidation process commences. This oxidation peaks at 1070 mV and then at 1120 mV a further oxidation process commences – this is assumed to be the main oxidation of the sample material. On the reverse sweep there is a shoulder at *ca.* 920 mV beyond which a reduction peaks commences which peaks at 680 mV. A second broad reduction peak is observed at 300 mV.

The CV for the TTh-ZnPor-TTh solution is much simpler than that for TTh-Por-TTh. Here the first oxidation occurs at 420 mV, which is *ca.* 150 mV more positive than for the TTh-Por-TTh. The oxidation peak has a maximum at 850 mV, starts to decrease, followed by assumed main sample material oxidation occurring at 940 mV. On the reverse sweep, what appears as a shoulder in the TTh-Por-TTh CV is now a peak for the TTh-ZnPor-TTh sample, with a maximum at 706 mV. A distinct reduction peak is observed at 342 mV in contrast to the smaller, broad peak on the reduction sweep for the TTh-Por-TTh sample (*ca.* 300 mV).

Based on these CVs, a potential of 1200 mV was chosen for the electrochemical deposition of material under CA experiments. Both samples were electrochemically deposited onto polished GC discs at 1200 mV for a fixed time of 4000 s. At the completion of each of these depositions periods the CE and RE were removed, the monomer solution discarded and the electrode cell and WE were rinsed with a clean solution of 0.1 M TBAP/ DCM three times. The cell was refilled with further 0.1 M TBAP/DCM so that post growth CVs could be collected.

3.2.3 *Post-polymerisation*

Figures 3.4 and 3.5 show the post growth CVs for the TTh-Por-TTh sample. Figure 3.4 shows the first post growth CV cycle. This demonstrates that electroactive

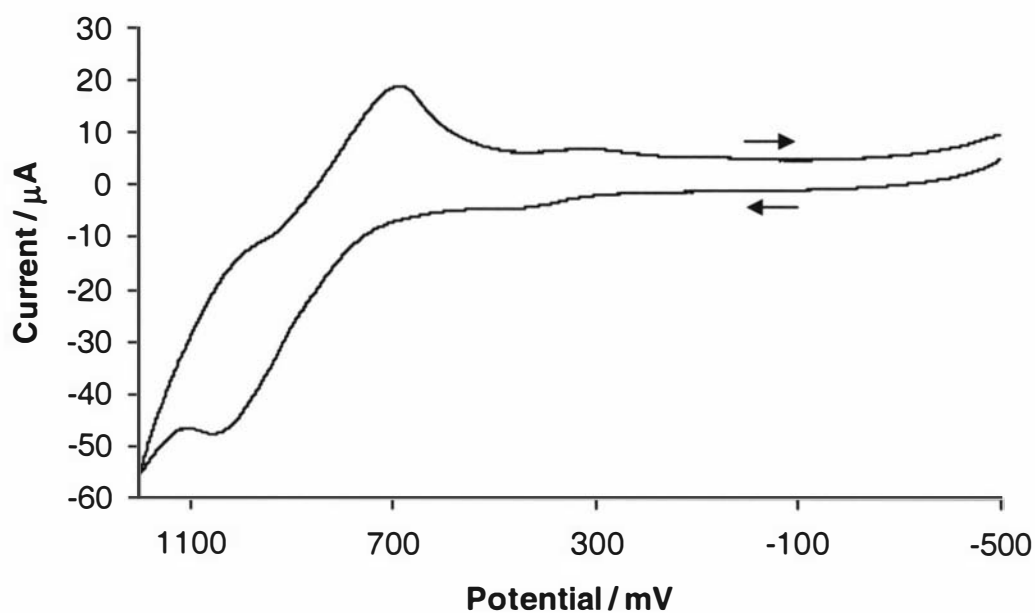


Fig. 3.2 CV of the electrochemical deposition of the bis terthiophene porphyrin, TTh-Por-TTh, onto a GC working electrode.

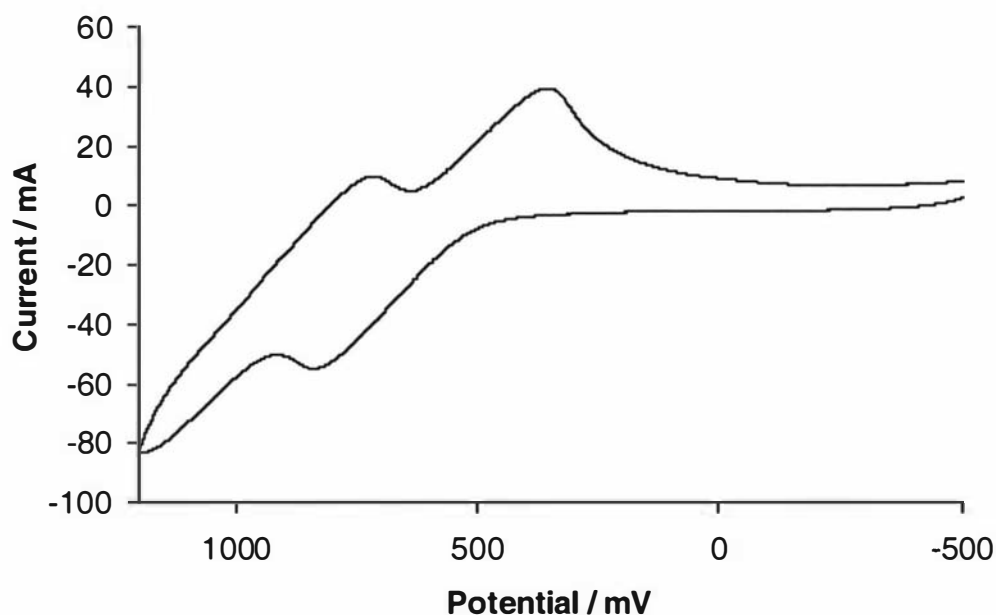


Fig. 3.3 CV of the electrochemical deposition of the zinc coordinated bis terthiophene porphyrin, TTh-ZnPor-TTh, onto a GC working electrode.

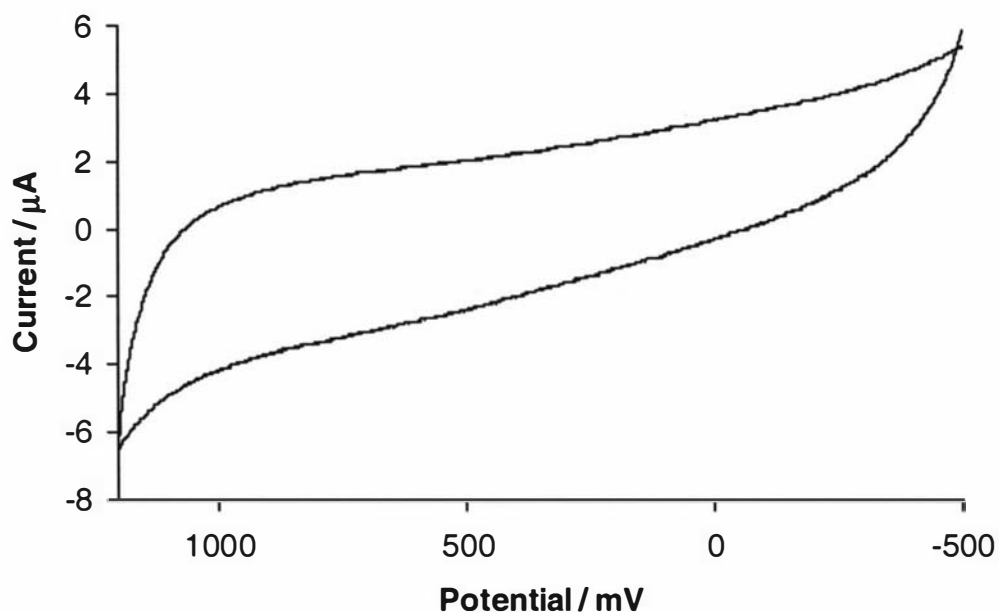


Fig. 3.4 Post growth CV of the electrochemically deposited bis terthiophene porphyrin, TTh-Por-TTh, (first cycle) at 100 mVs⁻¹, 0.1 M TBAP, in DCM.

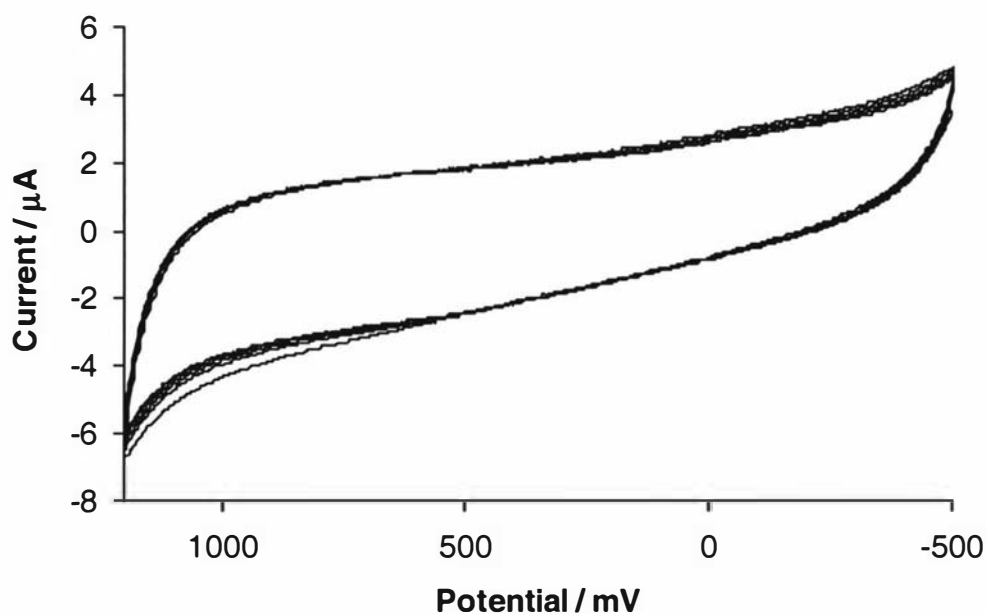


Fig. 3.5 Post growth CVs (cycles 1-5) of the electrochemically deposited bis terthiophene porphyrin, TTh-Por-TTh, at 100 mVs⁻¹, 0.1 M TBAP, in DCM.

material was electrochemically deposited during the CA experiment and that it had remained in electrochemical contact with the GC working electrode throughout the rinsing process. Figure 3.5 shows five subsequent repeating cycles of post growth CVs. This was performed to assess whether there was any change in response of the deposited material with time. Examination of Fig. 3.5 shows negligible changes to the response with cycling. Post growth CV cycles were also performed on the TTh-ZnPor-TTh electrode. The first cycle shown in Fig. 3.6 is consistent with electroactive material having been deposited onto the GC disc electrode. Five subsequent post growth CV cycles again show negligible changes (Fig. 3.7).

The material which was deposited onto the GC disc was blue/black in colour.

3.3 Ion Beam Analysis

3.3.1 *Film durability*

The first measurements performed using IBA were to investigate the durability of these porphyrin based samples under ion bombardment. In general, higher intensities of ion beams may result in destruction of organic materials through carbonisation^[113-115]. If damage was to be incurred, then the experimental parameters would have to be changed, and damage was still occurring to the sample due to bombardment then no further work in this area could be performed.

Before the RBS data collection commenced, two regions of interest were set in the energy spectrum. The first region was set from channels 100 to 200 (0.38 MeV to 0.64 MeV, $C < Z \leq O$) for light elements and the second region was set from channels 200 to 450 (0.64 MeV to 1.30 MeV, $O < Z \leq Ag$) for heavier elements. Figure 3.8 shows a spectrum for the TTh-Por-TTh sample where these two regions of interest are displayed. The first region starts near the surface edge of carbon and covers nitrogen and oxygen. The second region encompasses Al, S, and Cl predominately. The channels below 100 (0.38 MeV) are not included in the first region of interest because the substrate onto which these materials were deposited onto was GC, hence there would always be a large amount of carbon detected even if the material did not withstand the ion beam bombardment. There are also other artefacts that are more dominant at low energies (e.g. noise due to the detector), which make this region of

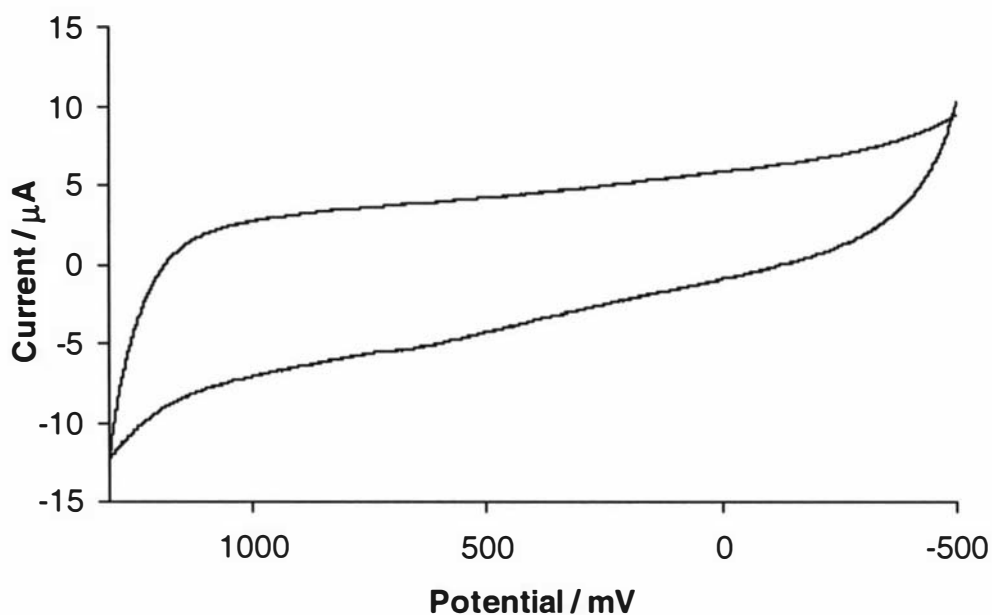


Fig. 3.6 Post growth CV of the electrochemically deposited zinc coordinated bis terthiophene porphyrin, TTh-ZnPor-TTh, (first cycle) at 100 mVs^{-1} , 0.1 M TBAP , in DCM.

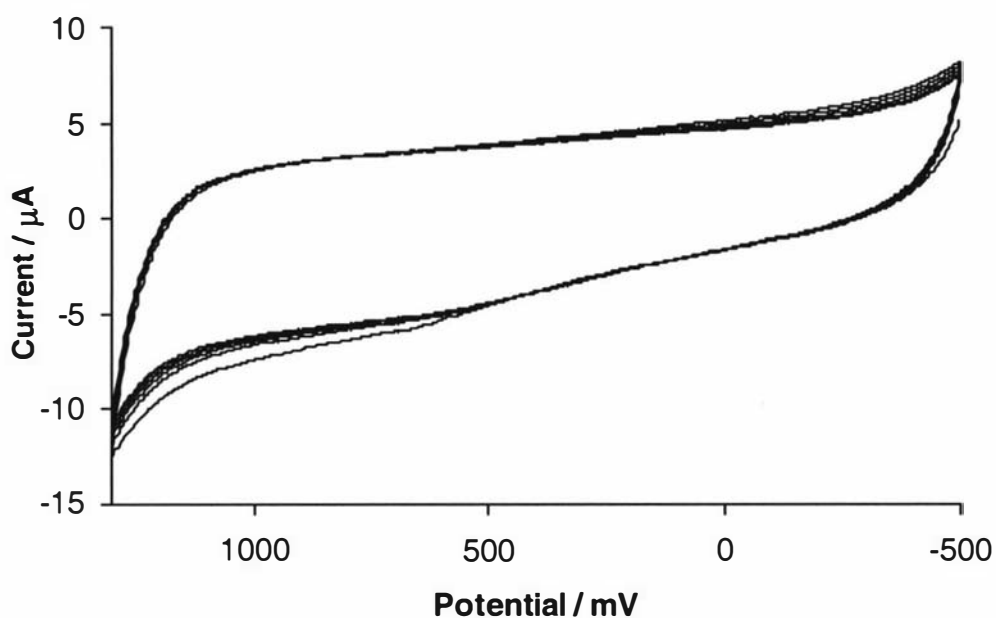


Fig. 3.7 Post growth CVs (cycles 1-5) of the electrochemically deposited zinc coordinated bis terthiophene porphyrin, TTh-ZnPor-TTh, porphyrin at 100 mVs^{-1} , 0.1 M TBAP , in DCM.

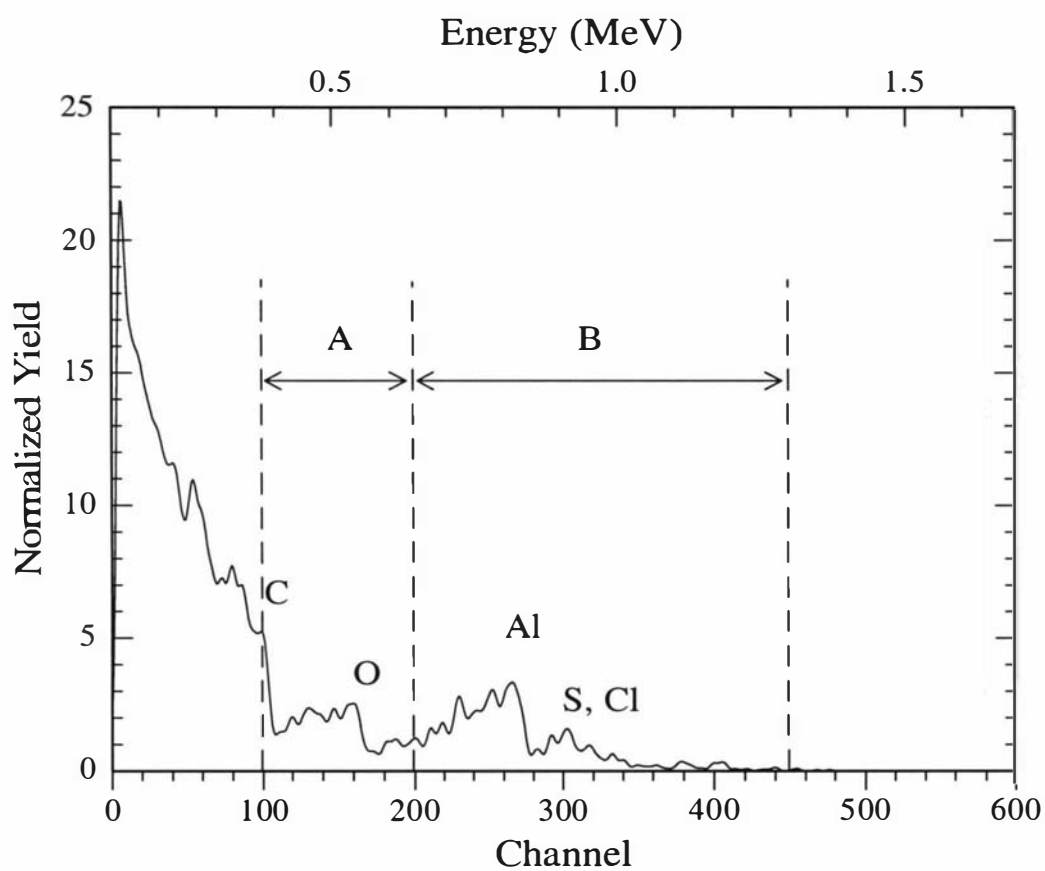


Fig. 3.8 RBS spectrum of the bis terthiophene porphyrin, TTh-Por-TTh, to show the regions of interest which were set for the film durability test.

the spectrum unreliable from an quantitative point of view ^[103].

During the experiment RBS spectra were measured at intervals of 20 μC (65 nA, *ca.* 300 s) until the total accumulated charge which the sample had been subjected to was 400 μC . Figure 3.9 shows the dependence of the total number of counts across all channels in the set regions of interest as a function of the accumulated charge. Figure 3.9 shows that no significant change in the composition of the sample material was measured over a long period of time ($t_{\text{total}} = 6150$ s, accumulated charge = 400 μC , beam current = 65 nA, beam diameter = 2 mm). The charge measured in region A, the light element region (N, and O)) appear to have increased by about 10 % throughout the duration of this experiment. This increase can be accounted for by the continuous deposition of a carbon film onto the surface of the sample material originating long-term measurement. With a residual gas pressure of 1×10^{-6} mbar this is a common feature in long-term IBA measurements ^[113]. Region B, that of the heavier elements, shows that no loss of material was detected for these elements.

This investigation into the durability of the sample was undertaken for all subsequent sample types in this Chapter. In each case there was no evidence obtained to suggest a loss of material over the measured time. It was concluded that the RBS experiments could be undertaken with the knowledge that the samples would not degrade with time when exposed to an ion beam.

3.3.2 *Rutherford Backscattering – RBS*

Representative RBS spectra of the TTh-Por-TTh, cycled TTh-Por-TTh, soaked TTh-Por-TTh, and TTh-ZnPor-TTh samples are shown in Figs. 3.10–3.13 respectively. The full RBS spectrum range ranges from channels 0 to 500. For the purposes of these samples, however, the area of interest lies between channels 100 and 500, covering the elements ranging from nitrogen to bromine. The solid line in these spectra represents the simulation of the RBS spectrum-using RUMP.

Figure 3.14 shows a flow diagram of the analysis process undertaken after the RBS spectra had been obtained. After the initial experimental parameters had been entered

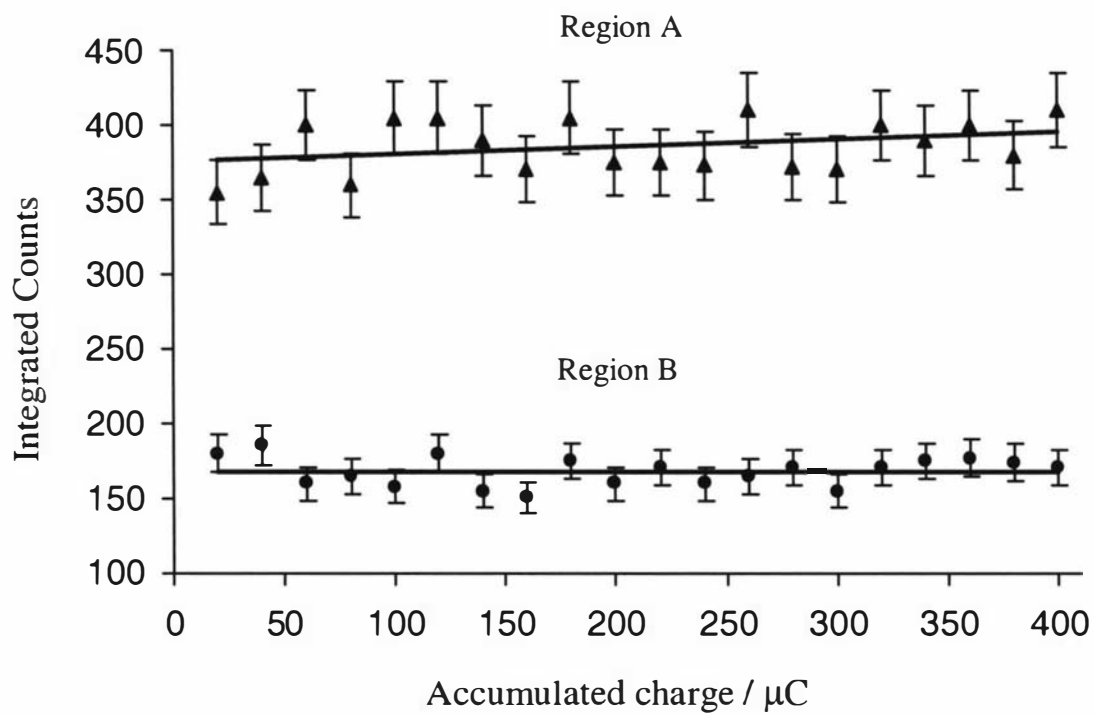


Fig. 3.9 Film durability results, plot of accumulated charge vs counts.

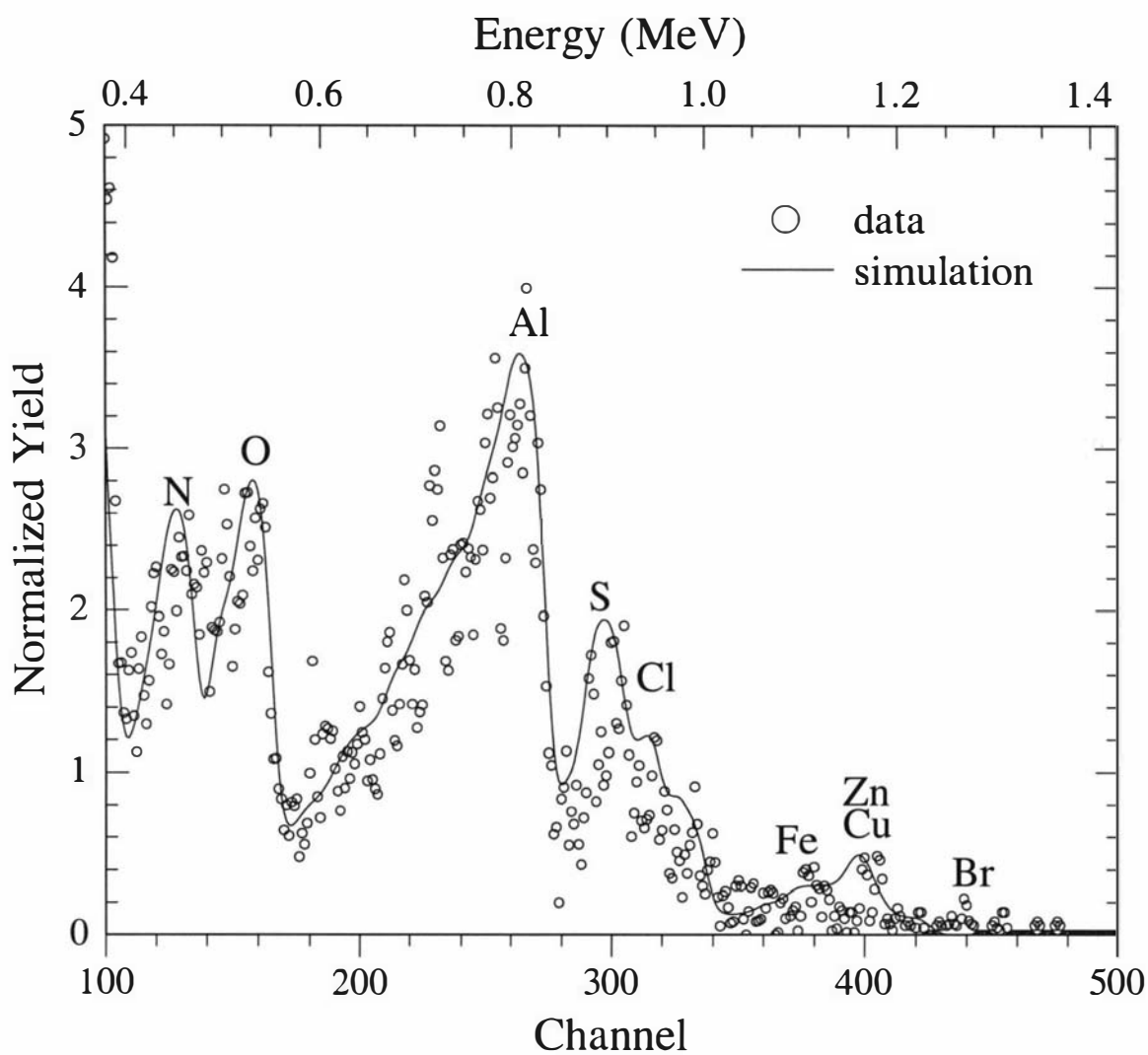


Fig. 3.10 RBS (channel 100 to 500) for a bis terthiophene porphyrin, TTh-Por-TTh. Simulation data is tabulated in the Appendix (Table A.1)

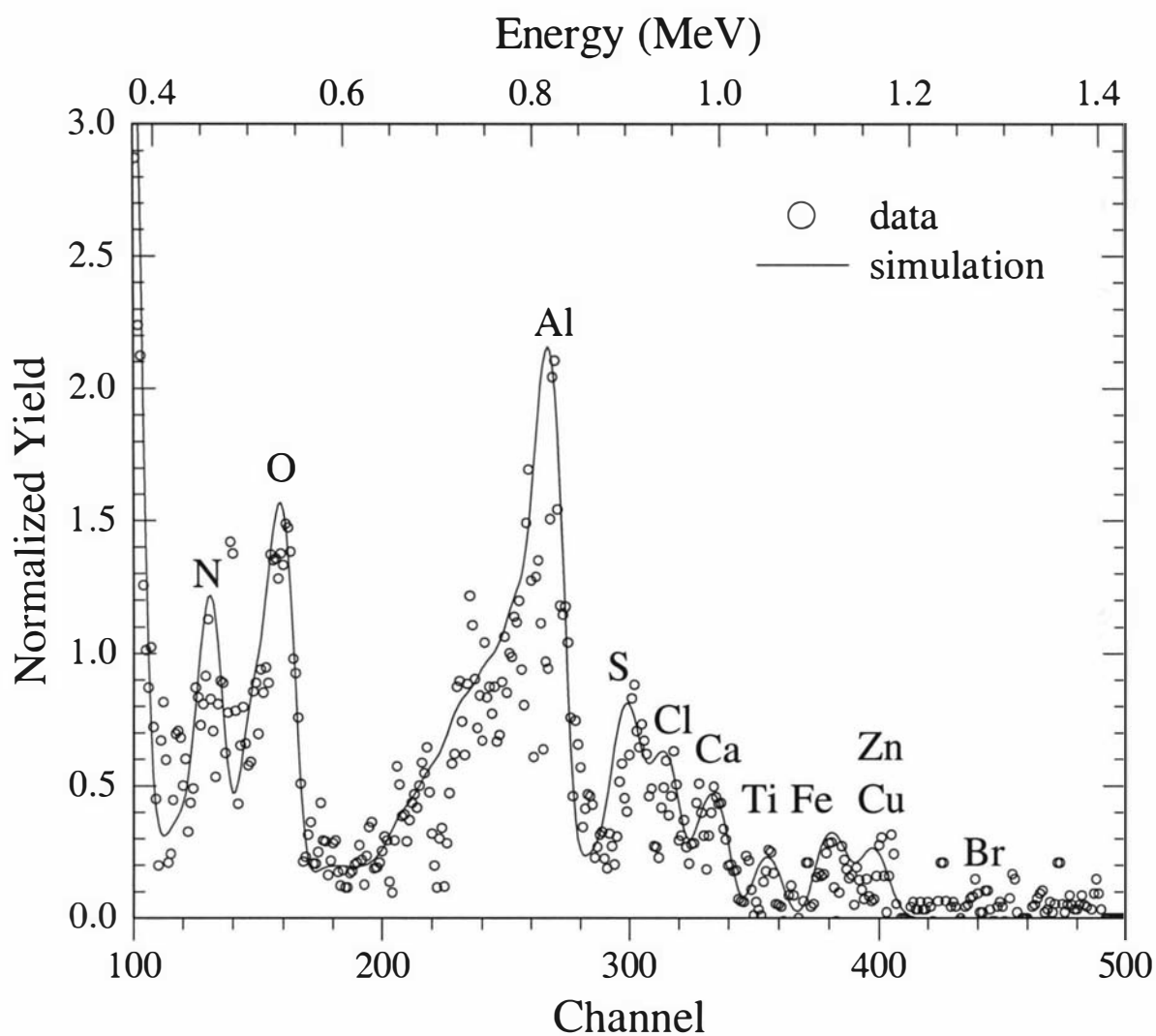


Fig. 3.11 RBS (channel 100 to 500) for a cycled bis terthiophene porphyrin, cycled TTh-Por-TTh. Simulation data is tabulated in the Appendix (Table A.2)

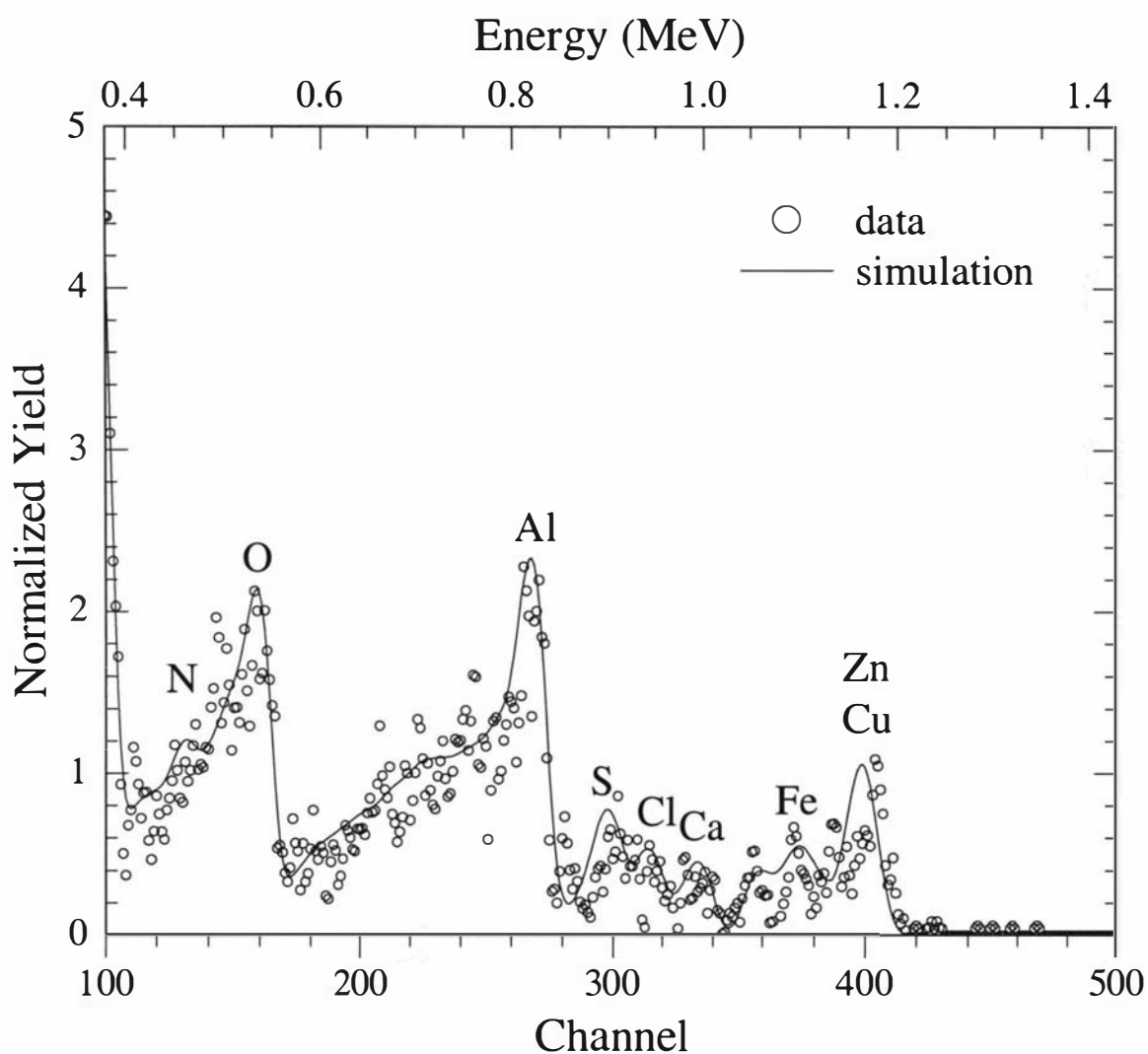


Fig. 3.12 RBS (channel 100 to 500) for a soaked bis terthiophene porphyrin, soaked TTh-Por-TTh. Simulation data is tabulated in the Appendix (Table A.3)

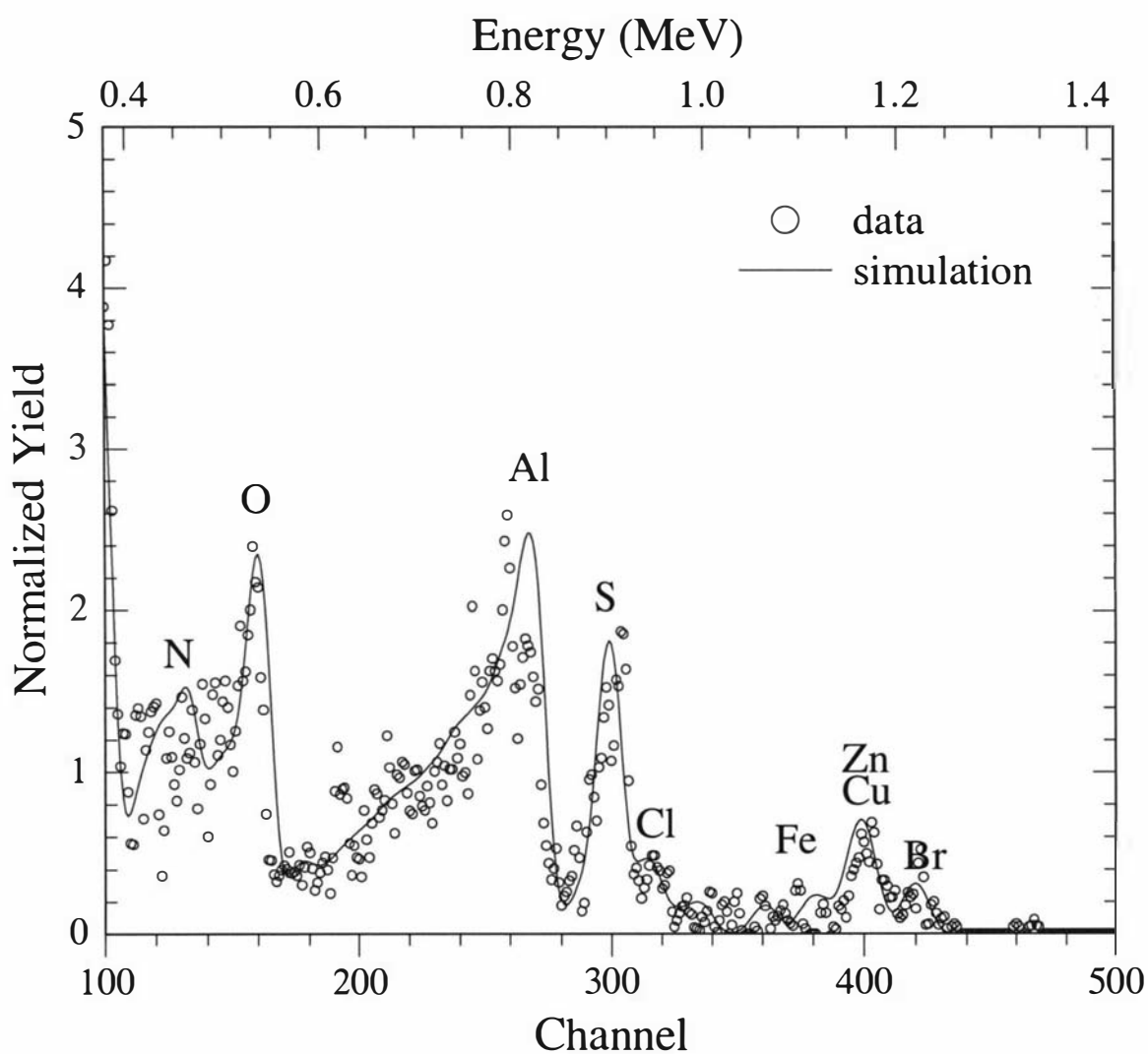


Fig. 3.13 RBS (channel 100 to 500) of zinc coordinated bis terthiophene, TTh-ZnPor-TTh. Simulation data in tabulated in the Appendix (Table A.4)

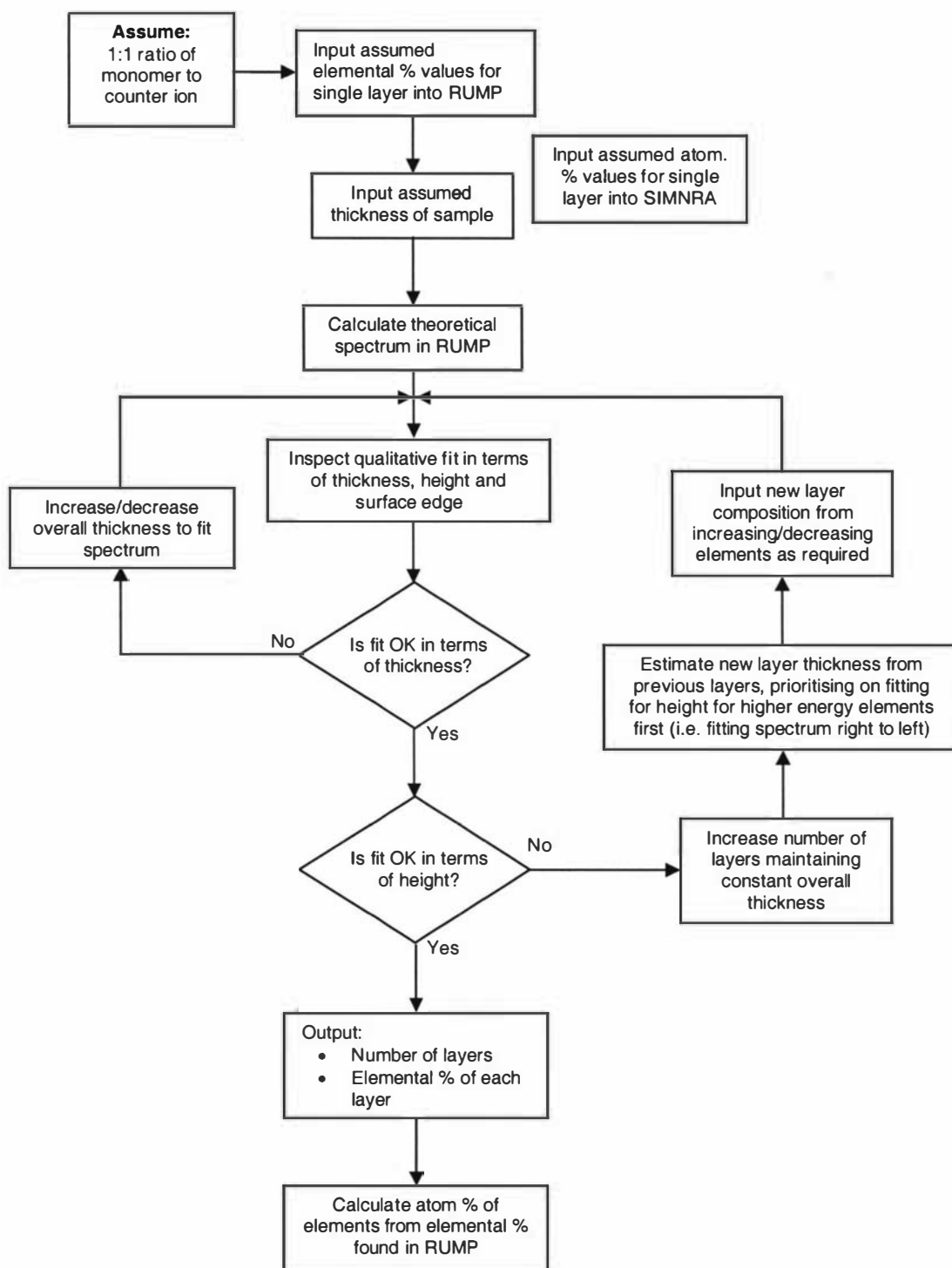


Fig. 3.14 Flow diagram of the steps undertaken to obtain elemental results from TTh-Por-TTh and TTh-ZnPor-TTh samples.

into RUMP, and the calibration completed, there was a progression of steps to perform (sometimes iteratively), to obtain a satisfactory simulation of the experimental data. Step 1 was to calculate the first attempt of the chemical stoichiometry for a one layer sample as mass percent value. The first attempt was always to assume a 1:1 monomer to counter ion ratio. Step 2 was to input a layer thickness. The amount of carbon which was entered was much higher than the amounts of any other elements due to the backscattering contribution from the substrate. If the sample had a continuous chemical stoichiometry throughout the thickness of the sample, there would only be the need for a single-layer simulation. If the spectrum was not simulated using a single layer, a new layer was required, maintaining the overall detectable sample thickness constant. The elemental composition of the new layer was altered depending on what could be observed from the simulation. For example, does the second layer require less oxygen? If so, the amount of oxygen in the second layer was decreased. This process was continued until the simulated spectra best represented the collected data. Once the simulation had been completed the mass percents of elements were converted into atomic percents relative to the total composition of the sample, layer by layer.

The major elements of interest found from the analysis of the RBS spectra, the atomic percent, and the thickness of the samples, are given in Table 3.1.

The total average thickness of the four samples was *ca.* 300 nm. This was carried out using an assumed density of the sample of 0.85 g/cm³. Throughout the thickness analysed, all the elements which were expected from the chemical stoichiometry of the monomers were detected. However, additional elements were observed to a depth ranging from 110–160 nm into the deposited material. These unexpected elements together with the maximum depth to which they were detected are shown in Table 3.2.

The most pronounced element peak which can be observed in Figs. 3.10 – 3.13 is that of Al. This element is not listed within Table 3.1 because for the purpose of calculating those concentrations Al was omitted. This was because aluminium was clearly not a component of the deposited organic material, nor had it been used as a reagent in the production of the monomer. The amount of aluminium detected was

Table 3.1 A list of the elements in each of the four samples as expected from the chemical stoichiometry (except that of carbon and hydrogen).

Sample	Atomic %					Thickness
	N	O	S	Cl	Zn	(nm)
TTh-Por-TTh	19.92	22.40	3.70	2.50	0.01	422
Cycled TTh-Por-TTh	12.01	12.01	1.26	1.20	0.12	374
Soaked TTh-Por-TTh	12.64	20.23	4.04	1.01	0.46	310
TTh-ZnPor-TTh	11.73	16.76	1.12	1.12	0.67	348

Table 3.2 A list of the common RUMP values of unexpected elements found from the RBS spectra.

Sample	Element			
	Fe	Cu	Br	Al
TTh-Por-TTh	0.17	0.15	0.05	9.05
Cycled TTh-Por-TTh	0.24	0.06	-	5.66
Soaked TTh-Por-TTh	0.05	0.05	0.15	7.05
TTh-ZnPor-TTh	0.17	0.06	-	6.28

significant and not at trace levels unlike the other unexpected elements that were detected. One explanation for this contribution is that before the electrochemical deposition of these samples took place, the GC electrodes, which acted as the working electrode and the substrate for these materials, were polished with a BAS electrode polishing kit (Bioanalytical Systems Inc., West Lafayette, Indiana, USA) in which a polishing aluminium oxide polish was employed. The polishing aluminium oxide had a grain size of 0.05 μm . When aluminium peaks were observed within the RBS spectra it was concluded that the ion beam was not only measuring the elemental composition of the deposited organic material, but it was also measuring a proportion of the substrate in which alumina, from the polishing procedure, had been embedded. From this information, and the fact that the surface edge of the Al peak was observed at the correct energy indicating that it was detected at the surface of the deposited material (and not shifted to a lower energy indicating that the Al was originating some depth below the sample material), it was calculated that the Al from the polishing procedure had penetrated the GC electrode to a depth of *ca.* 1.2 μm .

The results for the TTh-Por-TTh sample are now discussed in greater detail. A higher nitrogen concentration than anticipated was determined in the film. Based on the stoichiometry of the sample monomer, a nitrogen value of *ca.* 5 % was expected. However, a much higher nitrogen concentration was determined using RUMP, ranging from *ca.* 12-20 %. The electrolyte cation used during the electrochemical preparation of these materials was tetrabutylammonium ($(\text{Bu})_4\text{N}^+$). One possible explanation for this high nitrogen value may be ascribed to entrapment of these electrolyte cations in the growing film.

A higher than anticipated oxygen concentration was also measured in the TTh-Por-TTh sample. The only oxygen that had been anticipated to have been found was that from the perchlorate (ClO_4^-) from the electrolyte, which was expected to be associated with the oxidised film as a counter ion. If it were assumed that there was one counter ion per monomer unit within the sample matrix then the concentration of oxygen would have been expected to be *ca.* 6 %. In contrast, 22 % oxygen content was determined using RUMP. One explanation of this greatly increased oxygen concentration is that absorbed water or oxygen molecules may be present within the

matrix. Some organic materials, like polypyrrole, have the ability to absorb water molecules, which is how sensors can be built using these materials ^[116-118]. There could be a possibility that these TTh-Por-TTh materials have this same ability. Another possibility for this increased oxygen may be from the aluminium oxide polishing material. As aluminium was detected, oxygen could also be being detected (as Al_2O_3), hence increasing the observed oxygen concentration.

The concentration of sulfur given by the RBS simulation using RUMP was much lower than that expected. This sulfur originates from the two terthiophene side chains attached to the porphyrin. It could be possible that oxidation of the terthiophene chains may have occurred, cleaving them, so that they were not deposited with the main porphyrin unit.

The assumption of one ClO_4^- counter ion to charge balance every one TTh-Por-TTh monomer unit should have yielded a chlorine concentration of *ca.* 3 %. The calculated chlorine concentration from the RUMP simulation is slightly lower than this, but again is consistent with extra nitrogen and oxygen from exogenous material.

The comparison of the TTh-Por-TTh sample to the other sample follows.

Generally, the concentrations of the major elements were found to be higher in the TTh-Por-TTh sample compared to the other three samples for the elements N, O, S, and Cl, whereas the concentration for Zn was the lowest of the four in this sample. Zinc was of interest, since it was desirable to determine whether different concentrations would be seen from the differently prepared samples. Cl was also an interest as this element would be the indicator for the amount of counter ions within each sample. From the RUMP simulation for the cycled TTh-Por-TTh the detected concentration was found to be similar to the control TTh-Por-TTh sample which had not been exposed to zinc acetate. The soaked TTh-Por-TTh sample, in contrast, had a higher zinc concentration, one much closer to the result obtained for the TTh-ZnPor-TTh sample.

The concentration for chlorine is highest within the control TTh-Por-TTh sample. The

chlorine concentration is directly related to the number of ClO_4^- counter ions required to charge balance the sample. The decreased concentrations of chlorine in the cycled TTh-Por-TTh, soaked TTh-Por-TTh, and TTh-ZnPor-TTh samples correlate to the need for only one ClO_4^- counter ion per three porphyrin monomer units. The increased concentration in the control TTh-Por-TTh relates to need for more than the 1:3 counter ion to monomer ratio the other three samples have, and is closer to 2:3 in this case.

3.3.3 *Proton Induced X-ray Emission – PIXE*

The presence of the low-level unanticipated elements found in the RBS analysis (Table 3.2) required further investigation using a technique that was more sensitive to trace element, PIXE. The use of PIXE was required due to the limited mass resolution of RBS, not permitting unambiguous identification of low levels of elements with closely related energies in the RBS spectrum. For example Fe ($E = 1.13$ MeV), Cu ($E = 1.17$ MeV), and Zn ($E = 1.18$ MeV), using 1.5 MeV $^4\text{He}^+$ incident particles. Figure 3.15 shows the PIXE spectrum of the TTh-Por-TTh material measured with 2.5 MeV protons. From this spectrum it can be observed that the unanticipated elements from Table 3.2 can be identified (Fe, Cu, and Br), but other elements (P, K, Ca, Mn, and Si) are also detected. The most feasible conclusion for the origins of these trace elements is from the chemical formation of the monomers. The elemental synthesis of the porphyrin monomer material involved several different chemical synthetic stages. At the completion of each of these stages the newly formed compounds were washed with a range of solvents, of which water was one. Water carries trace amounts of metals and substances in it, and porphyrins readily coordinate many metals. It is considered that this might be the origin of these elements. In other synthetic analytical techniques such as Nuclear Magnetic Resonance (NMR) the concentrations of these elements would be sufficiently low that they are not detected, whereas IBA techniques, in particular PIXE, show much greater sensitivity for low levels of elements.

3.4 **Conclusions**

The successful electrochemical deposition of novel new TTh-Por-TTh materials were achieved onto GC working electrodes and the deposition materials were successfully

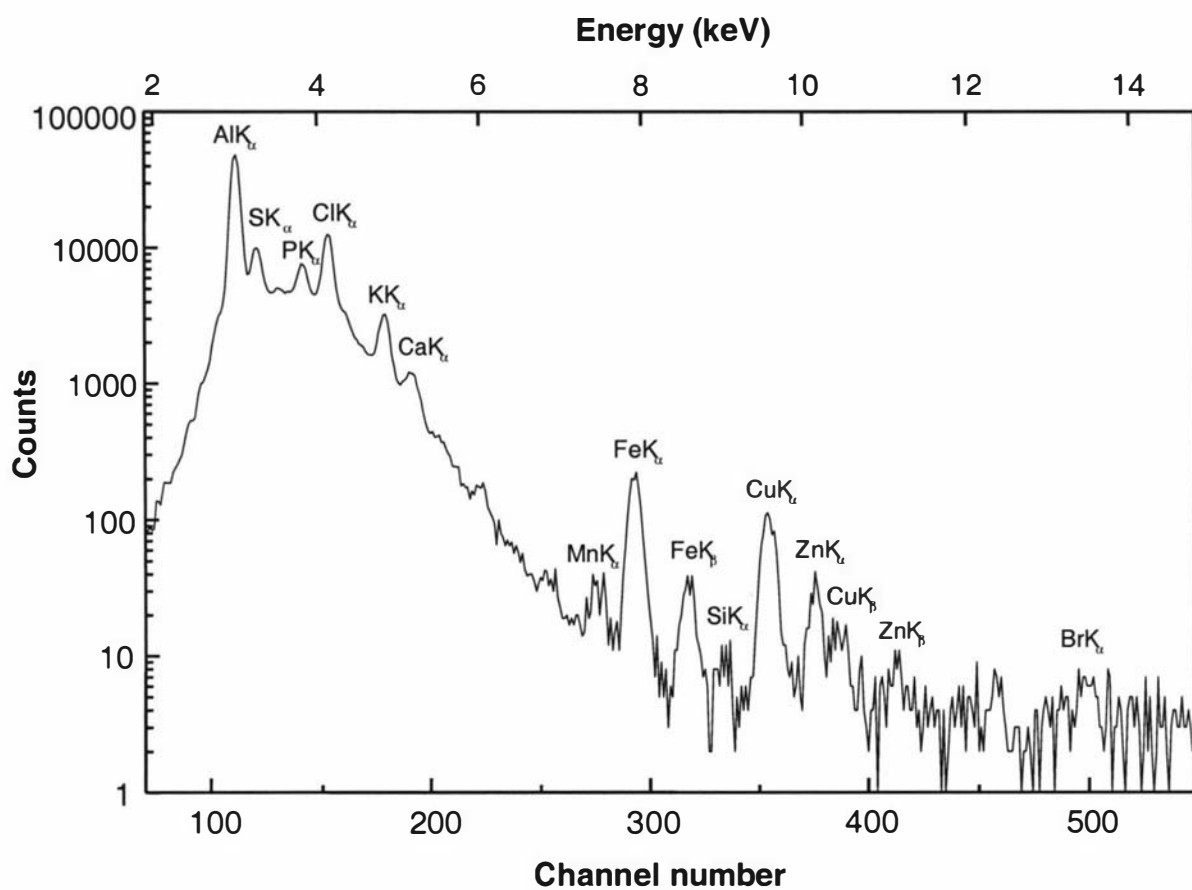


Fig. 3.15 PIXE spectrum of bis terthiophene porphyrin, TTh-Por-TTh, sample together with element identification by emission type K_α and K_β.

measured using the IBA techniques of RBS and PIXE. Repeated measurements on these new materials showed no deterioration under ion beam bombardment. RBS and PIXE analysis showed significant discrepancies for a wide range of elements compared to the expected stoichiometry.

The most significant findings were: (i) that a difference in zinc uptake between samples soaked and cycled in zinc acetate was found, (ii) unexpected high oxygen and nitrogen concentrations, (iii) the indication of counter ion to monomer ratios that the Cl concentration was able to show, and the differences in those ratios between samples, (iv) the ability to detect trace contaminant elements which other analytical techniques employed for soft organic based material can not show, and (v) that a signal due to the polishing of the GC working electrode prior to the electrochemical deposition was detected suggestive that the sample did not uniformly cover the surface of the working electrode.

From the finding of the work carried out in this scoping study it was determined that the use of IBA on soft organic based materials was possible. The determination of whether counter ion to monomer ratios, and unexpected elements not consistent with the known chemical stoichiometry, change with depth in conducting polymers may be useful in gaining a better understanding of the properties of these materials. For example, conducting polymers which have a different conductivity on the surface compared to the bulk of the material, being able to use IBA techniques on these types of materials may help to understand why this occurs.

Another important conclusion to be drawn from these results was associated with the technique employed for the mounting of the samples. Transferring the samples on a GC electrode turned out to not be the ideal method, since the deposition of the material was very thin and did not cover the entire electrode, part of the electrode substrate was also measured. As well as detecting aluminium, and possibly oxygen, as they had been embedded into the electrode, there would also have been detection of carbon from the GC. Without the capability of distinguishing the carbon from GC and the carbon from the organic sample material, the analysis is incomplete. A criteria for all further work was that peelable, stand alone films which can be removed from the working electrode surface were required for analysis of organic based samples.

CHAPTER 4

Polypyrrole

4.1 Introduction

Having gained knowledge that IBA techniques may be used to analyse soft organic materials, and that useful analytical information could be obtained without significantly altering the sample, further analysis of organic materials were contemplated, in particular, those organic materials known as conducting polymers. In the work presented in this chapter, studies took a step back and focused on a simpler system, that of polypyrrole (PPy). The electrochemical production of PPy is shown in Scheme 4.1. Pyrrole itself is a much simpler molecule than that of the TTh-Por-TTh monomer, the subject of the previous chapter.

The aim of this study was the use of IBA techniques to determine monomer to counter ion ratios for a range of PPy films prepared with varying counter ions. The reason for determining the counter ion to monomer ratios within the polymer films is that this information relates to the oxidation state for the polymer film. This is of interest since knowledge of the oxidation state of the polymer may provide insights into controlling the physical and chemical properties of conducting polymers, which is of importance depending on the final application of the conducting polymer^[119, 120].

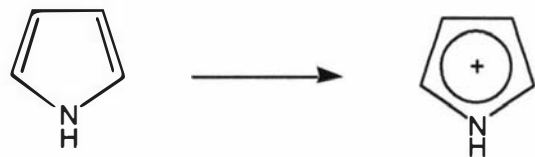
4.2 Experimental Conditions

4.2.1 *Reagents*

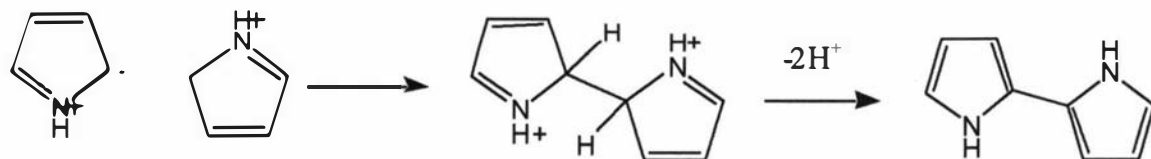
All chemicals and reagents used were of analytical reagent grade and used without further purification. Pyrrole (99 %, Acros Organics, New Jersey, USA) was distilled under nitrogen immediately prior to use.

The electrochemical cell used for the polymer depositions is described in Section 2.2.3.2.

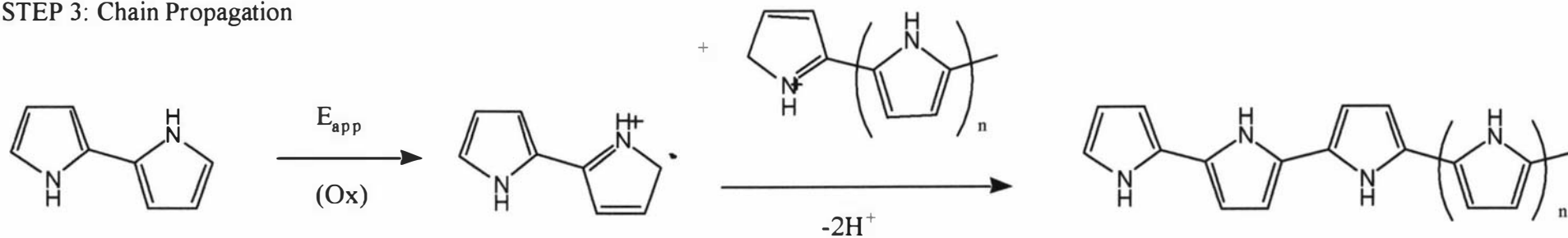
STEP 1: Monomer oxidation



STEP 2: Radical-radical coupling



STEP 3: Chain Propagation



Scheme 4.1 Chemical scheme of the production of polypyrrole electrochemically.

Aqueous solutions of pyrrole (0.1 M) and the relevant counter ion (0.1 M) were prepared and deoxygenated for 15 minutes with argon gas. Each pyrrole solution also contained dodecylbenzenesulfonate (DBS) (0.001 M) to aid in uniform film growth on the electrode surface ^[121] (Section 2.2.3.2).

Six different counter ions were used in this work. They were DBS, 3-nitrobenzenesulfonate (NBS), 4-hydroxybenzenesulfonate (HBS), methane sulfonate (MS), 4-sulfobenzoate (SB), and 4-toluenesulfonate (PTS). All counter ions were obtained as sodium salts except SB, where a potassium salt was used.

4.2.2 *Electrochemistry*

Freestanding PPy films were formed galvanostatically under oxidative conditions (EG&G Instruments, Scanning Potentiostat, Model 362) at a constant current density of 30 mA cm⁻² for one hour in a two electrode cell (Fig. 2.2). The potential during the deposition of these PPy films was not monitored, but typically increased from 1500 – 1700 mV over the course of this time.

The working electrode and counter electrodes were both 25 cm² in area and were constructed of stainless steel (Grade 316). The inner faces of the two electrodes were polished to a mirror finish using Autosol metal polish (Dursol Fabrik Otto Durst GmbH & Co. KG, Solingen, Germany). The outer faces of the electrodes were masked with a waterproof adhesive tape. This was used to constrain deposition to the inner face and to fix the surface area of each electrode fixed at 25 cm². A filter paper separator (Whatman No. 42) was mounted midway between the two electrodes to prevent the H₂ gas evolved at the counter electrode disrupting film growth at the working electrode ^[121].

After galvanostatic growth, the films were peeled from the surface of the working electrode, washed in distilled water, dried in air, and then stored in re-sealable plastic bags until analysis. The PPy films were typically of the order of 30 μm thick. This is calculated from the polymer density (0.85 g/cm³), the transfer of 1 e⁻ per monomer and Faradays Law.

4.2.3 *Ion Beam Analysis Techniques*

4.2.3.1 PIXE

The PIXE analysis was carried out using a Si(Li) detector (energy resolution, 150 eV), set at a distance of 8.5 cm, with a 75 μm Be film attachment. A 2.1 MeV, 1 mm diameter proton beam was used with a beam current of 7 nA.

GC, TaO, and Si/N on Si were the standards used in this work. The six PPy samples were each analysed twice, once with the 'solution side' of the film facing the beam, and the second with the 'electrode side' of the film facing the beam.

4.2.3.2 RBS

The RBS analysis was carried out using a 1.5 MeV, 1 mm diameter, $^4\text{He}^+$ beam. The detector was set at 165 ° and incorporated a snout and a 500 nm collimator. The RBS simulations carried out in this work was performed using the data analysis program RUMP.

4.2.4 *Combustion analysis*

Combustion elemental microanalysis was performed at the University of Otago, NZ. 10 mg of each of the PPy films were analysed.

4.3 **Ion beam analysis**

4.3.1 *Film durability*

One energy region was selected from channels 180 to 500 to cover all elements of interest for these PPy samples in a similar method to that described in Chapter 3. An ion beam bombardment durability experiment was carried out on a sample of the PPy-DBS film. RBS spectra were collected at intervals of 20 μC beam charge until the total accumulated beam charge the sample had been subjected to was 400 μC . Figure 4.1 shows the graph of the accumulated charge vs counts for this experiment. It can be observed from this graph that there was no discernable deterioration of the RBS response of the PPy-DBS film. Given that all films were PPy based it was assumed that this result would be the same for all films.

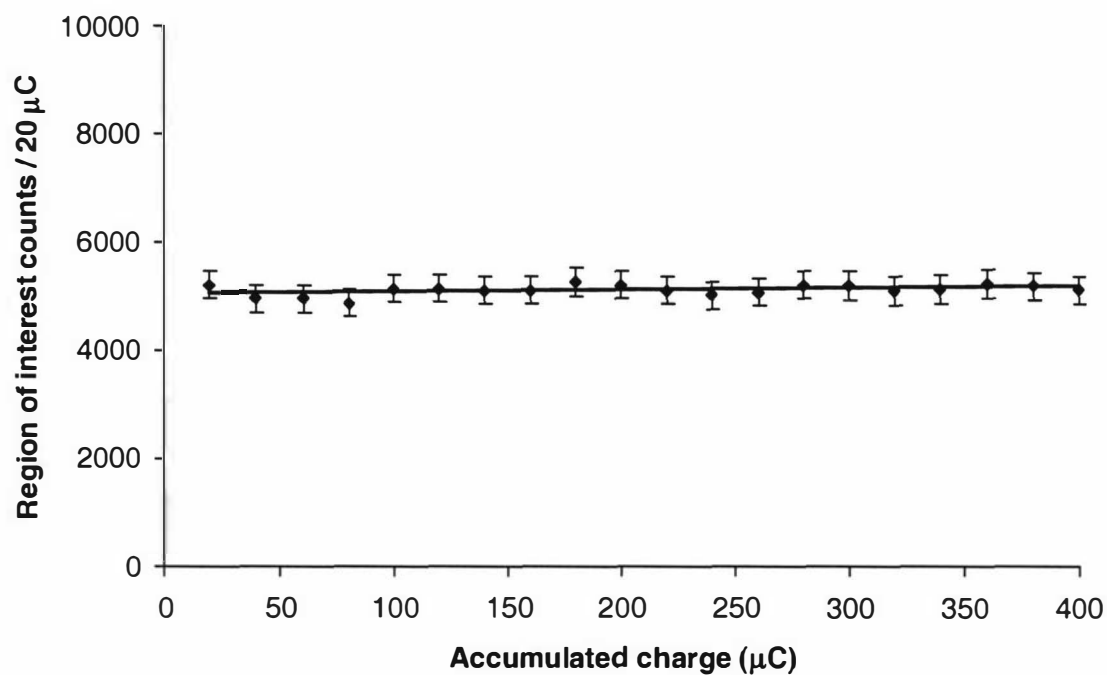


Fig. 4.1 Accumulated charge for polymer durability on PPy-DBS film (solution side), for region of interest ranging from channels 150 to 500.

4.3.2 *PIXE – trace elements*

From the work carried out in the previous chapter on the organic bis terthiophene porphyrin materials, it was established that PIXE analysis had detected trace levels of unexpected elements. With this in mind, the PPy samples were first examined by PIXE.

The PIXE data was collected for 6 μC for each of the standards and PPy samples. Once the data had been collected and calibrated the peaks within the spectra were assigned. A number of unanticipated elements were found in these films. Trace amounts of a number of elements were identifiable in the films. Al, S, Cr, Fe, and Cu were found in all films with occasional presence of Si, Cl, K, Ca, Ni, and Zn. Due to the electrochemical deposition occurring on stainless steel working electrodes, it could have been possible that the origin of these unexpected elements was due to oxidation of the stainless steel and the incorporation of the elements into the polymer matrix as film growth occurred.

Figure 4.2 - 4.7 show the 'solution side' PIXE spectra for each of the six sample films. One feature, which is present within all of the films, is that there are two peaks for sulfur (energies 2.307 keV and 4.614 keV). The peak at 2.307 keV is the K_{α} peak for sulfur and the peak at 4.614 keV is a pileup peak for SK_{α} . This pileup peak is a result of too many sulfur X-rays entering the detector and the detector recording peaks at double the correct energy for sulfur. There were high counts for sulfur detected in all samples due to sulfur being present in all counter ions. A further element which is observed in relatively high counts in these PPy samples is Al. These samples had been removed from the electrode surface on which they had been deposited, and those electrodes had not been polished with alumina, so the presence of Al could not be attributed to the same reasons as in previous Chapter. In this section of work the Al presence has been attributed to 'beam halo'. Beam halo occurs when the incident beam is not only striking the sample but also stray particles are striking other objects in the sample chamber, in this case the sample holder (made of Al). The backscattered particles from the sample holder are recorded and it appears the sample has Al present. In Chapter 3, Al was only observed within the spectra of the sample and not those of the standards, here the spectra of pure, non Al containing standards,

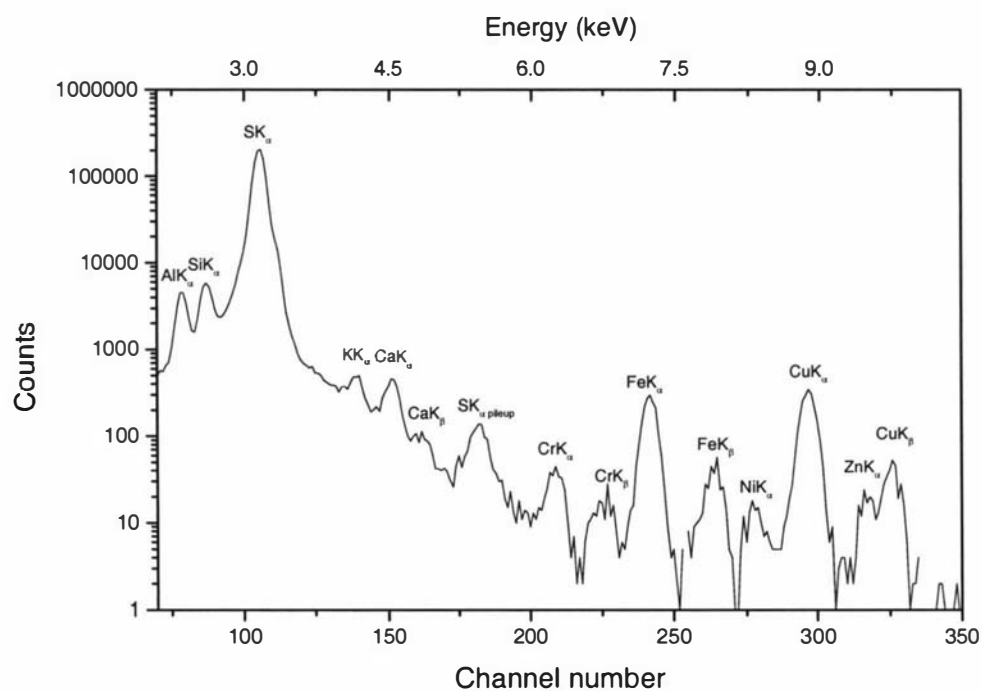


Fig. 4.2 PIXE spectrum (channels 70 – 350) for PPy-DBS, solution side.

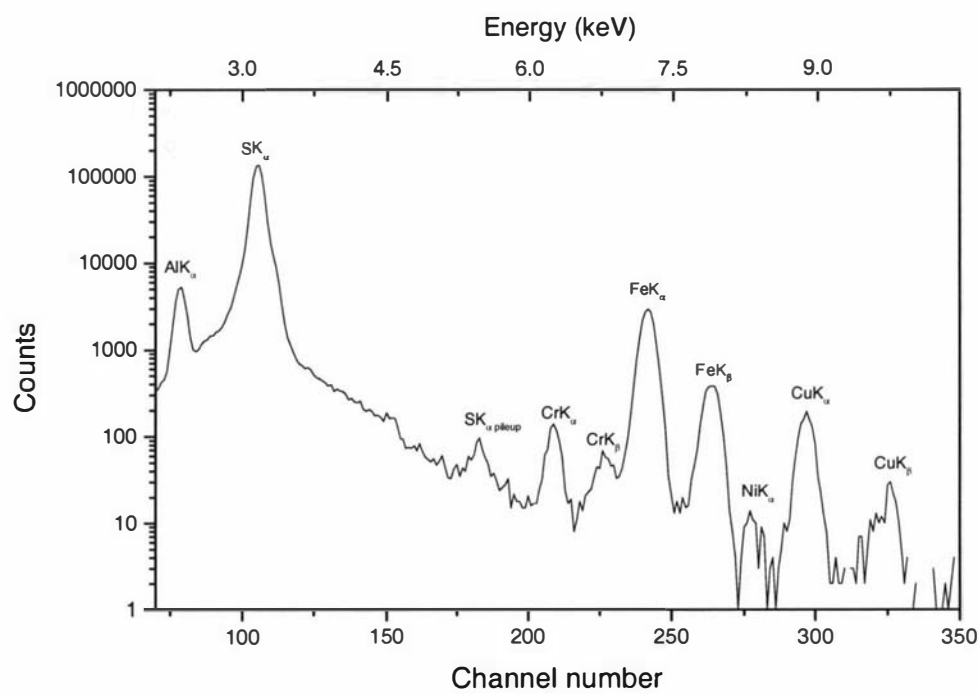


Fig. 4.3 PIXE spectrum (channels 70 – 350) for PPy-NBS, solution side.

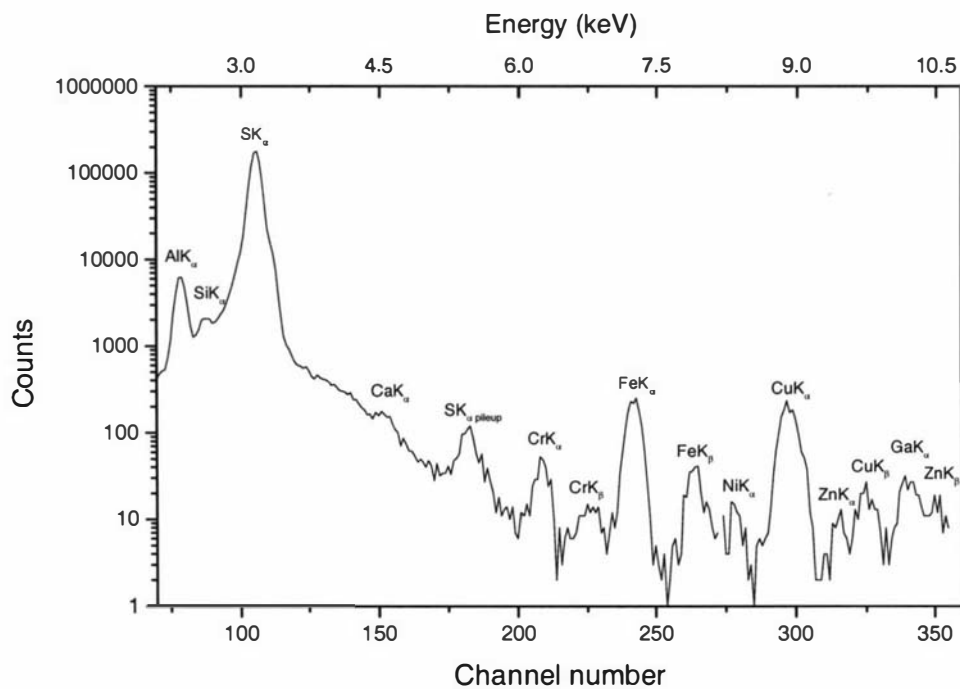


Fig. 4.4 PIXE spectrum (channels 70 – 350) for PPy-HBS, solution side.

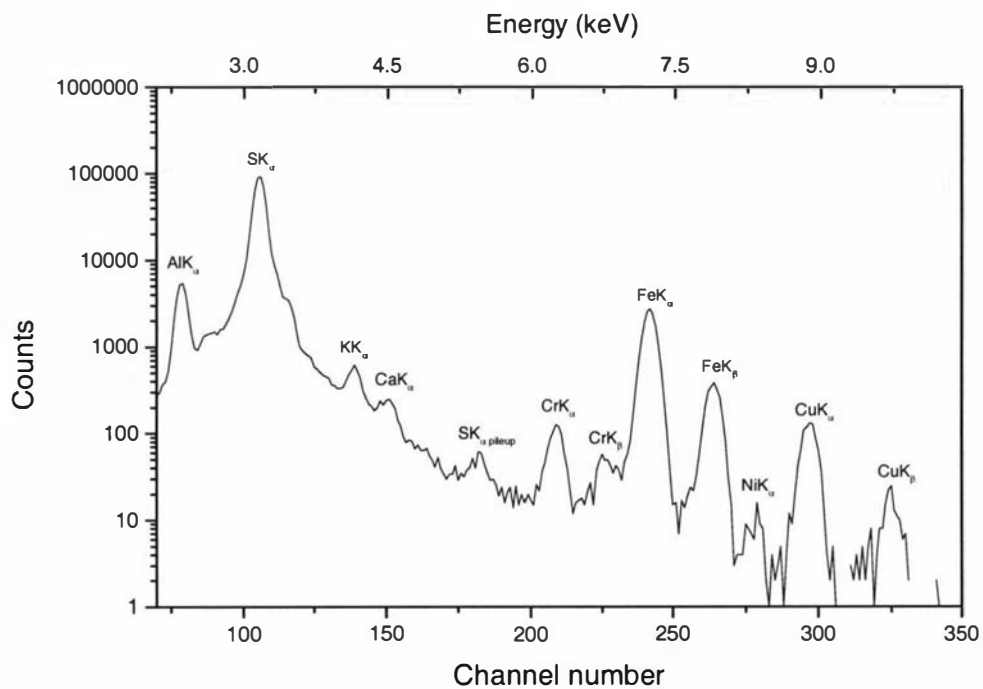


Fig. 4.5 PIXE spectrum (channels 70 – 350) for PPy-MS, solution side.

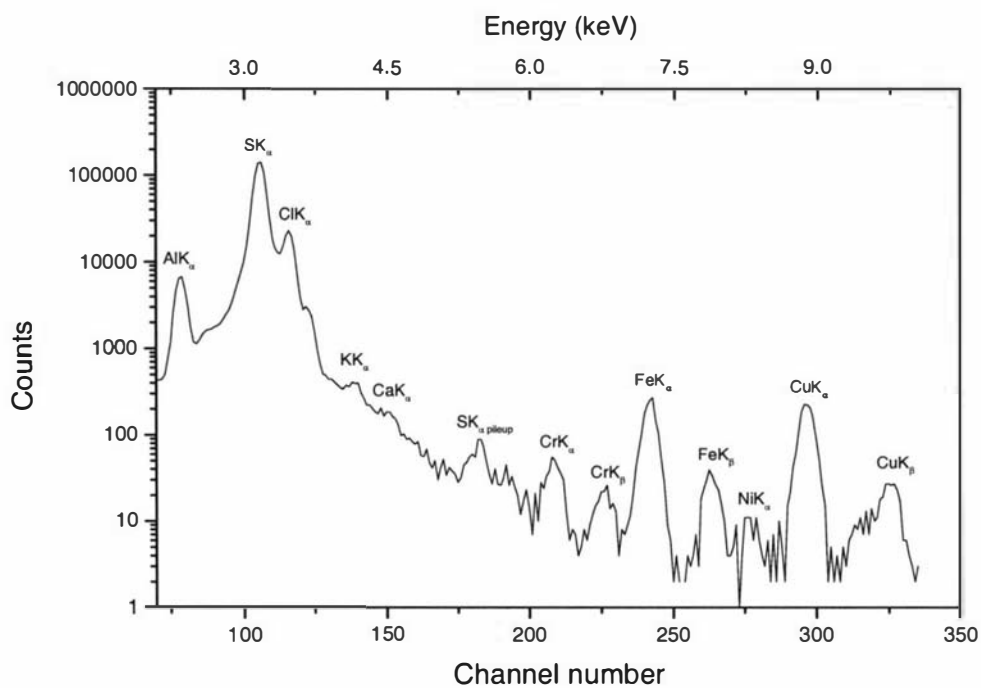


Fig. 4.6 PIXE spectrum (channels 70 – 350) for PPy-SB, solution side.

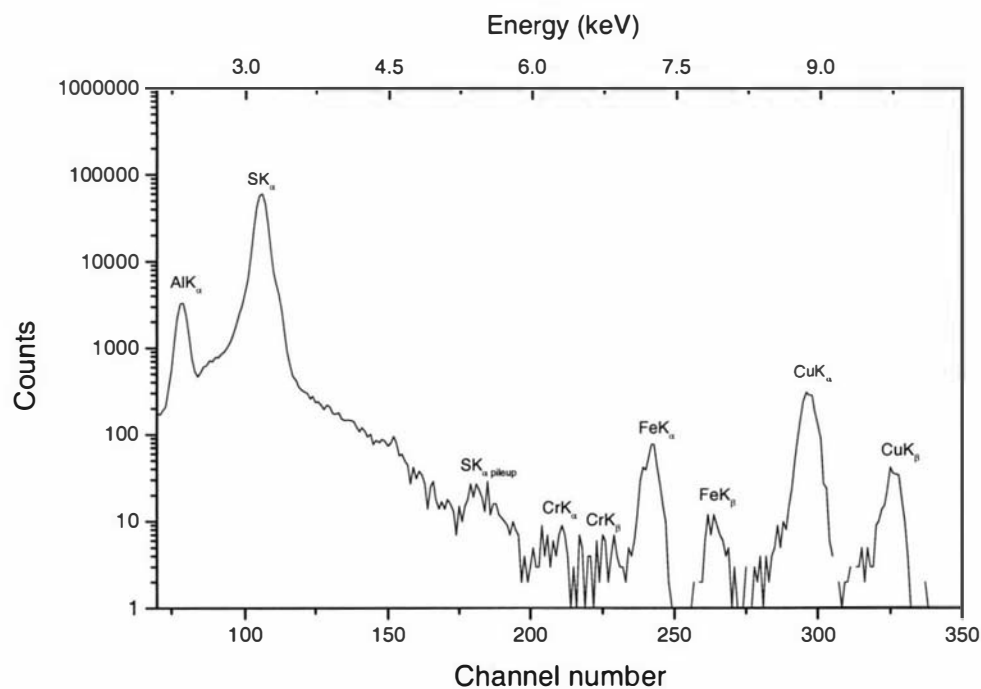


Fig. 4.7 PIXE spectrum (channels 70 – 350) for PPy-PTS, solution side.

Al was observed. Here Al was observed in the sample and the standards, and therefore has been attributed to beam halo. Due to these reasons S and Al are labelled, but they will not be discussed in any further PIXE discussion.

Figures 4.2-4.7 relate to the solution side of each of the PPy films. An example of an overlaid PIXE spectrum for both sides of a PPy-DBS film is shown in Fig. 4.8. In this figure it can be seen that all the same element peaks can be seen and that there are no significant differences between the spectra. This was found to be the case for each of the PPy samples.

The program GUPIX was used to gain quantitative interpretation. The final results gained from the GUPIX program gave concentrations in ng/cm^2 of the elements present within the samples, and a level of detection (LOD) value, also in ng/cm^2 . These concentrations were converted into ppm values. From the element concentration and the LOD concentration it can be determined whether or not the element of interest was present at, or above, the level of quantisation, or below the LOD, or not at all. An example of this is for the elements Ca and Mn from the PPy-DBS GUPIX analysis. The Ca concentration found by GUPIX was 594 ppm and the LOD for Ca was 97 ppm, so it could be said with some certainty that Ca was present. In the case of Mn within that same sample, the concentration found by GUPIX was 17 ppm, while the LOD for Mn was 101 ppm, so it could also be said with some certainty that Mn was not present at a detectable level.

The results found by GUPIX and those indicated by qualitative peak assignment varied. For most of the elements identified by qualitative analysis concentrations from GUPIX were identified, but not in all cases. In the PPy-HBS, solution side, case, a Zn peak was qualitatively assigned. However, using GUPIX the concentration of Zn was below the LOD, and therefore could be assumed to not be present in the sample. The reverse also occurred, where a peak was not qualitatively assigned, but GUPIX determined a concentration well above the LOD. This was the case for Cl in the PPy-DBS sample. When the Cl region of the PIXE spectrum is examined more closely, a shoulder on the right hand side of the S K_α peak can be discerned (Fig. 4.9) at the energy of the Cl K_α peak. In the former case, when peaks are assigned in the

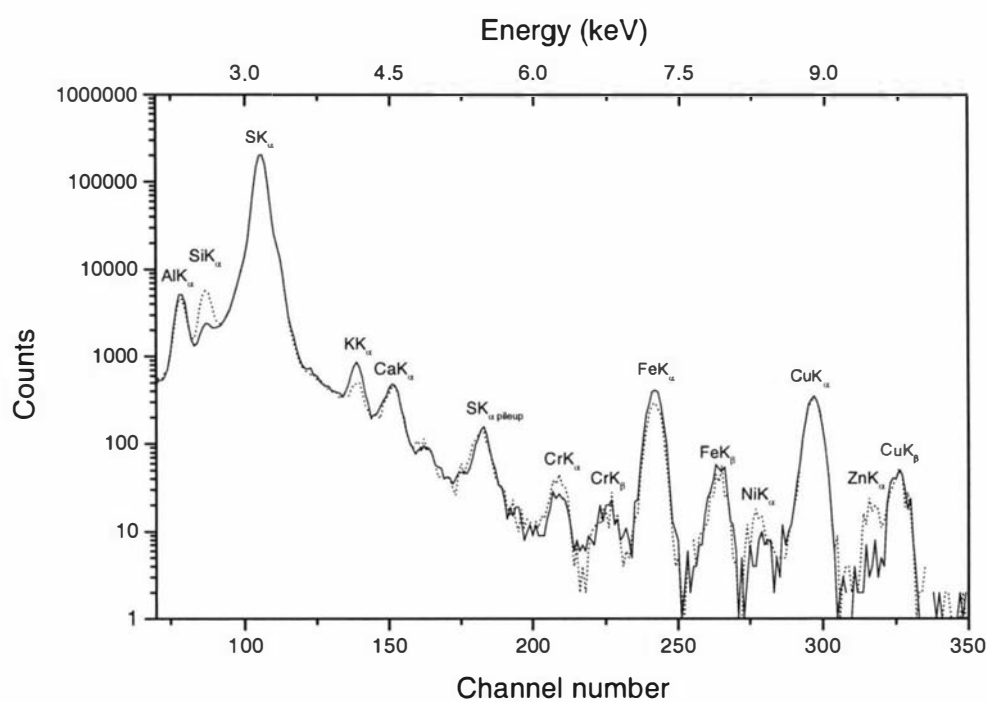


Fig. 4.8 Overlaid PIXE spectra of both sides of PPy-DBS, solution side , electrode side — .

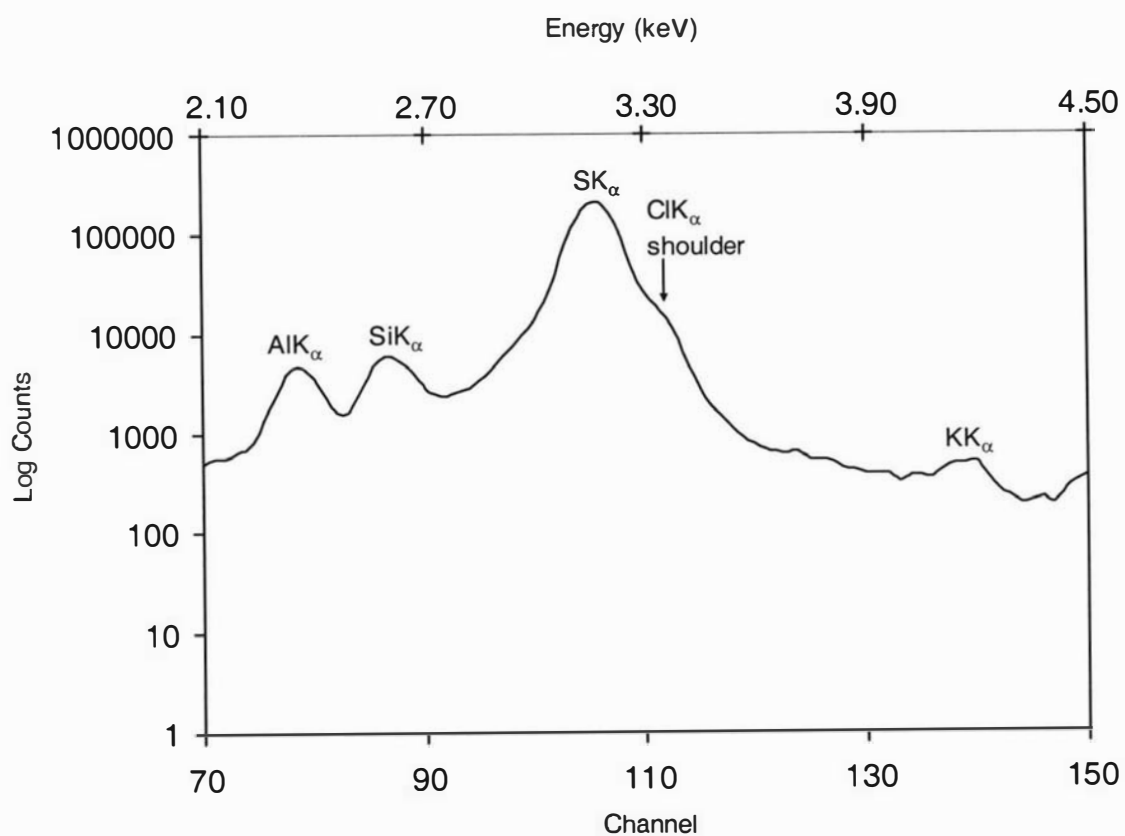


Fig. 4.9 Expanded PIXE spectrum of PPy-DBS to show presence of Cl

PIXE spectrum but not found at the concentrations above the LOD, this is due to the fact that the PIXE spectra are considered on a log count scale. In the case of the Zn K_{α} peak in the PPy-HBS, spectrum, the counts for this are less than 10, so it is not until GUPIX analysis is performed that it is found that the concentration is below the LOD.

This dependency of qualitative peak and hence element assignment also impacted on differentiation between sides of PPy films. Table 4.1 shows the comparisons between the qualitative and quantitative results for the solution and electrode sides for PPy-DBS.

In the case of PPy-DBS the qualitative results for each of the polymer films sides identified the presence of the same elements. All listed elements were assigned peaks except for Cl. In the PIXE spectra of both sides of this sample a peak for Zn was assigned but not found to a level near the LOD in GUPIX, and no peak was assigned for Cl, but ppm concentrations were found in GUPIX. Similar conflicting results were found for the other films. By comparison of the quantitative results for each of the polymer films sides it was found in most cases that the concentrations of the elements were higher on the electrode side. Only Cl, K, and Ni showed lower concentrations on the electrode side, and for the most these values only differed by a few 10s of ppm.

No trend in the PIXE analysis results could be found at this point. The high energy end of the RBS spectra for these samples was investigated to corroborate these PIXE results. Figure 4.10 shows overlaid RBS spectra (0.95 – 1.20 MeV) for the two sides of the PPy-DBS film. RBS is not as sensitive for element identification as is PIXE, and because of this, only some elements identified by PIXE are assignable by RBS. For PPy-DBS, those elements are Cl, K, Ca, Cr, Fe, Ni, and Cu. Figure 4.10 is consistent with the GUPIX interpretation showing that most of the elements in this sample were present in higher abundance on the electrode side than they were on the solution side. Figure 4.11 shows the RBS simulation of the electrode side of PPy-DBS together with the experimental data. The simulation of these high-energy end elements showed that on both sides of each film, these unexpected trace elements were only detected to a maximum depth of 30 nm. This was also the case for the electrode side. From this information, it is unlikely that these impurities are associated

Table 4.1 Qualitative and quantitative results for the solution and electrode sides of the PPy-DBS polymer film.

Element	<u>Solution side</u>		<u>Electrode side</u>	
	Qualitative	Quantitative (ppm)	Qualitative	Quantitative (ppm)
Si	√	1933	√	2207
Cl	—	1398	—	1174
K	√	330	√	271
Ca	√	594	√	640
Cr	√	214	√	260
Fe	√	444	√	800
Ni	√	129	√	109
Cu	√	28	√	259
Zn	√	—	√	—

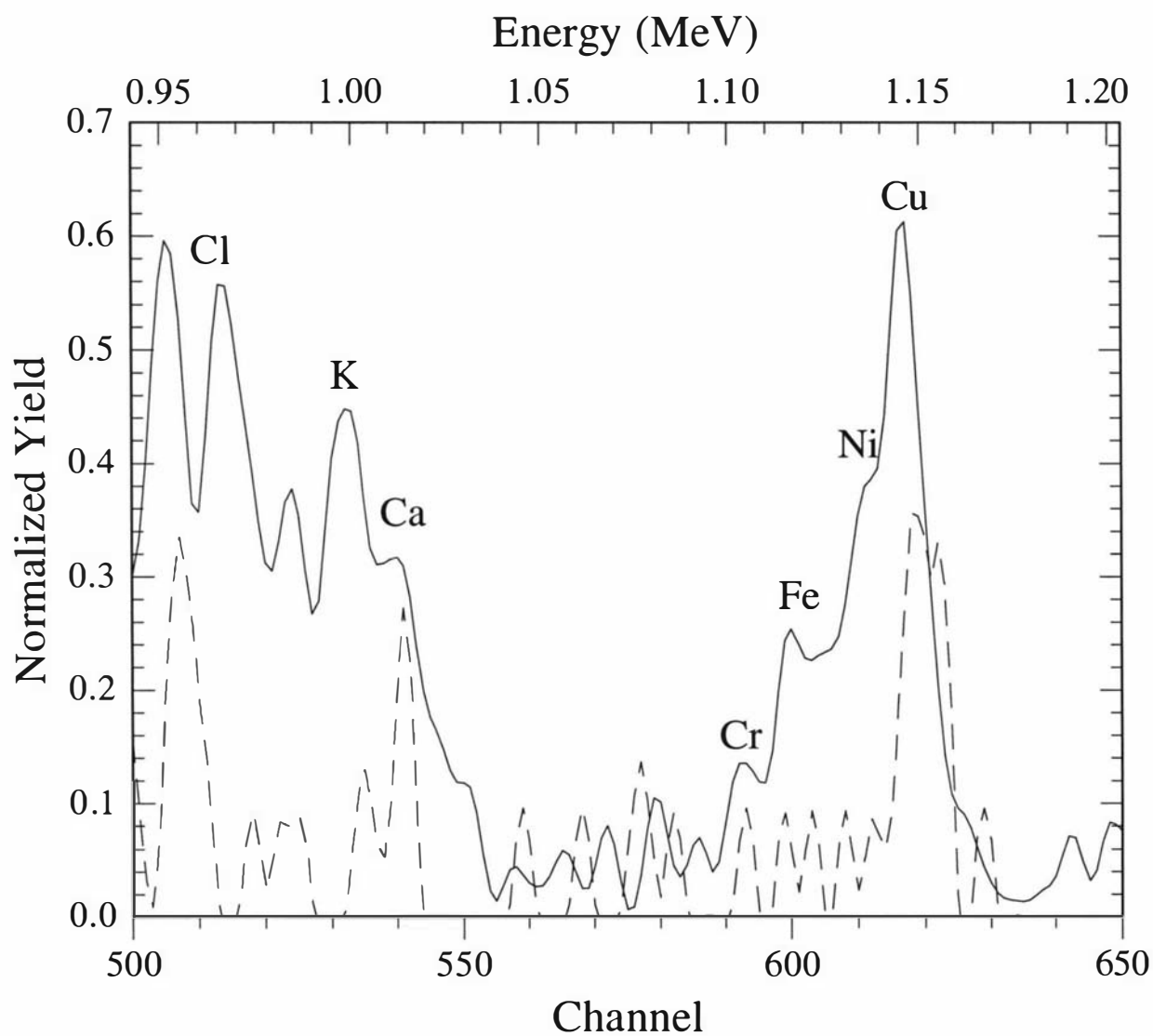


Fig. 4.10 Overlaid high energy region RBS spectra for PPy-DBS,
 solution side ----
 electrode side —

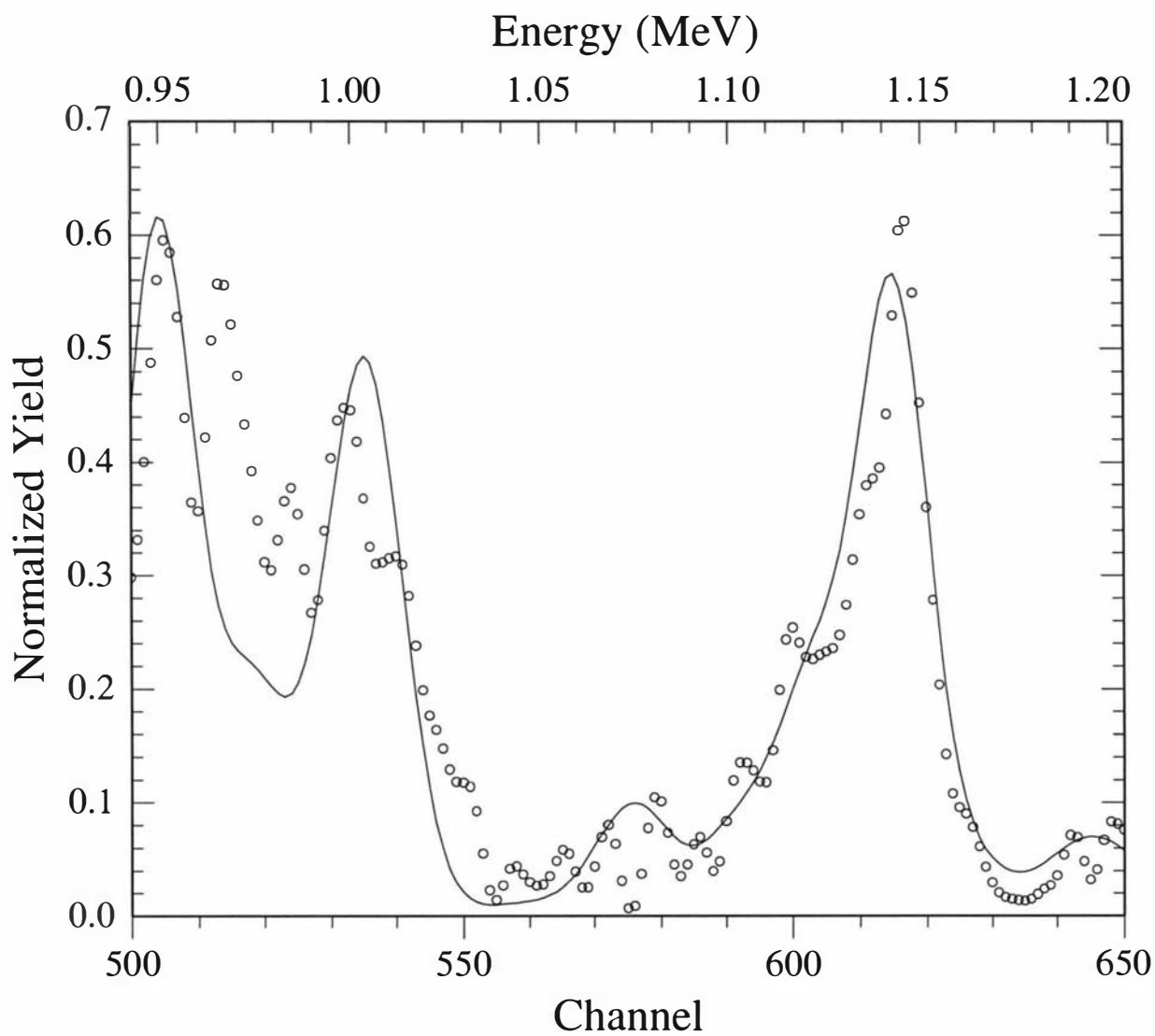


Fig. 4.11 Simulation of high energy region of PPy-DBS film, electrode side
(data \circ , simulation —).

with the oxidation of stainless steel during the polymerisation. If they were due to oxidation of the working electrode, then it would be expected that these elements would be found throughout the bulk of the film, not only for the outermost 30 nm of each side. Another possible origin for these trace elements was that of water. The PPy films were all washed and rinsed with deionised water after removal from the working electrode face. This water might be considered to be a likely source of the impurities. However, the solutions from which the polymers were formed were also based on this deionised water. Therefore, if this were the source of the impurities then it would be expected that the low level elements would be found throughout the polymer film, not confined to the outermost 30 nm. It is interpreted then that this low level of exogenous material must have arisen during subsequent handling and storage of the films.

4.3.3 *RBS – monomer to counter ion ratios*

With the issue of the unexpected low level elements dealt with, the main aim of this study could be moved onto. This aim was to use RBS analysis to provide a distribution of counter ions through the polymer films using a depth profiling approach.

The data analysis package RUMP was used to identify discrete modelled layers, each with an optimised elemental composition. The composition and layer thicknesses were varied manually until the smooth theoretical curve fitted the experimental data. Figures. 4.12 – 4.17 show the RBS spectra and simulations for the solution side for each of the PPy films (electrode side analysis was identical). All of the major elements (other than hydrogen) present within the PPy polymer films are identified for all spectra. Carbon is the highest abundance element in each film. This is consistent with carbon being the major elemental constituent in both the pyrrole units and in the counter ions. Sulfur derives from the counter ions, nitrogen from the pyrrole units, oxygen is present in the counter ions, and sodium is likely to have originated from the salts of the counter ions. Sodium was not observed in PIXE due to it being below the element detection limit.

An iterative approach was required to optimise the elemental composition and layer thicknesses for each layer. The elemental composition values for each layer within the samples were converted into atomic % values. To determine the counter ion to

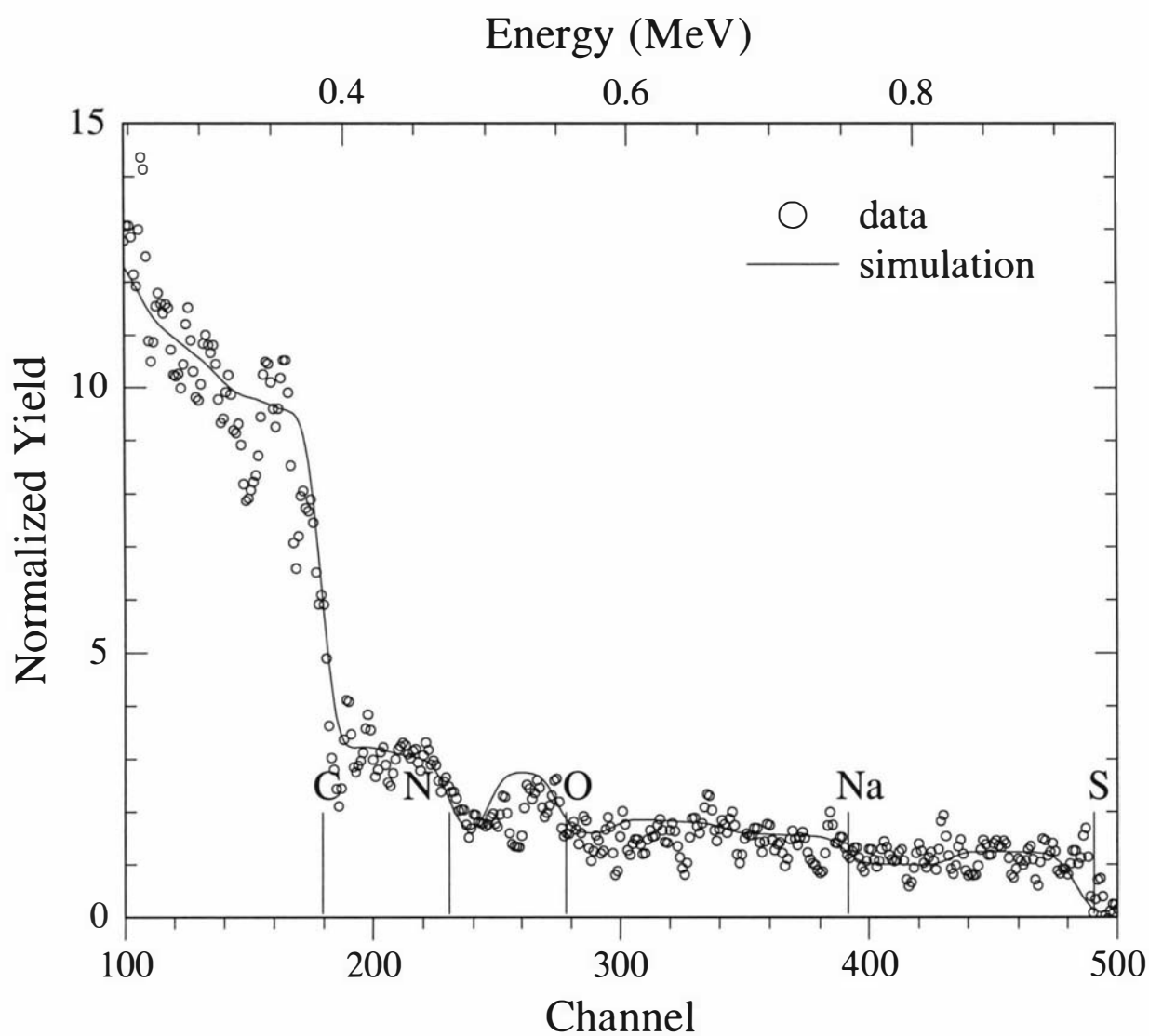


Fig. 4.12 RBS simulation and data for PPy-DBS film, solution side (data \circ , simulation). Simulation data is tabulated in the Appendix (Table A.5)

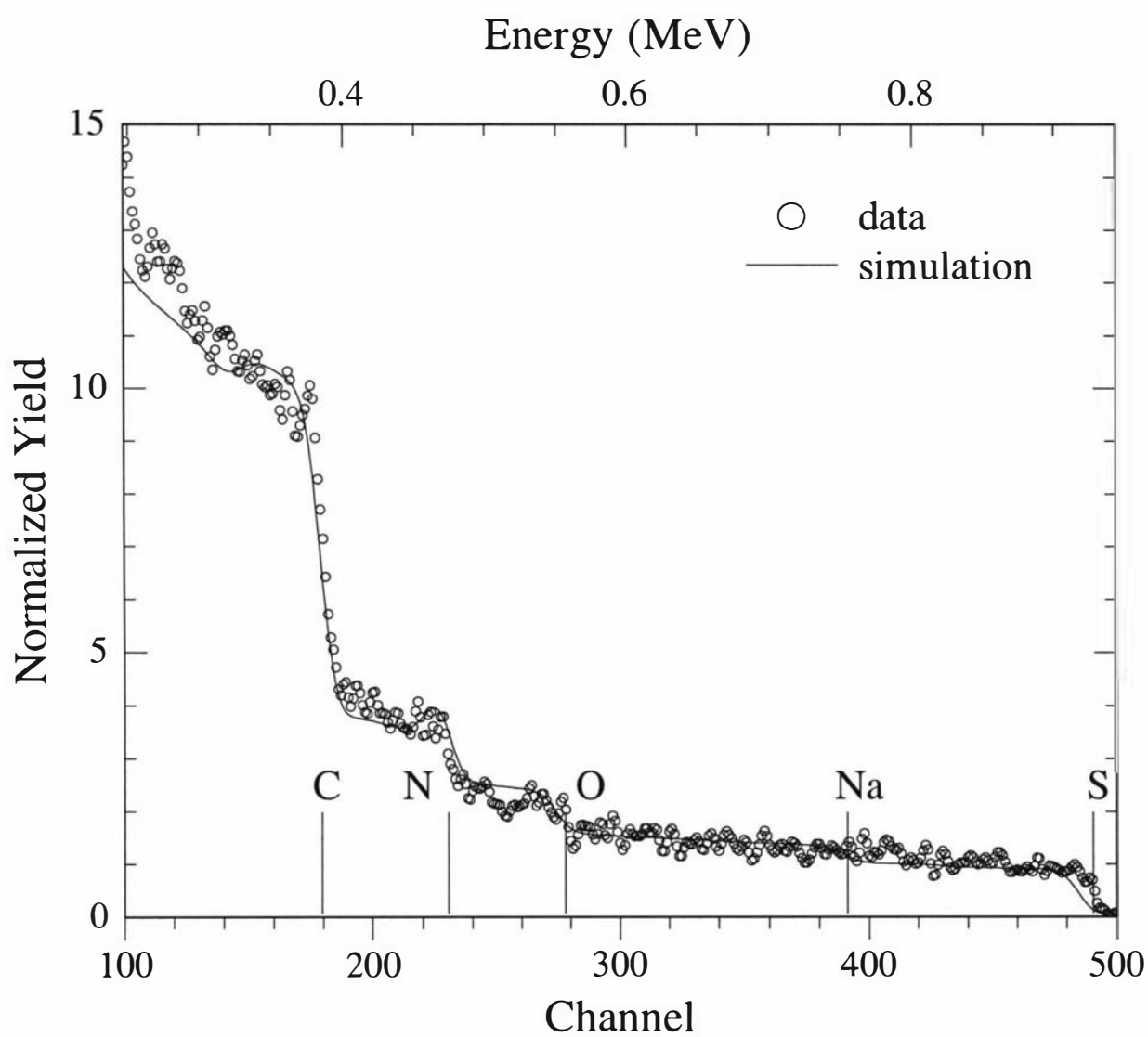


Fig. 4.13 RBS simulation and data for PPy-NBS film, solution side (data \circ , simulation). Simulation data in tabulated in the Appendix (Table A.6)

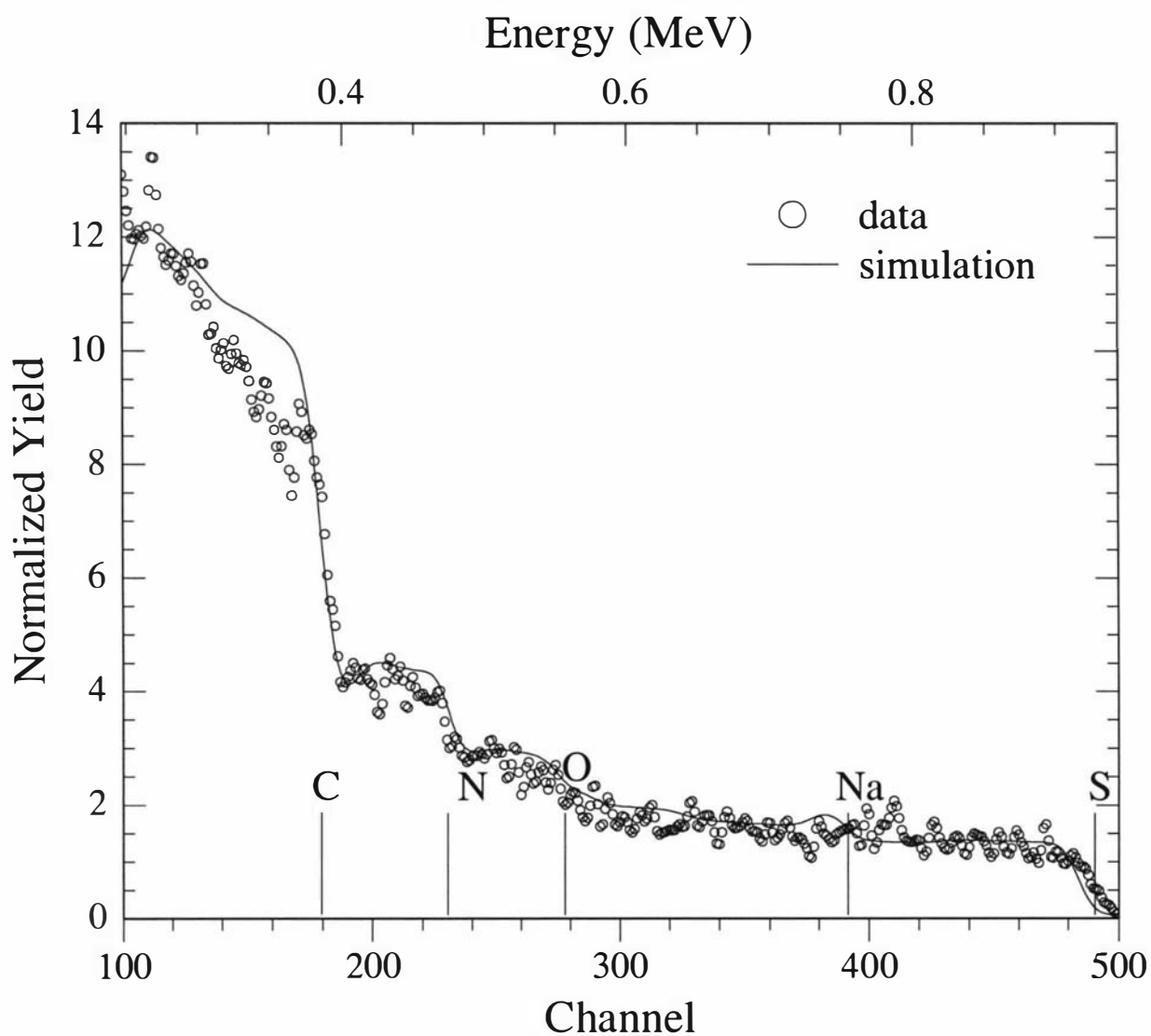


Fig. 4.14 RBS simulation and data for PPy-HBS film, solution side (data \circ , simulation). Simulation data is tabulated in the Appendix (Table A.7)

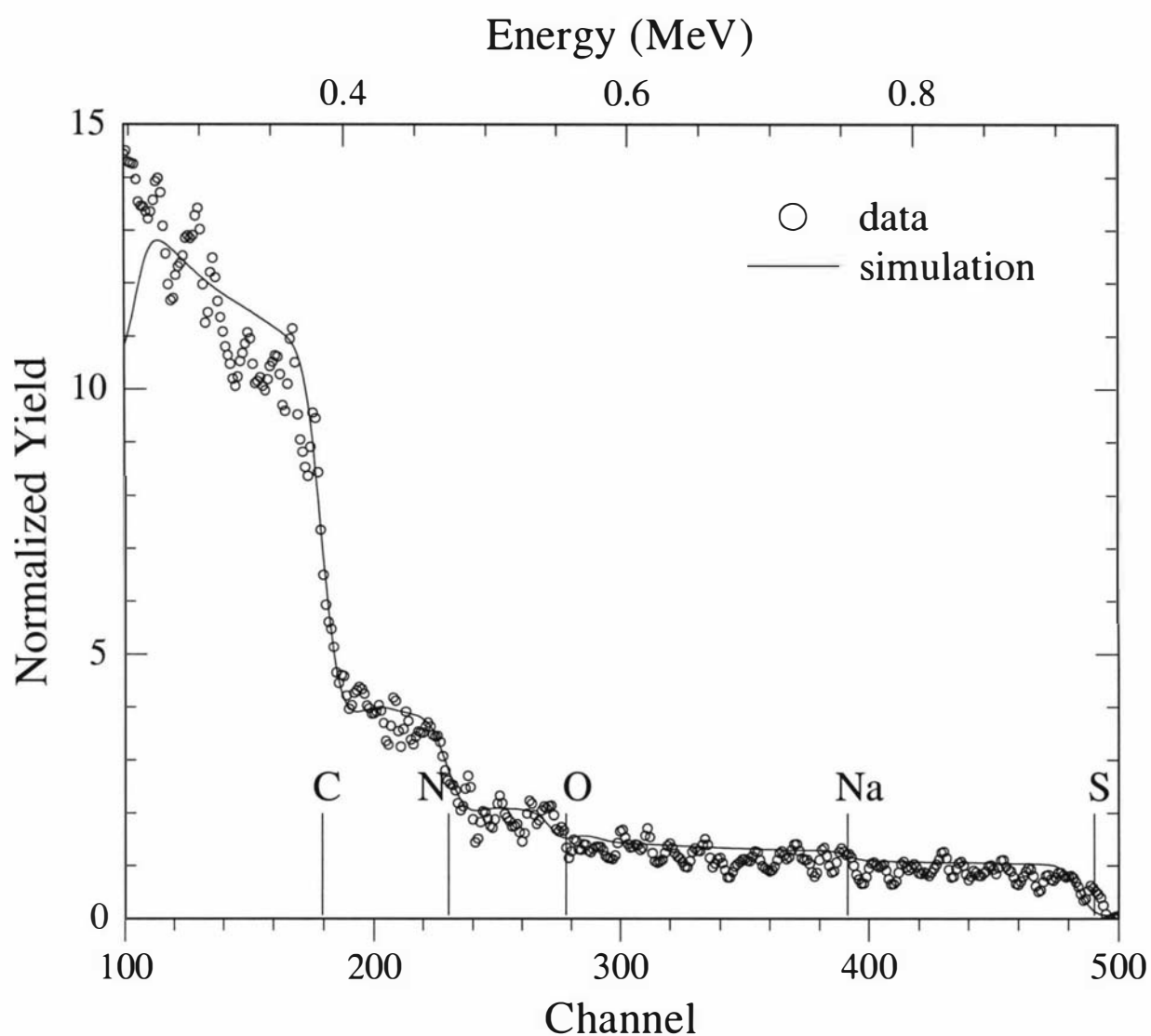


Fig. 4.15 RBS simulation and data for PPy-MS film, solution side (data \circ , simulation). Simulation data in tabulated in the Appendix (Table A.8)

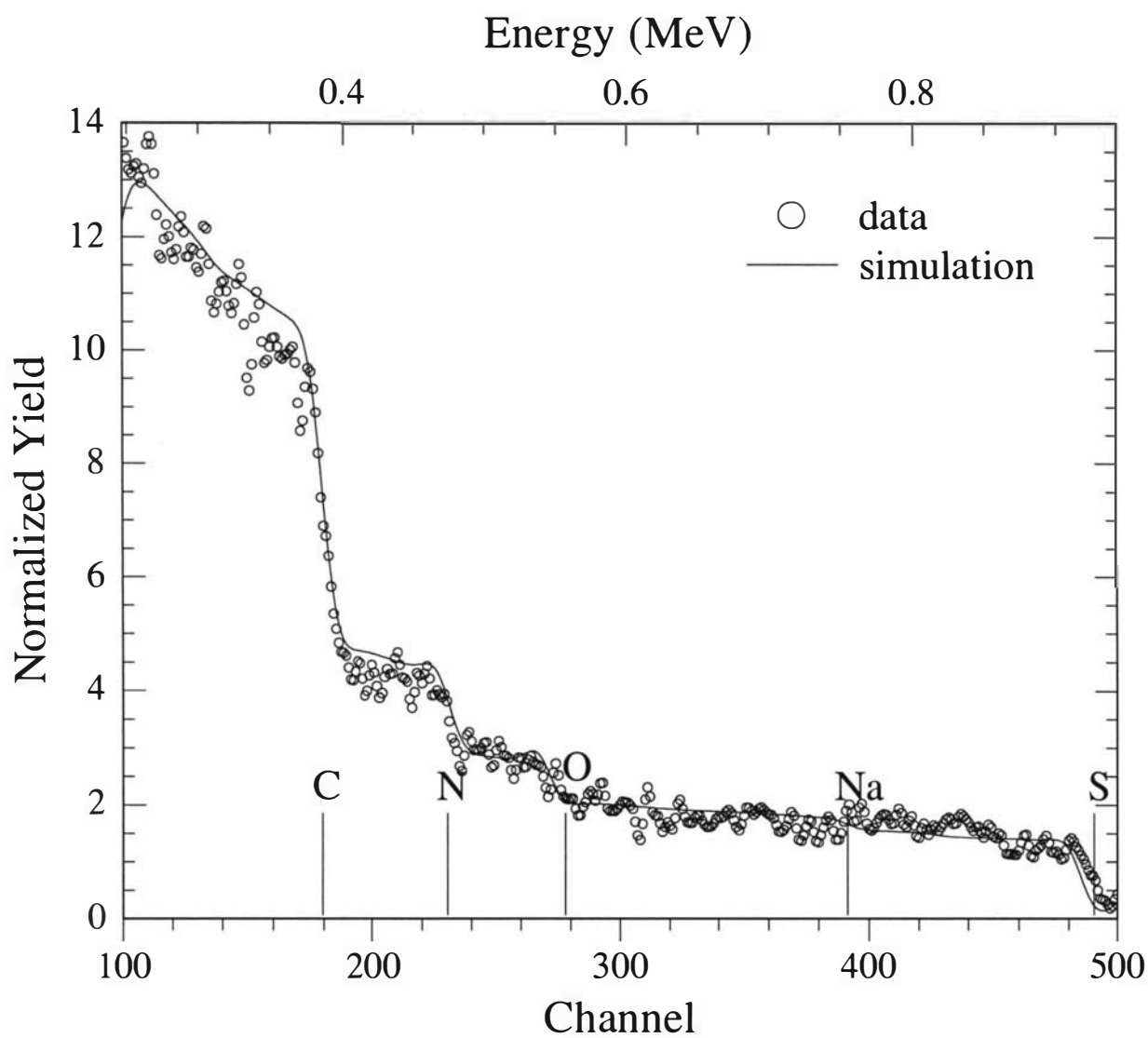


Fig. 4.16 RBS simulation and data for PPy-SB film, solution side (data \circ , simulation). Simulation data in tabulated in the Appendix (Table A.9)

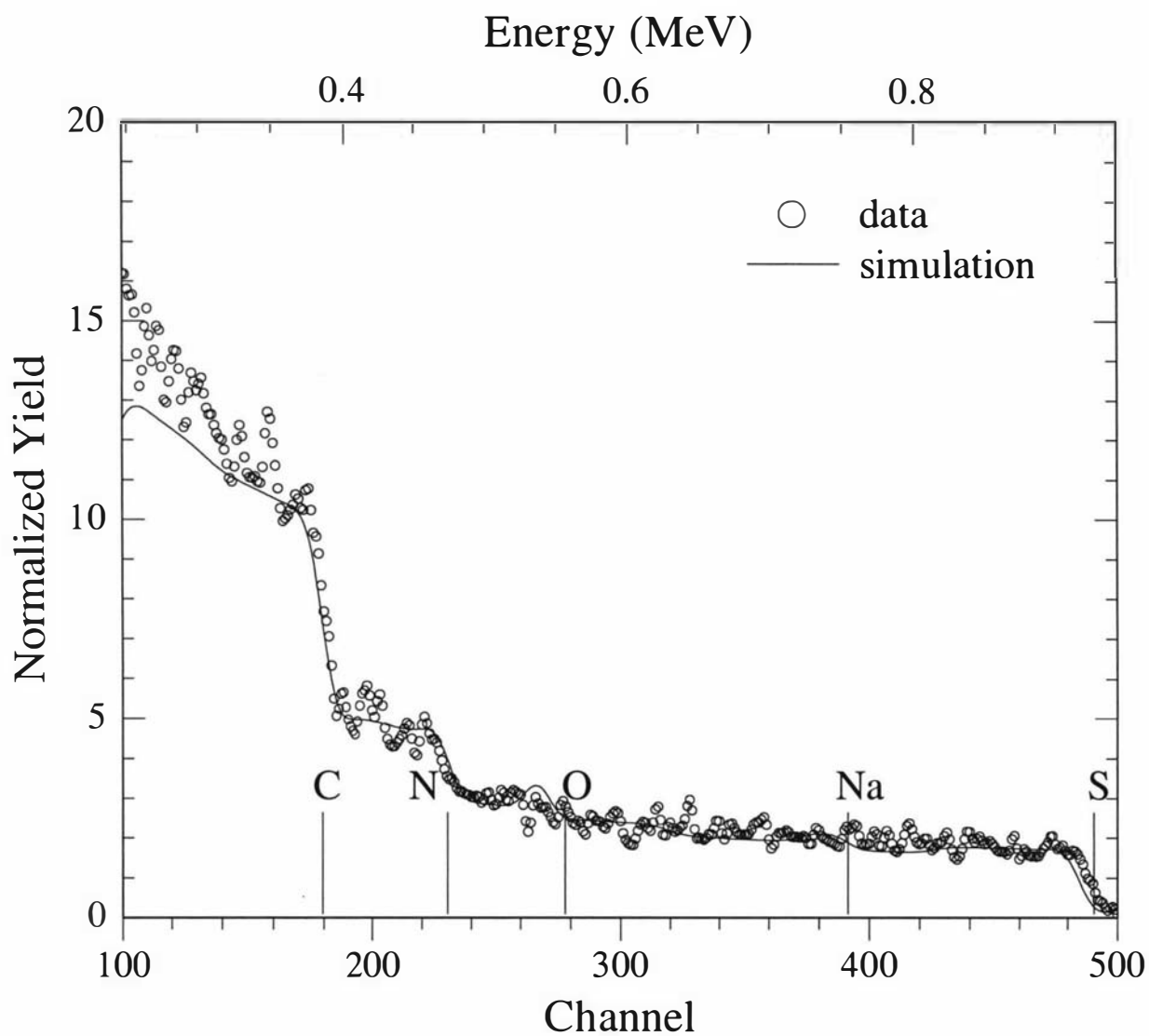


Fig. 4.17 RBS simulation and data for PPy-PTS film, solution side (data \circ , simulation). Simulation data in tabulated in the Appendix (Table A.10)

monomer ratios, the atomic percent of N was divided by the atomic percent of S. By doing this, counter ion to monomer ratios were found for each layer within each sample. To perform the next stage, a value for H had to be established. This H value was estimated from the amount of C found in RUMP, and using their chemical stoichiometry. A flow diagram of the step performed to obtain counter ion to monomer ratios and sample layer thicknesses is shown in Fig. 4.18. Table 4.2 lists the calculated optimised monomer to counter ion ratios and layer thicknesses for the solution sides of the six pyrrole film corresponding to the best fits to the RBS data shown in Figs. 4.12 - 4.17.

Layer 1 commences at the solution side of the film with subsequent layers located progressively deeper into the film. Five layers were sufficient to describe the RBS data in most cases, however for PPy-DBS and PPy-NBS six layers were required to adequately simulate the RBS spectra. In all cases the layer closest to the film-solution interface contained the trace constituents, and was found to be 30 nm thick, while subsequent layers ranged from 222 to 275 nm. For each film, the second and subsequent layer thicknesses were constant within ± 5 nm. The maximum depth of analysis ranged between 1.0 to 1.2 μm into the solution side of the film, where as the total film thickness was *ca.* 30 μm .

Figure 4.19 shows the plot of the monomer to counter ion ratios through the modelled layers of each PPy film. PPy-MS was found to have a constant monomer to counter ion ratio of 3.5, to the maximum depth analysed from the solution side of the film. This result suggests that there is on average 7 PPy monomer units to every two MS counter ions associated with the polymer chain. It does not confirm, however, that the average charge on each monomer unit is +0.29 since there exists the possibility that the counter ions could be entrained in the polymer matrix together with sodium (or other cations) to form an anion-cation pair not involving the polymer backbone. Na is observed in the RBS spectrum and the possibility of H^+ pairing with the polymer dopant anions can not be ruled out. This depth-independent ratio of 3.5 for PPy-MS falls within the range of 2 – 7 reported by other groups for bulk elemental analysis of PPy films ^[122].

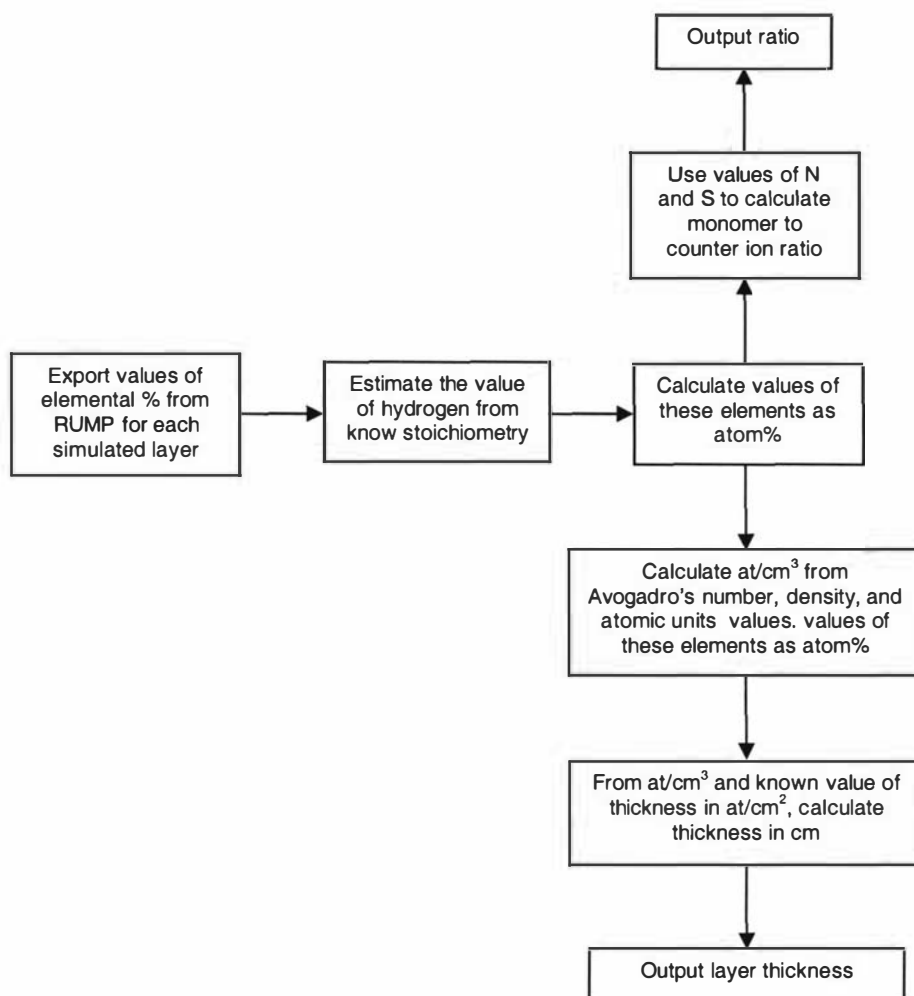


Fig. 4.18 Flow diagram of the steps undertaken to obtain monomer to counter ion ratios and layer thicknesses.

Table 4.2 Monomer to counter ion ratios with depth into PPy polymer films, plus combustion analysis monomer to counter ion ratios for bulk material, where l is the thickness measured, n is the number of PPy monomers, and x is the number of counter ions determined to charge balance the polymer.

Polymer	Layer 1		Layer 2		Layer 3		Layer 4		Layer 5		Layer 6		Combustion analysis
	l/nm	n/x	l/nm	n/x	l/nm	n/x	l/nm	n/x	l/nm	n/x	l/nm	n/x	$(n/x)_{\text{CA}}$
PPy-DBS	30	3.5	229	3.5	227	2.9	222	2.2	222	2.2	222	2.2	2.6
PPy-NBS	29	5.25	255	5.25	251	4	249	3.5	249	3.5	249	3.5	2.4
PPy-HBS	32	3.25	270	3.25	266	3.8	264	4.55	263	4	—	—	2.8
PPy-MS	31	3.5	253	3.5	254	3.5	259	3.5	258	3.5	—	—	5.2
PPy-SB	32	2.8	275	2.8	270	2.7	269	2.5	269	2.5	—	—	4.9
PPy-PTS	33	2.6	281	2.6	275	3	274	3.5	275	3	—	—	3.0

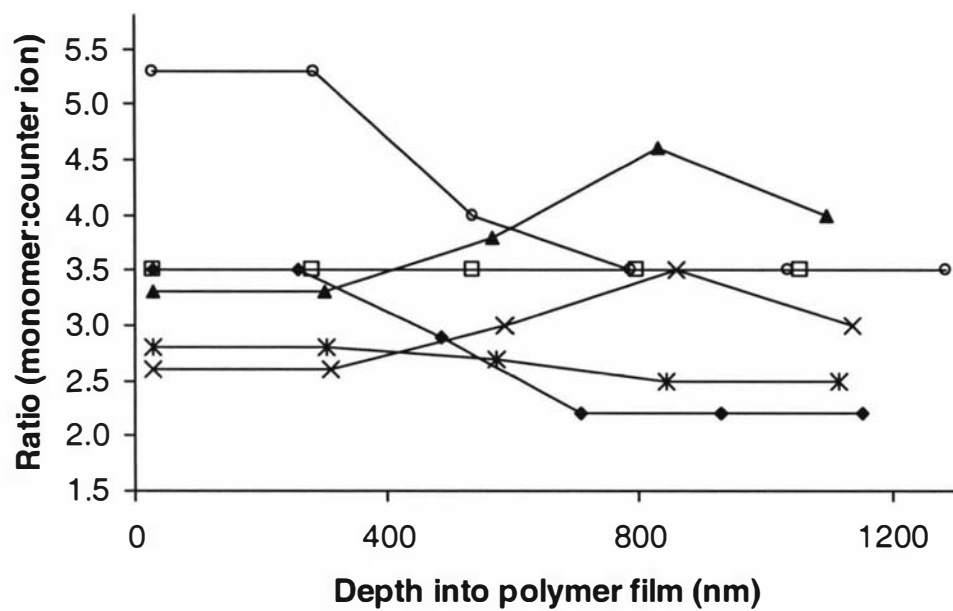


Fig. 4.19 Pictorial figure of the monomer to counter ion ratios for the solution side of each PPy films. ●– PPy-DBS, ○ – PPy-NBS, ▲ – PPy-HBS, ◻– PPy-MS, * - PPy-SB, × - PPy-PTS.

Taking PPy-MS as an arbitrary benchmark, the five other PPy polymer films appear to fall into two categories. First, PPy-PTS and PPy-HBS show an initially increasing monomer to counter ion ratio (i.e. indicative of decreasing oxidation state) with increasing depth into the film. In both cases at 830-860 nm depth a maximum monomer to counter ion (35-40 % higher than at the surface) ratio is observed followed by a decline at the next deepest modelled layer. This may well indicate that the surface of those two films are more oxidised than the bulk. Secondly, PPy-DBS, PPy-NBS, and PPy-SB exhibit a decline in monomer to counter ion ratio with depth (indicative of increasing oxidation state). This decline is only 11 % over the depth analysed in the case of PPy-SB, but is more pronounced in the case of PPy-NBS (34 %) and PPy-DBS (37 %). Moreover, if it is assumed that each counter ion is associated with one positive charge on the polymer chain (ignoring the question of other cations pairing with the counter ions), this would indicate that the PPy-NBS film is in a relatively reduced state with 5.3 monomers for every +1 charge at the surface of the film. However, at greater than 785 nm depths, this ratio decreases significantly to 3.5 monomers for every +1 charge.

In general, according to this RBS elemental analysis PPy-NBS and PPy-HBS are formed in a less oxidised state to the depth analysed than the arbitrary bench mark, PPy-MS, while the remaining polymer films are present in a higher state of oxidation than PPy-MS.

4.3.4 *Comparison with combustion analysis*

The combustion analysis results were performed at Otago University and reported in terms of atomic percent for the elements C, H, N, S, and Cl. The atomic percent of O required estimation (as combustion analysis does not give the O content of samples), to deduce the monomer to counter ion ratios. In Fig. 4.20 the combustion analysis results are in the column named 'Observed %'. The columns to the left of this are to work out the 'calculated polymer %'. This was calculated from the amounts of pyrrole and counter ion from the ratio. The ratios for pyrrole to counter ion, were optimised by minimising the sum of the square of the difference between the calculated and observed percentages. This was achieved using the Solver add-in function in Microsoft Excel.

Polypyrrole - p -
toluenesulfonic acid

ratio
pyrrole:counter
ion 2.98

ratio
water:counter
ion 1.46

		<u>pyrrole unit</u>			<u>counter ion</u>			<u>Calculated Polymer</u>			<u>Observed</u>	$(obs-calc)^2$
		No.	mass	%	No.	mass	%	No.	mass	%	%	
C	12.01	4	48.04	74.9852	7	84.07	48.82	18.912498	227.1391	58.352612	58.425	0.00524
H	1.008	2	2.016	3.14675	8	8.064	4.683	16.871673	17.006646	4.3690508	4.475	0.0112252
N	14.01	1	14.01	21.8681	0	0	0	2.9781244	41.723523	10.718879	10.375	0.118253
S	32.06	0	0	0	1	32.06	18.62	1	32.06	8.2362957	7.975	0.0682754
Cl	35.45	0	0	0	0	0	0	0	0	0	0.46	
O	16	0	0	0	3	48	27.88	4.4577121	71.323394	18.323162	18.29	0.0010997
Other	n/a											
											sum deviations	0.2040933

Fig. 4.20 Example from spreadsheet of how monomer to counter ion ratios for the combustion analysis results.

Comparisons may be made between the IBA-determined monomer to counter ion ratios and those which were determined by combustion analysis. In general, there was not good correlation between elemental analysis of the bulk film with that of the surface (to a depth of *ca.* 1 μm). Only in the case of PPy-PTS could a direct agreement between the surface and bulk composition be established. In the case of PPy-NBS and PPy-HBS, the bulk polymer film appears to be on average at a higher oxidation state than the oxidation state at the surface. In contrast, the PPy-MS and PPy-SB polymer films appear to be in a more reduced state in the bulk than at the film surface.

4.4 Conclusions

The polypyrrole conducting polymers were successfully analysed using PIXE and RBS. The PIXE analysis showed trace levels of unanticipated elements within the polymer film, and that there were differences detectable between the qualitative and quantitative analysis techniques. It is proposed that these trace elements were incorporated during the storage and handling stages since their presence was only detected on the outermost 30 nm of each side of the films.

RBS analysis enabled depth profiling of the monomer to counter ion ratio to a depth 1.0-1.2 μm . Information on counter ion to monomer ratios throughout these depths were determined for each film. It was established that these surface ratios varied from film to film. Depending on which counter ion was employed, the ratios either remained constant, increased, or decreased, with depth into the polymer. The monomer to counter ion ratios varied from 6:1 to 2:1. Given that no non-polymer cations such as K^+ or Na^+ were detected, which might have formed cation-anion pairs in the film matrix, it is then proposed that the average charge per pyrrole unit varied from 0.17 to 0.5. This relies on the assumption that H^+ -anion pairing within the film has not taken place.

RBS may well prove to be useful for surface elemental analysis and depth profiling of organic films and polymers but of limited use (in a similar manner to most surface techniques) at providing information on bulk materials.

There is not strong agreement between the monomer to counter ion ratios deduced using RBS analysis and those found in the bulk using combustion analysis. Given that RBS is well-established as a quantitative technique, this implies that in the case of the PPy films examined here that the surface composition and indeed, likely performance as conducting polymer is not reflected well in exploring bulk properties alone.

CHAPTER 5

Electrochemical Preparation of Terthiophene-ferrocene copolymers

5.1 Introduction

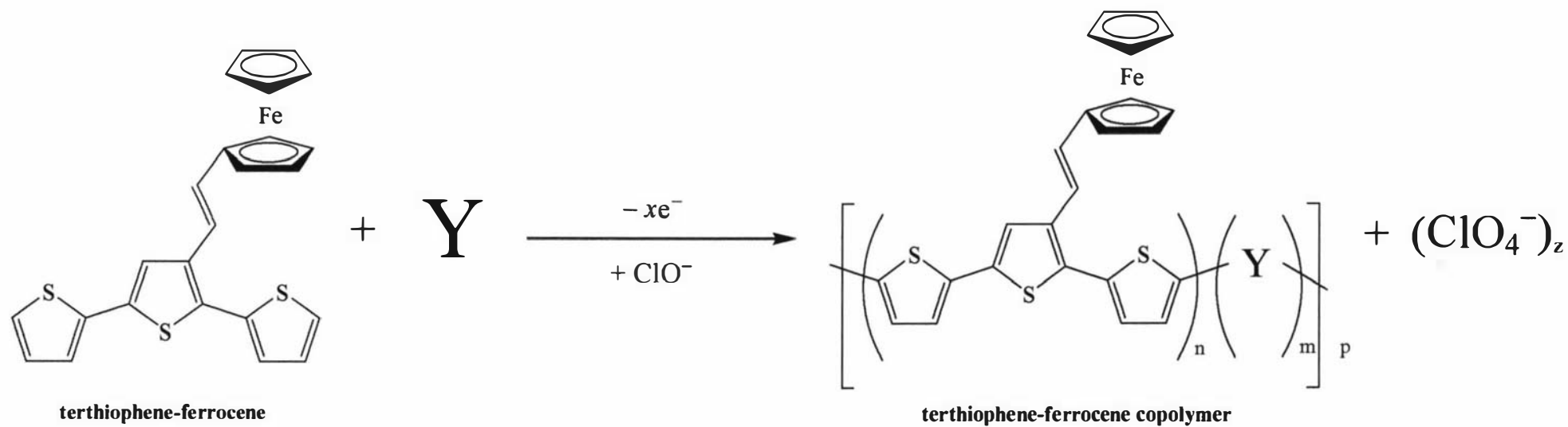
The terthiophene-ferrocene (TTh-Fc) monomer has two important chemical groups within the molecule (Fig. 5.1). The first is the terthiophene backbone through which a conjugated polymeric chain can be formed chemically, or in this case, electrochemically, from which a conducting polymer may evolve. The second is the ferrocene group attached to the central thiophene or the terthiophene. Ferrocene is a very good redox active molecule which can store charge and then release it. Consequently, with ferrocene combined with terthiophene we have a molecule which can carry charge to a group which can store it, and this group can then release the charge which can again travel through the terthiophene backbone. An end aim of this molecule is in applications such as plastic batteries ^[123].

The aim of this work was to form stand-alone durable films of this molecule copolymerised with other copolymer monomers, such as pyrrole and EDOT, at varying ratios and then subjected to IBA analysis. The electrochemical scheme for the preparation of these TTh-Fc copolymer is shown in Scheme 5.1.

5.2 Deposition of Terthiophene-ferrocene

Preliminary work on this deposition study rapidly demonstrated that to achieve the formation of films which could easily be removed in large pieces from the electrode surface ('peelable' films) from the monomer TTh-Fc, not only was the system dependant on the type of working electrode used, but also the solvent, and counter ion also. This section briefly reports the progression of experiments required to establish a system from which peelable films of TTh-Fc could be produced.





Scheme 5.1 Chemical scheme of the production of terthiophene-ferrocene copolymer films electrochemically, where Y represents one of the five copolymer monomers, Py, bithiophene, EDOT, TTh-Por-TTh, or Bridging TTh.

It had previously been reported that polymer films of TTh-Fc could be formed from solutions of TTh-Fc (10 mM) in DCM on Pt disk working electrodes ^[123]. However, in the present work these conditions resulted in a loose black deposit on the Pt working electrode. Further, when post polymerisation CVs were performed in acetonitrile ^[123] it was observed that the electroactivity of this material rapidly decreased from initial currents of 0.1 mA to 0 A. To overcome these problems many systems were investigated. First, a solvent system of TTh-Fc (0.01 M) and tetrabutylammonium perchlorate (TBAP) (0.1 M) in dimethyl sulfoxide (DMSO) with a Pt working electrode was employed ^[124]. At a constant potential of +1600 mV (vs Ag wire) there was no visual evidence for any deposition. Employing a Au disc working electrode with this solution did give a small amount of deposition only after 3 hours of potentiostatic growth. A Au disc electrode was attempted because of the affinity that S has for binding to gold. However, this system did not work well as the material which was deposited onto the Au working electrode was not stable and re-dissolved back into solution. The next system attempted was a 2:1 DCM / Hexane solvent mix, with 0.1 M tetrabutylammonium hexafluoro-phosphate (TBAHFP) (98 %, Aldrich) as the electrolyte ^[125]. This solvent + electrolyte system afforded film growth on Pt disc, Au disc, and Au sheet working electrodes. However these films, while electrochemically active, were not sufficiently thick or sufficiently substantial to allow separation of the films from the electrode to give a self-supporting material for use in IBA.

When ITO glass electrodes were employed in this solvent + electrolyte system a greater extent of deposition took place but this black material was poorly adhered to the ITO electrodes and flaked off the surface while still immersed in the electrolyte solution.

Conversely, when this electrode was used together with the first solvent + electrolyte system of TTh-Fc (0.01 M), TBAP (0.1 M), in DCM substantial and robust peelable, stand-alone films formed which could be removed in one piece from the face of the ITO glass. Such films typically had dimensions of 1 cm × 1.5 cm.

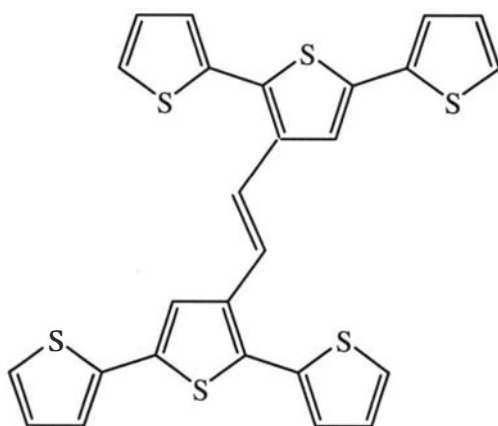
Having established a system which produced the required films the influence of electrolyte (and hence polymer counter ion) was assessed by using TBAHFP^[126-129] and tetrabutylammonium tetrafluoroborate (TBATFB)^[130, 131]. With DCM solutions of TBAHFP poorly adherent black powder formed. With DCM solutions of TBATFB, films were formed but were inferior to those formed with TBAP. Consequently, all further films were prepared with a solvent + electrolyte system of DCM and TBAP on ITO glass working electrodes, for both film deposition and subsequent post polymerisation CVs.

A range of monomers were used to form copolymers of TTh-Fc / pyrrole (Py), bithiophene, EDOT, TTh-Por-TTh, and a bridging TTh. The chemical structures and films arising from TTh-Por-TTh and Py are discussed in Chapters 3 + 4 (Fig. 3.1 and Scheme 4.1 respectively). The chemical structures of the remaining copolymer monomers can be seen in Fig. 5.2.

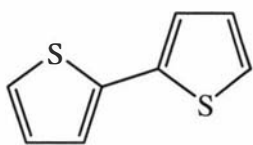
For each of the three copolymer monomers Py, bithiophene, and EDOT, five films of each were prepared with TTh-Fc to copolymer monomer solution concentration ratios of 1:10 (10 mM : 100 mM), 1:20 (5 mM: 100 mM), 1:50 (2 mM: 100 mM), 1:100 (1 mM: 100 mM), and 1:1 (5 mM: 5 mM). For the remaining two copolymer monomers (bis terthiophene porphyrin and bridging TTh) lower ratios had to be used due to the limited availability of the copolymer monomer materials and their limited solubility. In the case of the monomer TTh-Por-TTh ratios of TTh-Fc to copolymer monomer were 2:1 (10 mM: 5 mM), 1:5 (1 mM: 5 mM), 2:5 (2 mM: 5 mM), and 1:1 (5 mM: 5 mM). Even lower ratios were used for bridging TTh (TTh-Fc: copolymer monomer) 1:10 (1 mM: 10 mM), 1:1 (5 mM: 5 mM), and 10:1 (10 mM: 1 mM) used employed.

5.3 Electrochemistry

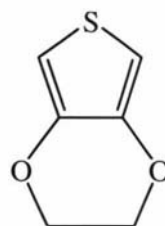
Identical electrochemical procedure was used for the preparation of each film. The first deposition was using CV to form a thin film from which post polymerisation CVs were performed, and a second deposition which was a potentiostatic deposition for fixed times to produce substantial films for IBA analysis and scanning electron microscope (SEM) images.



Bridging Terthiophene (Bridging TTh)



bithiophene



3,4-Ethylenedioxythiophene (EDOT)

Fig. 5.2 Chemical structure of Bridging terthiophene (Bridging TTh), bithiophene, and 3,4-Ethylenedioxythiophene (EDOT).

5.3.1 Stepping potential

Each of the CVs run throughout this section of work commenced at negative, reduction potentials.

The sets of potential dependence experiments for the TTh-Fc copolymers had E_0 and E_2 at either -800 or -1000 mV, and E_1 values increasing from 1000 to 1800 mV in steps of 100 mV.

Figure 5.3 shows the overlaid CVs of the 1:20 ratio of TTh-Fc to Py. It can be seen from Fig. 5.3 that as the value of E_1 becomes more positive, the formation of an oxidation peak commences, first appearing at *ca.* 700mV for $E_1 = 1300$ mV. As the value of E_1 is increased towards 1800 mV this oxidation peak becomes more pronounced and shifts anodically in potential. Oxidation commences at a potential of *ca.* 350 mV for the first cycle, and shifts to more anodic potentials as cycling proceeds. On the reverse sweep, a reduction peak is observed which has a peak at *ca.* 150 mV. On subsequent reverse sweeps, for more anodic E_1 potentials, this peak increases, and the peak maximum shifts to more negative potentials. On the reverse sweeps for $E_1 > 1500$ mV, a shoulder to a second reduction peak forms, commencing at -500 mV. The complete reduction of the polymer has not occurred by the completion of the CVs but the focus of these CVs was to establish an oxidation potential for the constant potential growth of the films, not an electrochemical study of these materials. This was the case in all of the TTh-Fc copolymer materials formed. Based upon these CVs 1600 mV was chosen for the electrochemical deposition for TTh-Fc / Py copolymers.

The overlaid CVs for increasing the potential of E_1 for a 1:20 ratio, for TTh-Fc to bithiophene, is shown in Fig. 5.4. The oxidation of TTh-Fc / bithiophene copolymer commences at *ca.* 300 mV. An oxidation wave with a peak at *ca.* 900 mV commences at $E_1 \geq 1500$ mV. On the reverse sweep when $1000 \text{ mV} \leq E_1 \leq 1200 \text{ mV}$ an anodic wave with a peak at *ca.* 100 mV was observed. On the reverse sweep when $E_1 = 1300$ mV a second anodic peak was observed forming at slightly more cathodic potentials (*ca.* 250 mV) to that of the peak at *ca.* 100 mV. This peak was seen to increase in magnitude and shift to more anodic potentials with subsequent cycles,

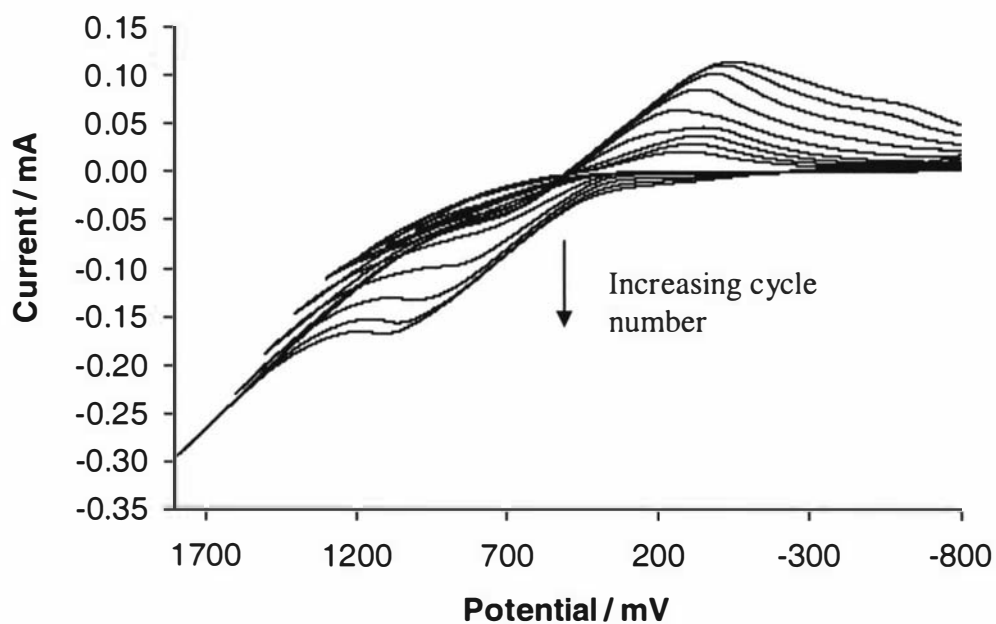


Fig 5.3 Overlaid CVs of 1:20 TTh-Fc / Py solution, stepping the potential from 1000 to 1800 mV, TBAP as counter ion.

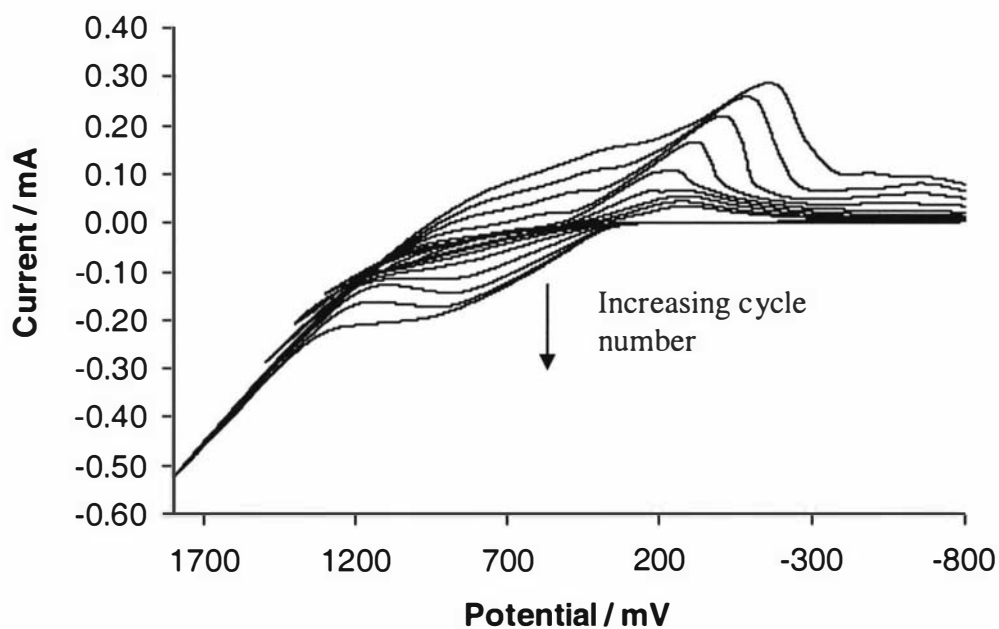


Fig. 5.4 Overlaid CVs of 1:20 TTh-Fc/ bithiophene solution, stepping the potential from 1000 to 1800 mV, TBAP as counter ion.

consuming the smaller anodic peak at *ca.* 100 mV in the process. At the E_1 potential of 1500 mV a third anodic wave was observed to be commencing with a peak at *ca.* -600 mV. When $E_1 > 1500$ mV this peak increased in magnitude. Based upon these CVs 1500 mV was chosen for the electrochemical deposition for the TTh-Fc / bithiophene copolymers.

Figure 5.5 shows the overlaid CVs of the 1:20 ratio of TTh-Fc to EDOT solution (E_0 and E_2 -100 mV) for cycles where E_1 varied from 1000 to 1800 mV. At cycles where $E_1 \leq 1200$ mV the initial oxidation was observed to commence at *ca.* +450 mV and one oxidation peak was observed with a maximum at *ca.* 1000 mV. After the first few cycles there is a large shift in the onset of oxidation from +450 mV to -200 mV, not observed in Fig. 5.4. After the initial oxidation the oxidation continued to occur continuously for +200-300 mV until *ca.* +400 mV where a second oxidation process commenced. This second oxidation process developed into a new oxidation peak with a maximum at *ca.* +600 mV, which shifted to more cathodic potentials with cycling. This second oxidation peak lead into the major film oxidation peak. On the reverse sweep when $E_1 \leq 1200$ mV one reduction peak was observed with a maximum at *ca.* 100 mV. At $E_1 > 1200$ mV three new reduction peaks, each of which shifted to more anodic potentials with subsequent cycling, were observed. A potential of +1400 mV was chosen for the electrochemical deposition for the TTh-Fc / EDOT copolymers based upon these CVs.

Figure 5.6 shows the overlaid CVs (E_0 and E_2 -1000 mV) form a solution of 1:1 TTh-Fc and TTh-Por-TTh with E_1 varying form +1000 to +1800 mV. The initial oxidation onset potential at $E_1 = 1000$ mV commenced at *ca.* +400 mV, and shifts to more anodic potentials with subsequent cycles to a final value of +100 mV when $E_1 = 1800$ mV. As the value of E_1 was increased the formation of two oxidation peaks were observed with maximums at *ca.* +800 mV and +1400 mV. On the reverse sweep two reduction peaks with maximums occurring at *ca.* +300 mV and -700 mV were observed. With subsequent reverse sweeps both these two reduction peaks increased in magnitude, and the peak at *ca.* +300 mV also shifted to more anodic potentials. At $E_1 \geq 1500$ mV a third reduction peak at *ca.* +800 mV commenced and also shifted to

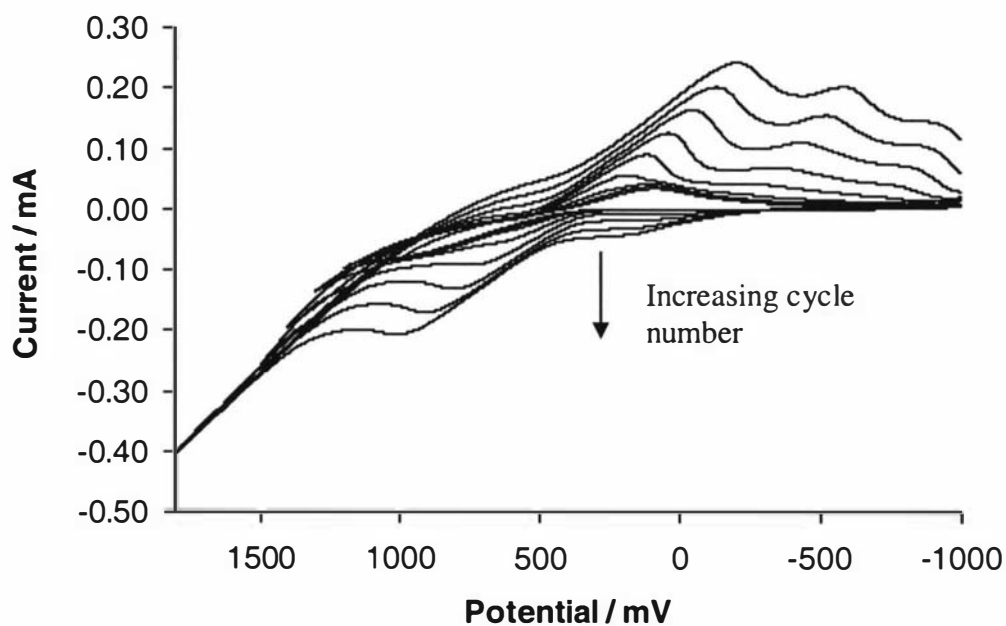


Fig 5.5 Overlaid CVs of 1:20 TTh-Fc / EDOT solution, stepping the potential from 1000 to 1800 mV, TBAP as counter ion.

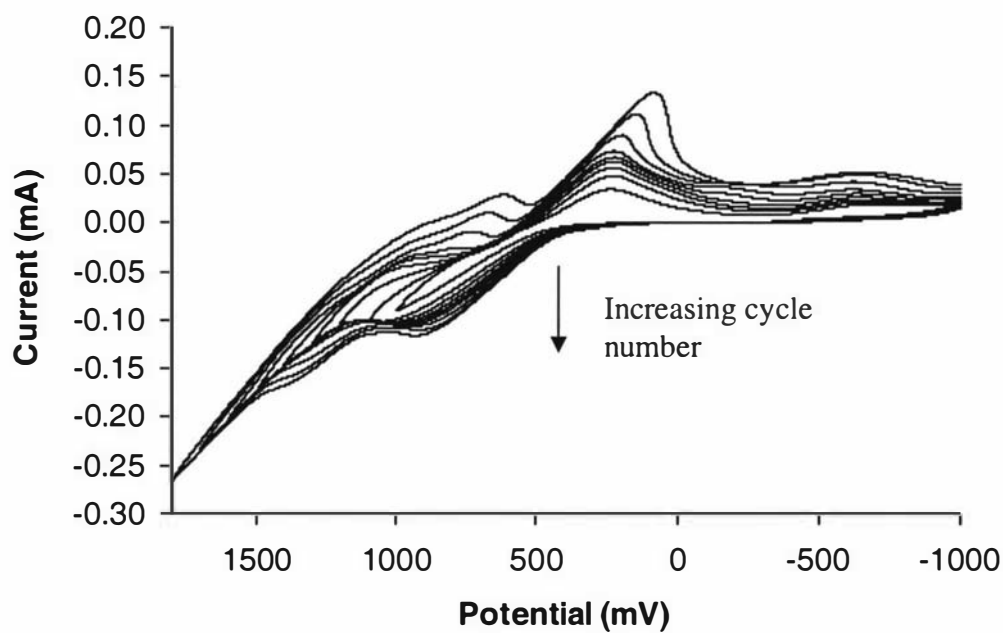


Fig 5.6 Overlaid CVs of 1:1 TTh-Fc / TTh-Por-TTh solution, stepping the potential from 1000 to 1800 mV, TBAP as counter ion.

more anodic potentials with subsequent cycles. Based upon these CVs of TTh-Por-TTh / TTh-Fc copolymers the value of +1500 mV was chosen for the electrochemical deposition of these films.

The overlaid CVs from a 1:1 solution of TTh-Fc and Bridging TTh, with E_1 increasing from 1000 to 1800 mV, can be seen in Fig. 5.7. The initial oxidation of the first cycle commenced at *ca.* +250 mV and did not alter with subsequent cycling. No isolated oxidation peaks were observed in the cathodic region of these CVs, but the oxidation wave did increase in magnitude with each cycle. On the reverse sweep when $E_1 \leq 1200$ mV one reduction peak was observed with a maximum occurring at *ca.* +200 mV. At $E_1 > 1200$ mV this first reduction peak was observed shifting to more anodic potentials, and a second reduction peak commences, first appearing at *ca.* +650 mV. This second peak increases in magnitude and shifts to more anodic potentials upon cycling, merging into the first reduction peak. When $E_1 = 1800$ mV a third reduction peak was observed at *ca.* -400 mV. Based upon these CVs observed for TTh-Fc / Bridging TTh copolymers the value of +1400 mV was chosen for the electrochemical deposition of these films.

Figure 5.8 shows three CV cycles from a solution containing only the TTh-Fc monomer (0.01 M) and TBAP (0.1 M) in DCM. A comparison of Fig. 5.8 to Figs. 5.2-5.6, it can be said with some certainty that in the electrochemical deposition of the copolymer we are not only observing the deposition of the TTh-Fc monomer. Figures 5.9-5.11 show the CVs of three of the copolymer monomers, Py, bithiophene, and EDOT, respectively. A comparison of these CVs to their corresponding copolymer:TTh-Fc CVs (Figs. 5.2-5.4) it can again be seen that they are different. The observation that within the copolymer : TTh-Fc CVs using Py, bithiophene, and EDOT, different oxidation and reduction waves are observed than in the CVs of the individual monomer components CVs, this supports the assumption that the films which were deposited are copolymer films consisting of unknown copolymer monomer to TTh-Fc ratios. CVs of only TTh-Por-TTh and bridging TTh with TBAP were not run due to the restrictions of minimal material being available.

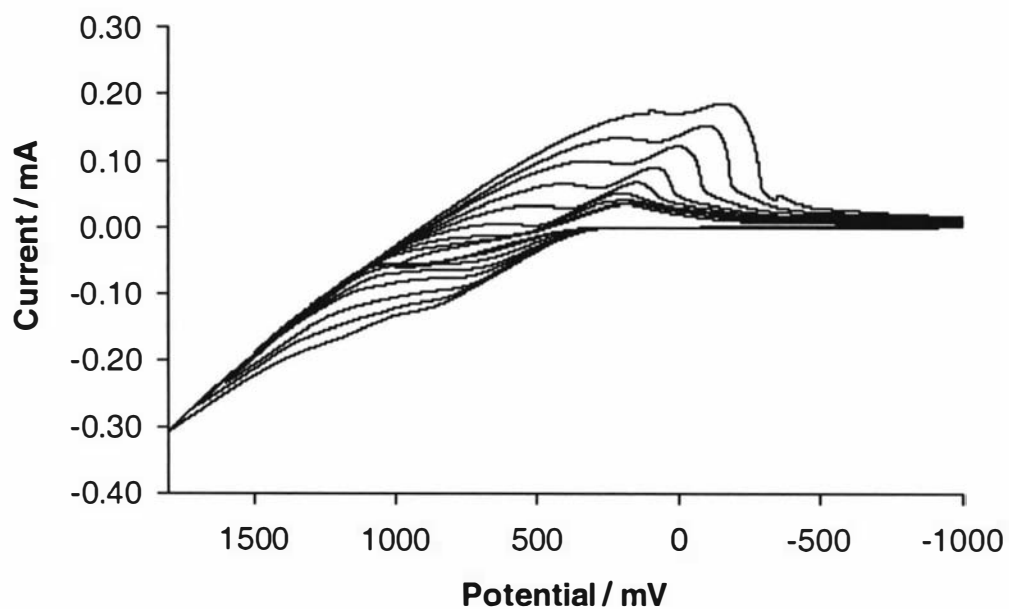


Fig 5.7 Overlaid CVs of 1:1 TTh-Fc/ Bridging TTh solution, stepping the potential from 1000 to 1800 mV, TBAP as counter ion.

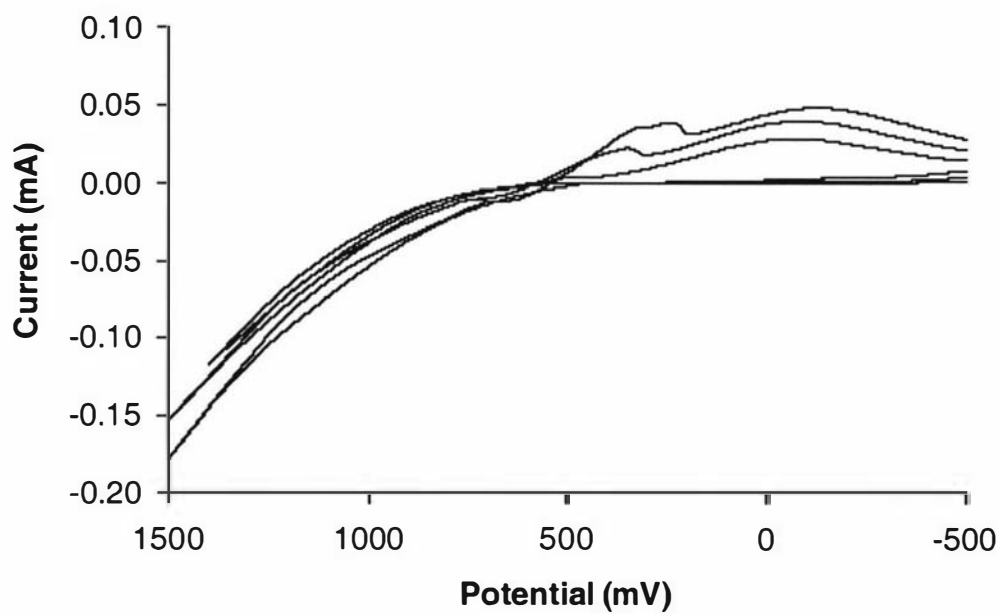


Fig 5.8 Three overlaid CVs of TTh-Fc monomer only with TBAP as the counter ion.

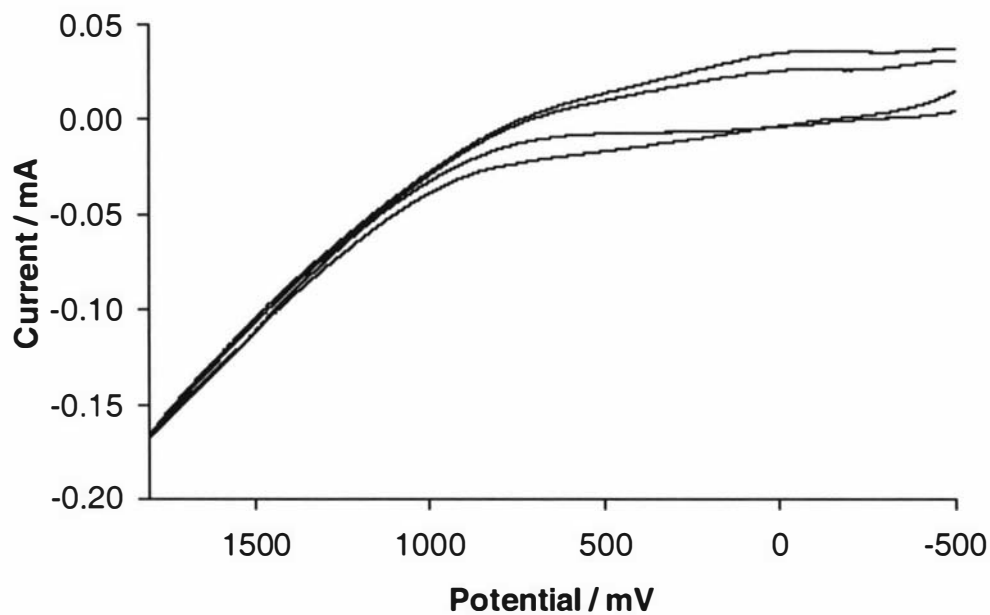


Fig 5.9 Two overlaid CVs of the pyrrole monomer only with TBAP as the counter ion.

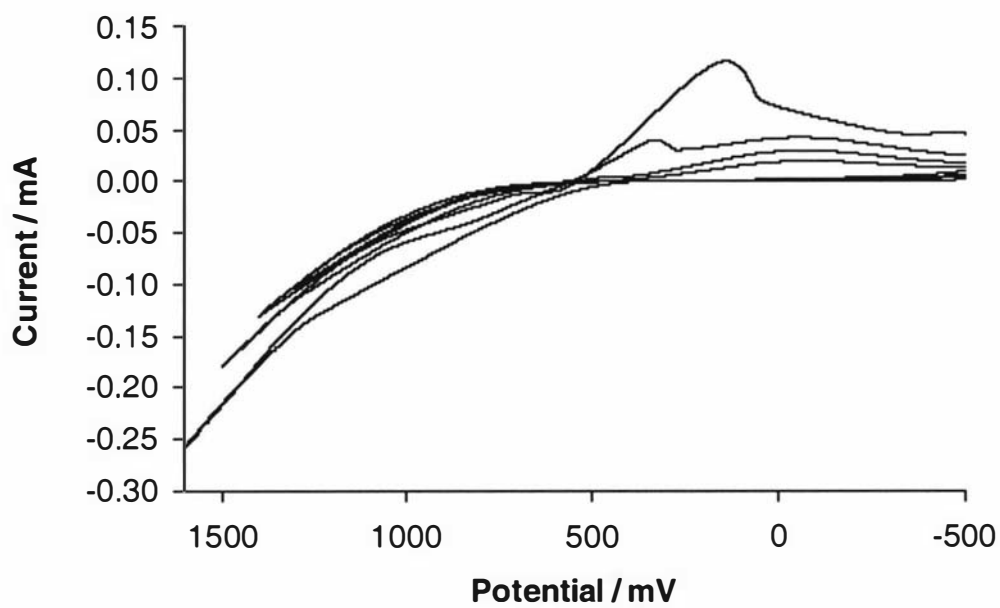


Fig 5.10 Three overlaid CVs of the bithiophene monomer only with TBAP as the counter ion.

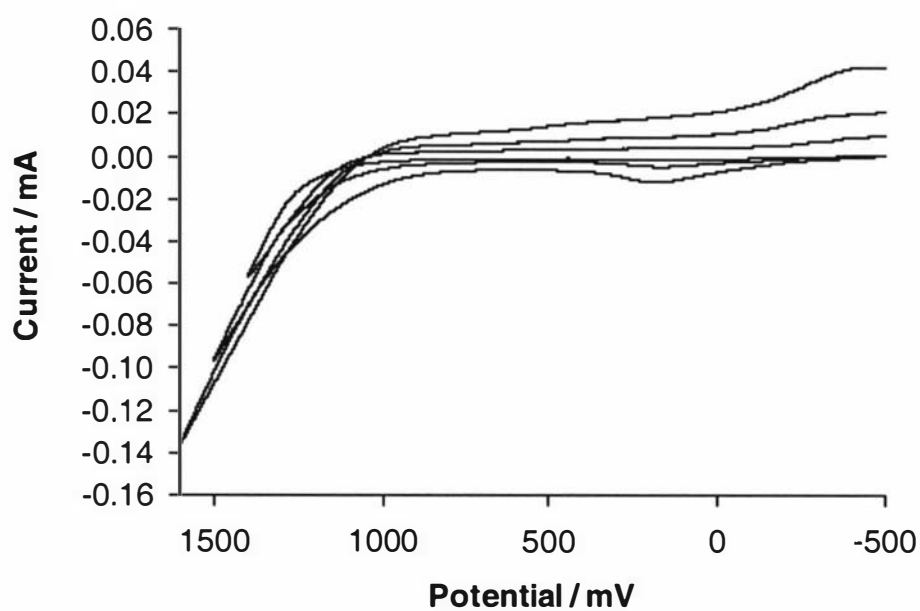


Fig 5.11 Three overlaid CVs of the EDOT monomer only with TBAP as the counter ion.

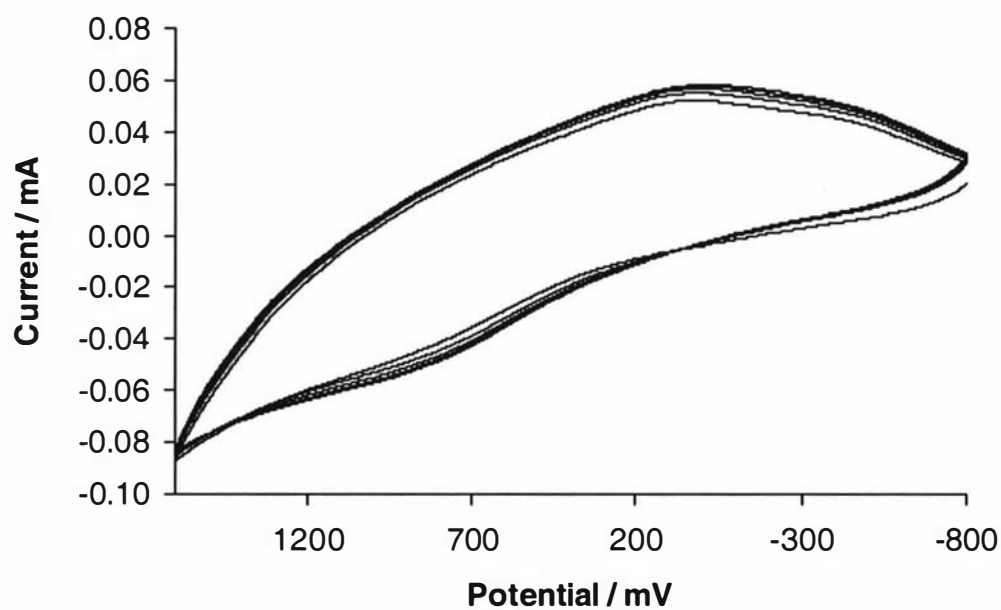


Fig 5.12 Post polymerisation CVs for 1:20 TTh-Fc / PPy film, first five cycles.

5.3.2 *Post polymerisation analysis*

Thin films of each TTh-Fc copolymer on ITO glass working electrodes were formed using the conditions listed in Table 5.1. The number of cycles required to form a substantial and peelable film was dependent upon the copolymer monomer.

After each of the films had been formed, all of the electrodes (reference, counter, and working) were removed from the copolymer solution and rinsed with DCM to remove traces of monomer and short chain oligomers. Once rinsed, all three electrodes were placed into a fresh, monomer-free solution of TBAP (0.1 M) in DCM. Consequently, the electrochemical response in this fresh electrolyte could be ascribed to copolymer redox processes accompanied by movement of the counter ion (ClO_4^-) in and out of the film. Identical CV conditions were applied to all copolymer films.

Figures 5.12 – 5.16 show the first five cycles for these post polymerisation CVs for copolymer monomers PPy, bithiophene, EDOT, bis terthiophene porphyrin, and bridging TTh respectively. In each case the electrochemical response was substantial and invariant indicating the film remaining in electrochemical contact with the ITO electrodes. In some cases slight decreases were observed (TTh-Fc / Py + TTh-Fc / TTh-Por-TTh) but this was only *ca.* 5 % over five cycles.

5.3.3 *Ion beam analysis and scanning electrode microscope images of films*

Having established the electrochemical preparation and post polymer properties of the film, the next step was to produce peelable films which could be used for IBA and SEM analysis. These films were formed potentiostatically for varying lengths of times, again dependent on the copolymer monomer. Table 5.2 lists the potential and times required to form suitable films for each copolymer.

Once films had been formed they were washed while still attached to the ITO glass electrode, with DCM, then the film was cut with a scalpel along the edges of the film covered ITO, removed by peeling, and washing once more in clean DCM. For each TTh-Fc copolymer film, three replicate films were produced for comparison. Each of these three films were cut into at least two pieces, one piece for a sample for IBA studies, and the other piece for SEM studies.

Table 5.1 Copolymer monomers and their associated deposition potential and time for potentiostatic growth of IBA quality films.

Copolymer monomer	E_1 Potential	Number of Cycles
Py	1600	2000
bithiophene	1500	2000
EDOT	1400	2500
TTh-Por-TTh	1600	3000
Bridging TTh	1400	750

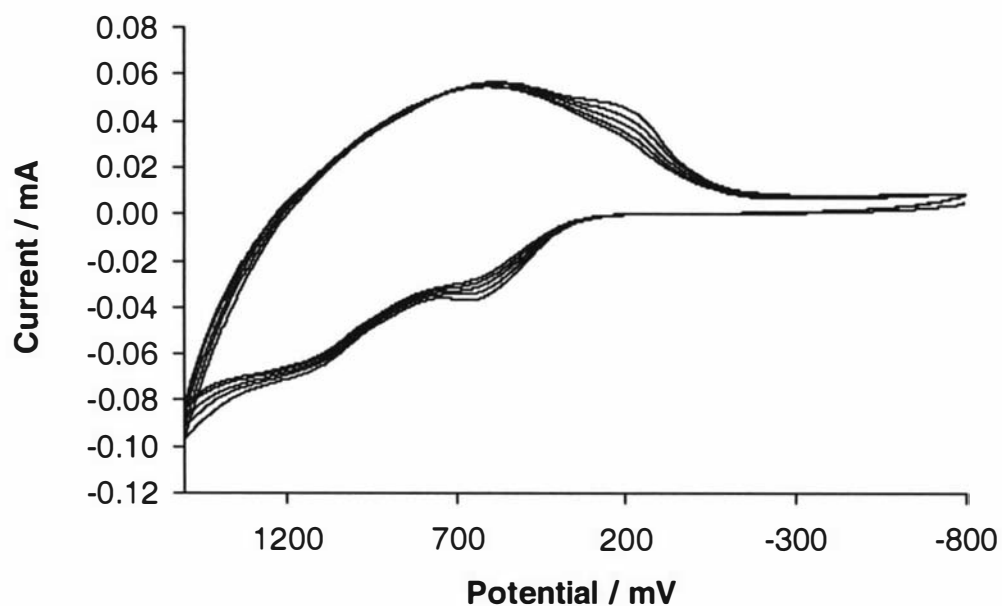


Fig 5.13 Post polymerisation CVs for 1:20 TTh-Fc / bithiophene film, first five cycles.

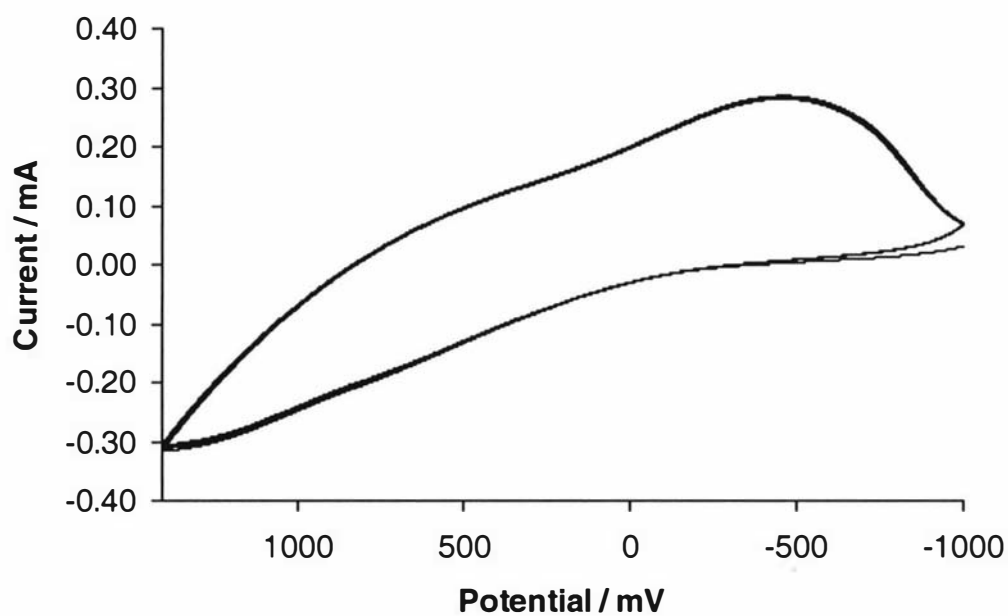


Fig 5.14 Post polymerisation CVs for 1:20 TTh-Fc / EDOT film, first five cycles.

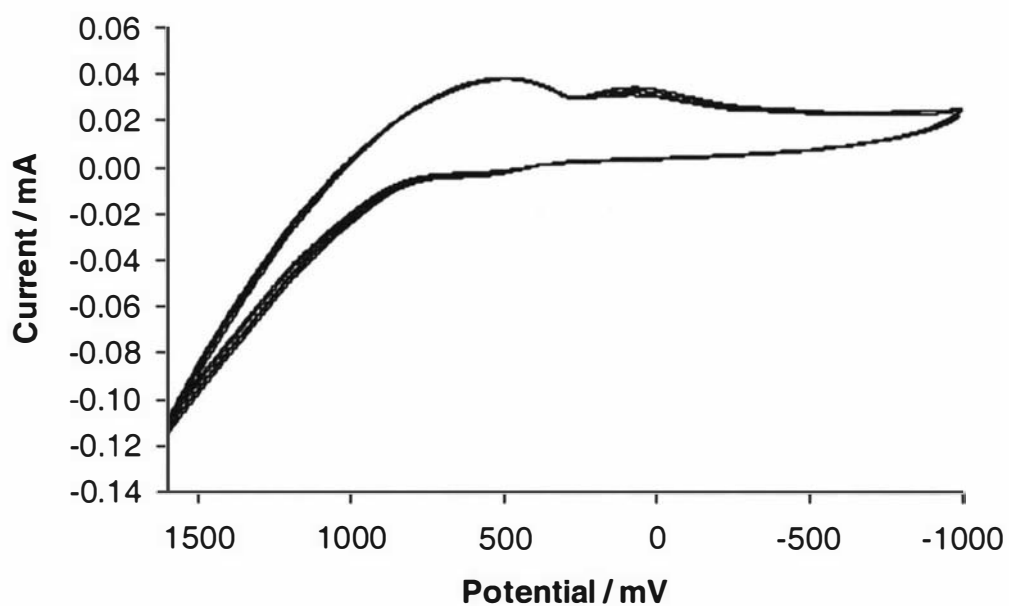


Fig 5.15 Post polymerisation CVs for 1:1 TTh-Fc / TTh-Por-TTh film, first five cycles.

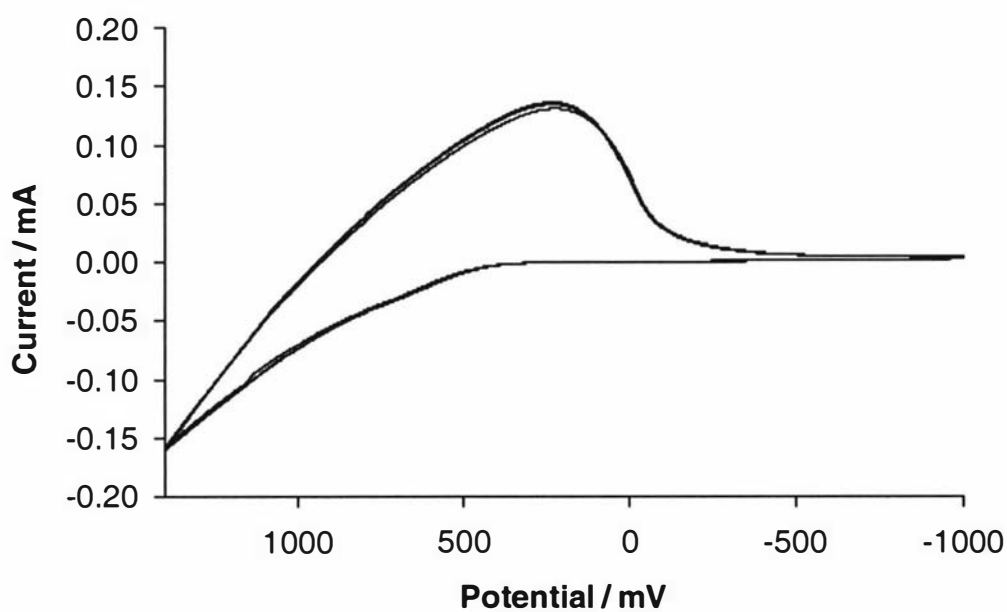


Fig 5.16 Post polymerisation CVs for 1:1 TTh-Fc / Bridging TTh film, first five cycles.

Table 5.2 Copolymer monomers and their associated potential and number of cycles required to produce the films used for the post polymerisation CV analysis.

Copolymer monomer	E_1 Potential (mV)	Number of Cycles
Py	1600	20
bithiophene	1500	40
EDOT	1400	25
TTh-Por-TTh	1600	30
Bridging TTh	1400	15

CHAPTER 6

SIMNRA modelling

6.1 Introduction

All of the results in Chapter 7 arose from experimental work performed using a proton beam with a beam energy of 2.5 MeV. The RBS analysis was first attempted with a 1.5 MeV $^4\text{He}^+$ beam as in Chapters 4 and 5, this being the common beam type and energy for most RBS. However, after only 5 s of a 1.5 MeV $^4\text{He}^+$ any TTh-Fc copolymer film samples disintegrated. Upon opening the sample chamber a distinct odour of burnt material was evident. It was established that this odour was due to the decomposition of the samples. The high energy of the $^4\text{He}^+$ ions and presence of high concentrations of oxygen in an organic material resulted in the samples being burnt ^[132]. It was rapidly established that use of a 2.5 MeV proton beam did not result in the destruction of the samples and RBS spectra. This is despite the higher energy; this implies that the size of the impacting incident ion is more significant than the energy.

A different program, SIMNRA, which could take into account non-Rutherford interactions, with greater ease than RUMP, was utilised. This is not widely used for the analysis of RBS spectra, and the development of a new analysis approach was required because the simulation of RBS spectra received from proton RBS was more difficult to analyse than those spectra obtained using $^4\text{He}^+$ RBS.

One major difference between using $^4\text{He}^+$ and proton incident beams was that when using $^4\text{He}^+$ beam, as in the work reported in Chapters 3 and 4, was that total film penetration was never observed, unlike that found here. The spectra obtained in Chapter 3 and 4 were similar in appearance to those of infinitely thick films (e.g. Fig. 2.19 (e)). In the spectra obtained for the TTh-Fc copolymers the RBS spectra displayed film penetration to some degree (e.g. Fig. 2.19 (a)-(d)).

The following sections describe the development of the final analysis model which was used to determine the compositional results found for these copolymer films. This development will be described through a series of key stages (Models I to III) that led to establishment of the final Model IV.

6.2 Model I

The first model used to attempt the simulation of these TTh-Fc copolymers using SIMNRA required three initial starting points to be made, each necessarily oversimplified and requiring progressive refinement as the modelling developed. First, that there existed a fixed 1:3 ratio of counter ion to TTh-Fc monomers within the film. Secondly, that there was a fixed copolymer monomer to TTh-Fc monomer ratio of 1:1. Thirdly, that the film thickness was assumed to be 15000×10^{15} atoms/cm². A further assumption was also made in this model, that the spectra of these copolymers could be simulated using one homogeneous layer. A flow diagram of the steps undertaken in this Model I is shown in Fig. 6.1.

The process of attempting to obtain a theoretical simulated spectrum of the experimental data was iterative. From the starting points, the total atomic percentage of the assumed polymer matrix was calculated. These values were entered into SIMNRA and the theoretical simulated spectrum calculated. The simulation was then inspected in terms of the qualitative fit of the surface edges, height, thickness, and tailing. If the simulation for the tailing and gross features was unsatisfactory then the overall thickness was increased or decreased as required. When the tailing and gross features were satisfactory, then the atomic percent for the overall composition was inspected in terms of height. If this was not satisfactory then the original ratios and atomic percents were modified and the process repeated.

The first of the two starting points provided an assumed chemical stoichiometry for each sample film which was then converted into atomic percent (atom %) values for entry into SIMNRA together with the assumed thickness value, so that the theoretical simulated spectrum could be calculated. This theoretical simulated spectrum was then inspected in terms of surface edge (*i.e.* were the correct elements being accounted for?), height (composition correct?), thickness, and low energy surface tailing from the carbon peak. If the simulated spectrum did not fit well for the low energy surface

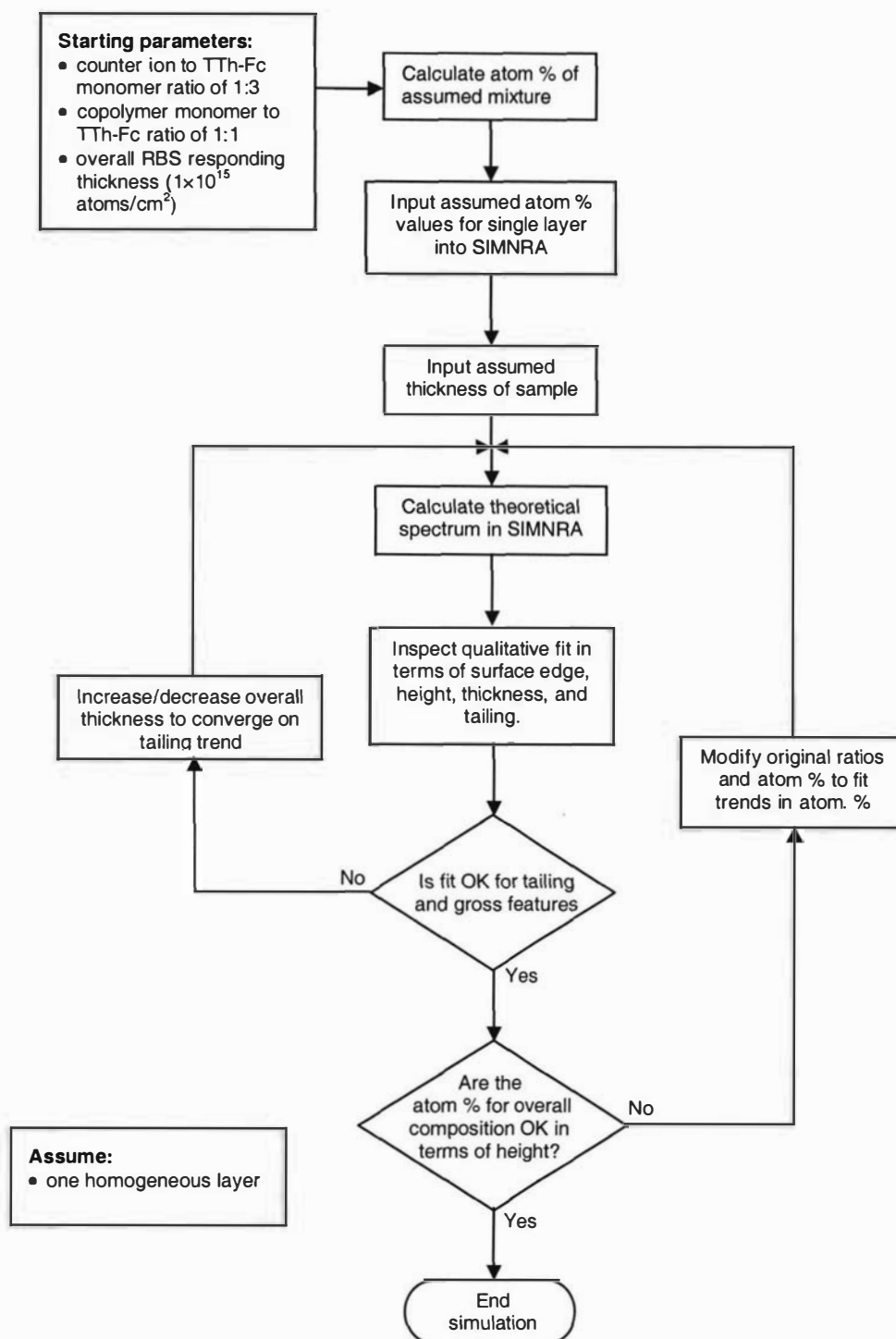
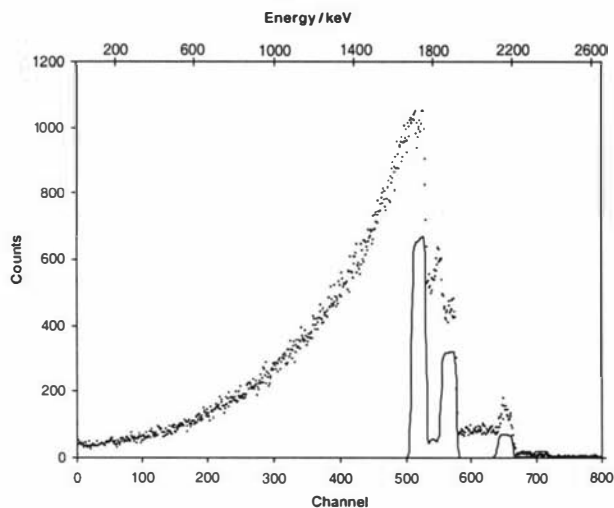


Fig. 6.1 Flow diagram of Model I for simulation of spectra using SIMNRA.

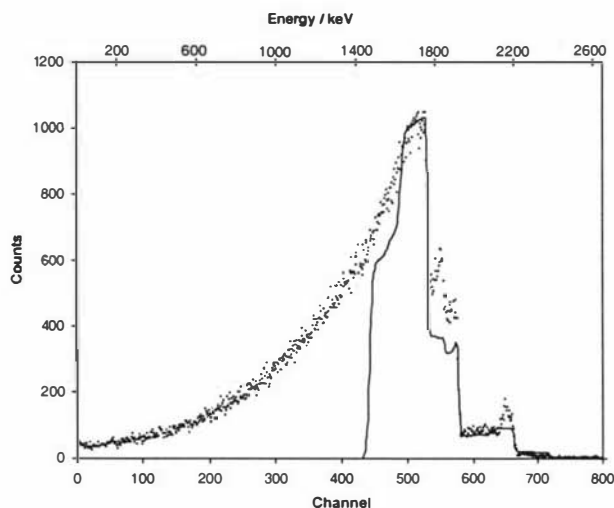
tailing and gross features of the experimental data, then the overall thickness was increased or decreased depending on which was required to converge on the observed low energy surface tailing trend. Figure 6.2 shows four RBS spectra of the solution side of a 1:10 Py / TTh-Fc copolymer, each together with different simulation spectra overlaid. Through the progression of Fig. 6.2 (a) – (d) the composition of each simulation does not vary in any way. The only parameter that was altered was that of the layer thickness. It can be seen that the thickness of Fig. 6.2 (a) (15000×10^{15} atoms/cm²) has grossly been underestimated. When the thickness was increased to 55000×10^{15} atoms/cm² (Fig. 6.2 (b)) the simulation was improved, but the low energy tailing was not fitting. Figure 6.2 (c) the thickness was once again increased (85000×10^{15} atoms/cm²). Now it can be seen that more of the low energy tailing has been simulated than in the previous two spectra, but now the fit near the maximum of the C peak (channels 450 – 550) is not as good, indicating this part is now simulated too thick. When the thickness is increased once more to 105000×10^{15} atoms/cm² (Fig. 6.2 (d)) more of the low energy tailing is being accounted for, but the fit at the C peak has become worse. This process continued to be repeated iteratively until the best fit of the observed experimental thickness of the sample had been achieved.

The next stage was to inspect the spectrum in terms of height, for the overall composition of the sample. If the heights of the elements within the experimental spectrum were not simulated correctly, then the original ratios of copolymer monomer to TTh-Fc monomer and counter ion to TTh-Fc monomer were altered and the resulting atom % from these new ratios were used to attempt to fit the spectrum features.

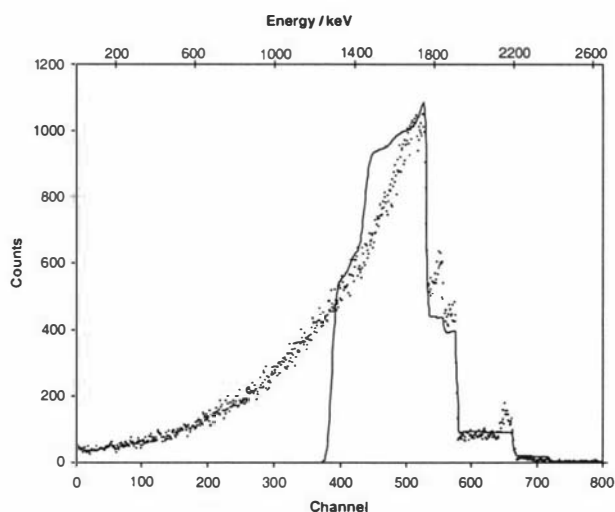
It became clear after several attempts to fit spectra that this model was unsatisfactory for the simulation of the copolymer materials. One of the major problems with this model was the assumption that the samples could be modelled using only one homogeneous compositional layer. This did not appear to be the case as parts of the simulation would fit while others didn't, and if a parameter was altered to change one part, this would affect the parts which previously fitted. Consequently, modifications were carried out to produce Model II.



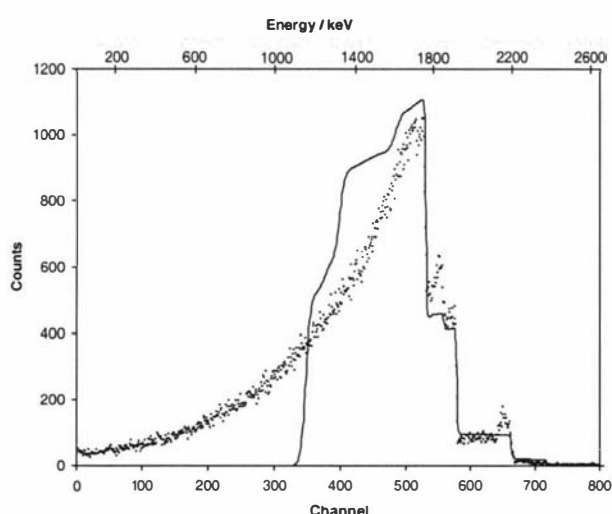
(a)



(b)



(c)



(d)

Fig. 6.2 Four spectra of the solution side of TTh-Fc / Py copolymer film electrochemically formed from a 1:10 solution of TTh-Fc / Py together with simulations of the same spectrum. The only parameter being changed between the simulations (a) – (d) is the layer thickness is increasing from 15000, 55000, 85000, and 105000×10^{-15} atoms/cm² respectively.

6.3 Model II

This second model was based on the first model and a flow diagram of Model II is given in Fig. 6.3. The ratios and atom % which resulted in the best simulations for Model I were used as a starting point for entry into Model II. The first difference in this model was removal of the assumption that the sample was chemically homogenous throughout the sample thickness. If the atom % of the overall composition was not satisfactory, the number of layers was increased by one. The thickness of this new layer was estimated by inspection of the sample spectrum and prioritising on fitting for the higher energy elements first (i.e. fitting from right to left across the spectrum) but always maintaining the overall thickness of the sample. The composition of the layer closest to the incident beam was maintained while the composition of the new layer was varied iteratively. For example, if a single layer sample simulation with a thickness of $20000 \times 10^{15} \text{ atom/cm}^2$ visually appeared to fit the experimental data right to left for the first $10000 \times 10^{15} \text{ atom/cm}^2$, but not the second $10000 \times 10^{15} \text{ atom/cm}^2$, then that one $20000 \times 10^{15} \text{ atom/cm}^2$ layer was split into two $10000 \times 10^{15} \text{ atom/cm}^2$ layers. Due to the simulation fitting for what was now the first of two layers, the composition of that first $10000 \times 10^{15} \text{ atom/cm}^2$ layer was maintained and only the composition of the second layer varied in an attempt to acquire a better fit of the observed experimental data. This process was repeated with as many layers as was required to achieve a satisfactory simulation of the copolymer spectra were obtained.

There was a second new feature introduced into the modelling procedure in Model II, that of sample 'roughness'. The SIMNRA program permitted consideration of sample roughness on RBS. The effect of the surface roughness on the shape of RBS spectra can be observed in Fig. 6.4. Here six simulated RBS spectra for a single element sample are shown with the first spectrum (a) being that for a totally smooth sample surface. As the roughness of the sample surface becomes progressively larger, ((b)-(f)) the resulting change in the RBS spectra can be observed. If the roughness variation is much smaller than the mean film thickness, only the low energy surface tail of the sample is affected, and becomes broader. With increasing roughness the broadening of the low energy tail increases until the high energy surface edge of the sample also begins to decrease. So that in spectrum (f) the height of the surface edge is significantly lower than that found for a smooth surface (a).

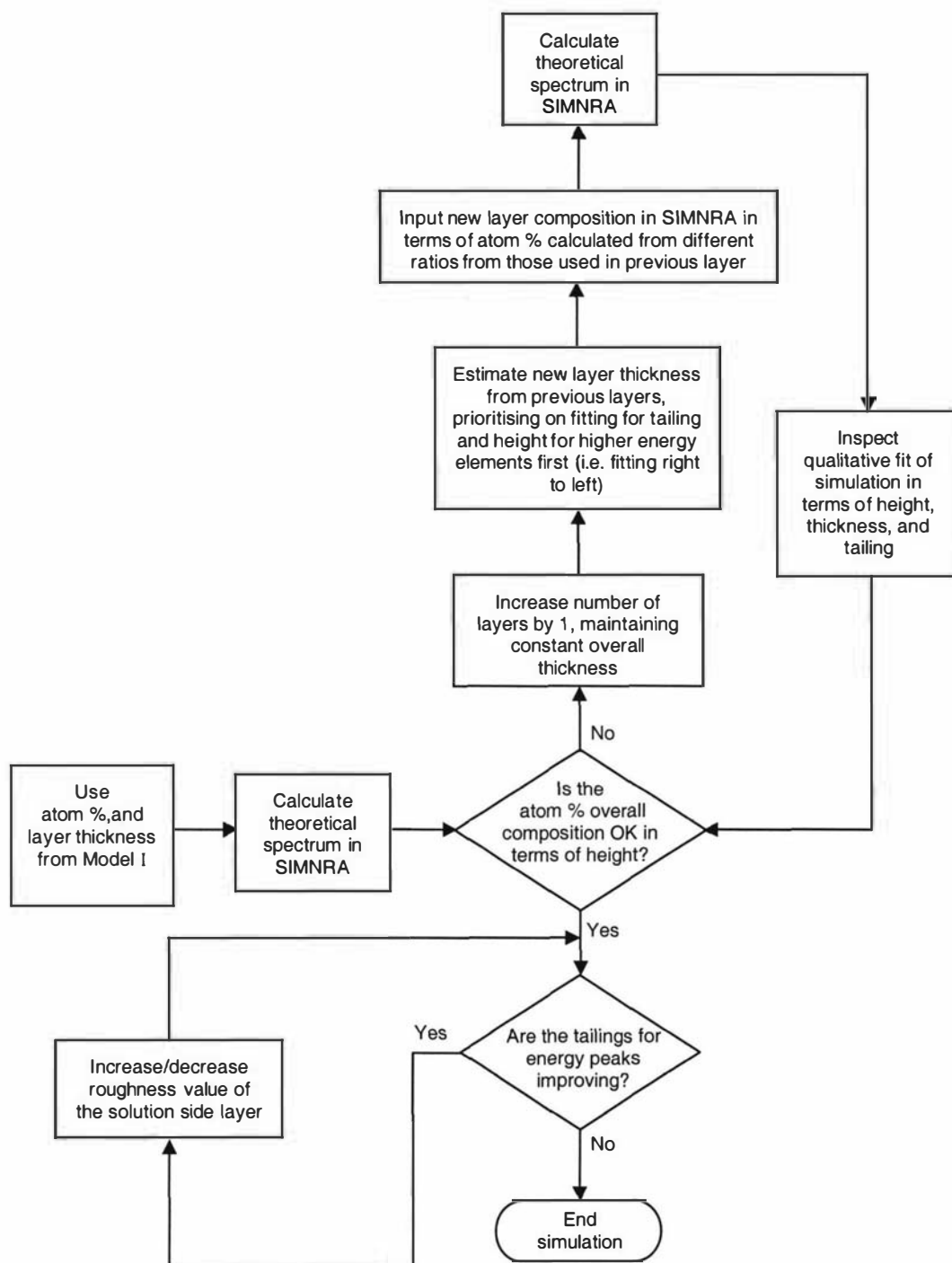


Fig. 6.3 Flow diagram of Model II for simulation of spectra using SIMNRA.

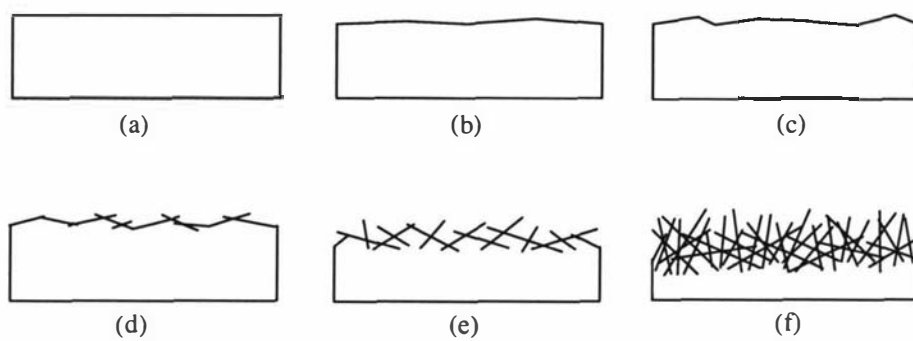
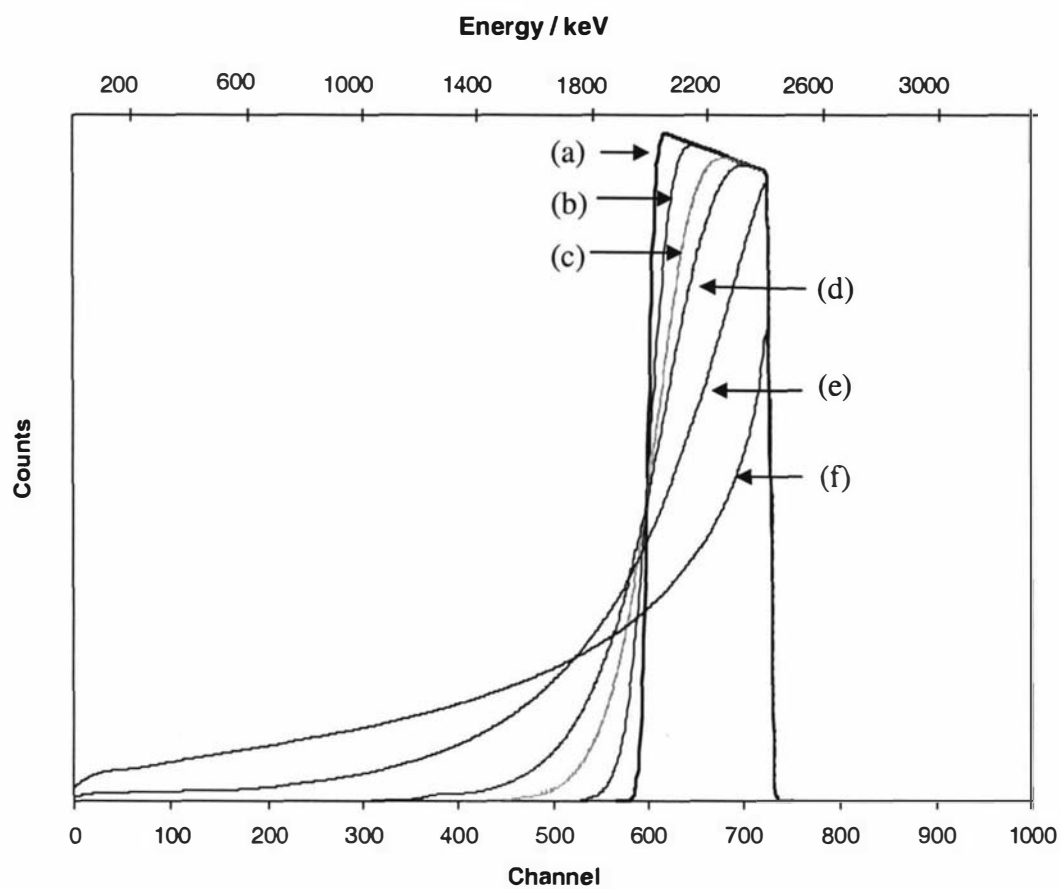


Fig 6.4 Schematic RBS spectra and corresponding surface representations of six Au samples with a 2.5 MeV proton beam, $\theta = 165^\circ$. Increasingly higher roughness factors are shown moving (a) to (f).

It was determined that this roughness was associated with the solution side of the samples through SEM investigation. Figure 6.5 shows two SEMs for the same film with Fig. 6.5 (a) being the solution side, and (b) the electrode side. It can be seen from the comparison between these two sides that the 'rough' side was that of the solution side. The same trend was seen throughout all of the samples, to varying effect. It is assumed that the 'smooth' surface of the ITO electrode imposed morphological constraints at the initial stages of film growth. The roughness was therefore associated with the rough side of the sample. Therefore, depending on which side of the samples were being analysed by RBS, the roughness factor would either be on the first layer or the last layer as shown schematically in Fig. 6.6.

Figure 6.7 demonstrates the improvement that the roughness in Model II had upon the simulations. Figure 6.7 shows the experimental spectrum of the solution side of a 1:10 TTh-Fc / Py copolymer and two simulated spectra of that experimental spectrum. The first without roughness and the second simulation has identical composition, number of layers, and thickness, but with a roughness value used.

The simulations were now significantly superior to obtainable simulations using Model I. However, they were still inadequate. Areas within the experimental spectra, although superior, could not be simulated sufficiently from the atom % which were being obtained from varying the ratios of copolymer monomer to TTh-Fc and counter ion to TTh-Fc.

6.4 Model III

Models I and II were predominately reliant on determining the optimum elemental composition by altering the counter ion to TTh-Fc and copolymer monomer to TTh-Fc ratios. This method was not working as well as had been hoped. It became apparent that the elemental composition of these TTh-Fc copolymers was not solely due to copolymer monomers, TTh-Fc monomers, and counter ions, but significantly more complex. Consequently, instead of attempting to simulate within these chemical constraints to establish the compositional atom % the elemental fit of the theoretical spectrum to the experimental data was attempted by eye. The flow diagram of the steps performed in Model III is shown in Fig. 6.8.

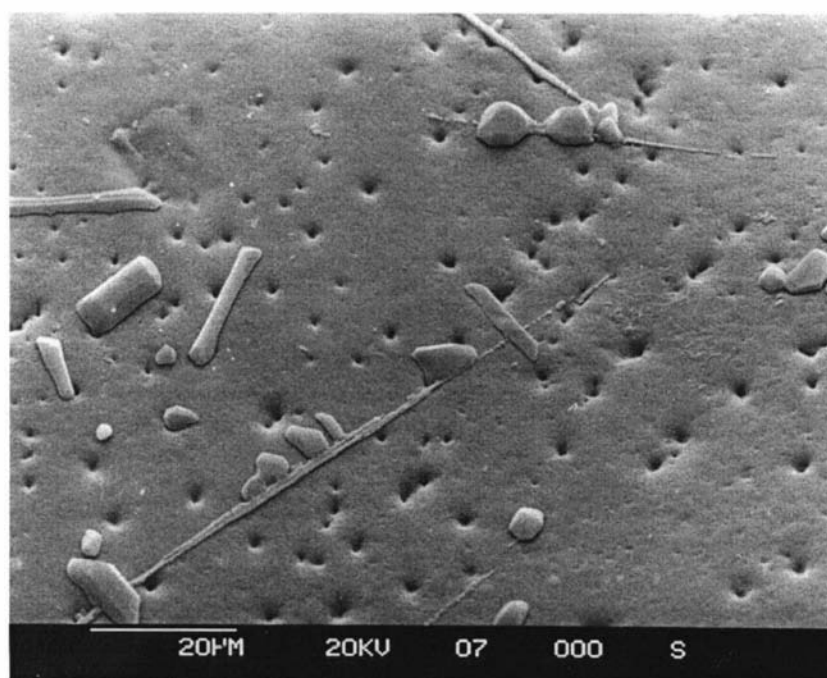
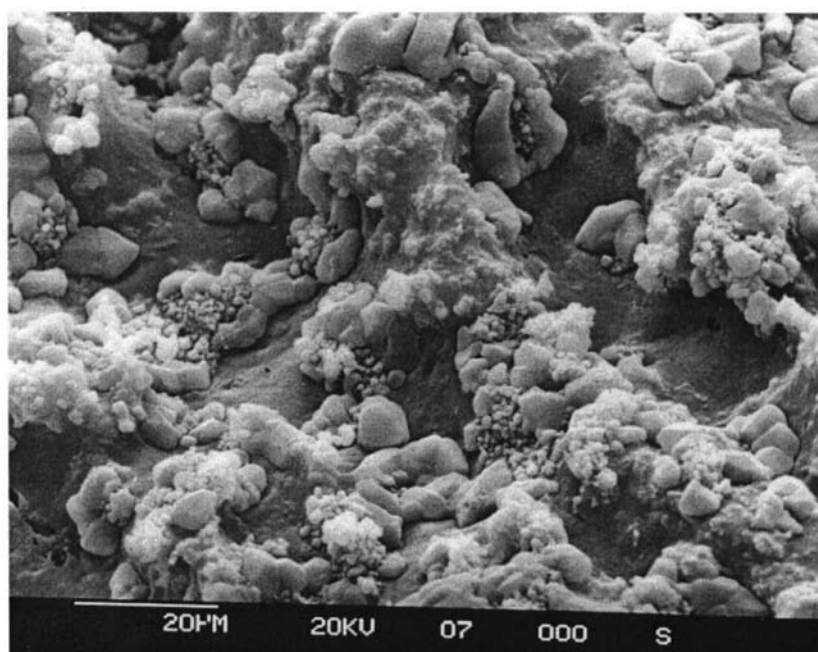


Fig. 6.5 SEM images of a 1:100 TTh-Fc / Py copolymer, scale 20 μ m, (a) solution side, (b) electrode side.

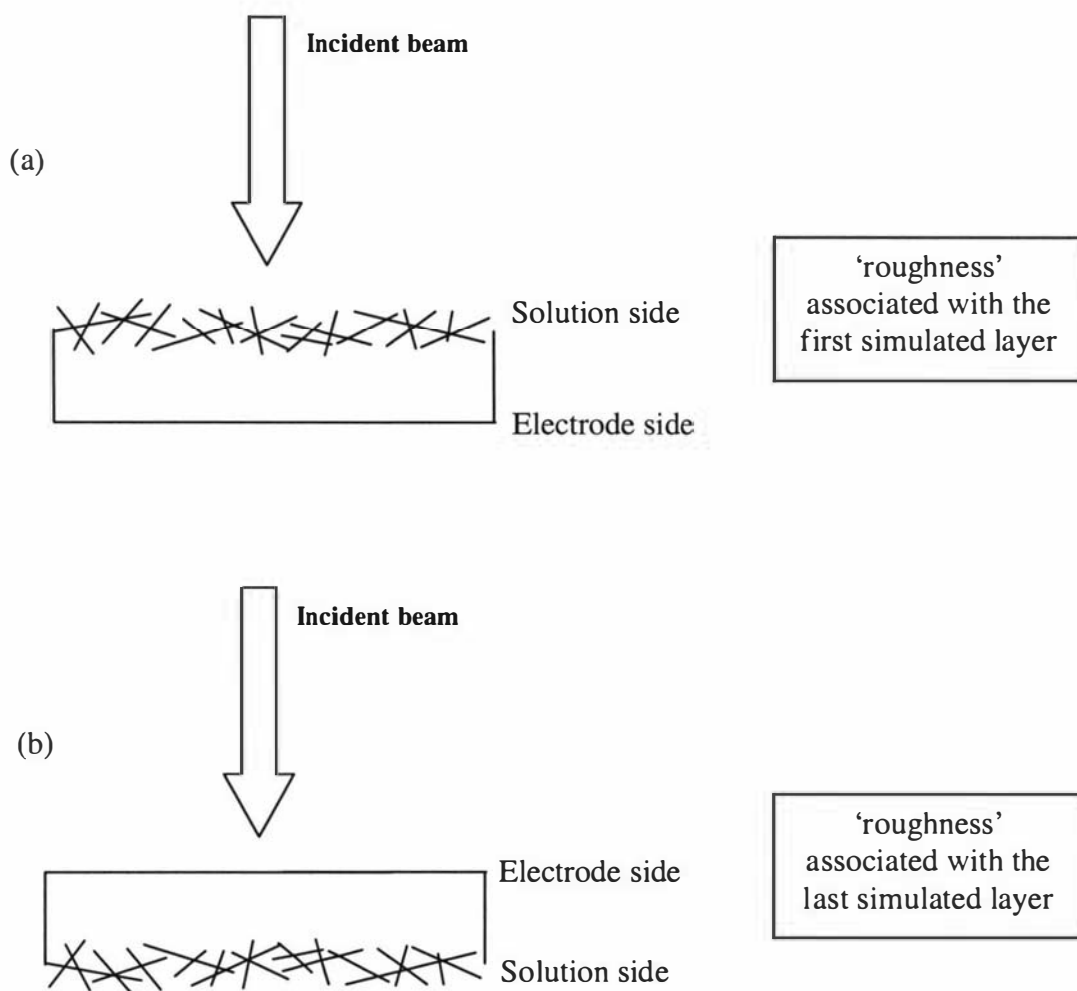


Fig. 6.6 Schematic diagrams showing the two sides of the samples and which layer in the simulation would have the roughness factor associated with it according to which side was closer the incident beam.

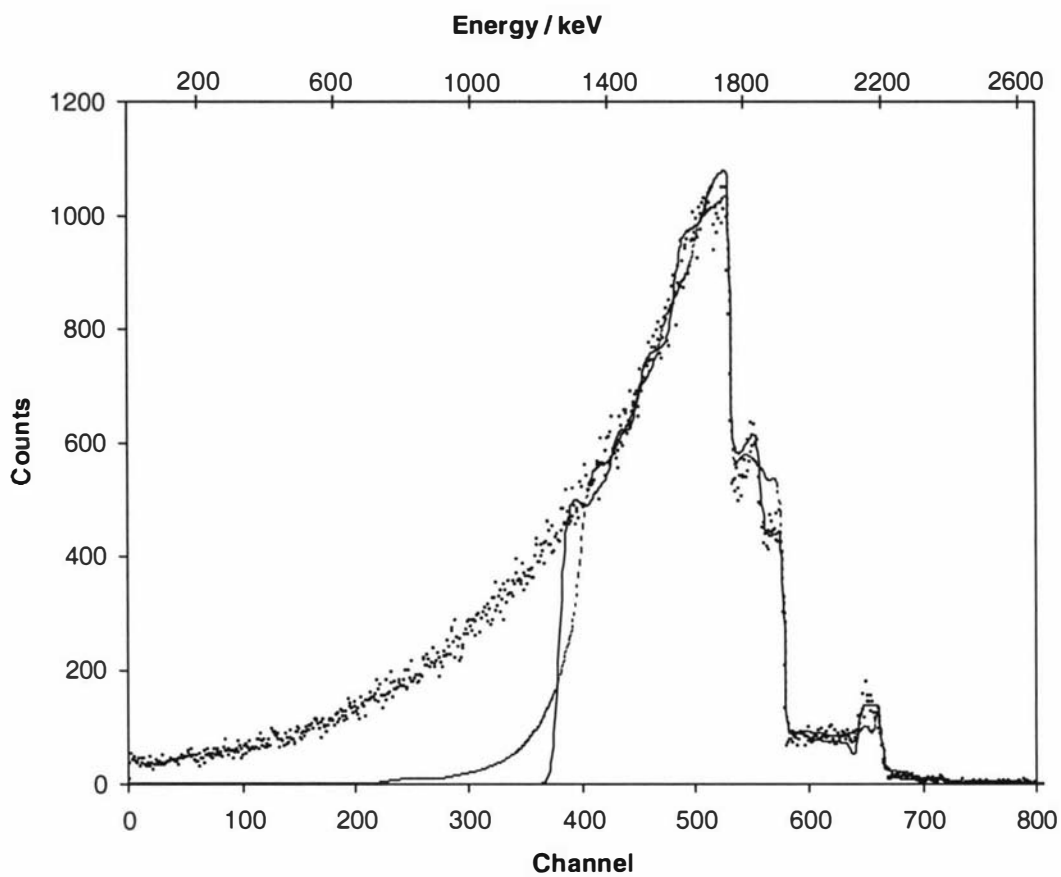


Fig. 6.7 Overlaid RBS spectra showing the experimental spectrum (●) and two simulations, the first with no roughness (—), and the second with roughness (····).

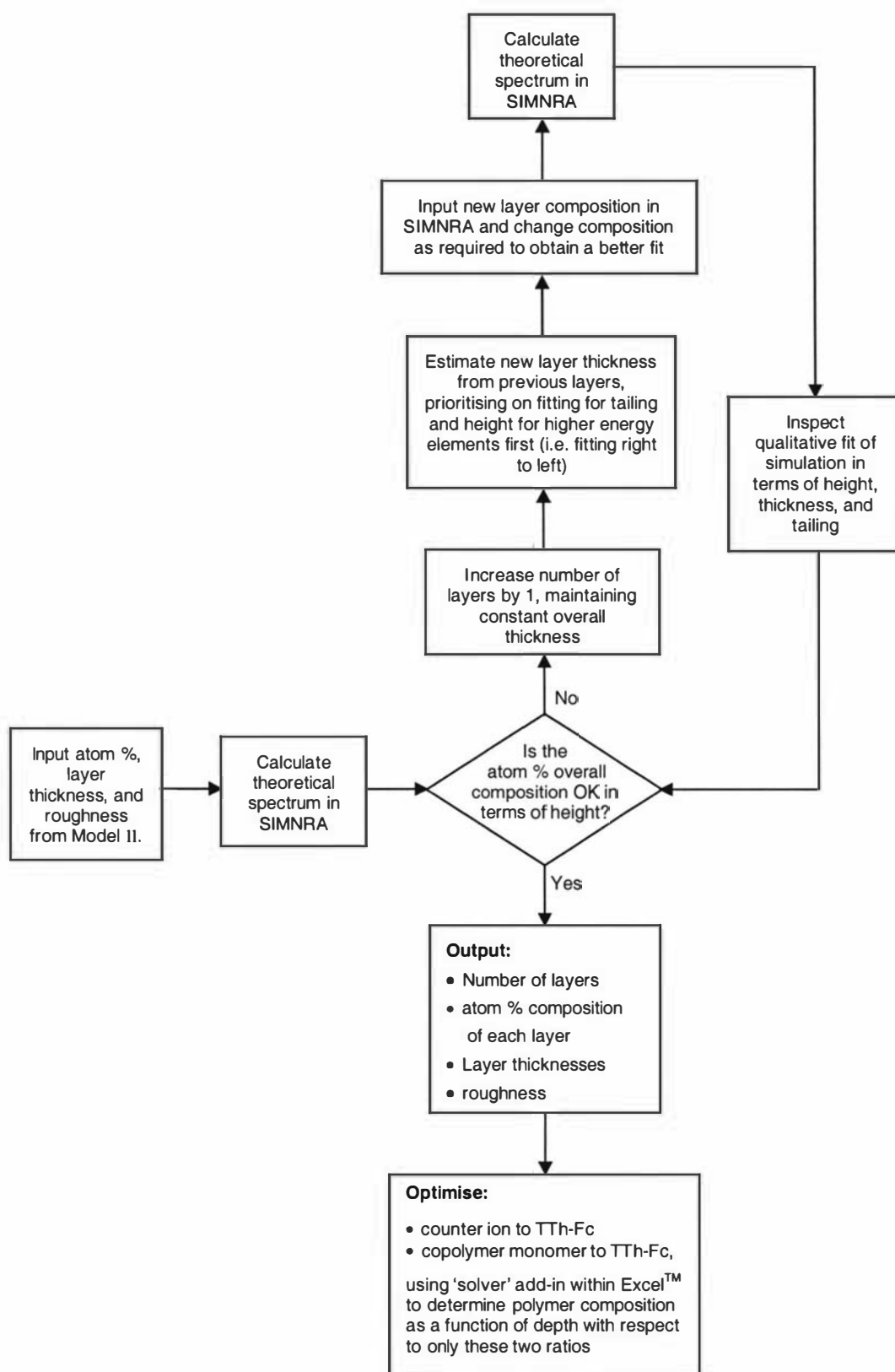


Fig. 6.8 Flow diagram of Model III for simulation of spectra using SIMNRA.

Model II was used as the base for Model III. The same procedure as that used in Model II for the thickness and roughness parameters were still performed in this model, as well as the same method to successively increase the number of layers. The major difference in this model was when it came to changing the elemental compositional atom % within the layers. In Model I and II the new atom % values were found by altering new counter ion to TTh-Fc and copolymer monomer to TTh-Fc ratios. In Model III, the individual elemental atom % values were increased or decreased according to direct observation and not constrained to chemical knowledge. For example, if it could be observed that in a layer more Fe and less O was required to improve the simulation, then these element compositions would be adjusted accordingly. Figure 6.9 shows three simulations for a bithiophene copolymer where the successive changing of elements atom % values resulted in the best fit for this sample.

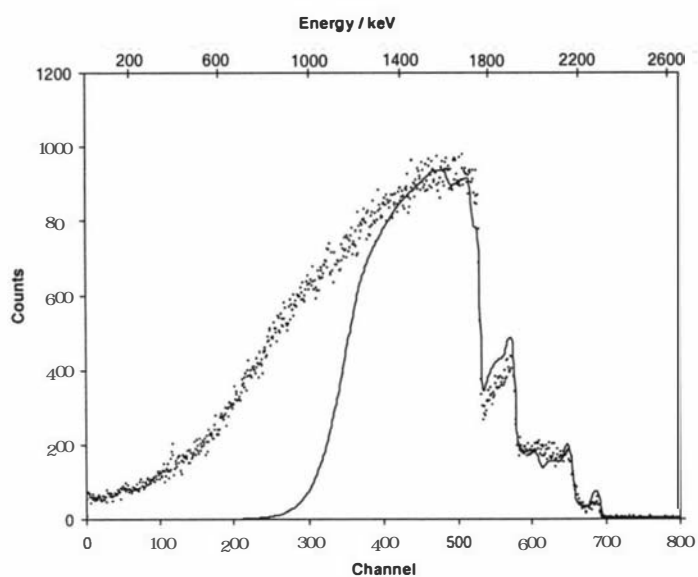
Once an experimental spectrum had been simulated as best as it could be using the known parameters one was left with a spectrum which fitted well, but an atom % for which likely made no sense from a chemical point of view.

Using the atom % values from SIMNRA (observed data) and by calculating a 'theoretical' polymer in terms of atom % of the elements using the parameters of the TTh-Fc monomer, the copolymer monomer, and the counter ion (calculated data) the square of the sum of deviations between the observed and calculated data was determined. This value was optimised to its minimum value by using the 'Solver' add-in within Microsoft ExcelTM. By performing iterative optimisations of the TTh-Fc monomer, copolymer monomer, and counter ion ratios, the closest match between the observed and calculated data was attained.

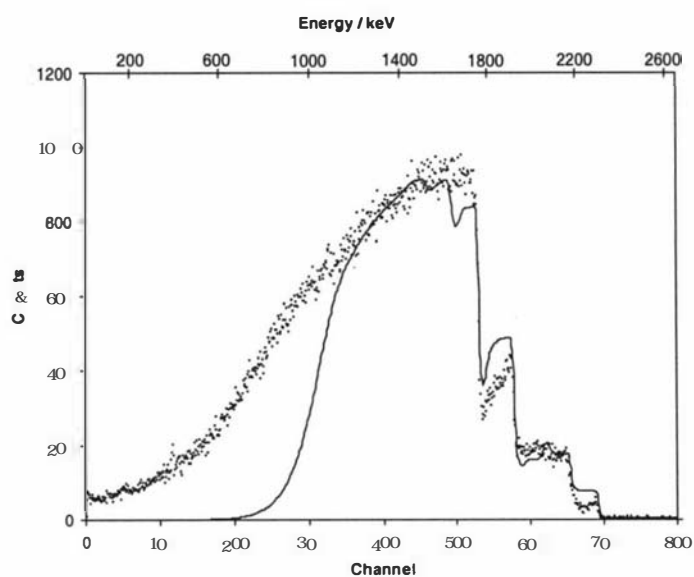
The value for the sum of deviations even though it had been optimised, however, was unsatisfactory. This led to the development of Model IV.

6.5 Model IV

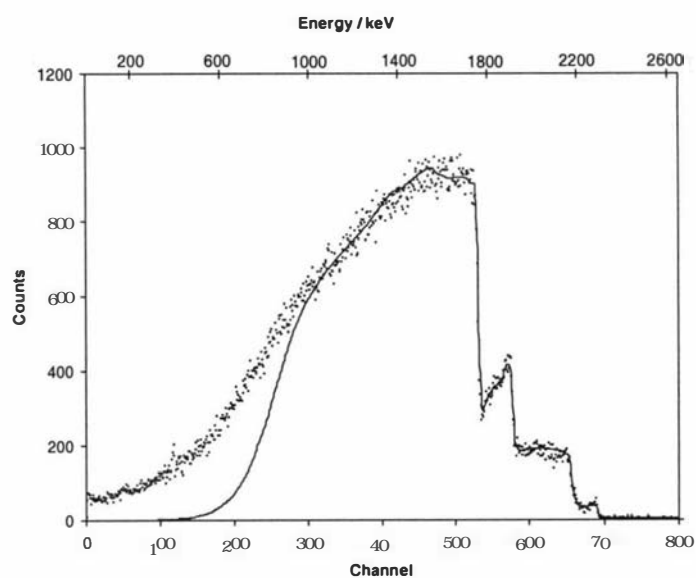
If the sample which was being analysed was of totally unknown composition, Model III would have been the point at which the analysis would have been sufficient.



(a)



(b)



(c)

Fig. 6.9 Three simulations for a bithiophene copolymer ((a), (b), and (c)), where the successive changing of elemental atom % values resulted in the best fit for this sample. Data for final result (c) from Model 4 can be found in Table A.21.

The analysis could have been stopped because one would have attained a simulation which fitted the experimental data from which sample thickness, roughness, and elemental composition information could have been obtained. That was not practical in this work. One of the advantages of dealing with soft material films, the building blocks of the films are assumed to be repeating units (eg for TTh-Fc one should be able to assume that for every 1 Fe that there would be 24 Cs and 3 Ss, that will be maintained in the monomer unit). Rather than simply optimising each element contribution individually, the method used in Model I and II in terms of species ratios were reintroduced. The 'extra' elemental content was now considered in terms of additional species that may have become incorporated into the film.

Consequently, DCM was included as a parameter since this was the solvent in which the films were electrochemically deposited, and cleaned in. Water and dioxygen from the atmosphere were also included since they may have become entrained in the film after formation. Tetrabutylammonium could also have been included within the polymer matrix during the deposition. The last parameter to be included was that of carbon, for reasons referred to in Chapters 3 and 4, where carbon may be deposited onto the surface of sample during IBA analysis.

When the optimisation was run including these new parameters the results for the sum of deviations were much better.

The results which were now being obtained by using Model IV were far superior to the previous models. The surface edge, heights of the peaks, and the low energy tailing were well simulated. Some parts of the experimental spectra could not be fitted for reasons which will be discussed in the next Chapter in relation to the relevant film.

Now better correlations between the observed and calculated compositions of the films were obtained, a further step was added into the procedure as a check of the results. Once the calculated composition had been acquired these values were taken and re-entered into SIMNRA to recalculate the simulation. If the resulting simulation from the calculated composition still fitted the experimental data, the values of the parameters were used to calculate the relevant ratios of counter ion to TTh-Fc and copolymer monomer to TTh-Fc. If the simulation did not fit the experimental data, the

elemental compositions were again increased or decreased where required, and then these new values were taken and used as new observed values, and the process repeated until a satisfactory simulated fit of the calculated composition to the experimental data was obtained.

Figure 6.10 shows a flow diagram of the steps carried out in Model IV.

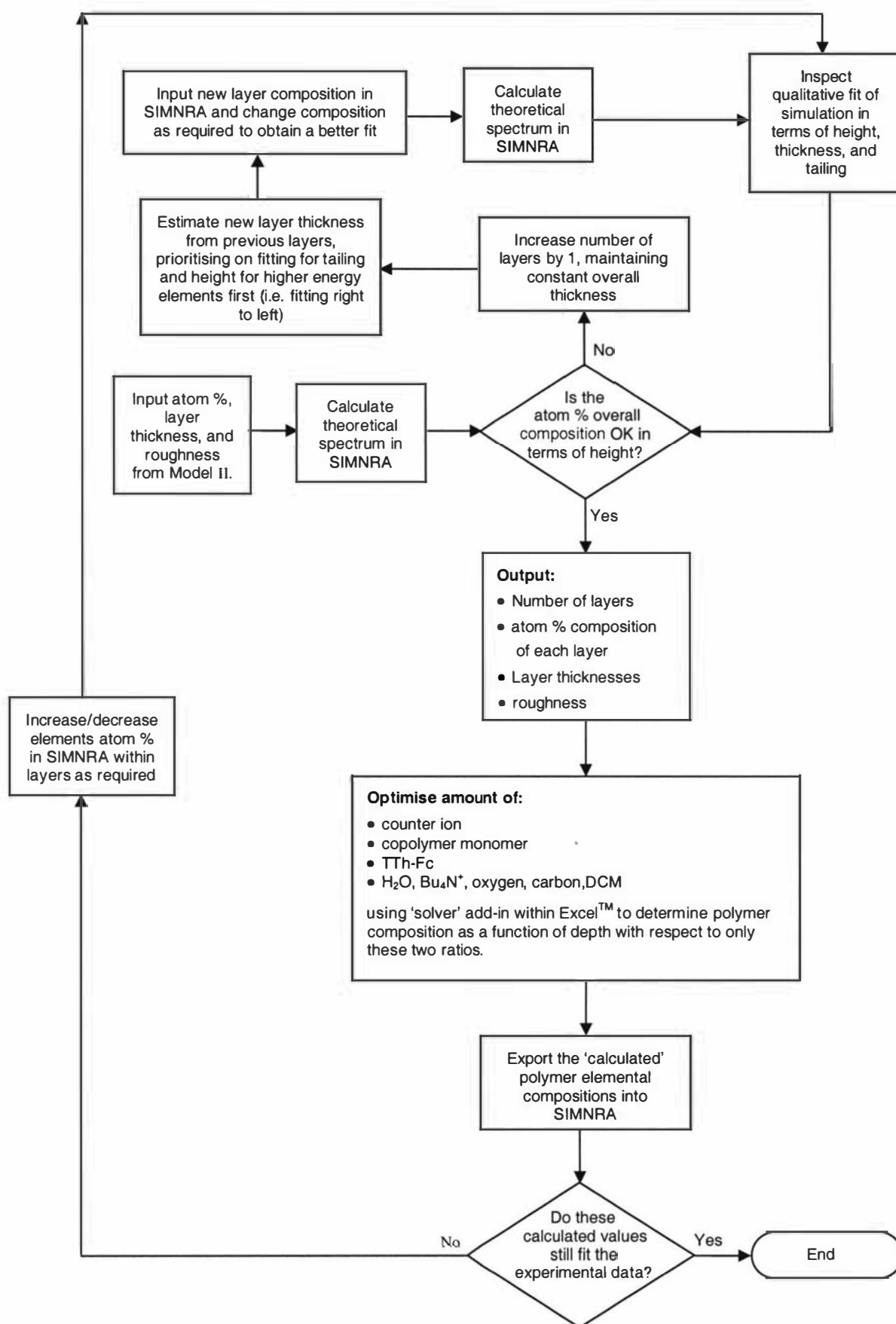


Fig. 6.10 Flow diagram of Model IV for simulation of spectra using SIMNRA.

CHAPTER 7

Analysis of TTh-Fc copolymers

7.1 Introduction

The series of TTh-Fc copolymer films in this section were prepared electrochemically (Chapter 5). The general scheme for the assumed copolymers formed in this study is given in Scheme 5.1, and is reproduced here for convenience. The analysis and discussion of the RBS spectra obtained for a series of TTh-Fc copolymer films, together with their SEM images, and the results from the calculations carried out from the simulation data of each of the RBS spectra will follow in this chapter. Due to the numerous figures and tables accompanying the discussion of the copolymer films (Sections 7.7.1 – 7.7.5), these appear together at the end of the chapter (pgs. 189-260). A summary of the significant findings preceding these sections is in Section 7.6.

It is not the aim of this chapter to provide a detailed chemical interpretation of the specific TTh-Fc copolymer film results obtained, but to display the scope of the RBS technique in the analysis of complex organic materials.

7.2 Classification of spectra types

Three broad types of spectra were identifiable upon examination of the experimental RBS spectra obtained from these copolymer samples. The variations between these three types of spectra were observed at the low energy end (*ca.* channel 0-500) of the spectra and were predominantly associated with the low energy tails of the C peaks.

Operational definitions for each of these three types of spectra follow here: 'Type 1' spectra (Fig. 7.1) are the least complex examples of the spectra observed throughout this section. No low energy tail extending from the C peak is observed as a result of the proton beam penetrating through the total thickness of the sample. Figure 7.2 shows an example spectrum of the second type, 'Type 2'. The difference between Type 1 and 2 is the presence of a low energy tail in the Type 2 spectrum. In a Type 1

spectrum on the left hand side the decrease to zero counts occurs over only a few channels and there is no significant low energy tail. In contrast, for Type 2 spectra the low energy tail has a relatively sharper concave decrease from the maximum backscattering intensity, tending to zero counts at low backscattering energies. This indicates that total thickness penetration also occurs here. 'Type 3' spectra (Fig. 7.3) are similar to those for Type 2 spectra, however the tailing does not exhibit a sharp concave decrease and significant counts are observed at channel zero. Instead a decline in RBS counts is observed and the samples are thus not subjected to total penetration by the proton beam.

Although the shapes of Type 2 and 3 spectra differ, the reason for their shape varying from that of Type 1 spectra, are thought to be similar. Experimental spectra together with schematic diagrams of the assumed sample surface are shown in Fig. 7.4 - 7.6 to assist with an explanation for the variety of RBS spectral responses observed for these copolymer films.

Figure 7.4 shows the experimental RBS spectrum for a TTh-Fc / Bridging TTh copolymer (Type 1) and a schematic representation of the sample surface. The slight deviation from what might be anticipated for a thin, smooth, sample is due to surface roughness (as shown schematically in Fig. 7.4 (a)). The degree of this roughness can be accounted for by SIMNRA.

In cases where Type 2 and 3 spectra were observed, it was established that the SIMNRA surface roughness factor alone could not be used to simulate the low energy tails. In these cases it is proposed that parts of the analysed area of the sample are substantially thicker than in other places.

Figure 7.5 shows the experimental RBS spectrum for a TTh-Fc / Py copolymer (Type 2). The simulation of this spectrum could not be manipulated to fit all of the experimental data, particularly so for the low energy tail of C. In Fig. 7.5, areas of the experimental RBS spectrum have been shaded (Fig. 7.5 (b)), as have corresponding parts of the schematic structural diagram (Fig. 7.5 (a)), to assist with the interpretation described below. It can be seen from the schematic diagram that parts of the analysed area are thicker than the majority of the sample. The extent of these thicker parts of

the sample is too great to be totally accounted for by the surface roughness factor in SIMNRA alone. The RBS analysis can not distinguish between a certain depth x μm into the sample from the top of a column or from the main sample surface (indicated by the different shading in Fig. 7.5 (a) and (b)). Most of the RBS spectrum (channel > 490) is due to the major sample depth (lightest shading). Some parts of the sample are thicker (intermediate shading). These give rise to the response observed from *ca.* channel 410-490. Even less of the sample has an even greater thickness (darkest shading) which gives rise to a small RBS response at low energies due to attenuation (*ca.* channels 300-410). There are contributions from elements with greater mass than carbon (the spectrum to the RHS of the carbon surface edge, *ca.* channel 540) but these are not clearly discernable due to their lower concentrations.

A schematic of the sample surface of one of the Type 3 TTh-Fc / bithiophene copolymers together with the accompanying experimental RBS spectrum are shown in Fig. 7.6 (a) and (b) respectively. The shading, again, is a representation for those parts of the RBS spectrum that arise from each part of the sample. In Type 3 RBS spectra it is interpreted that much more of the overall sample is thicker than for Type 2 spectra, despite both Type 2 and 3 spectra arising for the same reasons. The number of counts being recorded in channels lower than *ca.* 400 is much greater in the case of Type 3 spectra than are observed in the Type 2 spectra.

The variation of sample thickness across the analysed area (typically 1.5 mm diameter beam spot) gives rise to the low energy tailing. The surface roughness interpretation routines in SIMNRA do not deal adequately with the thickness variation deduced to be present for a number of the copolymer samples. In particular, this roughness can only be associated with a single simulation layer. Because of these factors, this leads to the inability to fit the low energy tail for some experimental spectra.

7.3 Roughness Factors

The roughness factors, f_r , used for this work are operationally defined by Eq. 7.1.

$$f_r = \frac{\text{total thickness} - \text{roughness value}}{\text{total thickness}} \quad 7.1$$

This value defines the ‘smoothness’ of the surface. The closer the roughness factor value is to 1, the smoother is the sample.

Scanning electron microscope (SEM) images of the TTh-Fc copolymer films show that there are significant morphological differences between the two sides of each sample. The ITO glass substrates upon which these copolymer films were deposited are relatively smooth, and consequently, the electrode sides of the copolymer films are smooth also. In contrast, the solution sides of the copolymer films are significantly rougher in many films. This is thought to be due to the kinetics and mechanisms of growth individual to each copolymer. The SIMNRA program is limited to evaluating roughness for a single layer of each sample and therefore the layer which requires the roughness value has been selected as the ‘solution side’ layer. If the solution side of the sample is closest to the incident ion beam, then the roughness value is associated with the first simulated layer. Conversely, if the ‘electrode side’ of the sample is closest to the incident ion beam, then the roughness value is associated with the last simulated layer. Schematic diagrams of each of these situations are provided in Fig. 7.7.

7.4 Other parameters used in RBS simulation

The two copolymer monomers and the counter ion were the only entities were considered during the model development for determination of the film composition in the previous chapter (Section 6.4). It was soon established during analysis of these series of films, however, that this rigid approach did not afford adequate spectra fitting in many cases and inclusion of additional species in the film were considered. The species DCM, H_2O , $\text{N}(\text{nBu})_4^+$, oxygen, and carbon were considered for the following reasons. DCM was the solvent for the TTh-Fc monomer. It is possible that DCM could have become incorporated into the copolymer matrix during deposition. Oxygen and water were considered as they may have been adsorbed into the copolymer matrix during storage. The counter ion anion used throughout this section of work was ClO_4^- , but the cation from the counter ion, $\text{N}(\text{nBu})_4^+$, would have also been present in the original co-monomer solution. During the post-deposition CV cycling there exists a possibility that in the film reduction process that the cation $\text{N}(\text{nBu})_4^+$ moved into the film instead of anion ejection. The formation of elemental

carbon on the film was discussed in Section 3.4.1. All, or some of these five species, together with the relevant copolymer monomer, TTh-Fc, and ClO_4^- , were used to optimise the calculated composition for each film. As an example, Table 7.1 lists the parameters used to calculate the elemental composition required for use in SIMNRA for the solution side of the TTh-Fc / Bridging TTh (1:10). Here, only two of the extra five parameters were required, DCM and C. In most cases these were the only two parameters required. However, in a limited number of samples the others were also found necessary.

The parameters required and their values for each copolymer film samples are listed in Table A.11 in the Appendix.

7.5 Ion beam durability

One copolymer film from each group of copolymers was used to establish durability in the ion beam. Only one ratio film was tested since it was assumed that variation of ratios of the monomers within the films would not significantly alter the film durability. Using a 2.5 MeV proton beam with a beam current of 4 nA, and a 1.5 mm beam diameter, 10 measurements of 1 μC each were performed on each sample. Figure 7.8 shows the plot of RBS counts vs accumulated charge for the TTh-Fc / Py (1:20) copolymer film. It can be seen from Fig. 7.8 that no significant degradation in RBS response of this sample is observed throughout the experiment. This was also the case for all other copolymer samples tested.

7.6 Overview of Significant Features in RBS Data

The majority of this chapter is concerned with the description of each of the copolymer types and the observations and trends associated with each of them. In contrast to the earlier chapters in this thesis, this summary of conclusions is presented in this chapter before the detailed description. This structure is designed to assist the reader in dealing with the necessarily repetitive nature of the description for each copolymer film type.

The first general feature is that all of the RBS spectra obtained from these copolymer films can be identified as Type 1, 2, or 3 spectra (as operationally defined in

Section 7.2). In the following section (Section 7.7) each of the RBS spectra which were successfully simulated are shown and discussed. However, in some cases it was not possible to adequately simulate some of the experimental RBS spectra, and therefore no results were determined for these copolymer samples (e.g. as in the case for the solution side of the 1:10 TTh-Fc / Py copolymer film (i.e. prepared from 1 mM: 10 mM parent solution, as described in Section 5.2)). The experimental RBS spectra, without any simulations, of un-simulated films are provided in the Appendix (Fig. A.1 – A.3) together with Table A.12 which provides a list of the ‘Type’ of each of these spectra for comparison. That not all of the copolymer films could be adequately simulated is a major limitation of the RBS technique as applied to organic films. The question of why some experimental data can not be simulated while others can is beyond the scope of this study and should be the focus of further study.

A second feature observed throughout the IBA analysis of these copolymer films concerns the operationally defined roughness factor (Section 7.3). To a greater or lesser degree each of the films required a roughness factor value. The SEM images which accompany each of the copolymer samples provide visual evidence for the degree of roughness present in each sample that must be accounted for in the analysis of each RBS spectra. In many of the SEM images coral-like growth, of varying degree, was observed on the solution side of the films (e.g. 1:10 TTh-Fc / Py film). For example, the solution side of the 2:5 TTh-Fc / TTh-Por-TTh film (Fig. 7.63) has a greater degree of coral-like growth compared to the 2:1 TTh-Fc / TTh-Por-TTh film (Fig. 7.57). It was found that when coral-like growth was present, the films had a lower roughness factors than for those not exhibiting coral-like growth (i.e. smooth in terms of Eq. 7.1) (e.g. roughness factor for the 2:5 TTh-Fc / TTh-Por-TTh film is 0.56 compared to that of the 2:1 TTh-Fc / TTh-Por-TTh film which is 0.76). Films such as the bithiophene copolymers did not have coral-like growth but instead overlapping hemispherical growth to varying degrees. When this type of growth was observed the roughness factor values were much higher, reflecting smoother surfaces. Since in each case the SEM images support the conclusions made by examination of the experimental RBS spectra, it would appear that the RBS spectra can provide an indication of thickness uniformity and surface roughness of a sample before any simulations are carried out. However, it should be noted that if only thickness information and surface roughness information is required, then RBS is an unwieldy

technique and SEM would be used in preference. It is the opportunity to obtain low atomic number elemental depth profiling that is RBS's advantage.

In general, for all copolymer films trends could not be found between the copolymer monomer to TTh-Fc ratios and the counter ion to TTh-Fc ratios. Consider the case for the series of bithiophene copolymer films (Figs. 7.37-7.40, Section 7.7.2). The calculated values of each type of ratio here obviously follow no trend. However, in some cases trends were apparent which followed the expected chemistry. As an example, in the Bridging TTh copolymers the calculated Bridging TTh / TTh-Fc ratios followed the same trends as the parent solutions prepared for the electrochemical depositions. The observation that in general no trends could be found suggests that the overall chemical makeup of these copolymer films is predominantly dominated by electrokinetic issues and not chemical ratios of the monomers in the original parent solutions as in the case of the TTh-Fc / Bridging TTh films. However, because such trends were not observed for all samples, where they might be expected, this may prove to be a second major limitation of this technique.

A common feature throughout the copolymer films was that, in all cases, the solution sides were rougher than the electrode sides. In addition, it was often seen in SEM images, predominantly in the case for Py and EDOT copolymer films (Section 7.7.1 and 7.7.3), that on the electrode side of the films, a 'folding' of the surface was also observed. The films were easily removed from the working electrode surface, and these 'folds' developed as the films dried in open air after washing with solvent. The SEM and IBA samples were cut from the same film and therefore this feature is common to both techniques. This folding might be related to the observation that the electrode sides never had reversed composition to that of the solution sides as might be expected in cases where full film penetration was achieved. If the folding was layered there would be differences in the calculated composition from an area where this 'folding' had not occurred. However, in a case where total film penetration was achieved in a sample it would expect the compositional layers arising from the RBS analysis of the solution and electrode sides to be **identical** but **reversed** in layer order. For example, if the ratio of copolymer to TTh-Fc calculated increased from 2 to 10 over a total film thickness of 10 μm from the solution side of the film, examining the

same film from the other side (the electrode side) over that total film thickness of 10 μm then the copolymer monomer to TTh-Fc ratio would be expected to decrease from 10 to 2. This was not the case in **any** of the films, regardless of whether total RBS film penetration had taken place or not. This observation has not been addressed in any detail in the present work and is worthy a separate study in itself. However, it does highlight a significant limitation of the RBS analysis of organic materials and is of great concern.

Another important conclusion which can be drawn from this section of work is that there is a significant limitation of this technique if and when dealing with organic samples of unknown composition. It was established here that the RBS analysis without any constraints could, in the absence of a knowledge of polymer components, result in a number of different compositional solutions to solving a simulation. During the early stages of the model development, a spectrum of one of the TTh-Fc / Py films was sent to Matej Mayer at the Max-Planck Institut für Plasmaphysik (software developer for SIMNRA). In absence of any knowledge of film composition this researcher solved the spectrum. The resulting near perfect fit to the experimental data is shown in Fig. 7.9. Although the experimental data is very well simulated, the composition does not make chemical sense in terms of the known elemental ratios for the copolymer monomers and counter ions. In this TTh-Fc / Py copolymer example, the only source of iron and sulfur is from the TTh-Fc monomer and that there should also be a fixed 1:3 iron to sulfur ratio. Similarly, there should be a 1:4 Cl to O from the perchlorate counter ions ratio (in absence of any excess Cl or O). This was not the case in the composition of the simulation; here there was more Fe than S, and more Cl than O. Further more this analysis did not include N as a component. Since this sample was a TTh-Fc / Py copolymer, N must be present in pyrrole monomers. By not considering this element in this unconstrained analysis these results must be meaningless. Despite this the simulation fits the experimental data perfectly and is therefore of concern.

A further problem which may be encountered when dealing with a totally unknown sample is when two elements are present which have similar surface edge energies. In this work, a prime example of this is Cl and S. One peak in each spectrum is due to

the combined response from Cl and S. If there were no internal reference ratios from known building blocks (i.e. monomers) for these films, the identical experimental spectra could have simulations incorporating Cl:S ratios of 8:2, or 1:1, or 2:8, or any other combination of these two elements, each giving the same overall response, but with differing film compositions. If working with a totally unknown organic sample, it would be impossible to uniquely identify the real sample matrix. This is a severe limitation for the technique suggesting that it cannot be a general analytical technique for organic materials in the way that combustion elemental analysis is. However, in those cases where adequate and unambiguous interpretation is possible, RBS offers the possibility of providing depth profiling of low atomic number elements.

Another limitation is that some of the SEM images show mats of rod-like crystalline / fibrous structures on the electrode side surface which appear not to be copolymer film. If this material is exogenous its elemental composition will influence the first layer of the electrode side, at least, and also influence the roughness factors. Candidates for this material include electrolyte, short chain oligomers of TTh-Fc, copolymer monomer, or TTh-Fc copolymer. The possibility that it is electrolyte, tetrabutylammonium perchlorate, is mitigated by washing these films in solvent, in which this electrolyte is soluble. However, if during copolymer film formation the electrolyte is (as tetrabutylammonium and perchlorate ion pairs) is entrained in the film, then this may elute during the washing phase and deposit on the outer face. However, if this was the case one would expect this material to be found on both sides of the film, not just the electrode side. Attempts to identify this material using EDAX elemental analysis failed to yield meaningful results due to the sparse coating of this exogenous material. Consequently, the handling of this material remains an unresolved issue of this study but it is interpreted as being confined to the outer most solution side layer (or first electrode side layer).

One additional common feature throughout this section is found in the plots of the copolymer monomer to TTh-Fc, and counter ion to TTh-Fc ratios. In these plots, at the end of each simulated layer there is a new ratio calculated. These ratios increase, decrease, or remain the same. This is not a realistic representation of what would be happening in the sample material itself. In the real sample there would be a more gradual change in these ratios. However, from the point of simulating this data, to

represent gradual changes from one ratio to another would require a number of thin simulated layers in the changing areas. This, from a simulating point of view, is not practical. So the simulation process has a limitation where if something is changing over a small depth, it is not practical to insert many thin simulation layer to obtain a more realistic profile.

Despite the conclusions and the limitations detailed here, if some prior chemical knowledge (e.g. polymer building blocks) to some extent is known, meaningful results may be obtained using this technique. The greatest advantage of this technique is the possibility of obtaining low atomic number elemental composition information with depth into samples. However, more investigation into concerns which have been raised in this work is required, before this technique could be used widely for the characterisation of soft organic materials, such as conducting polymers.

7.7 TTh-Fc copolymers

This section details the observations and interpretation for each copolymer by copolymer monomer type. Further supporting data for the following sections are provided in the Appendix (Tables A.13-A.47) (simulation data).

7.7.1 *Pyrrole copolymers*

Four TTh-Fc / Py copolymer films were electrochemically prepared from solutions with TTh-Fc / Py monomer concentration ratios of 1:10, 1:20, 1:50, and 1:100. Both the solution side and electrode side of each TTh-Fc / Py film was analysed by RBS. The RBS spectrum for the 1:10, solution side, TTh-Fc / Py film could not be simulated even with the addition of other species. Therefore no information for this sample is reported, however, the experimental RBS spectrum is provided in the Appendix (Fig. A.1).

The experimental RBS spectra and the simulations for each sample are provided in Figs. 7.10 – 7.16. All of the TTh-Fc / Py RBS spectra are Type 2 spectra, except for that of the electrode side of the 1:20 film (Fig. 7.11) which is Type 3. Of the seven spectra, only the electrode side of the 1:100 film (Fig. 7.16) could be simulated successfully. For all of the other film samples the major features of the spectra were fitted but the low energy tail of the C peak could not.

If Figs. 7.10 – 7.16 are examined in terms of the amount of the low energy tail which has not been simulated, and if this tail is due to parts of the sample being thicker than the rest of the sample, an estimation of the extent of variation of film thickness across the sample can be made. Most of the sample is totally accounted for by the simulation, but parts of the sample are thicker and are not adequately simulated, as shown in Figs. 7.10-7.11 and 7.13-7.15. Figure 7.12, when compared to the RBS spectra shown in Figs. 7.10-7.11, and 7.13-7.15. , appears to have significantly thicker areas of un-simulated copolymer film. In contrast to Fig. 7.12, Fig. 7.16 has been simulated almost entirely indicating that the surface on which the ion beam spot was focused was of relatively uniform thickness.

A further feature to note when comparing these TTh-Fc / Py RBS spectra is that the solution side and the electrode side differ even though they are from the same sample film. Assuming again that the low energy tail is related to the uniformity of the sample thickness, this observation indicates that across the sampled area of the copolymer samples, the thickness varies to a significant amount.

SEM images of each side of these samples were obtained and compared with the interpretation of RBS spectra. Figure 7.17 shows SEM images of the solution side and electrode side of the 1:10 ratio TTh-Fc / Py copolymer. It can be seen from the comparison of these SEM images that the electrode side of the film is substantially smoother than that of the solution side, although the electrode side is not totally free of surface roughness. The interpretation of the RBS spectra of each side of the film indicated significant differences in the roughness of each surface. The SEM images for this sample show how this result might arise. The 2 μm scale SEM image of the solution side of this sample shows that the surface has a porous material of crystalline needle fibres, to varying heights above the bulk of the film. The precise location of the incident ion beam focus (diameter 1.5 mm) on the sample would determine the extent of the low energy tailing, and total analysed depth through the sample due to this fibrous material (as discussed in Section 7.2).

The SEM images of the 1:20 ratio TTh-Fc / Py sample are shown in Fig. 7.18. The electrode side of this sample is significantly smoother than that of the corresponding

1:10 ratio film, as is also the solution side. The two corresponding RBS spectra of this sample suggest that some areas of the sample are substantially thinner than others. The ridges evident in the 100 μm image of the solution side of this sample provide some evidence for this interpretation. The 2 μm image of the solution side of the 1:20 film shows a differing structure of the copolymer when compared to the 1:10 ratio image, the solution side of the 1:20 film showing a coral-like structure.

Figure 7.19 shows the SEM images of the 1:50 TTh-Fc / Py ratio film. The solution side again is much rougher than the electrode side, but here the electrode side also shows some decrease of roughness. The features seen on the electrode side here are similar to those found on the solution side of the 1:10 ratio sample. The 2 μm solution side SEM image has a coral-like structure similar to the 1:20 ratio sample. The roughness over both sides of this sample appears to be much more uniform than in the 1:10 and 1:20 samples. The two RBS spectra obtained for this sample are similar in thickness, as might be expected with the more uniform surface topography observed in the SEM images.

The SEM images for the 1:100 TTh-Fc / Py film are shown in Fig. 7.20. It can be seen that the surface of the electrode side is smooth but has an extensive coverage of crystalline material ranging in size from 0.2 – 4 μm . The solution side is significantly rougher than that of the electrode side with coral-like material and is consistent with the RBS spectrum (Fig. 7.15).

The simulations of all copolymer films required a varying number of ‘layers’ to achieve the optimum simulation with SIMNRA. These layers varied in composition, thickness, and roughness. Table 7.2 lists the layer thicknesses, together with the total analysed depth for each sample and roughness factors. Zero values for roughness factors in Table 7.2 indicate that the roughness value used for that simulation was the same as the total thickness analysed. These roughness factors are associated with either the first layer or the last layer depending upon which side of the film was facing the incident ion beam as indicated in the table.

Table 7.3 lists the optimised ratio of Py monomers to TTh-Fc monomer (m/n), and the number of counter ions to TTh-Fc monomer (z/n), for each layer simulated.

Figures 7.21 – 7.24 show a graphical representation of the values listed in Table 7.3. Figure 7.21 is the plot of the ratio of Py to TTh-Fc monomers for all of the solution sides of each Py copolymer. It is observed that as the ratio in the parent monomer solution from which the films were formed increases, the amount of Py detected within the films also increases. With increasing depth into the polymer, it appears that there is little change in the ratios throughout these samples. Figure 7.22 provides a plot of the counter ion to TTh-Fc ratio for the solution sides of the Py copolymers. This plot indicates that the number of counter ions required to charge-balance the copolymer films also increases with increasing Py / TTh-Fc ratios. The counter ion to TTh-Fc ratios remains constant for the 1:20 and 1:50 films throughout the depth of the film. By contrast, the number of counter ion remains constant in the 1:100 film until a depth of *ca.* 3 μm where it increases to a higher value and maintains that ratio throughout the rest of the film, indicating that the oxidation state of the copolymer is remaining constant.

Figures 7.23 and 7.24 are plots of Py / TTh-Fc and counter ion / TTh-Fc ratios as a function of depth for the electrode side of the copolymer films. The 1:10 and 1:50 films appear to have constant values throughout the film depth for both Py and counter ion values. The 1:20 film shows the same trends in both Fig. 7.21 and 7.22, where at *ca.* 4 μm into the film there is a decrease in both ratios. The plots for the 1:100 film in both figures appears to follow the same general shape, where after *ca.* 1 μm when the value increases to a depth of *ca.* 3 μm when the values decrease.

The calculated results for each set of ratios from both the solution sides and the electrode sides of the TTh-Fc / Py films are similar in all cases except in the 1:20 ratio film. In the 1:20 ratio film the calculated values for the pyrrole to terthiophene-ferrocene monomer ratios are *ca.* 10 higher for the solution side than for the electrode side. This could be due to pyrrole being preferentially deposited onto the surface of the working electrode at the beginning of the deposition in this case.

7.7.2 *Bithiophene copolymers*

RBS spectra were collected from each side of the four TTh-Fc / bithiophene films.

The experimental RBS spectra from the analysis of both the solution and electrode sides of the 1:10 TTh-Fc / bithiophene film were both Type 3 spectra (Fig. 7.25 and 7.26). The simulation fits the experimental data adequately for channel numbers above 350 for the solution side as shown in Fig. 7.25. This is also observed in Fig. 7.26 for the electrode side. The low energy tail indicates that parts of the surface are substantially thicker than other areas of the film, to such an extent that the proton beam did not totally penetrate the sample. However, the shapes of the low energy tail differ, with the tailing from the electrode side having a more gradual decline. This is indicative of the sample where the electrode side spectrum region having a greater thickness than that of the region sampled on the solution side.

SEM images of the 1:10 TTh-Fc / bithiophene sample are provided in Fig. 7.27. Here the electrode side of the sample is smooth. The solution side 100 μm -scale image shows that the surface has an extensive coverage of coral-like material of overlapping hemispherical growth. However, it is a denser, more dispersed deposit than in the TTh-Fc / Py case (Fig. 7.17). It appears from the SEM images for the solution side that areas of the surface are higher in elevation, increasing the overall thickness, consistent with the observed RBS experimental spectra.

The experimental RBS spectra for the 1:20 TTh-Fc / bithiophene film (Type 3) are provided in Figs. 7.28 and 7.29. Based upon these RBS spectra the 1:20 film appears to be thicker than the 1:10 film. Consequently, a greater extent of the low energy tail in this sample could be simulated. When the SEM images for each side of this sample were inspected it was observed that the electrode side incorporated some crystalline material on the surface. These were not observed on the electrode side of the 1:10 film. The solution side appears to be rougher than the 1:10 solution side sample from the SEM images (Fig. 7.30), which compares well with the observation from the RBS spectra that this sample was thicker than the RBS spectra for 1:10 film (Fig. 7.25). The 2 μm image of the solution side is similar to that for the 1:10 film but the morphology of the surface is not as well defined.

The RBS spectra of the solution and electrode sides of the 1:50 TTh-Fc / bithiophene film are shown in Figs. 7.31 and 7.32. Whereas the 1:10 and 1:20 film both exhibited Type 3 spectra, here Type 2 spectra are observed, with most of the experimental RBS spectra being simulated in each case, including the tailing. Even though the spectra for this sample are Type 2, there do not appear to be any great differences in the RBS spectra obtained from the solution and electrode sides. The low energy tail in these two spectra is still present, however, in this case to a much lower extent than in the 1:10 and 1:20 TTh-Fc / bithiophene samples. The SEM images from the 1:50 film are shown in Fig. 7.33. The image from the electrode side shows a substantially smooth surface with only a few crystalline deposits in the field of view. The solution side images show a surface with the same coral-like surface but these appear to be lower in height, and therefore do contribute significantly to the thickness of the film. This is also observed in the RBS spectra where the spectra are consistent with a thinner film.

The RBS spectra for the 1:100 TTh-Fc / bithiophene film are shown in Figs. 7.34 and 7.35. In this case Type 1 spectra were observed. The SEM images for the 1:100 TTh-Fc / bithiophene film are given in Fig. 7.36. The electrode side of this film shows a higher degree of roughness when compared to the other TTh-Fc / bithiophene films. The surface not only has some crystalline material scattered across it, but indentations in the surface are also observed. These indentations are thought to be due to variations in the smooth surface of the ITO glass working electrode on which these films were deposited. The solution side again appears to be uniformly covered with coral-like material growth as was observed for the 1:50 sample.

Table 7.4 lists the number of layers required to achieve the best simulation for each side of these TTh-Fc / bithiophene films. Also listed are the individual layer thicknesses, the total depth analysed for each sample, and the roughness factor associated with each simulation. The roughness factor values calculated for these samples range from 0.38-0.78. Low roughness factors correspond to high surface roughness of samples (Eq. 7.1). When comparing the roughness factor values of the TTh-Fc / bithiophene films to those of the TTh-Fc / Py films (0.00-0.25) it can be seen that the TTh-Fc / bithiophene films have a significantly smoother solution side than those of the TTh-Fc / Py films, which is consistent with SEM images. The total thickness is a measure of the total thickness that could be simulated and consequently,

does not always represent the actual film thickness, except where the entire RBS spectrum could be simulated.

The optimised ratios of the bithiophene to TTh-Fc monomers (m/n), and the number of counter ions to the TTh-Fc monomer (z/n), for each layer simulated for the measured TTh-Fc / bithiophene copolymers are listed in Table 7.5. Figures 7.37-7.40 show graphical representations of the values listed in Table 7.5.

Figure 7.37 shows the bithiophene to TTh-Fc ratios for all the solution sides of the simulated bithiophene copolymers. The intervals at which the ratios change are due to the thickness of the modelled layers from the simulations. It can be seen from this plot that the ratios calculated for the 1:10 and 1:20 samples are constant at *ca.* 1.5 throughout the measured thickness. In the case of the 1:50 and 1:100 samples, although they differ in value, the trends are the same. At depths greater than *ca.* 2 μm there is a pronounced decrease to a constant value for a depth of *ca.* 2-4 μm , the ratios then increase again and remain stable throughout the remainder of the measured depth. The trends in monomer ratios that are observed from these four samples follow that of the parent solutions from which they were electrochemically deposited. The two samples that formed from the 1:10 and 1:20 parent solutions have the lowest bithiophene to TTh-Fc ratio, with the other two samples formed from the 1:50 and 1:100 parent solutions increasing correspondingly.

Figure 7.38 provides a plot of the counter ion to TTh-Fc ratios for the solution sides of the bithiophene copolymers. The counter ion to TTh-Fc ratio for the 1:10 sample remains relatively constant throughout the measured depth. The 1:20 sample displays a steady decrease in the ratio of counter ions to TTh-Fc throughout the analysed depth, and it is also lower than that for the 1:10 sample. For the first *ca.* 1 μm into the solution side of the 1:50 TTh-Fc / bithiophene film, the counter ion to TTh-Fc ratio is constant at *ca.* 1.6. At a depth greater than *ca.* 1 μm this ratio increases to *ca.* 2.5 where it remains constant for a further *ca.* 6 μm (two simulated layers), then after a total depth of *ca.* 7 μm this ratio decreases to *ca.* 1 where it remains for the rest of the analysed depth. The 1:100 sample has a counter ion / TTh-Fc ratio of *ca.* 4 for the first *ca.* 3 μm into the sample, at greater depths the ratio increases slightly to *ca.* 4.2

where it remains relatively constant. No significant trends in these ratios are discernable for these four samples.

The bithiophene to TTh-Fc and counter ion to TTh-Fc plots are displayed in Figs. 7.39 and 7.40 for the electrode side of the bithiophene copolymers. Unlike the bithiophene to TTh-Fc ratios found for the solution sides, no significant trends in these ratios could be determined for the electrode sides. At the surface the 1:10 sample has the lowest ratio (*ca.* 0.8) but at depths greater than *ca.* 7 μm this increases substantially to *ca.* 2.2 where it remains mostly unchanged. The 1:20 sample starts out with a ratio of *ca.* 1.4. After *ca.* 2 μm this increases steadily to a ratio of *ca.* 2 over a depth of *ca.* 25 μm . However, at greater depths there is a pronounced decrease in this ratio to *ca.* 1 for the remainder of the measured depth. The bithiophene to TTh-Fc ratio for the first 3 μm of the 1:50 sample was calculated to be *ca.* 5.2. At depths greater than this the ratio decreases to *ca.* 4, and then again to *ca.* 3.8 at depths greater than *ca.* 13 μm . The 1:100 sample might have been expected to have the highest bithiophene to TTh-Fc ratio, but this appears not to be the case. For the first 3 μm the ratio is *ca.* 3 and steadily decreases to *ca.* 1.5 over the total measured depth of *ca.* 9 μm .

Figure 7.40 displays the counter ion to TTh-Fc ratios calculated from the electrode side data. Again, no trends can be established, with all ratios varying in seemingly random fashion.

The results for the solution side and electrode side differ by a significant amount for these bithiophene copolymer samples, in contrast to the results found for the Py copolymers in the previous section.

7.7.3 EDOT copolymers

RBS spectra for all TTh-Fc / EDOT copolymer films were collected. However, only the solution side and electrode side spectra for the 1:10 and 1:50 ratio films, the solution side of the 1:20 ratio film, and the electrode side of the 1:100 ratio film are shown in this section. The remaining spectra are provided in the Appendix (Fig. A.2 and A.3). Although RBS spectra for the 1:20 electrode side and 1:100 solution side

were collected, spectra could not be suitably simulated and therefore have not been displayed in this section.

The experimental RBS spectra collected for the solution and electrode sides of the 1:10 TTh-Fc / EDOT film were both Type 3 (Fig. 7.41 and 7.42 respectively). The simulation of the solution side of this sample appears to fit the experimental RBS spectrum adequately for all channels above channel 300, whereas the simulation for the electrode side spectrum only fits adequately from channels 500-580, and then from *ca.* channels 640-700. The low energy tails of each of these spectra provide an indication of the thickness of the film at the location where the RBS analysis was performed. It can be seen that the area from which the solution side spectrum was obtained was on average thicker than that where the electrode side spectrum was obtained. The areas in Fig. 7.42 where the simulation does not fit (from *ca.* channel 580-640) the experimental data may be explained in terms of these areas of increased thickness. The simulation, in this case, is based on a sample which has total thickness of *ca.* 9 μm . It can clearly be observed from the low energy tail of the carbon peak that there are parts of the sample which are thicker than this simulated thickness and which are not being accounted for. The experimental data recorded between channels 580-670 are mostly due to S and Cl in the films. Again, the experimental data has counts from the thicker parts of the sample, but the simulation only accounts for a total thickness of 9 μm . The total thickness of the simulation could be made to fit more adequately, but this would be at the expense of the rest of the simulation because, as the thickness is increased, the simulation for the higher energy elements is greatly affected.

The SEM images of this 1:10 TTh-Fc / EDOT film are provided in Fig. 7.43. The electrode side of this sample is again much smoother than the solution side, which is expected due to the smooth electrode surface on which the films were deposited. The solution side images show that the surface has an extensive and even coverage by a coral-like material. The 100 μm scale image of the solution side shows that areas are not as thick as other parts (which appear darker in colour). This is consistent with observation from the experimental RBS spectra.

Only the experimental RBS spectrum from the solution side of the TTh-Fc / EDOT film was adequately simulated and is provided in Fig. 7.44. This RBS spectrum, although Type 3, has a low energy tail which decreases significantly at low energies, indicating that not all, or even most, of the beam spot analysis area was substantially thicker than the thickness that was simulated (*ca.* 20 μm).

The SEM images for the 1:20 TTh-Fc / EDOT film are provided in Fig. 7.45. These SEM images appear to differ in form to those observed for the 1:10 film. The SEM images of the 1:10 film showed the electrode side to have a smooth, relatively unchanging topography. In comparison, the electrode side of the 1:20 TTh-Fc / EDOT film has areas where the surface is smooth, with a constant topography, but there are also areas where the surface, while still smooth, appears to be 'folded'. One possibility for the formation of these folded areas is that upon removal from the electrode surface and after drying, this film has contracted and folded in the process. The solution side for the 1:20 film is similar to that for the solution side of the 1:10 film and appears to be a coral-like surface whilst the solution side surface appears to be extensively covered with this material. This coverage does not appear to be uniform. There are areas which appear to have an increased concentration of coral-like material than other areas. Overall, the 1:20 film appears to have a more irregular surface compared to that seen for the 1:10 film.

The solution side and electrode side RBS spectra for the 1:50 TTh-Fc / EDOT film are provided in Figs. 7.46 and 7.47 respectively. Both these experimental RBS spectra are Type 3, and appear to be similar to those in Figs. 7.41 and 7.42 for the 1:10 TTh-Fc / EDOT film, with the sample thickness varying greatly between the two spots from where the RBS spectra were collected.

Figure 7.48 provides the SEM images of the solution and electrode sides of the 1:50 TTh-Fc / EDOT film. The folding feature observed on the electrode side of the 1:20 film is also observed on the electrode side of the 1:50 film, but to a much greater degree. In this case the folding is so extensive that no areas appear to be flat. Some crystals are also observed on the electrode side surface. In the case of the 1:10 and 1:20 films, the solution side appeared to be totally covered by a coral-like material of

varying heights. In the case of the 1:50 film, the 100 μm scale image of the solution side appears to also have coral-like material on the surface, but here, smooth parts of the surface can be seen between the coral-like material. There appears to be less coral-like coverage overall with this 1:50 film sample than in the 1:10 and 1:20 films.

The electrode side experimental RBS spectrum for the 1:100 TTh-Fc / EDOT film is provided in Fig. 7.49. The solution side spectrum could not be adequately simulated. The spectrum observed in Fig. 7.49 is a Type 2 spectrum. The spectrum was adequately simulated for channels above *ca.* 470. The film has been totally penetrated in this case, which means that at the ion beam spot the thickest part of this film has an overall thickness less than the thickest part of all the other TTh-Fc / EDOT copolymers film investigated. The region from channels 580-610 was not simulated well for the same reason as that for channels 580-640 in the electrode side spectrum of the 1:10 TTh-Fc / EDOT film (Fig. 7.42).

The SEM images of both sides of the 1:100 TTh-Fc / EDOT film are provided in Fig. 7.50. The surface of the electrode side of this sample appear to have some crystals, but not as many as observed in the 1:50 film sample. The electrode side of the sample also appear to be smooth, with less folding. Again, the morphology of the solution side has a coral-like material, but it appears from the 100 μm scale SEM image that this material has grown in isolated areas rather than achieving an even surface coverage. Flat areas of the surface are observed to a greater extent than for the previous 1:50 sample, and the overall height of these features do not appear to be as pronounced as for the other TTh-Fc / EDOT samples. This observation is consistent for the RBS spectrum where total film penetration was achieved. The general trend across these EDOT copolymers is that the extent of the coral-like material decreases from the 1:10 film having the greatest amount of material to the 1:100 film having the least.

The number of layers required to achieve the best simulation and those layer thicknesses, together with the total simulated thickness and roughness factors are listed in Table 7.6. The analysed depths from sample to sample vary greatly, but also the analysed depths between two points within the same sample vary greatly, as can

be seen in the RBS spectra for a series of TTh-Fc / EDOT films (Figs. 7.41-7.42, 7.44, 7.46-7.47, 7.49). The roughness factors calculated for these samples also cover a large range (0.00-0.81). The large variation in the roughness factors calculated from the TTh-Fc / EDOT film simulations indicate that areas of the solution side of these samples are significantly smoother than other areas.

The optimised ratios of the EDOT monomer to TTh-Fc monomer (m/n) and the counter ion to TTh-Fc monomers (z/n), for each layer simulated in the TTh-Fc / EDOT copolymer films are listed in Table 7.7. Figures 7.51-7.54 show the graphical representation of the values listed in Table 7.7 and display the variation of the ratios with depth into the copolymer films.

Figure 7.51 shows the relationship between the ratio of EDOT monomer to TTh-Fc monomer with depth into the solution sides from the simulations of the TTh-Fc / EDOT copolymers. It can be observed from the data that at depths greater than *ca.* 2 μm into the 1:10 film, there is a decrease in this ratio from *ca.* 4 to *ca.* 3. At a depth of *ca.* 8 μm this ratio increases to *ca.* 4 where it remains relatively constant over a depth of *ca.* 30 μm , only increasing by *ca.* 0.2. The plots for both the 1:20 and 1:50 ratio films commence with surface layer ratios of *ca.* 7. These surface layer ratios remain constant to a depth of *ca.* 12 μm and only decrease slightly over the next *ca.* 10 μm to ratios of *ca.* 6.8. The general trends observed from these three samples follow those of the parent solutions from which they were electrochemically deposited, with the 1:10 film having the lowest EDOT to TTh-Fc ratios throughout the film. That the EDOT to TTh-Fc ratios for both the 1:20 and 1:50 films are close in value, may provide an indication that a ratio of 7:1 (EDOT / TTh-Fc) may be the optimum value obtainable for this copolymer.

Figure 7.52 provides a plot of the counter ion to TTh-Fc monomer ratios for the solution sides of the EDOT copolymers. The ratios calculated for the 1:10 film appear to increase and decrease within the limits of *ca.* 1.5 and *ca.* 3.6 over a depth of close to 40 μm . In the case of the 1:20 film, the counter ion to TTh-Fc ratio at the surface is *ca.* 6.2. This ratio remains constant for *ca.* 15 μm where there is a significant decrease to a value of less than 1 for the remaining *ca.* 6 μm . The surface ratios for the 1:50 film very similar to those calculated for the 1:20 film (*ca.* 6) for the first *ca.* 7 μm . At

this depth, a decrease in the ratio to *ca.* 4 was calculated. At depths greater than *ca.* 5 μm this ratio of 4 further decreases to *ca.* 3.

The plots of EDOT monomer to TTh-Fc monomer ratios from the electrode sides of the TTh-Fc / EDOT copolymers are provided in Fig. 7.53. The surface values of these ratios for the 1:10, 1:50, and 1:100 films all range from *ca.* 6.8 – 7.0. In the case of the 1:10 film the ratio is *ca.* 6.8 for *ca.* 3 μm after which it decreases to *ca.* 2.3 where it remains constant for the remaining *ca.* 6 μm . The surface value for this ratio is much higher than that calculated for the solution side of the same sample, but does decrease to a value closer to that found for the solution side. The ratios calculated for the 1:50 films surface are very similar to those found for the solution side, but unlike those found from the solution side, after *ca.* 1.5 μm there is a decrease in the ratio to *ca.* 4.5 where it remains constant for the remainder of the simulated depth. The EDOT to TTh-Fc ratios determined for the 1:100 film are constant at the surface for *ca.* 8 μm at *ca.* 7. At depths greater than *ca.* 8 μm there is only a slight decrease to *ca.* 6.8 in the ratio for this sample. The result is very similar to that found in the case of the 1:20 and 1:50 films from the solution side.

The plots for the counter ion to TTh-Fc ratios calculated from the electrode sides of the TTh-Fc / EDOT films are provided in Fig. 7.54. The results for the 1:10 film vary from that observed from the solution side. Here the surface ratio is *ca.* 5.5, then after *ca.* 2.5 μm depth this value decreases significantly to *ca.* 0.8 where it remains constant for the remainder of the simulated depth. The results for the 1:50 film are similar to those found for the solution side, where the surface ratio is *ca.* 6.5 and after *ca.* 1.5 μm decreases to *ca.* 2.5. The 1:100 film surface ratio starts at *ca.* 6.8. After *ca.* 2 μm this decreases to 4 and then at depths greater than *ca.* 6 μm decreases again to *ca.* 3, for *ca.* 3 μm .

Two general trends are observed when comparing the calculated results for the TTh-Fc / EDOT copolymer films for the solution sides and electrode sides. The same general trend between the solution side and electrode side results for the counter ion: TTh-Fc ratios are seen. Although the decreases in the counter ion: TTh-Fc ratios occur at varying depths into the samples, they do all exhibit a substantial decrease.

When the calculated results for the EDOT / TTh-Fc ratios for the solution sides and electrode sides are compared the trends between each differ. The EDOT / TTh-Fc ratios calculated for the solution sides show either a slight decrease or increase across the simulated depth, however, only one of the three electrode side film results show a constant ratio throughout the simulated depth (1:100 TTh-Fc / EDOT film). The other two films (1:10 and 1:50 TTh-Fc / EDOT films) exhibit a substantial decrease in the EDOT / TTh-Fc ratio after only a few microns depth into the film.

7.7.4 *TTh-Por-TTh copolymers*

Due to the restrictions on the quantity of TTh-Por-TTh monomer material available, the original parent solutions from which these films were electrochemically deposited differ in concentration range to those used for the Py, bithiophene, and EDOT, TTh-Fc copolymers. The concentration ratios used for the TTh-Fc / TTh-Por-TTh copolymers were 2:1, 1:5, 2:5, and 1:1. RBS spectra from both the solution side and electrode side were collected and simulated for each of these TTh-Fc / TTh-Por-TTh copolymers.

The experimental RBS spectra together with the simulated RBS spectra of the solution and electrode sides of the 2:1 TTh-Fc / TTh-Por-TTh copolymer film are provided in Figs. 7.55 and 7.56 respectively. The solution side experimental RBS spectrum for the 2:1 film is a Type 3 spectrum, while the electrode side experimental spectrum is Type 2. The simulations of both spectra were achieved with only a small part of the solution side spectrum (Channels 0 – 150) not simulated well. In the analysis of the TTh-Fc copolymers with Py, bithiophene, and EDOT, the RBS simulations did not routinely simulate the low energy carbon tail. This low energy carbon tail has been attributed to areas of the sample having thicker areas that could not be accounted for using the roughness parameter. In the case of the solution side 2:1 TTh-Fc / TTh-Por-TTh film, the low energy tail could be simulated. Only *ca.* Channels 0-150 were not simulated. The difference between the RBS spectra of this sample and one where the low energy tail could not be simulated (e.g. 1:20 TTh-Fc / bithiophene (Fig. 7.28)) is, that instead of having a sample where only some areas are much thicker than the majority of the sample, in this case the entire sample area of the film was thick. The low energy tail from the electrode side 2:1 TTh-Fc / TTh-Por-TTh RBS spectrum (Fig. 7.56) does not extend to the low energies

to which the solution side RBS spectrum does, indicating that this area is thinner. It appears from the electrode side RBS spectrum that the area from which this spectrum has been obtained was thinner than the area from where the solution side RBS spectrum was obtained, and that this copolymer had a relatively consistent thickness across the sample area.

The SEM images obtained for this 2:1 TTh-Fc / TTh-Por-TTh film are provided in Fig. 7.57. It is observed from the SEM images of Fig. 7.57 that the electrode side of this copolymer film is substantially smooth, with no features (e.g. crystals or 'folds') present. The solution side images also show a very smooth surface compared to that observed in previous copolymers. It can be seen from the 100 μm scale SEM image that there are parts of the film which are higher than others. The surface on the solution side is more coral-like. The 'rolling' surface morphology assists with an explanation for the RBS spectra. Between the solution side and electrode side, the RBS spectra showed substantial, definite, differences in thickness, this could be explained by assuming that the solution side spectrum spot was at the highest points and that the electrode side spot was obtained at a lower point on the surface. Since the solution side does not have significant growth out of the surface, the long low energy tail was not observed on the electrode side spectrum.

The solution side and electrode side experimental RBS spectra, together with their simulations, for the 1:5 TTh-Fc / TTh-Por-TTh copolymer film are provided in Figs. 7.58 and 7.59 respectively. The solution side spectrum of the sample is Type 3 and has been adequately simulated for channel numbers greater than 300. The area which the solution side 1:5 TTh-Fc / TTh-Por-TTh RBS spectrum was obtained appears to have parts of that sample area which are thicker than the majority of the sample (indicated by the un-simulated part of the low energy tail). The electrode side RBS spectrum is Type 2. In this case the entire spectrum has been adequately simulated, including the low energy tail. This is an indication that there are no major features on this sample surface spot which are substantially greater in thickness than the majority of the sample area.

Figure 7.60 provides SEM images of the solution and electrode sides of the 1:5 TTh-Fc / TTh-Por-TTh film. From these images it can be seen that the electrode side of this film is substantially smooth, and unlike the EDOT copolymers, featureless, and relatively free of other entities such as crystalline material. The solution side appears to have a nodular 'cauliflower-like' morphology, which is evenly spread across the surface. The differences in the observed sample thickness of the experimental RBS spectra are not inconsistent with the images obtained from the SEM images.

The experimental RBS spectra obtained from the solution and electrode sides of the 2:5 TTh-Fc / TTh-Por-TTh copolymer are provided in Figs. 7.61 and 7.62 respectively. Both these two RBS spectra are Type 2 spectra and total film penetration is achieved. The solution side RBS has been simulated well across channel numbers 450-700. The simulation for channels below channel number 450 while imperfect, is adequate, indicating that the surface area from where this spectrum was obtained has a predominantly uniform thickness. The RBS spectrum obtained from the spot on the electrode side was not as well simulated as that from the solution side. The simulation for this spectrum has been adequately achieved from channel numbers 470-700, but for those channels below 470 the simulation deviates significantly from the observed experimental RBS spectrum. It appears from Fig. 7.62 that more of the surface on the solution side than the electrode side is uneven.

Figure 7.63 provides SEM images for both sides of the 2:5 TTh-Fc / TTh-Por-TTh film. Again, it is observed that the electrode side of this film is smooth and mostly free from other material. The nodular cauliflower-like growths of material is also observed. However, this does not appear to be as extensive as the 1:5 sample. Larger gaps within the material is also observed in this 2:5 sample and this could account for differing film thickness in the two experimental RBS spectra obtained from this film.

Figures 7.64 and 7.65 provide the experimental RBS spectra and simulations for the solution and electrode sides of the 1:1 TTh-Fc / TTh-Por-TTh copolymer respectively. Both RBS spectra are Type 2, and both have been adequately simulated over the total channel range (solution side – 200-700, electrode side 300-700). Although both spectra have been well simulated, a difference in the observed thickness of the film is still observed.

The SEM images displayed in Fig. 7.66 are of the solution and electrode sides of the 1:1 TTh-Fc / TTh-Por-TTh copolymer. As anticipated, the electrode side (Fig. 7.66 b) of this film is smooth and featureless. The SEM images of the solution side (Fig. 7.66 a) show that this side for 1:1 ratio film is smoother compared to the other solution side surfaces of the other TTh-Por-TTh copolymers. The morphology of this sample is closest to that of the 2:1 ratio film, but in this case the flattened coral-like growth observed is even less prevalent. The solution side for the four TTh-Fc / TTh-Por-TTh copolymers (2:1, 1:5, 2:5, and 1:1) have surface morphologies which are smooth, with an accompanying constant thickness consistent with this. When there is a greater amount of the TTh-Por-TTh monomer present in the parent solution, then the solution side surface has a more coral-like morphology with growth of more material projecting from the surface. This produces a more uneven surface which appears to have increased porosity. This observation is reflected in the experimental RBS of the materials; when the amount of the TTh-Por-TTh monomer is greater in the parent solutions, greater variations between the observed thicknesses from the RBS spectra and the calculated thicknesses from the RBS simulations.

Table 7.8 lists the number of layers required to achieve the optimum simulation of the experimental RBS spectra and the thicknesses of each of those respective layer. Also listed in Table 7.8 are roughness factor values for each simulation and the value of the total simulated thickness. The roughness factors for the TTh-Fc / TTh-Por-TTh copolymers are generally all high compared to those observed for the other copolymer film samples. The surface morphology observed in the SEM images of these films is reflected in these roughness factors.

The optimised ratios of the TTh-Por-TTh to TTh-Fc monomer (m/n), and the counter ion to TTh-Fc monomer (z/n) ratios are listed in Table 7.9 for each of the simulated layers for each TTh-Fc / TTh-Por-TTh copolymer. Figures 7.67-7.70 provide graphical representations of the values listed in Table 7.8 and displays the change in the respective ratios with depth into the copolymers.

The change in the TTh-Por-TTh to TTh-Fc monomer ratios with depth into the solution sides of the TTh-Fc / TTh-Por-TTh copolymers is shown in Fig. 7.67. The values from the 2:5, 2:1, and 1:1 ratios are relatively stable across the measured depth into the film. The 1:5 film ratios decrease by a comparatively larger amount over the

first *ca.* 5 μm of the film but then remain stable for the remaining depth. The film with the greatest amount of TTh-Por-TTh monomer present is the 1:5 ratio, followed by 2:5, then 1:1, and finally the lowest amount of TTh-Por-TTh monomer present in the 2:1 ratio solution. It was expected that the TTh-Por-TTh / TTh-Fc ratios calculated for these copolymer films would follow the same trends as their respective parent solution ratios. Even with the decrease observed in the 1:5 films ratios, it still maintains the highest TTh-Por-TTh to TTh-Fc ratios. The next highest ratios are calculated for the 2:5 film, which was also expected. Although the values of the ratios in the two remaining films are small, what was calculated was not expected. The 2:1 film shows higher TTh-Por-TTh to TTh-Fc monomer ratios with depth into the film than the 1:1 film. This was unexpected since the amount of TTh-Fc in the 2:1 parent solution was twice that of the 1:1 parent solution.

Figure 7.68 provides the counter ion to TTh-Fc monomer ratios for the solution side of all TTh-Fc / TTh-Por-TTh films. The surface values of these calculated ratios lie between *ca.* 1-2. Over the first *ca.* 5 μm , these ratios all increase and then decrease, in some cases substantially. However, at depths greater than 5 μm all ratios become constant. The counter ion to TTh-Fc monomer ratios calculated from the RBS simulations for the 1:1 film has the highest ratio and the 1:5 film has the lowest ratio. The 2:5 and 2:1 ratio films come to approximately the same counter ion to TTh-Fc monomer ratios. The trend observed from these values is that once the ratios stabilise, the greater the ratio of TTh-Por-TTh to TTh-Fc present in the film, the greater the amount of counter ions. These counter ions are required to charge balance the polymer chain, hence, the greater the concentration of TTh-Por-TTh monomer present in the copolymer film, the higher the oxidation state of that film because of more TTh overall.

The TTh-Por-TTh to TTh-Fc monomer ratios for the TTh-Por-TTh copolymer films from the electrode side are provided in Fig. 7.69. The 1:1, 2:5, and 2:1 films appear to be relatively constant through the RBS analysed depth, similar to those values calculated from the solution side. There is also a substantial decrease and then increase (to *ca.* 0.8) in the monomer ratios calculated for the 1:5 film within the first 5 μm of the film depth. Although the values from the solution side and electrode sides for these TTh-Por-TTh to TTh-Fc ratios are not identical, a similar trend between the

samples was found, with the 1:5 sample having the greatest ratio values, and the 1:1 sample having the lowest.

Similarly to that observed for the counter ion to TTh-Fc monomer ratio for the solution side sample, over the first few microns (*ca.* 5 μm) the counter ion to TTh-Fc ratio increases and then decreases, before settling at a constant value for the electrode side (Fig. 7.70). The 1:5 sample has the lowest ratio values, as found for the solution side. However, in this case the 1:1 sample has low ratio values unlike the higher values found from the solution side. The 2:5 film has the highest ratio value. As a whole, the calculated ratio values are higher for the electrode side samples than they are for the solution side samples.

7.7.5 *Bridging TTh copolymers*

Due to limitations on the quantity of the Bridging TTh monomer material available, only three copolymers with TTh-Fc were produced. These films were formed from parent solutions with concentrations of 1:10, 1:1, and 10:1 TTh-Fc / Bridging TTh.

Figures 7.71 and 7.72 display the experimental RBS spectra (both Type 1), together with the simulated spectra, for the solution and electrode sides of the 1:10 film respectively. The solution side and electrode side RBS spectra were well simulated and total film thicknesses were obtained. The over estimation of the simulation thickness at the top of the C peak in the solution side spectrum is an indication that at this location the film does not have uniform thickness. The difference observed in the high energy part of each of the spectra also indicates that at parts of the solution side spectrum analysis spot are thinner than other parts. The thinner parts of the analysed area do not appear to be significantly greater than the bulk, but a variation in film thickness is observed.

The SEM images obtained for the solution and electrode sides of the 1:10 TTh-Fc / Bridging TTh film are provided in Fig. 7.73. The images of the electrode side (Fig. 7.73 (b), (d)) show a smooth surface. It is observed that this surface of this film has areas where more material deposition has occurred from the 100 μm scale solution side. These areas where more deposition has occurred are *ca.* 20 μm in

diameter on average. The 2 μm scale image shows that the surface morphology is an open structure coral-like growth. The morphological structure of the solution side film does not appear to be projecting from the surface significantly, and this is the reason why total penetration is observed in the RBS spectra in this case.

The solution side and electrode side RBS spectra for the 1:1 TTh-Fc / Bridging TTh film are provided in Fig. 7.74 and 7.75 respectively. The spectrum in Fig. 7.74 is Type 1, and the majority of the spectrum has been well simulated (channel numbers 380-650). However, there is a small low energy tail indicating that a minor proportion of the sampled area is thicker than the rest. The RBS spectrum obtained from the electrode side of this film is Type 1 also. The spectrum in Fig. 7.75 was simulated well across all experimental channels.

Figure 7.76 provides the SEM images of the 1:1 TTh-Fc / Bridging TTh film, both solution (Fig. 7.76 a, c) and electrode (Fig. 7.76 b, d) sides. The electrode side of this film is smooth as for the previous film. However, in these images small crystals are observed on the surface. The solution side surface images show that this film also has coral-like features, but in this case it has a denser, more closed structure. There are areas on the surface of this sample which appear to have more deposition, as in the previous sample. However, areas where more deposition has occurred have a maximum diameter of *ca.* 15 μm in this case.

The two experimental RBS spectra from the solution and electrode sides of the 10:1 TTh-Fc / Bridging TTh film are provided in Figs. 7.77 and 7.78 respectively. The solution side RBS spectrum is Type 2. This spectrum was adequately simulated and the films bulk thicknesses were calculated. The RBS spectrum obtained for the electrode side is Type 3. The analysed area has a large variation in surface height compared to the other TTh-Fc / Bridging TTh films analysed.

The SEM images for the 10:1 TTh-Fc / Bridging TTh film are provided in Fig. 7.79. The electrode side surface of this film (Fig. 7.79 b, d) shows a smooth planar surface, with some additional material present on the surface. A different type of film growth is observed from the 100 μm scale image of the solution side compared to that of the 1:10 and 1:1 samples, this film having a much more open structure. In the 2 μm scale

image a small granular growth is observed, with the growth nodules being *ca.* 2 μm in diameter and showing some overlap. The growth of this copolymer extends further out from the underlying bulk material than the other two TTh-Fc / Bridging TTh films. This feature accounts for why the RBS spectra for the electrode side has a more pronounced low energy tail than the other films. Over the beam spot area (1.5 mm diameter) the variation in the film thickness would be expected to be much greater than the variation in the other two films, giving rise to this low energy tail.

There appears to be a trend between the TTh-Fc concentration in the parent solution and the resulting morphology of the sample from examination of both the RBS spectra and SEM images of the three TTh-Fc / Bridging TTh copolymer films. When the amount of TTh-Fc monomer is less than the amount of Bridging TTh monomer in the parent solution, the resulting film has hemispherical coral-like growth, with a constant thickness. When the amount of TTh-Fc monomer is greater than the amount of Bridging TTh monomer in the parent solution then the morphology of the surface changes to a more granular, open structured growth, resulting in a more uneven film thickness.

The number of layers required to achieve each simulation, the individual layer thicknesses, the total simulated thickness of each sample, and the roughness factors for both sides of each TTh-Fc / Bridging TTh copolymer film are listed in Table 7.10. The total overall simulated thicknesses for all the Bridging TTh copolymers are similar, ranging from 12.5-17.5 μm . The variation between simulated thickness of each side of the same sample was at most only *ca.* 4 μm . The roughness factors calculated for these copolymers are the highest calculated for all the TTh-Fc copolymers and are above 0.5, with the highest value being 0.9. These roughness factors are a good indication of the smoothness of the solution side surfaces.

The Bridging TTh to TTh-Fc monomer ratios (m/n), and the counter ions to TTh-Fc monomer ratios (z/n), for each simulated layer of each sample, are listed in Table 7.11. Figures 7.80-7.83 provide graphical representations of the calculated values listed in Table 7.11 and display the variation of the respective ratios with depth into the copolymers.

The variation in the Bridging TTh monomer to TTh-Fc monomer ratio with depth into the film for the solution side samples are shown in Fig. 7.80. The ratios for the 1:10 film shows a substantial drop in the ratio after *ca.* 15 μm into the sample, but at greater than this depth the ratio was constant at *ca.* 8.8. Even after the drop in the ratio for the 1:10 film, the lowest ratio value (*ca.* 5.5) was still greater than ratios calculated for the 1:1 and 1:10 films. The ratios calculated for the 1:1 film were constant at *ca.* 3.5, as were the ratios for the 10:1 film at *ca.* 0.5. The calculated ratios for each of these three film samples follow the same trends as that of their original parent solutions, i.e. the less Bridging TTh monomer in the parent co-monomer solution, the less that is incorporated into the copolymer film.

A plot of the counter ion to TTh-Fc monomer ratios with depth into the solution side of the samples is provided in Fig. 7.81. The counter ion to TTh-Fc monomer ratios for the 10:1 TTh-Fc / Bridging TTh film at the surface was *ca.* 1.6 and over a depth of *ca.* 14 μm increase to a value of *ca.* 2.5. The ratios for the 1:1 TTh-Fc / Bridging TTh film are *ca.* 3.8 at the surface, however they decrease in value over a depth of *ca.* 15 μm to *ca.* 2. The 1:10 TTh-Fc / Bridging TTh film has the highest ratio value at the surface of all three films (*ca.* 5), then over a depth of *ca.* 14 μm it decreases to less than 1 and for depths greater than *ca.* 16 μm increases to *ca.* 4. For the first *ca.* 6 μm into these films it appears that the greater the ratio of Bridging TTh to TTh-Fc is, the greater the ratio of counter ions to TTh-Fc monomer is as well. This suggests that the copolymer is in a more oxidised state when the Bridging TTh to TTh-Fc ratio is high. However, this only appears to be the case within the first *ca.* 6 μm , after which point no significant trend in the counter ion to TTh-Fc monomer ratios between the three films is observed.

Figure 7.82 provides the plots of the calculated Bridging TTh to TTh-Fc monomer ratios for the three TTh-Fc / Bridging TTh films from the electrode side samples. Similar trends are observed for these ratios to those for the solution side samples, with the 10:1 film having the greatest values, then the 1:1 film, and lastly the 1:10 film having the lowest ratio values.

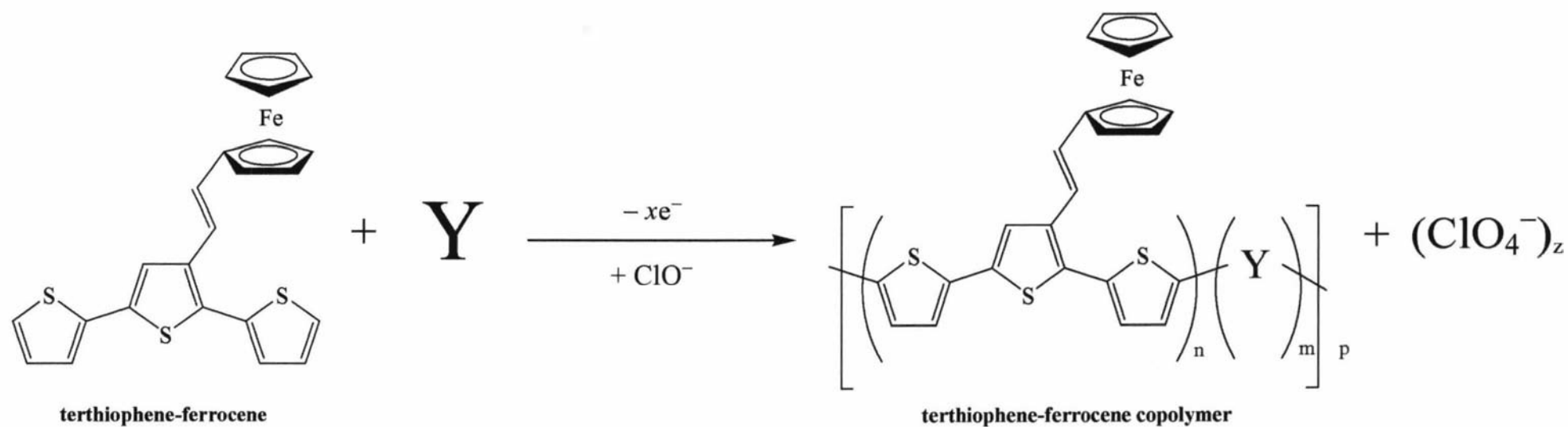
The counter ion to TTh-Fc monomer calculated ratios (provided in Fig. 7.83) vary greatly from the results observed from the solution side samples. The 1:1 TTh-Fc / Bridging TTh film has the highest counter ion to TTh-Fc monomer ratio, initially *ca.* 7, and decreasing to *ca.* 3.5 over *ca.* 16 μm . At a value of *ca.* 5, the 1:10 TTh-Fc / Bridging TTh film has the next highest surface value. This ratio decreases to *ca.* 2 over a depth of *ca.* 15 μm . The 10:1 TTh-Fc / Bridging TTh film is the only one of the three films whose counter ion to TTh-Fc monomer ratio remains constant over the simulated depth (*ca.* 14 μm) at a value of *ca.* 2. Again, no significant trend can be determined from these values.

7.8 Variation of film thickness

In all of the TTh-Fc copolymer experimental RBS spectra in this work, when the solution side and electrode side spectra of the same film were compared, variations in the measured film thickness of these samples were observed. These variations were in many cases small. However, in some cases the variation in observed film thickness was substantial. One possible cause for this film thickness variation could be the influence of polymer deposition due to the location of the counter electrode. To this point in the study, the counter electrode has been treated as indifferent and is present only to balance the faradaic process (Section 2.2.2.1). In the preparation of the films for IBA, a wire counter electrode was used (Fig. 2.4). This wire was poised *ca.* 1 cm from the centre of the working electrode. If the addition of electrolyte to the parent monomer solutions was insufficient to provide adequate solution conductivity, it is conceivable that the outer most edges of the working electrode face might experience a substantially different electrical field than the parts of the working electrode within close proximity to the counter electrode. Consequently, a second series of experiments were conducted using a gauze Pt counter electrode (1 cm^2) held immediately adjacent and parallel to the working electrode so that the entire film experienced the same electrical field during growth. The cell construction is shown in Fig. 7.84.

Two 1:10 TTh-Fc / Bridging TTh films were electrochemically deposited in ITO coated glass working electrodes at 1400 mV (*vs* Ag wire) for 750 sec using Pt wire and gauze counter electrodes.

In an attempt to determine whether or not the counter electrode was influencing the growth, and more importantly the thickness of the electrochemically produced films the following experiment was undertaken. Following electrochemical deposition and washing, the two films were mounted in the sample holder and five RBS spectra were collected from each film. The five spectra were obtained from areas moving left to right across each film (Fig. 7.85). When overlaid the low energy tails of the five spectra should give an indication of the relative film thicknesses at each position. If the counter electrode was influencing the growth to a large extent one might expect that the spectrum collected from position 3 (Fig. 7.85) would show the greatest film thickness in the case of the Pt wire electrode, with no large fluctuations in the thickness of the film produced using a Pt gauze counter electrode. Figure 7.86 displays the five overlaid RBS spectra for the film produced using the Pt wire counter electrode. It is observed here that the thickness of the film decreases moving across the film surface from left to right. If the counter electrode influenced the growth of the film it could be expected that the film grown with a Pt gauze counter electrode should have a more uniform thickness. The five RBS spectra collected across the surface of this film are displayed in Figure 7.87. The trend in thickness across the copolymer film which was deposited using a Pt gauze counter electrode in the cell is dissimilar to the trend in thickness observed across the copolymer deposited using a Pt wire counter electrode in the cell. The sample deposited using a Pt wire counter electrode showed the low energy carbon tailing decreasing as one moved left to right across the film. This is thought to be due to the Pt wire counter electrode being closer to the LHS of the film during the deposition stage. However, when the copolymer deposited using a Pt gauze counter electrode was examined, there were parts of the sample which had a greater extent of low energy carbon tailing than the previous Pt wire sample. As observed in the Pt wire films RBS spectra, there are areas of the Pt gauze film where no tailing was observed. The difference between the two films is that with the Pt wire film there was a trend in the extent of tailing observed moving across the sample. No such trend was observed when moving across the Pt gauze sample. From these two sets of experimental RBS spectra it can be assumed that the counter electrode is not the cause of the variation observed in film thickness from different areas chosen from the same sample.



Scheme 5.1 Chemical scheme of the production of terthiophene-ferrocene copolymer films electrochemically, where Y represents one of the five copolymer monomers, Py, bithiophene, EDOT, TTh-Por-TTh, or Bridging TTh.

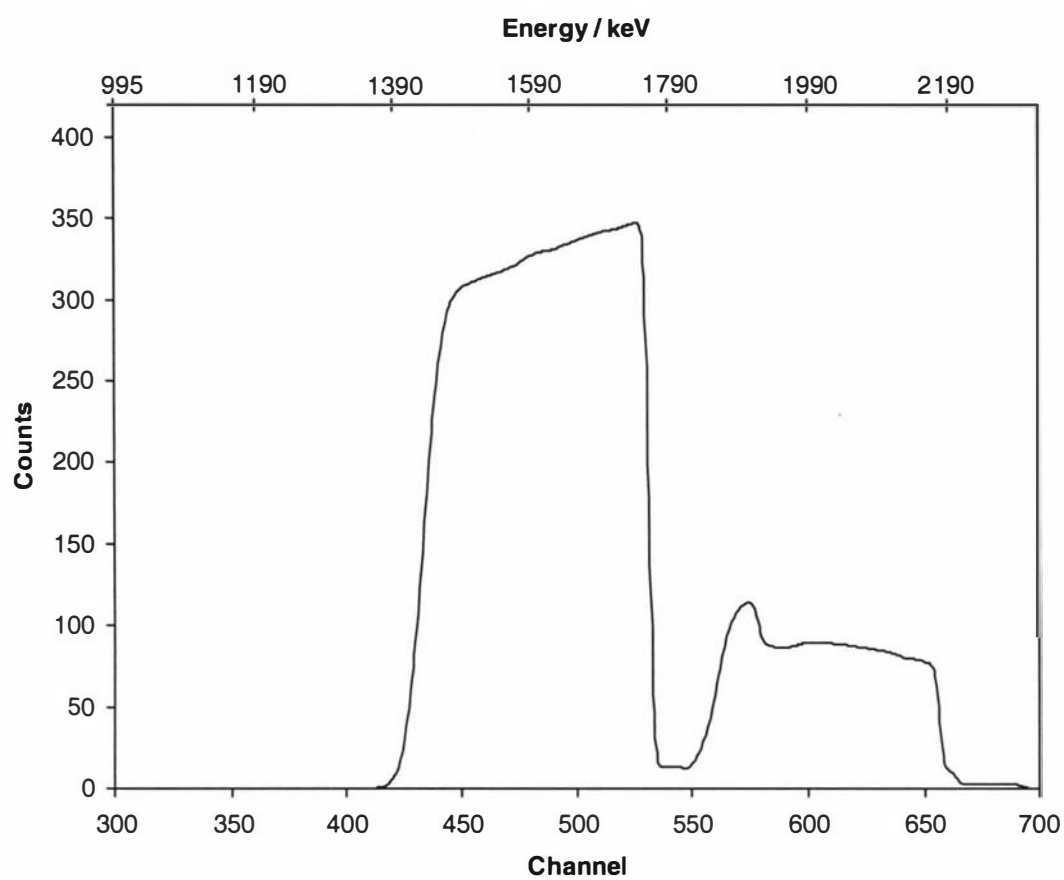


Fig. 7.1 A schematic representation of a Type 1 RBS spectrum.

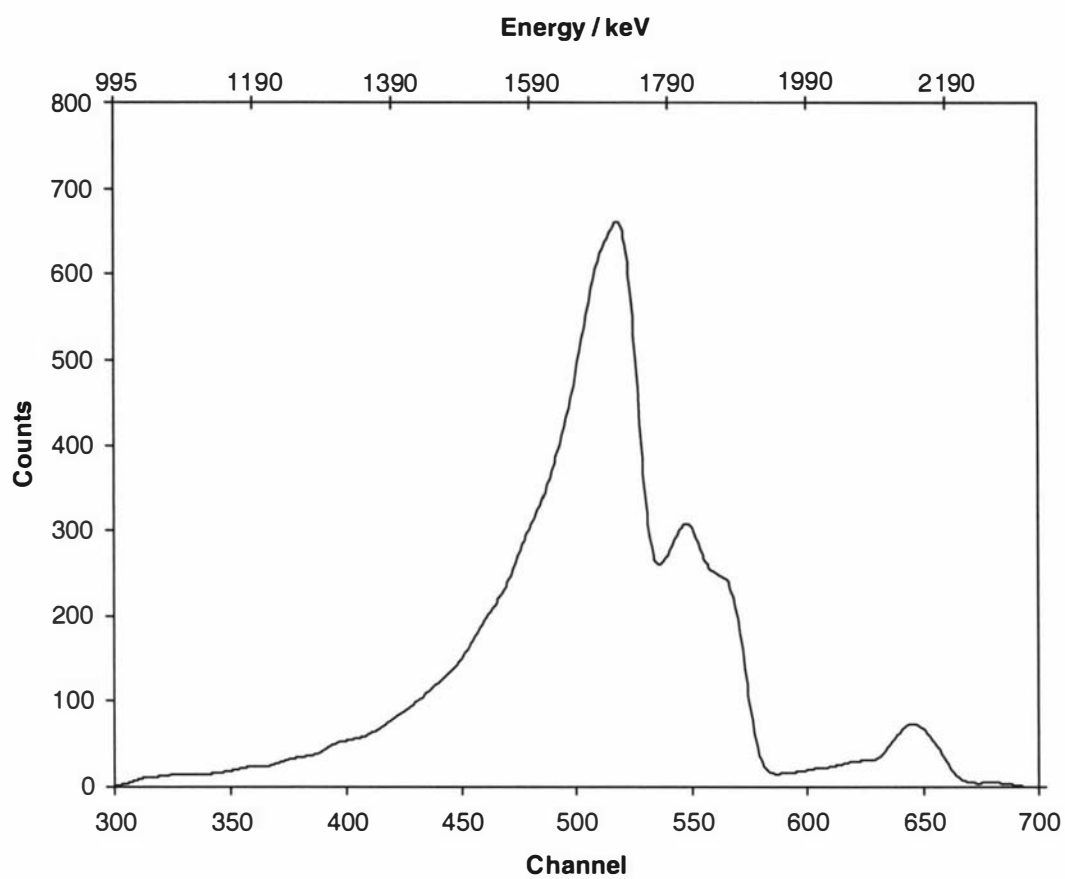


Fig. 7.2 A schematic representation of a Type 2 RBS spectrum.

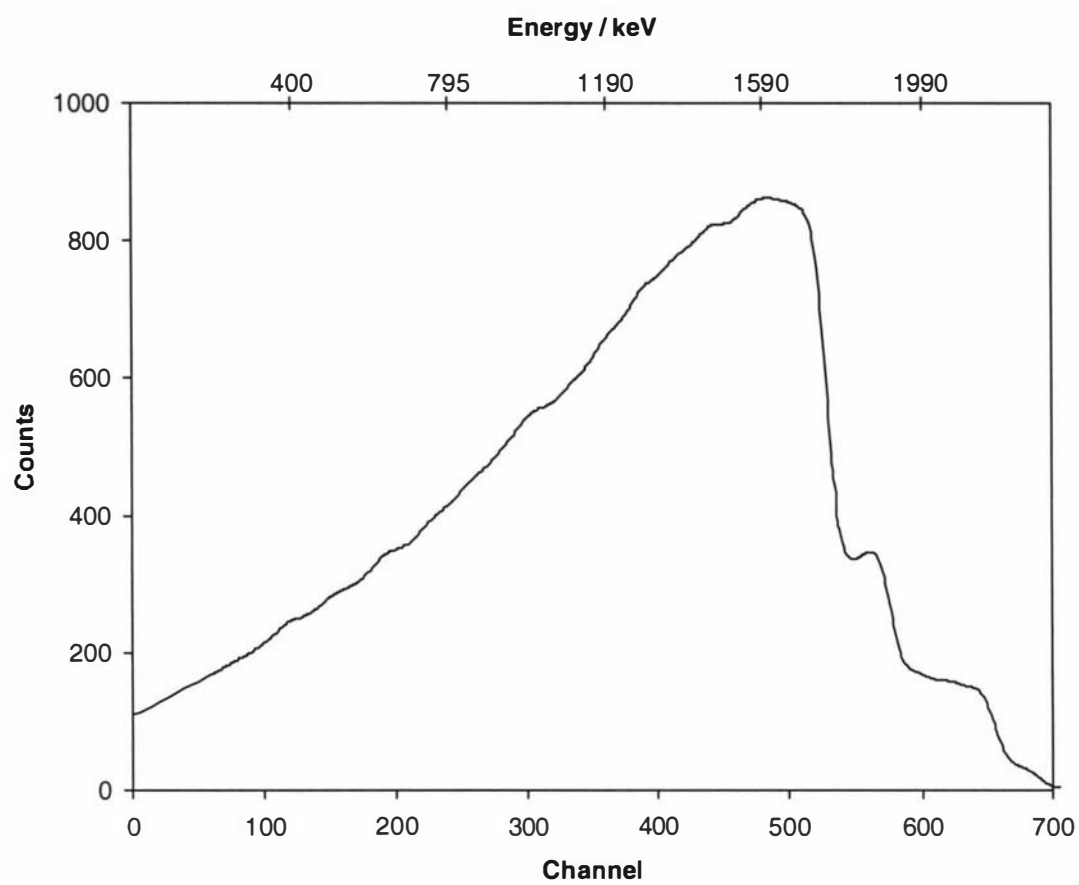


Fig. 7.3 A schematic representation of a Type 3 RBS spectrum.

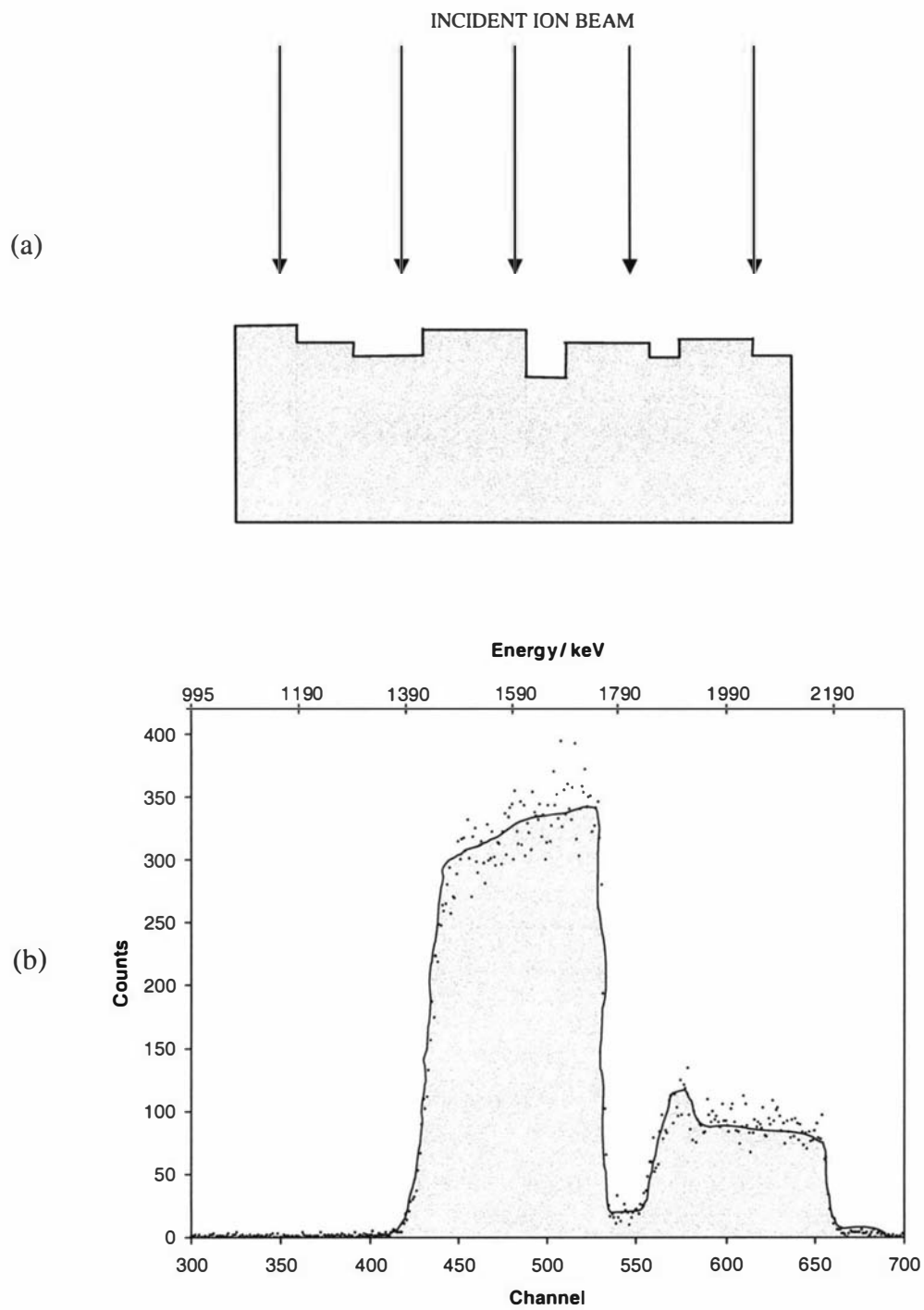


Fig 7.4 Schematic sample structural diagram (a) and a Type 1 RBS spectrum (b).

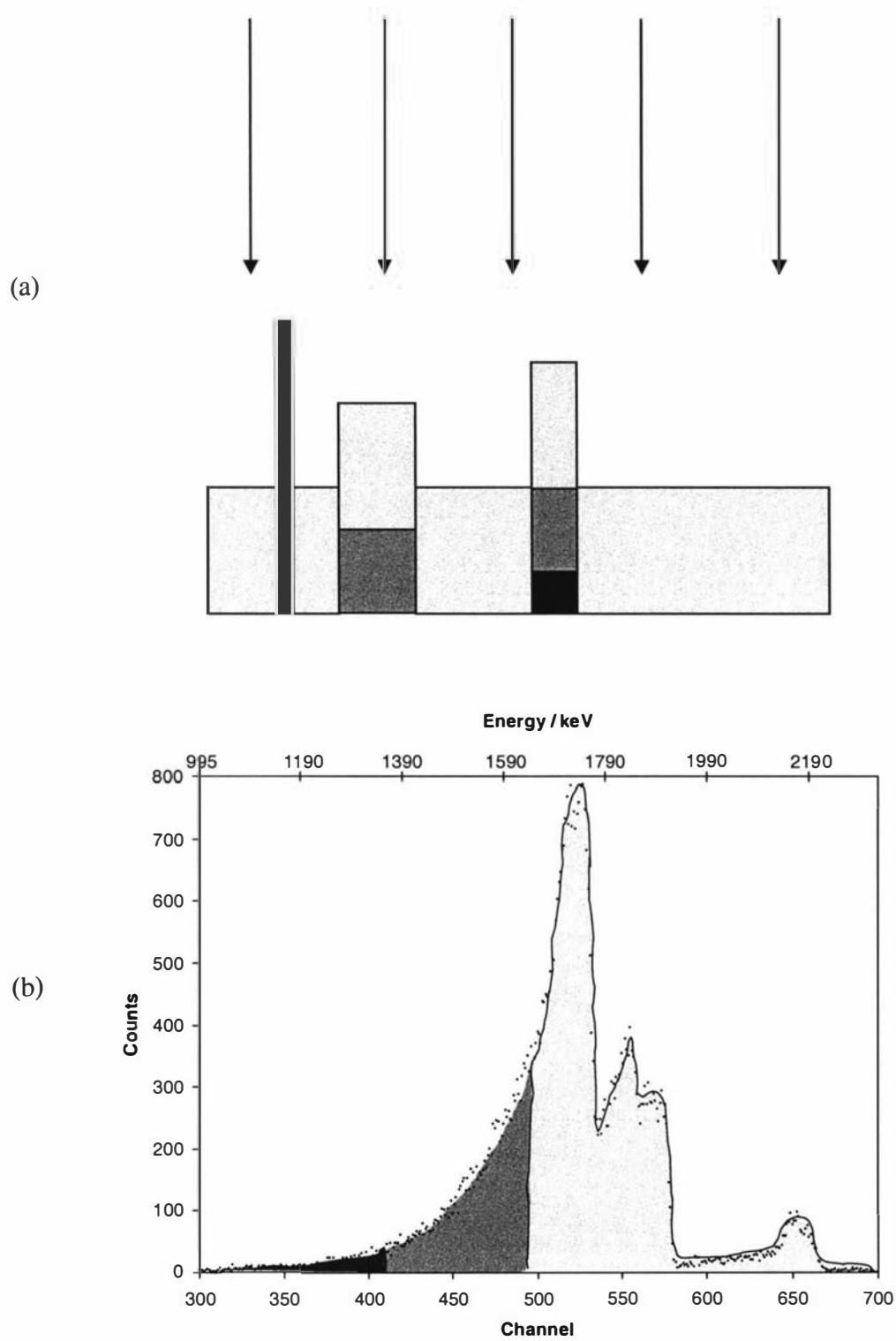


Fig 7.5 Schematic sample structural diagram (a) and a Type 2 RBS spectrum (b).

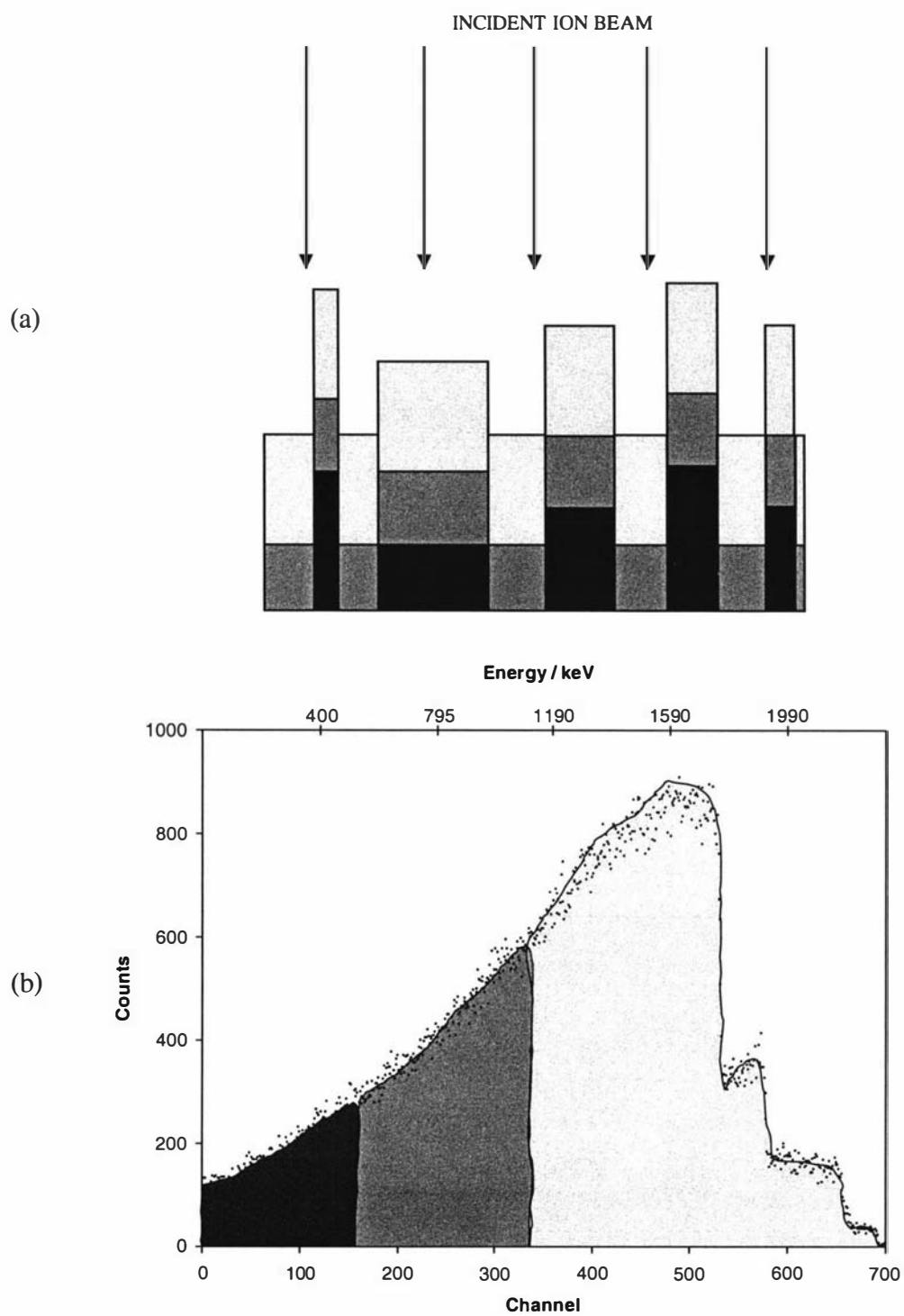


Fig 7.6 Schematic sample structural diagram (a) and a Type 3 RBS spectrum (b).

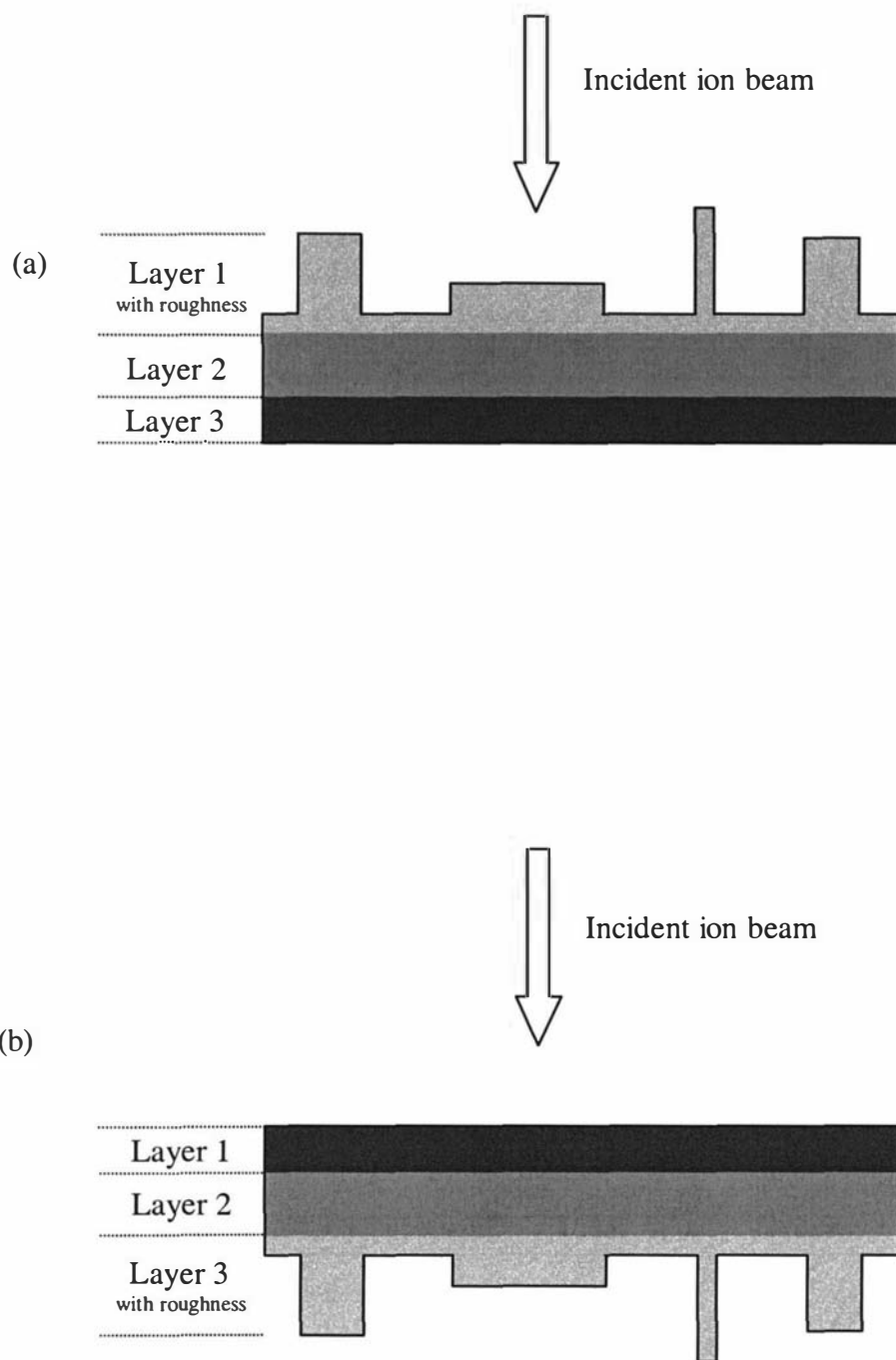


Fig. 7.7 Schematic diagram of a sample which requires three layers for the simulation indicating which layer requires the roughness, (a) solution side, and (b) electrode side.

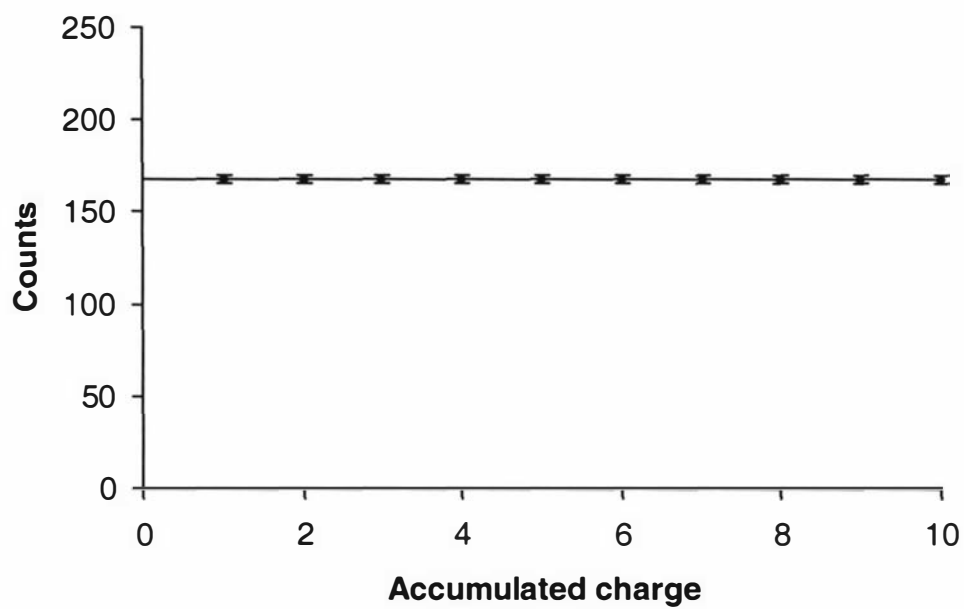


Fig. 7.8 Accumulated charge for polymer durability on 1:10 TTh-Fc / Py film (solution side).

Table 7.1 Extra entities used in the simulation of a 1:10 TTh-Fc / Bridging TTh copolymer film together with the ratios, with respect to one TTh-Fc monomer (Layer 1 is the layer closest to the ion beam).

TTh-Fc / Bridging TTh (1:10)				
Parameter	Layer 1	Layer 2	Layer 3	Layer 4
CH ₂ Cl ₂	0.171	0.254	0.263	0.273
Carbon	2.302	2.278	1.335	2.073

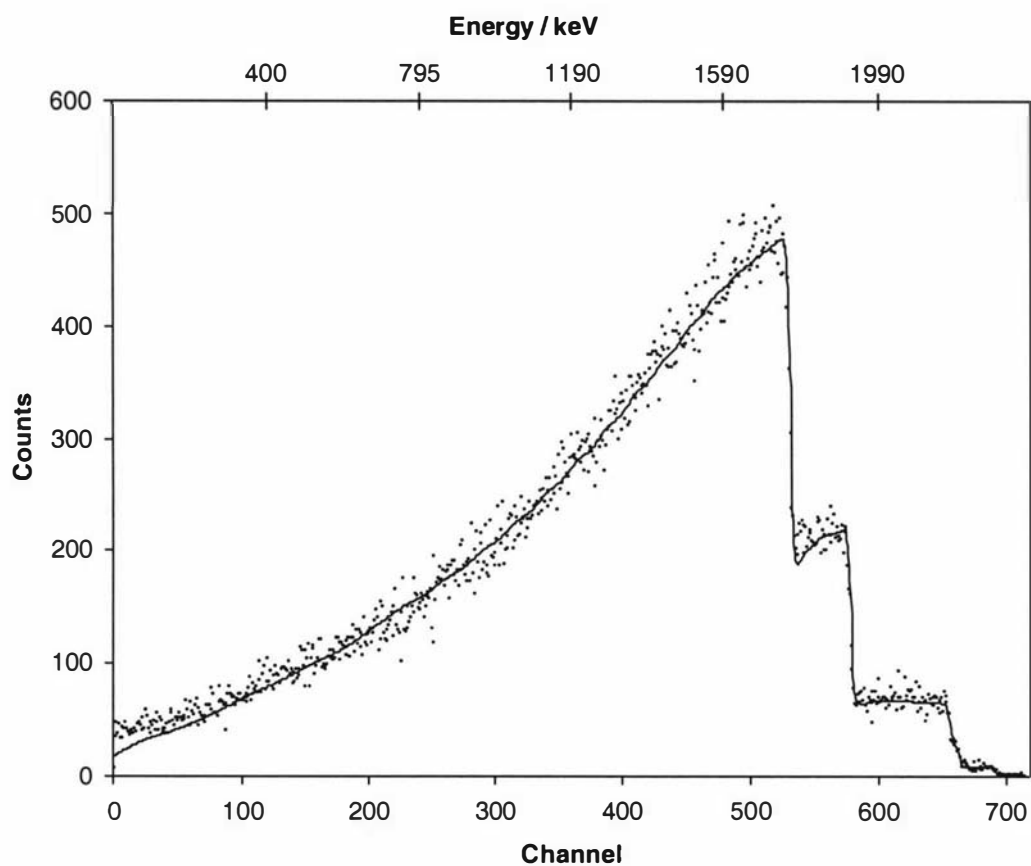


Fig. 7.9 RBS experimental (●) and simulated (—) spectra for the solution side of a TTh-Fc / Py copolymer (1:10) using a 2.5 MeV proton beam, as simulated by Matej Mayer at the Max-Plank Institut für Plasmaphysik (2003).

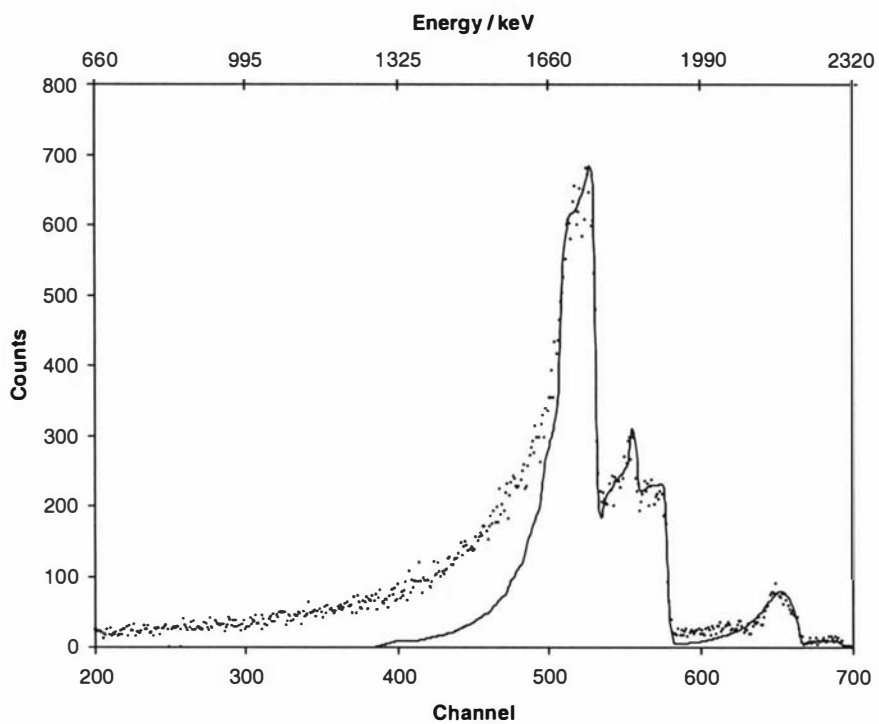


Fig. 7.10 RBS experimental (●) and simulated (—) spectra for the electrode side of a TTh-Fc / Py copolymer (1:10) using a 2.5 MeV proton beam.

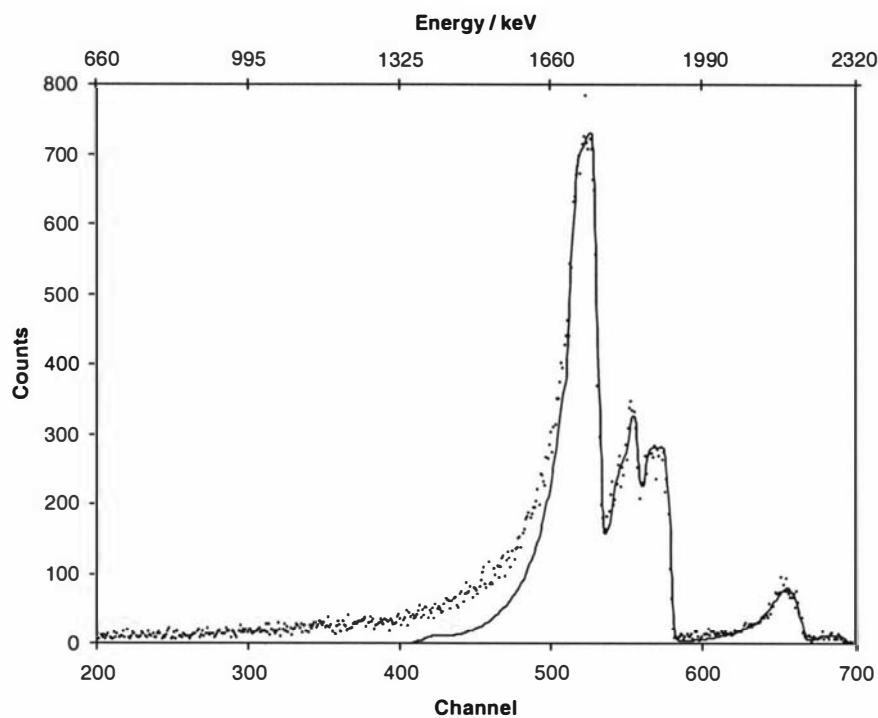


Fig. 7.11 RBS experimental (●) and simulated (—) spectra for the solution side of a TTh-Fc / Py copolymer (1:20) using a 2.5 MeV proton beam.

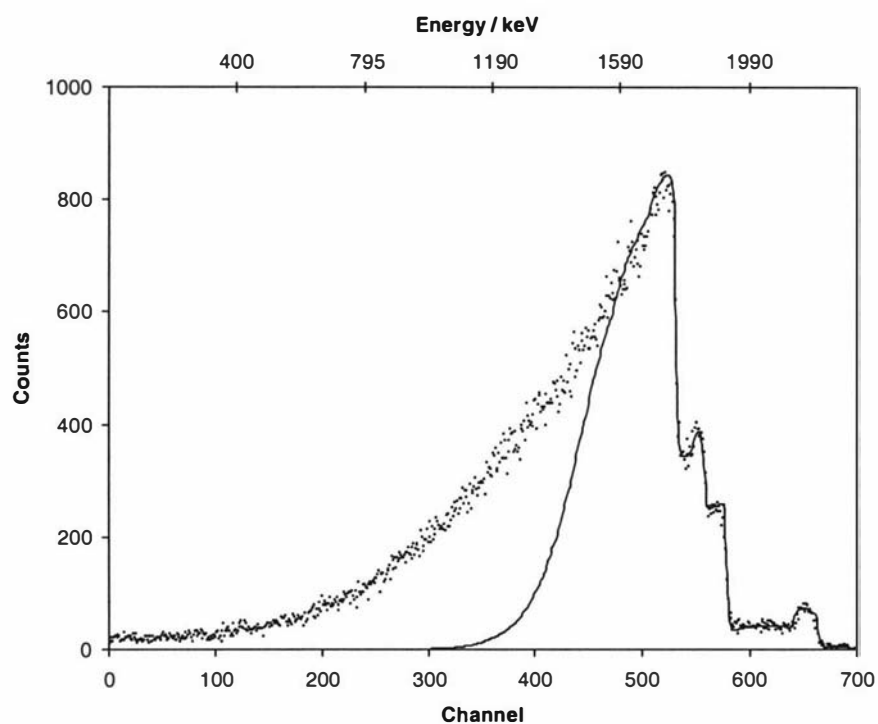


Fig. 7.12 RBS experimental (●) and simulated (—) spectra for the electrode side of a TTh-Fc / Py copolymer (1:20) using a 2.5 MeV proton beam.

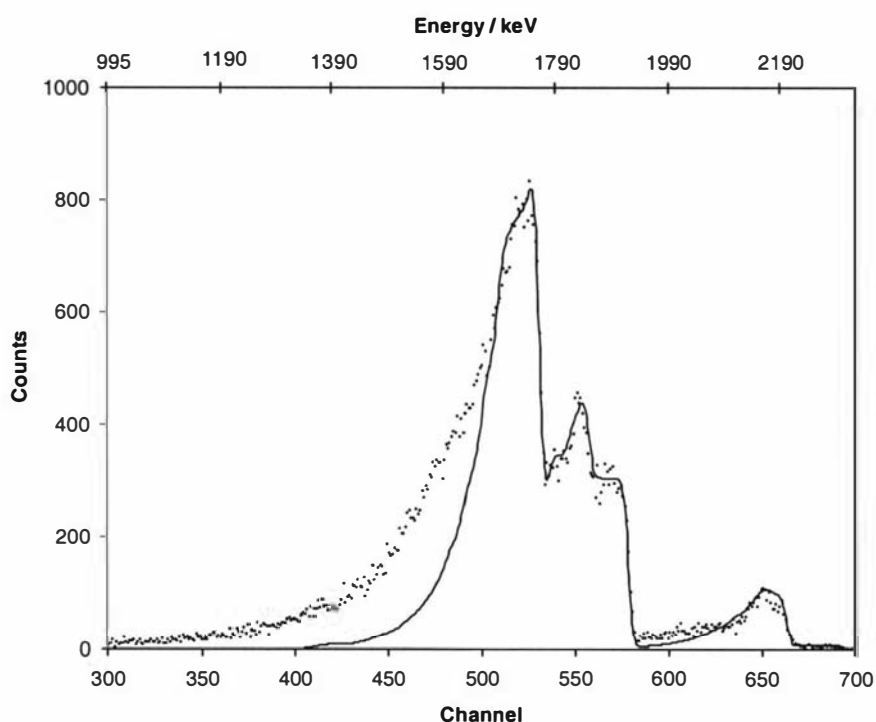


Fig. 7.13 RBS experimental (●) and simulated (—) spectra for the solution side of a TTh-Fc / Py copolymer (1:50) using a 2.5 MeV proton beam.

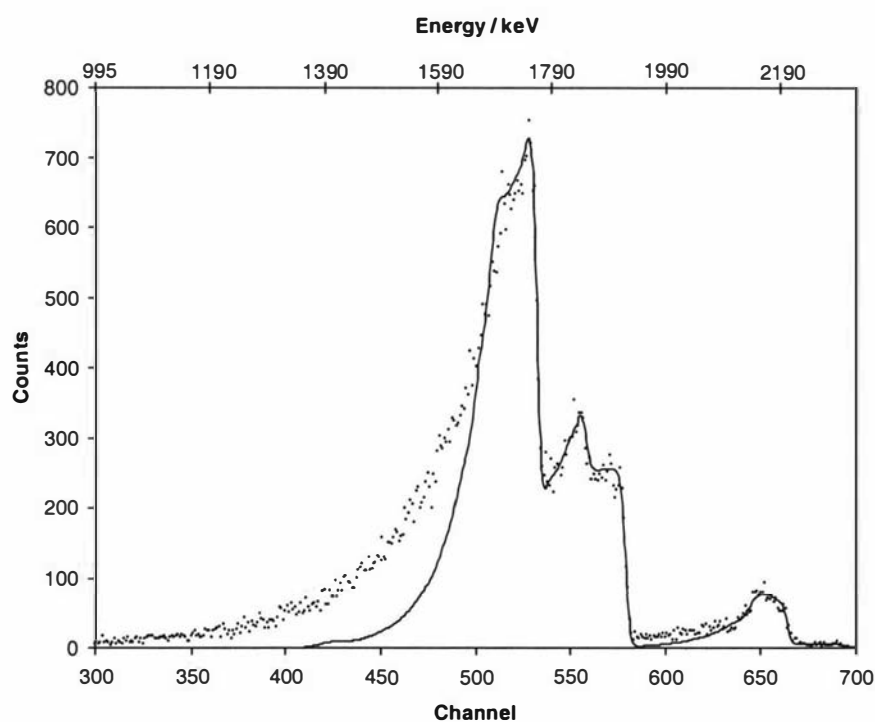


Fig. 7.14 RBS experimental (●) and simulated (—) spectra for the electrode side of a TTh-Fc / Py copolymer (1:50) using a 2.5 MeV proton beam.

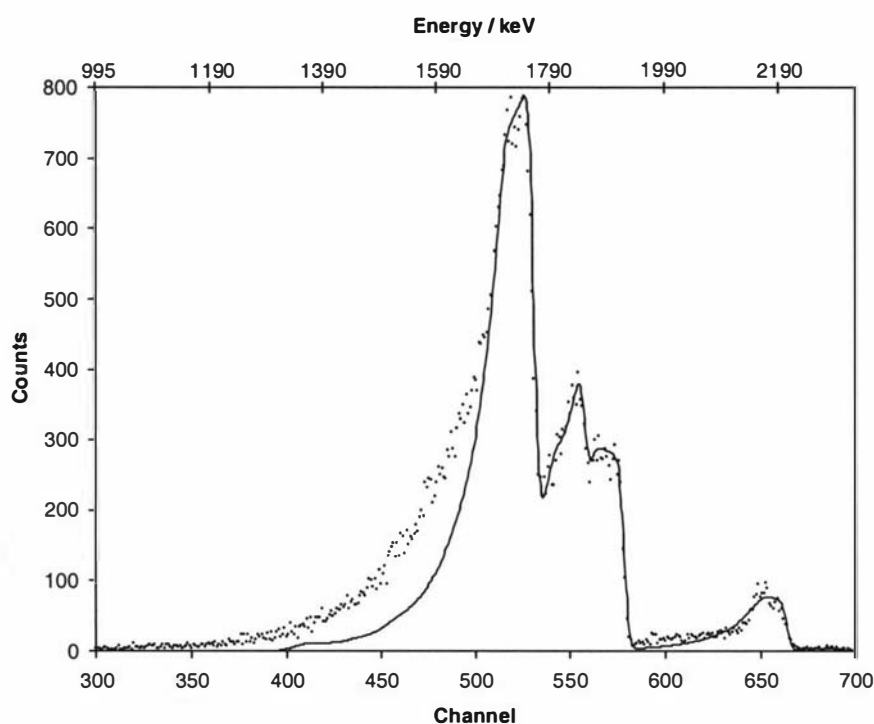


Fig. 7.15 RBS experimental (●) and simulated (—) spectra for the solution side of a TTh-Fc / Py copolymer (1:100) using a 2.5 MeV proton beam.

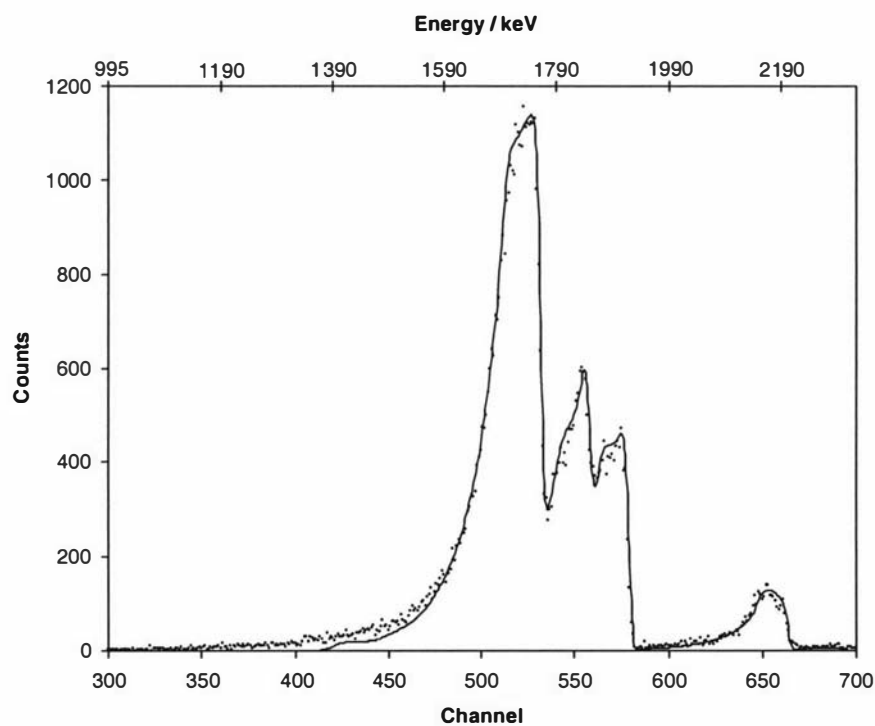
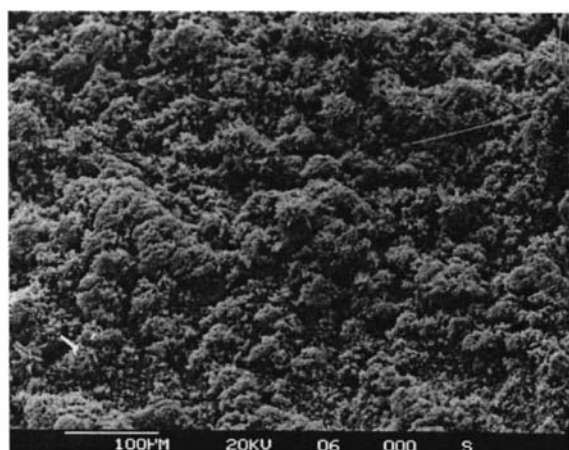
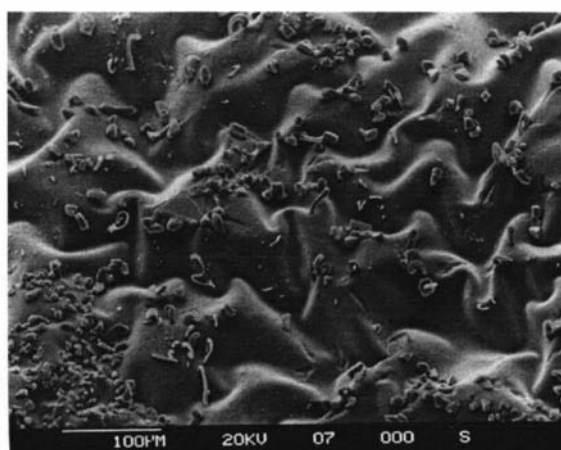


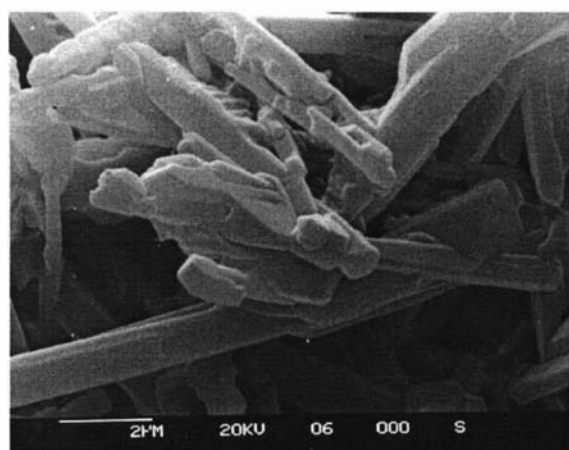
Fig. 7.16 RBS experimental (●) and simulated (—) spectra for the electrode side of a TTh-Fc / Py copolymer (1:100) using a 2.5 MeV proton beam.



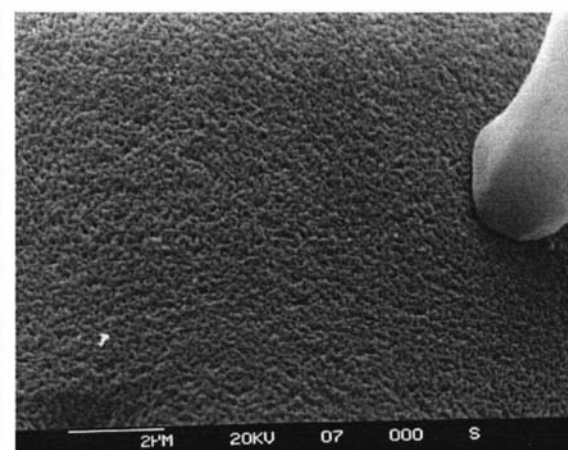
(a)



(b)

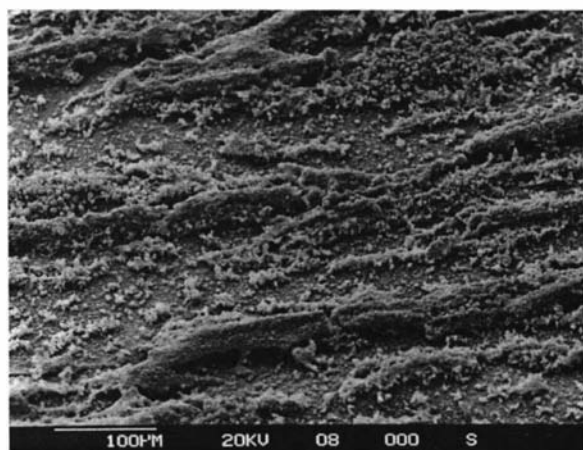


(c)

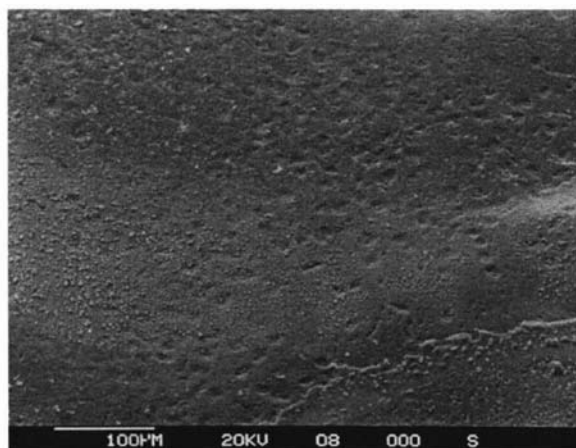


(d)

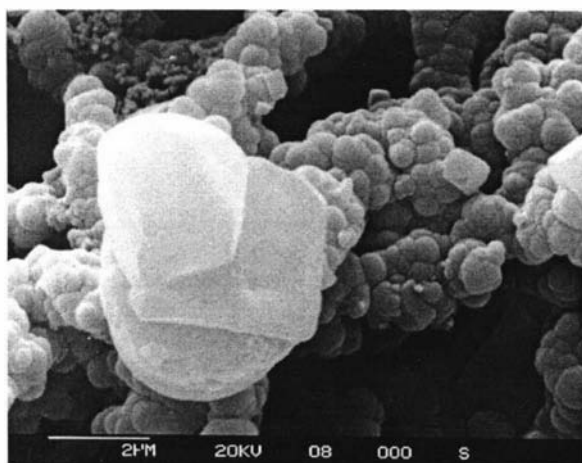
Fig. 7.17 SEM images of the solution and electrode side of the 1:10 TTh-Fc / Py copolymer: (a) 100 μm solution side; (b) 100 μm electrode side; (c) 2 μm solution side; (d) 2 μm electrode side.



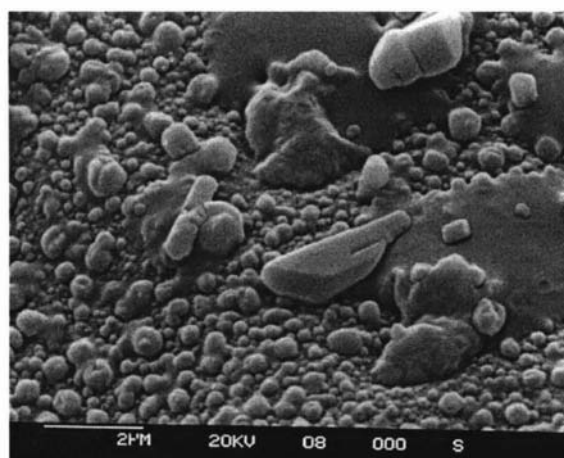
(a)



(b)

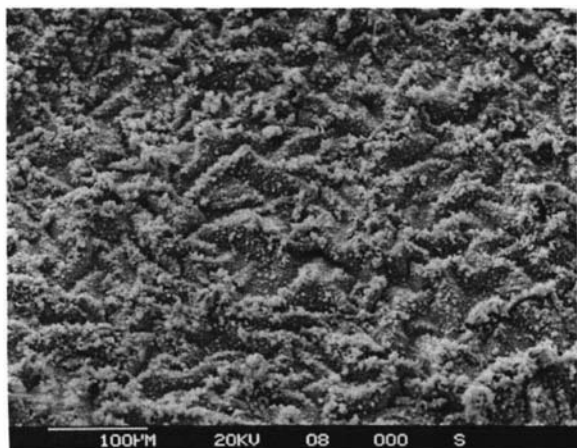


(c)

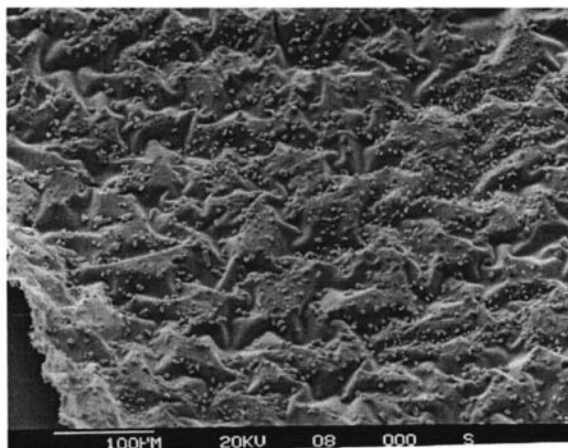


(d)

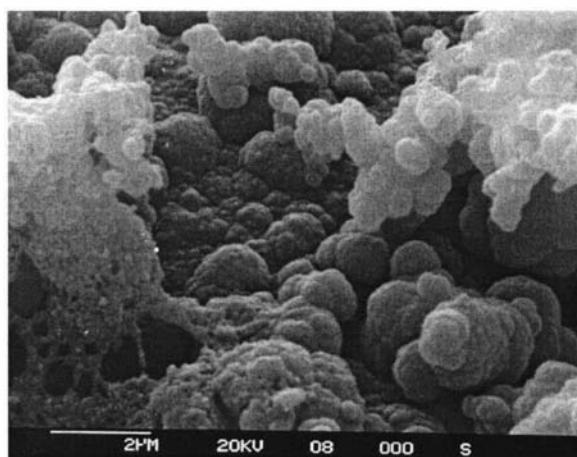
Fig. 7.18 SEM images of the solution and electrode side of the 1:20 TTh-Fc / Py :
(a) 100 μm solution side; (b) 100 μm electrode side; (c) 2 μm solution side; (d) 2 μm electrode side.



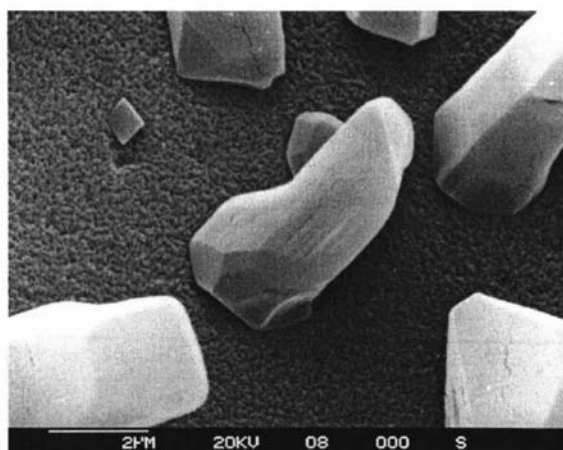
(a)



(b)

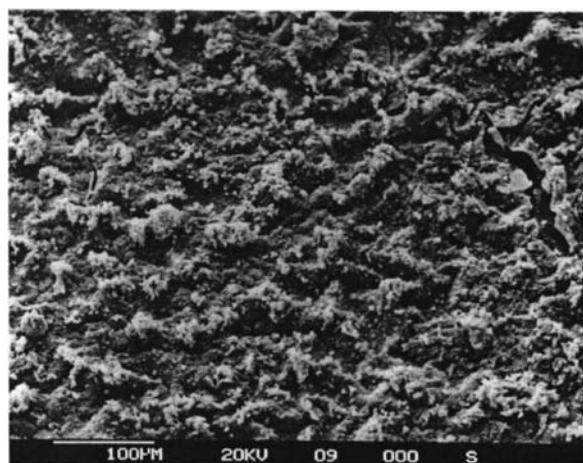


(c)

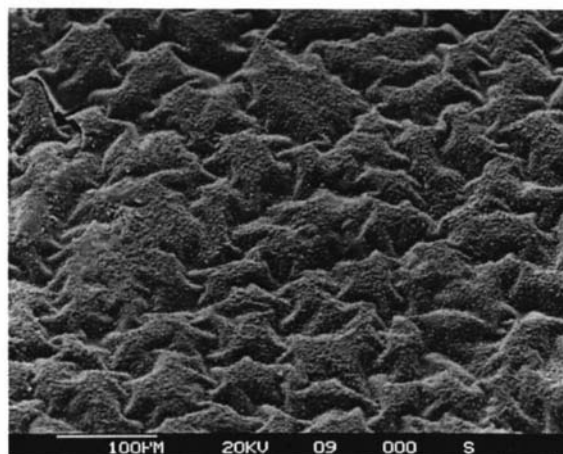


(d)

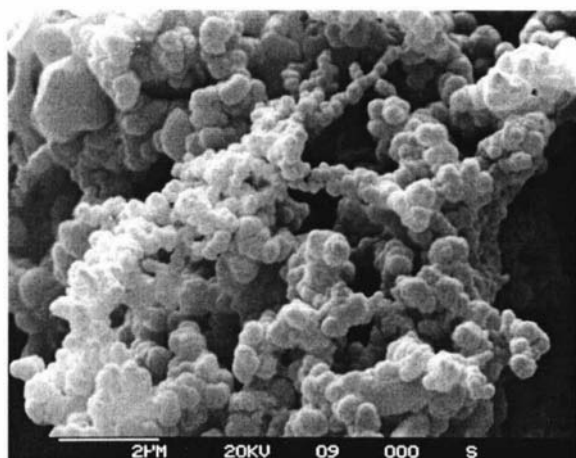
Fig. 7.19 SEM images of the solution and electrode side of the 1:50 TTh-Fc / Py :
(a) 100 μm solution side; (b) 100 μm electrode side; (c) 2 μm solution side; (d) 2 μm electrode side.



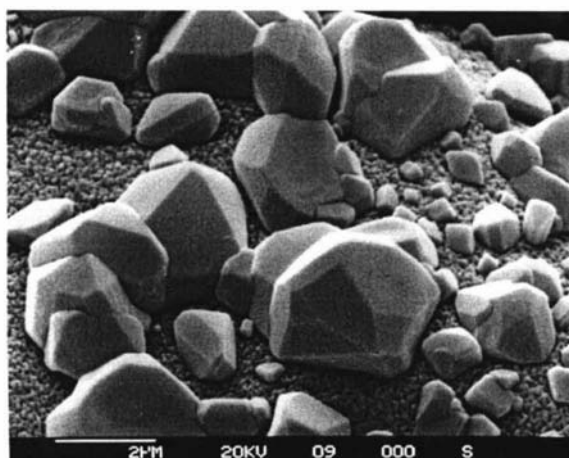
(b)



(a)



(c)



(d)

Fig. 7.20 SEM images of the solution and electrode side of the 1:100 TTh-Fc / Py copolymer : (a) 100 μm solution side; (b) 100 μm electrode side; (c) 2 μm solution side; (d) 2 μm electrode side.

Table 7.2 Layer thickness, roughness factors, and total analysed depth of each TTh-Fc / Py film sample. Roughness factor values denoted by * have the roughness factor associated with the last simulated layer.

	Layer 1	Layer 2	Layer 3		
Monomer ratios (TTh-Fc / Pyrrole)	Thickness (μm)	Thickness (μm)	Thickness (μm)	Roughness factor	Total thickness (μm)
1:10 electrode side	2.72	1.90	1.54	0.00*	6.16
1:20 solution side	2.48	1.34	0.85	0.00	4.67
1:20 electrode side	3.68	1.16	5.38	0.25*	10.22
1:50 solution side	1.73	0.86	3.49	0.00	6.08
1:50 electrode side	0.61	2.40	2.92	0.00*	5.93
1:100 solution side	2.78	1.90	0.70	0.00	5.38
1:100 electrode side	0.77	1.79	2.46	0.07*	5.02

Table 7.3 Listed are the pyrrole to terthiophene-ferrocene monomer ratios and counter ion to terthiophene-ferrocene monomer ratios for each simulated layer. All ratios are quoted with respect to one terthiophene-ferrocene monomer.

	Layer 1		Layer 2		Layer 3	
Monomer ratios (TTh-Fc / pyrrole)	Pyrrole (<i>m/n</i>)	Counter ion (<i>z/n</i>)	Pyrrole (<i>m/n</i>)	Counter ion (<i>z/n</i>)	Pyrrole (<i>m/n</i>)	Counter ion (<i>z/n</i>)
1:10 electrode side	25.4	11.2	21.1	11.1	22.4	9.2
1:20 solution side	25.3	11.7	19.8	11.1	18.6	10.4
1:20 electrode side	43.1	24.0	31.3	20.8	33.4	16.9
1:50 solution side	35.5	17.8	34.3	17.8	37.7	17.9
1:50 electrode side	36.3	17.2	35.4	17.7	35.6	15.5
1:100 solution side	78.8	30.0	75.2	38.6	80.2	37.0
1:100 electrode side	88.9	39.2	108.2	45.5	95.2	31.8

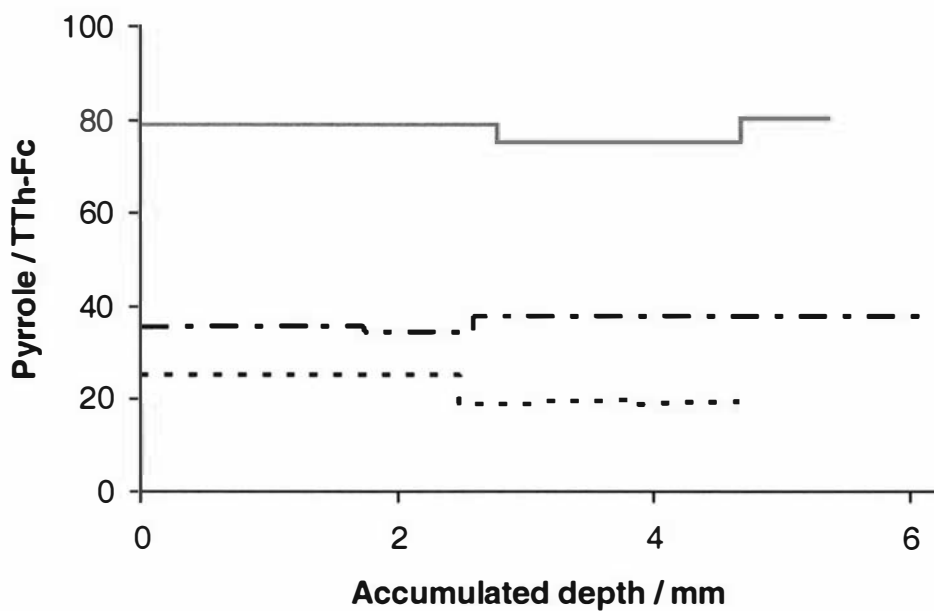


Fig 7.21 Plot of Py / TTh-Fc ratios changing with depth into the solution side of the copolymer, 1:20, — · — · 1:50, ——— 1:100.

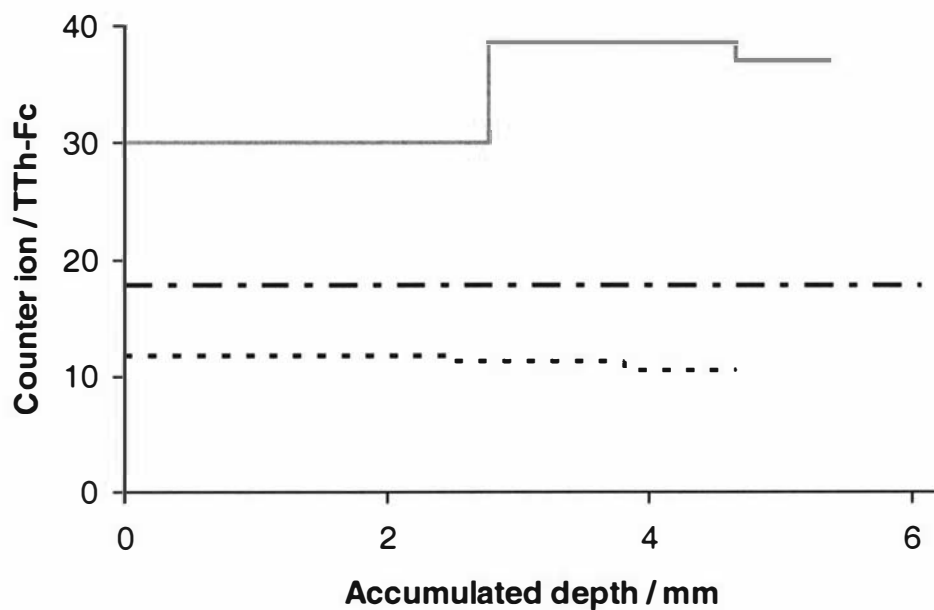


Fig 7.22 Plot of counter ion / TTh-Fc ratios changing with depth into the solution side of the Py / TTh-Fc copolymer, 1:20, — · — · 1:50, ——— 1:100.

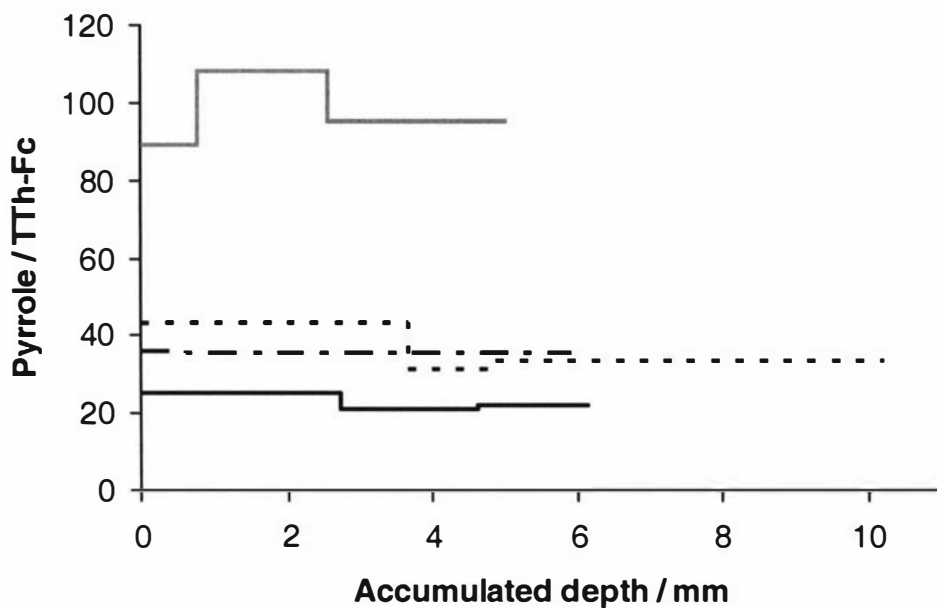


Fig 7.23 Plot of Py / TTh-Fc ratios changing with depth into the electrode side of the copolymer, — 1:10, 1:20, - · - · 1:50, — — — 1:100.

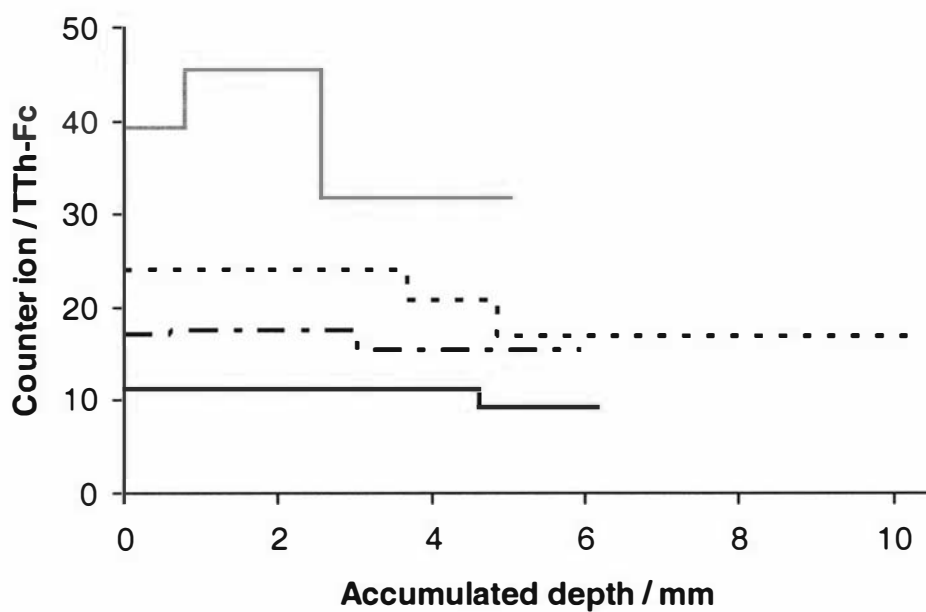


Fig 7.24 Plot of counter ion / TTh-Fc ratios changing with depth into the electrode side of the Py / TTh-Fc copolymer, — 1:10, 1:20, - · - · 1:50, — — — 1:100.

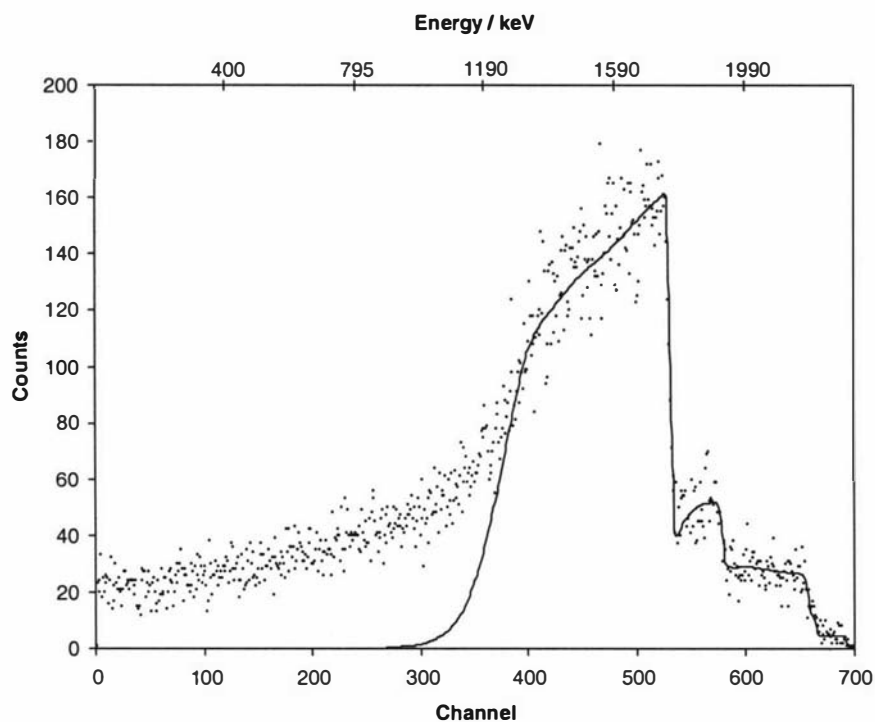


Fig 7.25 RBS experimental (●) and simulated (—) spectra for the solution side of a TTh-Fc / bithiophene copolymer (1:10) using a 2.5 MeV proton beam.

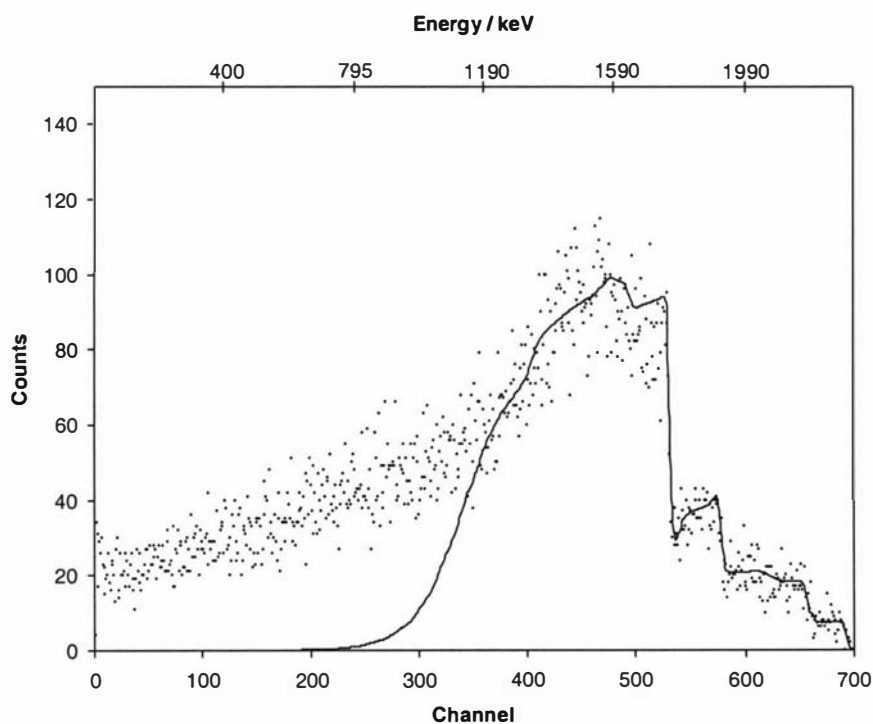
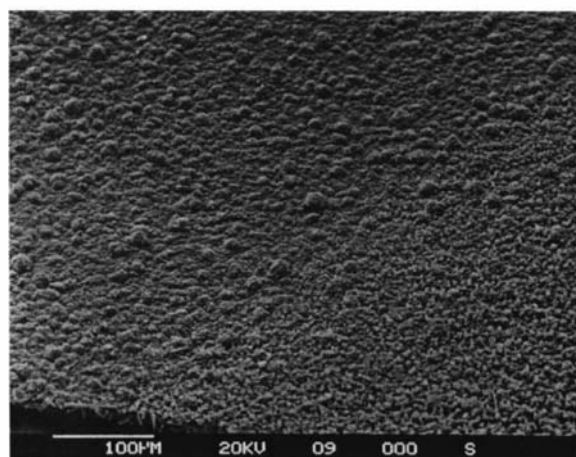
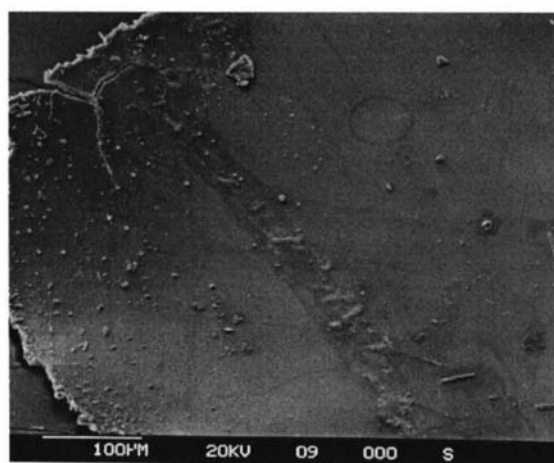


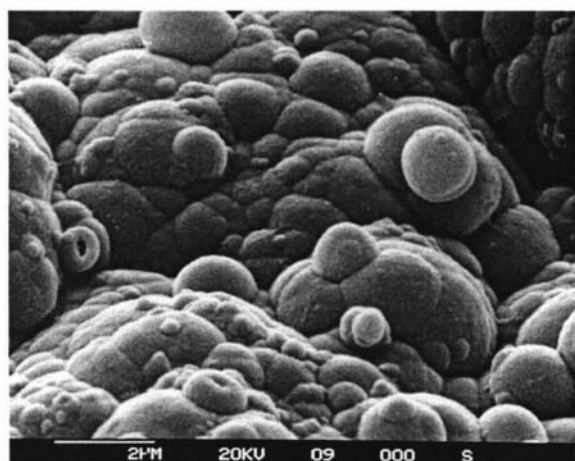
Fig 7.26 RBS experimental (●) and simulated (—) spectra for the electrode side of a TTh-Fc / bithiophene copolymer (1:10) using a 2.5 MeV proton beam.



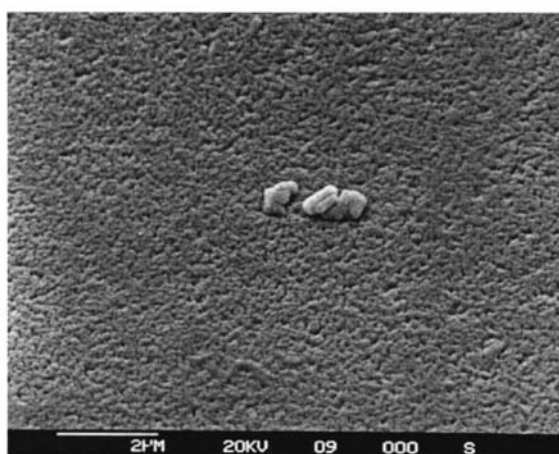
(a)



(b)



(c)



(d)

Fig. 7.27 SEM images of the solution and electrode side of the 1:10 TTh-Fc / bithiophene copolymer : (a) 100 μm solution side; (b) 100 μm electrode side; (c) 2 μm solution side; (d) 2 μm electrode side.

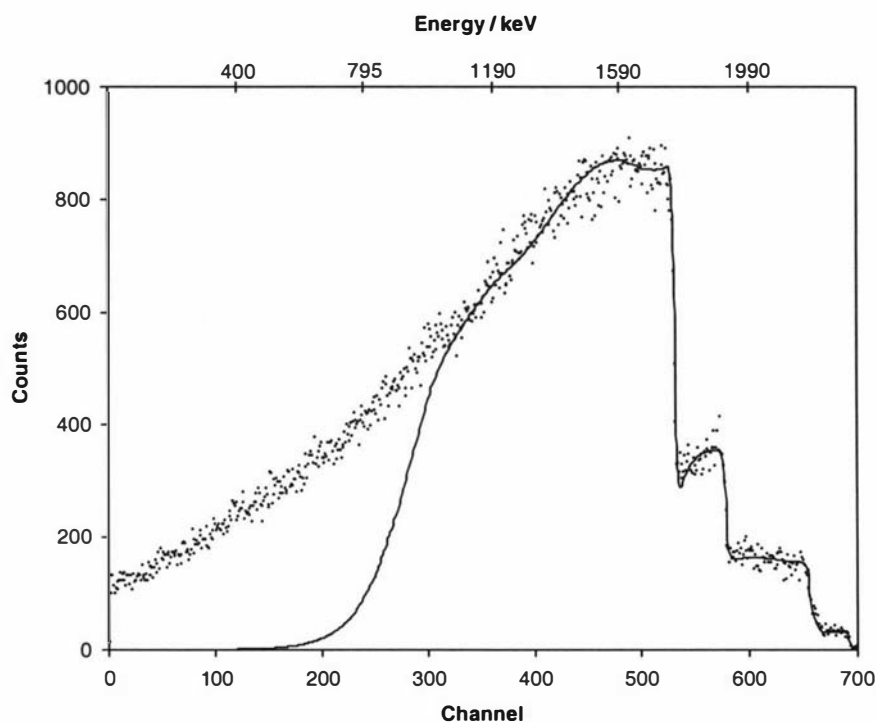


Fig 7.28 RBS experimental (●) and simulated (—) spectra for the solution side of a TTh-Fc / bithiophene copolymer (1:20) using a 2.5 MeV proton beam.

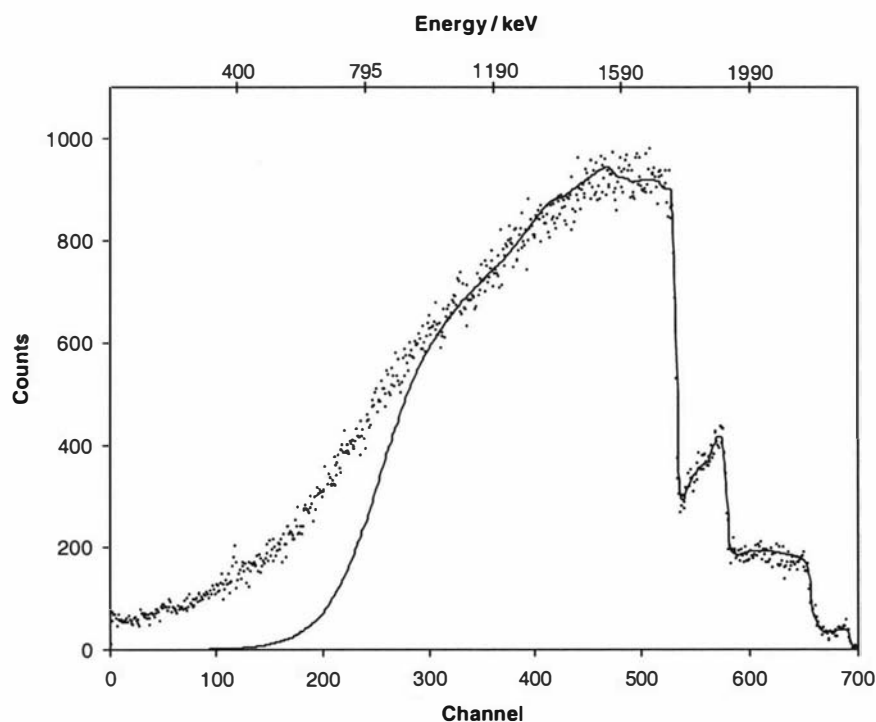
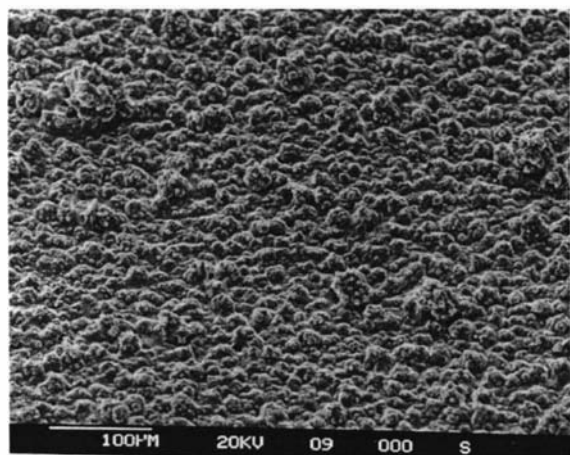
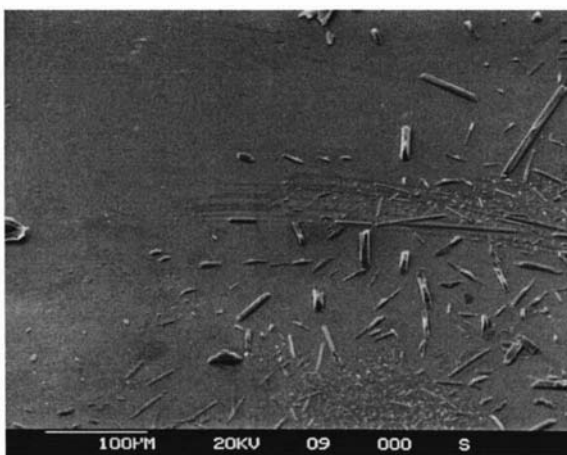


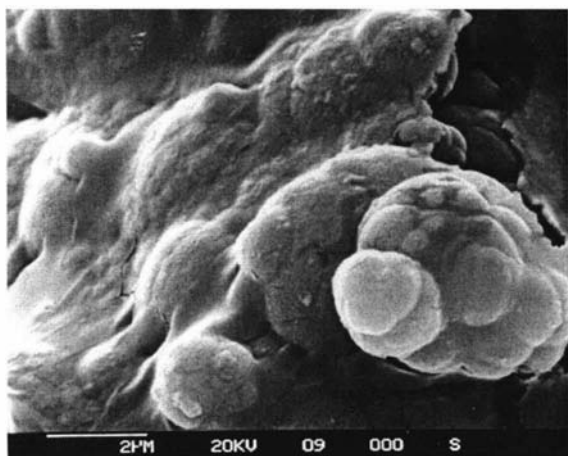
Fig 7.29 RBS experimental (●) and simulated (—) spectra for the electrode side of a TTh-Fc / bithiophene copolymer (1:20) using a 2.5 MeV proton beam.



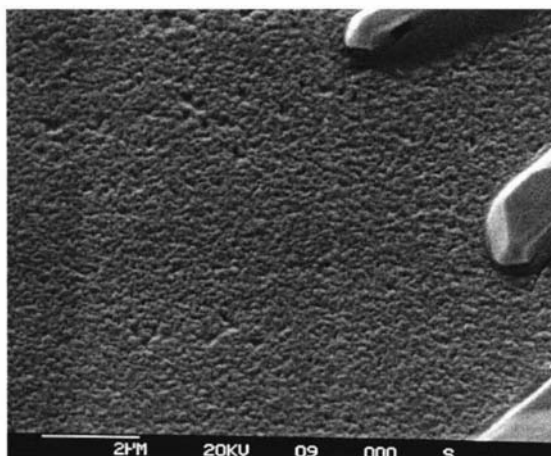
(a)



(b)



(c)



(d)

Fig. 7.30 SEM images of the solution and electrode side of the 1:20 TTh-Fc / bithiophene copolymer : (a) 100 μm solution side; (b) 100 μm electrode side; (c) 2 μm solution side; (d) 2 μm electrode side.

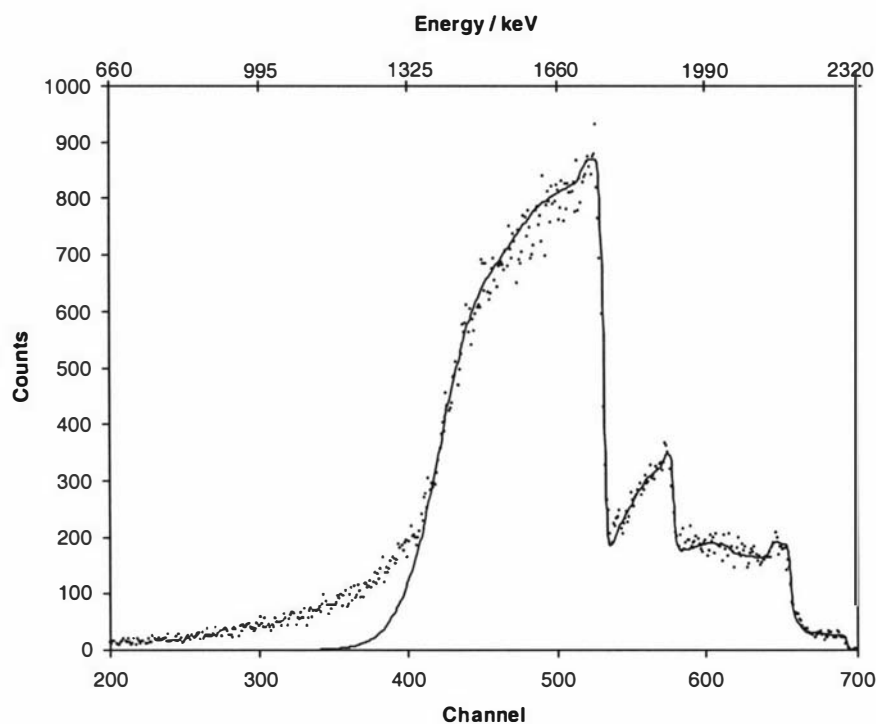


Fig 7.31 RBS experimental (●) and simulated (—) spectra for the solution side of a TTh-Fc / bithiophene copolymer (1:50) using a 2.5 MeV proton beam.

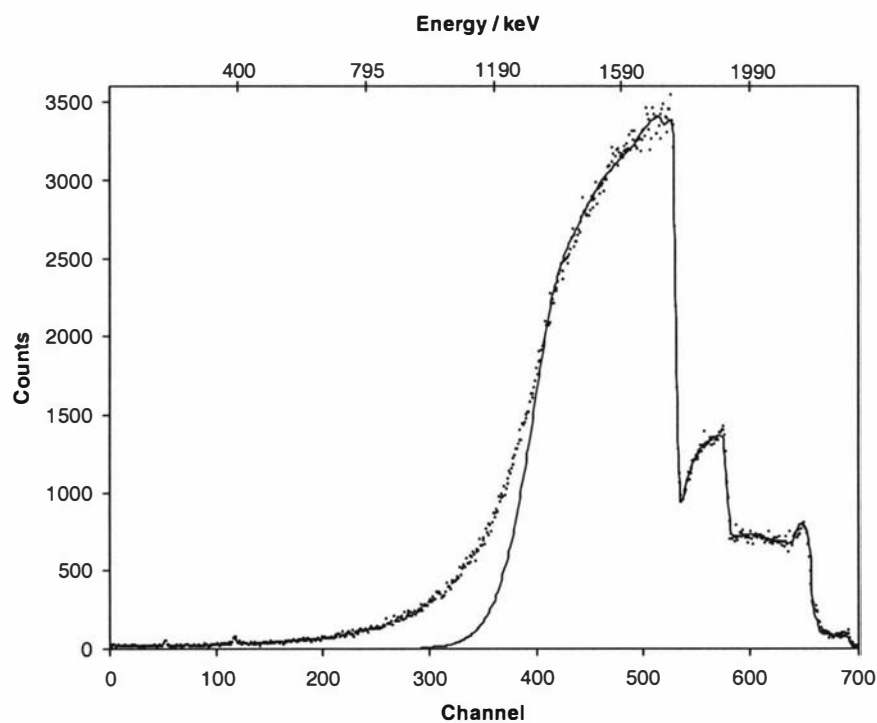
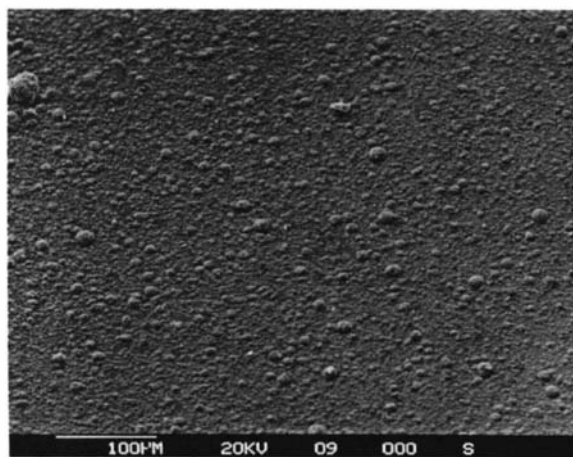
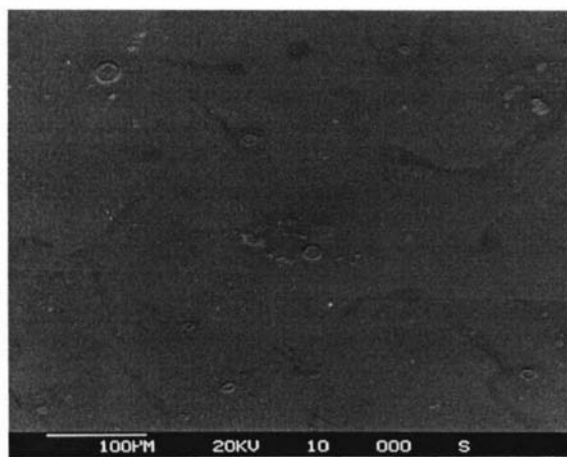


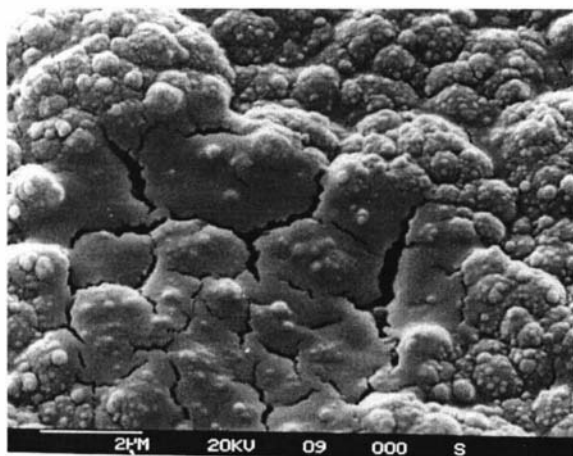
Fig. 7.32 RBS experimental (●) and simulated (—) spectra for the electrode side of a TTh-Fc / bithiophene copolymer (1:50) using a 2.5 MeV proton beam.



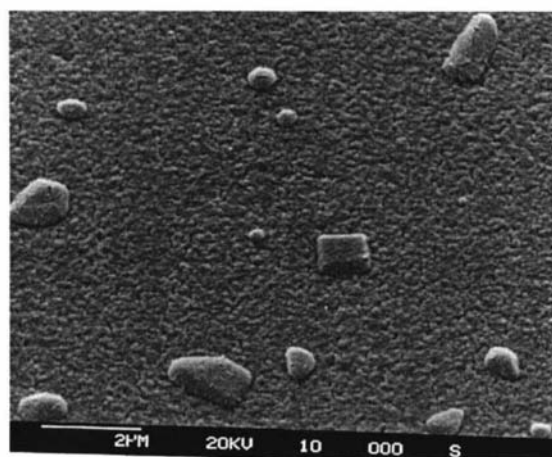
(a)



(b)



(c)



(d)

Fig. 7.33 SEM images of the solution and electrode side of the 1:50 TTh-Fc / bithiophene copolymer : (a) 100 μm solution side; (b) 100 μm electrode side; (c) 2 μm solution side; (d) 2 μm electrode side.

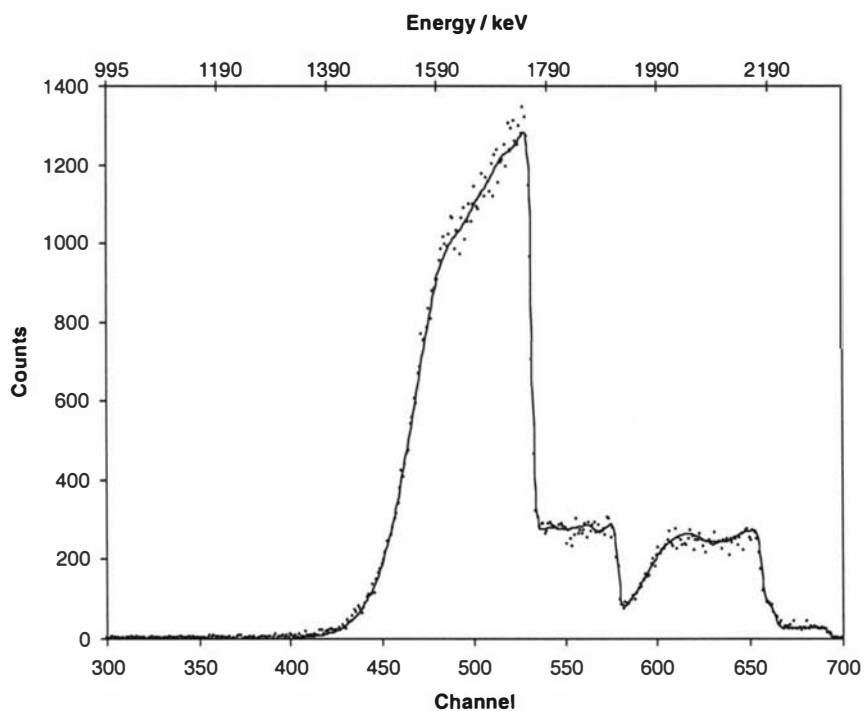


Fig. 7.34 RBS experimental (●) and simulated (—) spectra for the solution side of a TTh-Fc / bithiophene copolymer (1:100) using a 2.5 MeV proton beam.

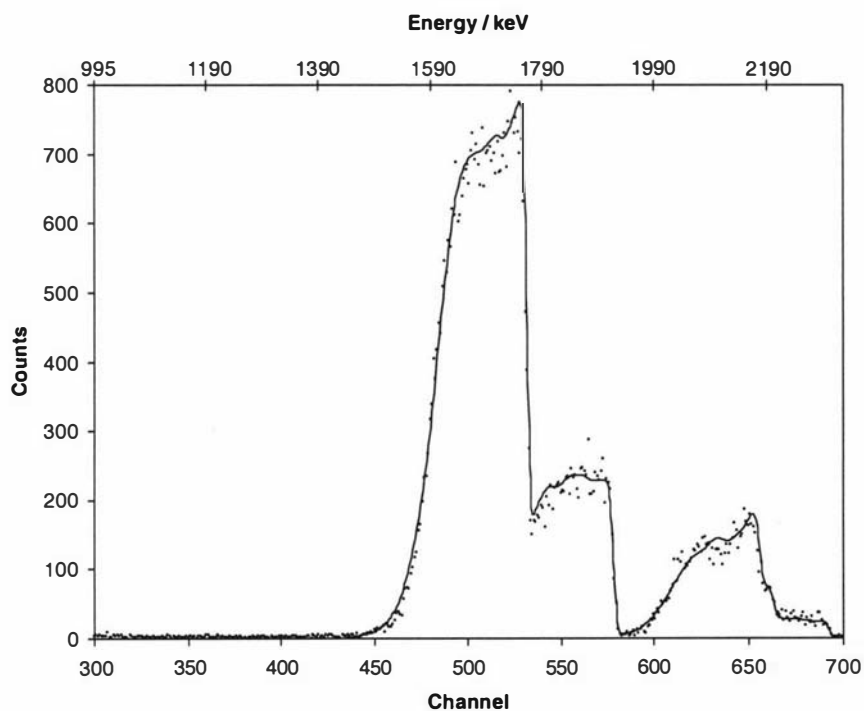
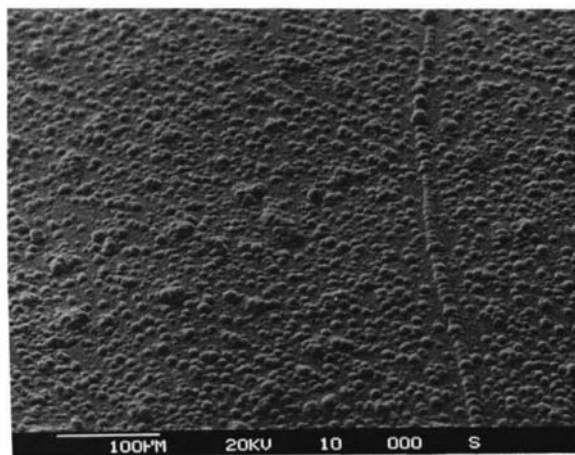
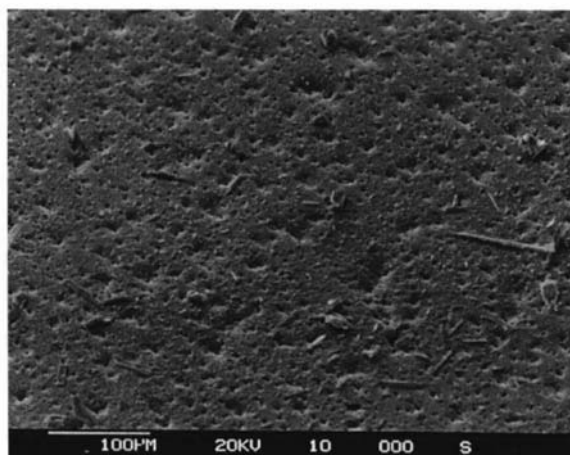


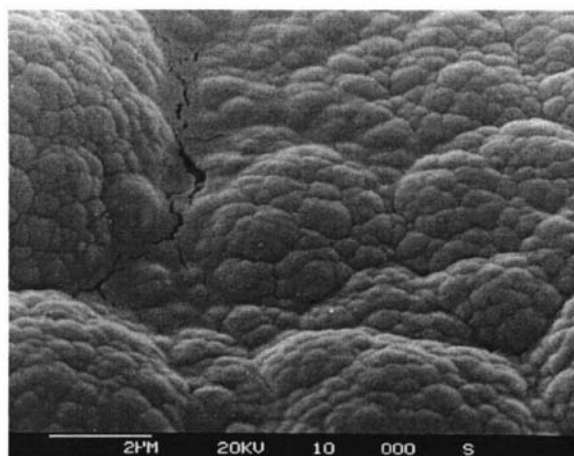
Fig. 7.35 RBS experimental (●) and simulated (—) spectra for the solution side of a TTh-Fc / bithiophene copolymer (1:100) using a 2.5 MeV proton beam.



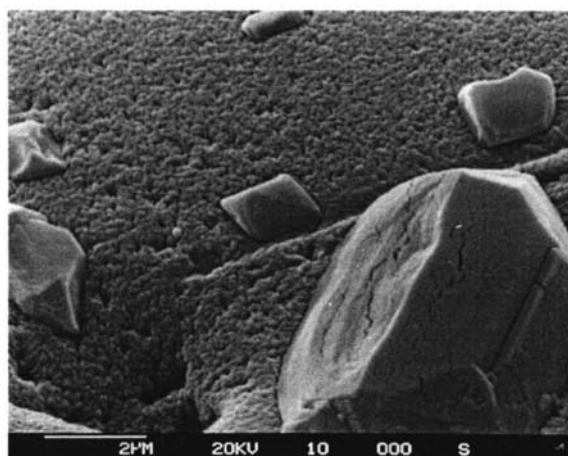
(a)



(b)



(c)



(d)

Fig. 7.36 SEM images of the solution and electrode side of the 1:100 TTh-Fc / bithiophene copolymer : (a) 100 μm solution side; (b) 100 μm electrode side; (c) 2 μm solution side; (d) 2 μm electrode side.

Table 7.4 Layer thickness, roughness factors, and total analysed depth of each TTh-Fc / Bithiophene film sample. Roughness factor values which have * have the roughness factor associated with the last simulated layer.

	Layer 1	Layer 2	Layer 3	Layer 4	Layer 5	Layer 6		
Monomer ratios (TTh-Fc / Bithiophene)	Thickness (μm)	Thickness (μm)	Thickness (μm)	Thickness (μm)	Thickness (μm)	Thickness (μm)	Roughness factor	Total thickness (μm)
1:10 solution side	8.04	8.08	7.63				0.70*	23.75
1:10 electrode side	5.82	2.15	5.59				0.38*	13.56
1:20 solution side	8.71	13.40	11.19				0.76	33.30
1:20 electrode side	2.10	4.78	2.06	7.51	7.65	13.89	0.78*	37.99
1:50 solution side	1.19	1.23	4.12	11.00			0.63	17.54
1:50 electrode side	2.35	10.46	8.57				0.66*	21.38
1:100 solution side	2.23	3.21	5.47				0.52	10.91
1:100 electrode side	2.35	1.99	3.75				0.52*	7.99

Table 7.5 Listed are the bithiophene (Th-Th) to terthiophene-ferrocene monomer ratios and counter ion to terthiophene-ferrocene monomer ratios for each simulated layer. All ratios are quoted with respect to one Terthiophene-ferrocene monomer.

	Layer 1		Layer 2		Layer 3		Layer 4		Layer 5		Layer 6	
Monomer ratios (TTh-Fc / bithiophene)	Th-Th (<i>m/n</i>)	Counter ion (<i>z/n</i>)	Th-Th (<i>m/n</i>)	Counter ion (<i>z/n</i>)	Th-Th (<i>m/n</i>)	Counter ion (<i>z/n</i>)	Th-Th (<i>m/n</i>)	Counter ion (<i>z/n</i>)	Th-Th (<i>m/n</i>)	Counter ion (<i>z/n</i>)	Th-Th (<i>m/n</i>)	Counter ion (<i>z/n</i>)
1:10 solution side	1.5	2.1	1.7	2.2	1.5	2.1						
1:10 electrode side	0.8	2.2	2.4	2.7	2.5	2.7						
1:20 solution side	1.5	1.1	1.5	0.9	1.5	0.5						
1:20 electrode side	1.4	1.6	1.8	2.4	2.1	2.6	2.0	1.4	2.2	1.6	1.1	1.4
1:50 solution side	3.3	1.7	3.2	2.7	1.5	2.4	2.1	0.9				
1:50 electrode side	5.3	3.4	3.9	3.3	3.5	2.8						
1:100 solution side	5.5	4.1	4.5	4.4	5.2	4.3						
1:100 electrode side	3.0	4.1	2.4	2.1	1.6	3.3						

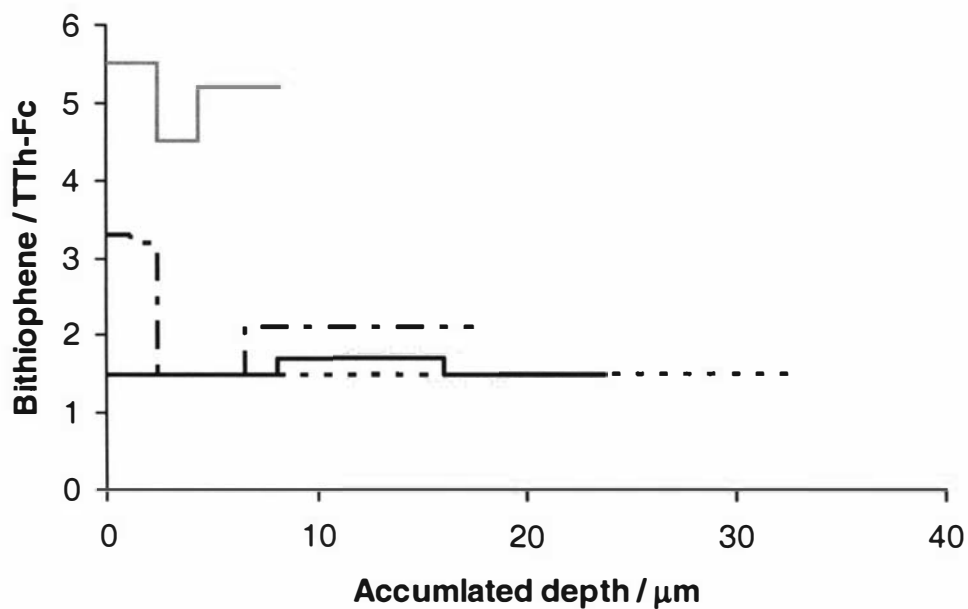


Fig 7.37 Plot of bithiophene / TTh-Fc ratios changing with depth into the solution side of the copolymer, — 1:10, 1:20, — · — · 1:50, — 1:100.

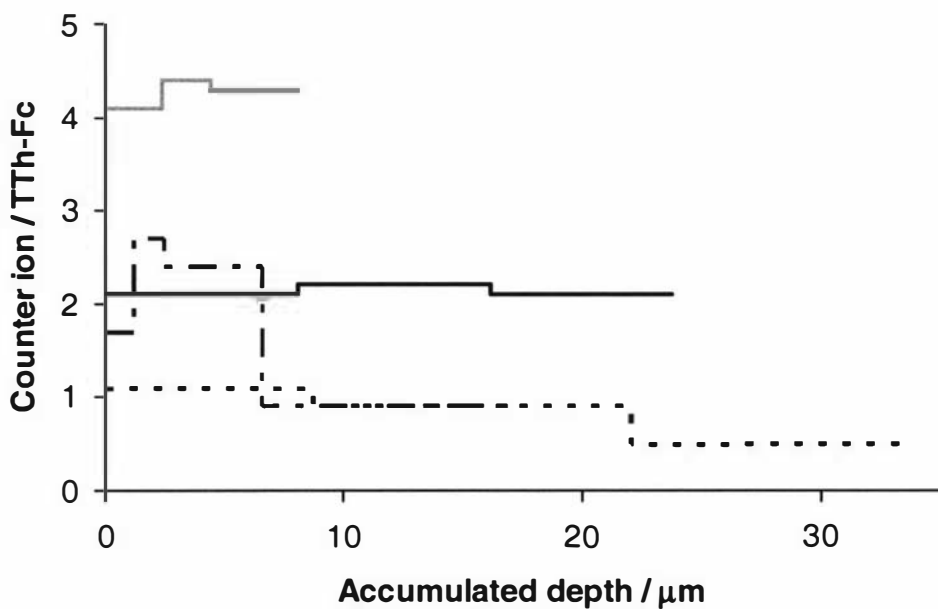


Fig 7.38 Plot of counter ion / TTh-Fc ratios changing with depth into the solution side of the bithiophene / TTh-Fc copolymer, — 1:10, 1:20, — · — · 1:50, — 1:100.

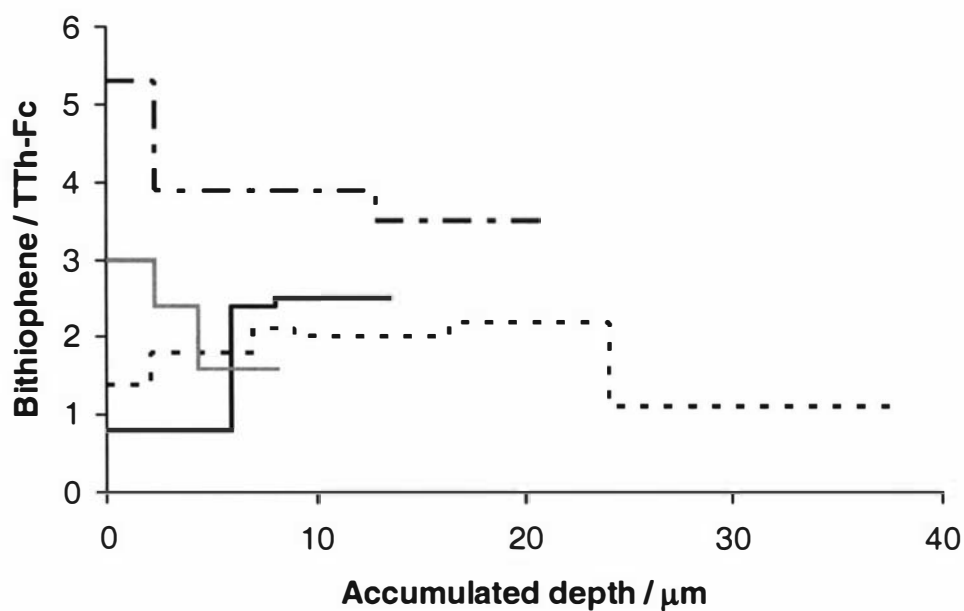


Fig 7.39 Plot of bithiophene / TTh-Fc ratios changing with depth into the electrode side of the copolymer, — 1:10, 1:20, — · — · 1:50, — — — 1:100.

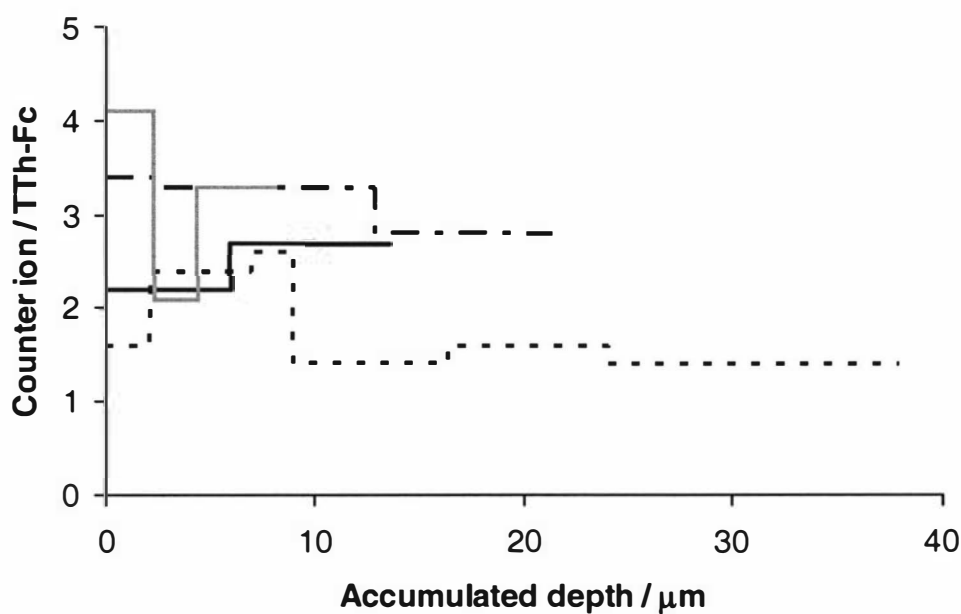


Fig 7.40 Plot of counter ion / TTh-Fc ratios changing with depth into the electrode side of the bithiophene / TTh-Fc copolymer, — 1:10, 1:20, — · — · 1:50, — — — 1:100.

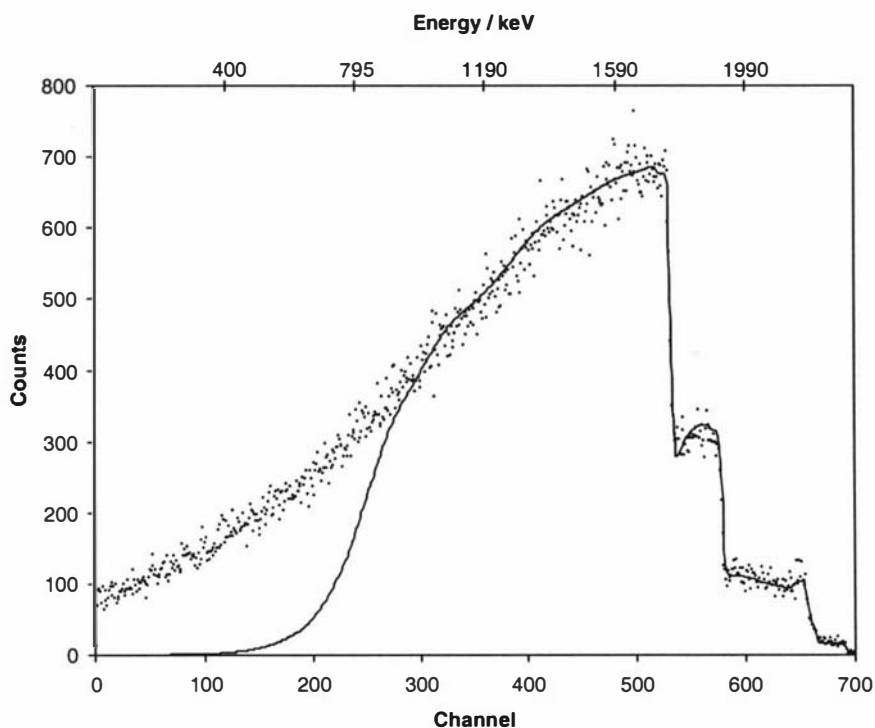


Fig. 7.41 RBS experimental (●) and simulated (—) spectra for the solution side of a TTh-Fc / EDOT copolymer (1:10) using a 2.5 MeV proton beam.

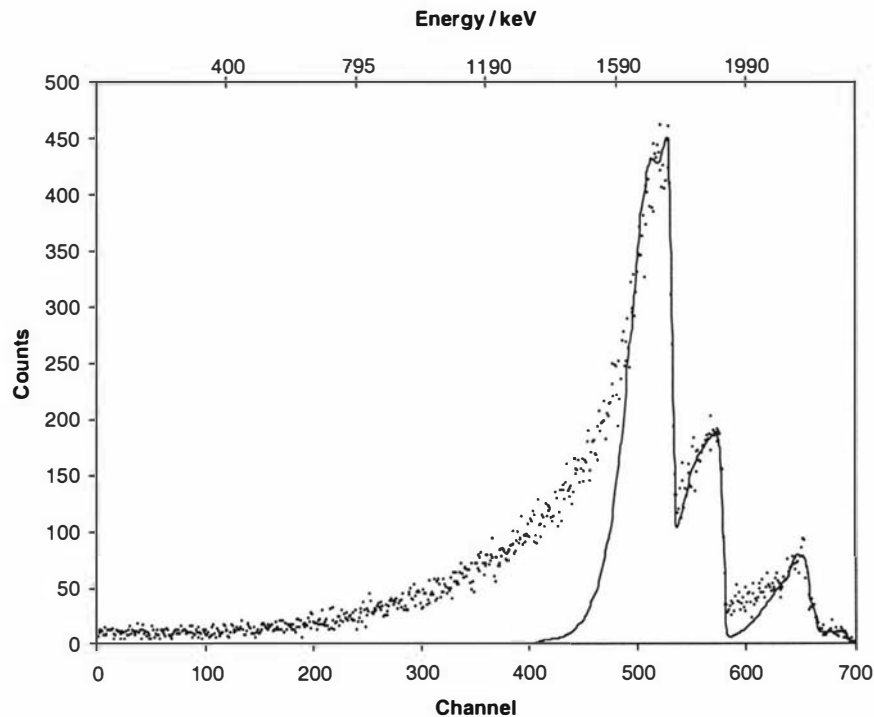
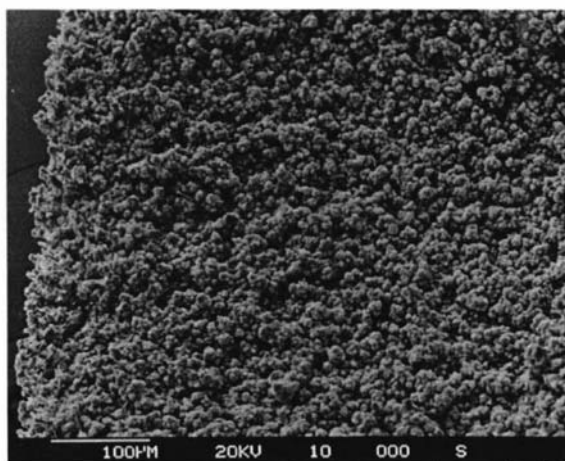
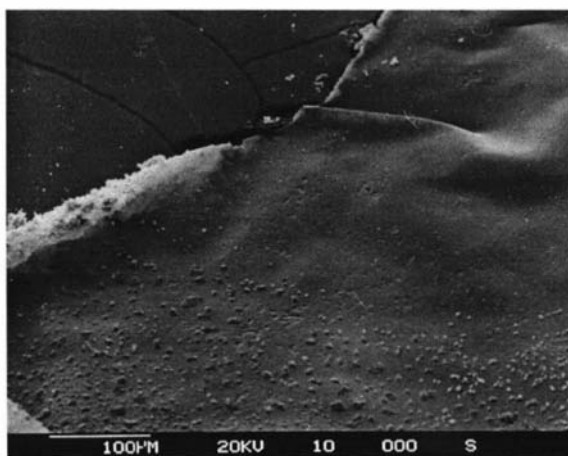


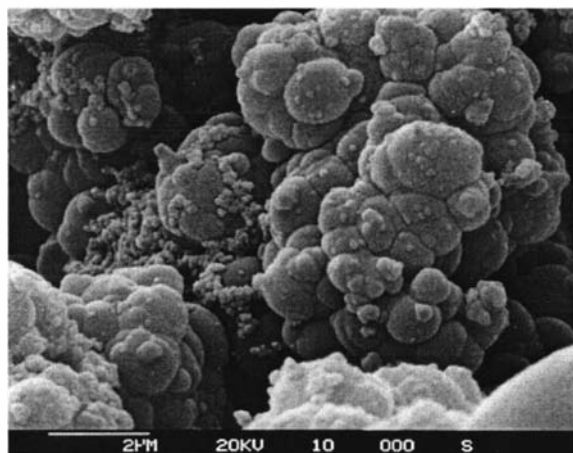
Fig. 7.42 RBS experimental (●) and simulated (—) spectra for the electrode side of a TTh-Fc / EDOT copolymer (1:10) using a 2.5 MeV proton beam.



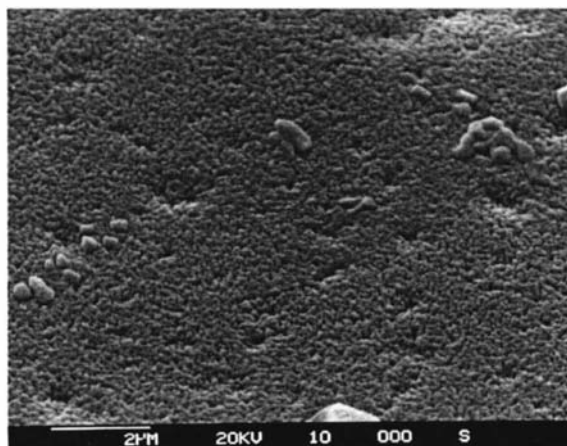
(a)



(b)



(c)



(d)

Fig. 7.43 SEM images of the solution and electrode side of the 1:10 TTh-Fc /EDOT copolymer : (a) 100 μm solution side; (b) 100 μm electrode side; (c) 2 μm solution side; (d) 2 μm electrode side.

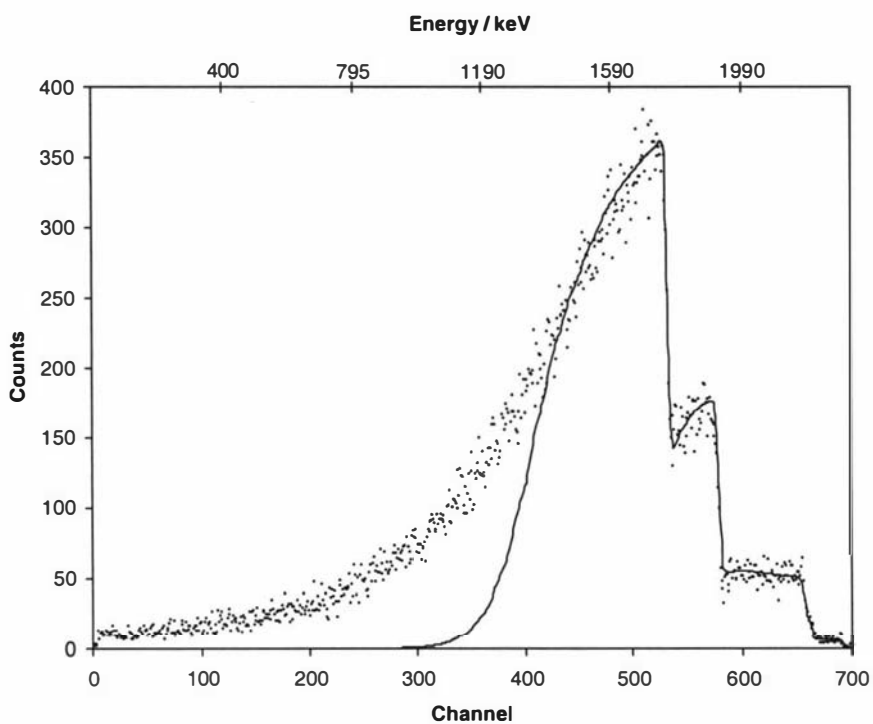
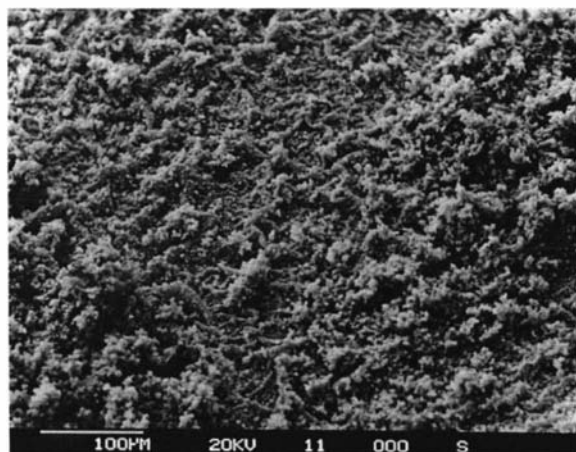
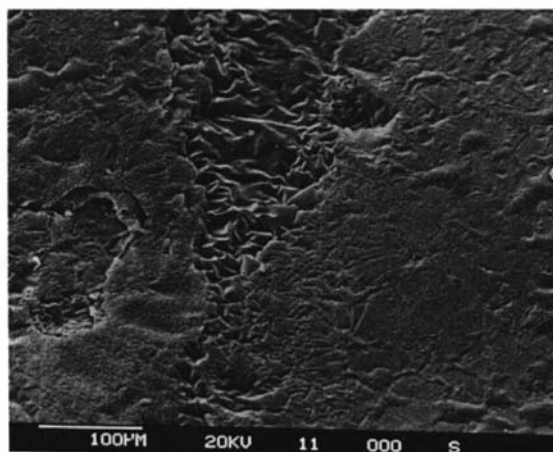


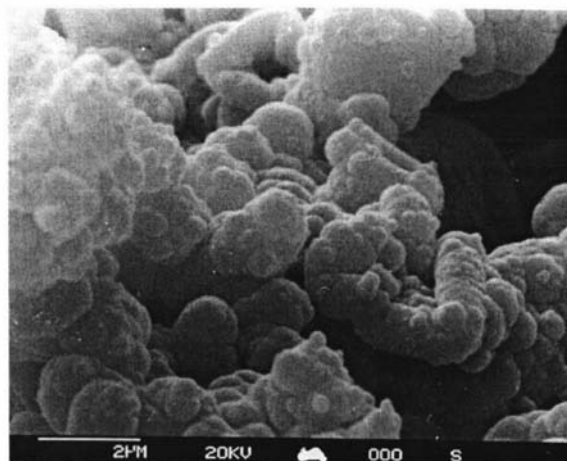
Fig. 7.44 RBS experimental (●) and simulated (—) spectra for the solution side of a TTh-Fc / EDOT copolymer (1:20) using a 2.5 MeV proton beam.



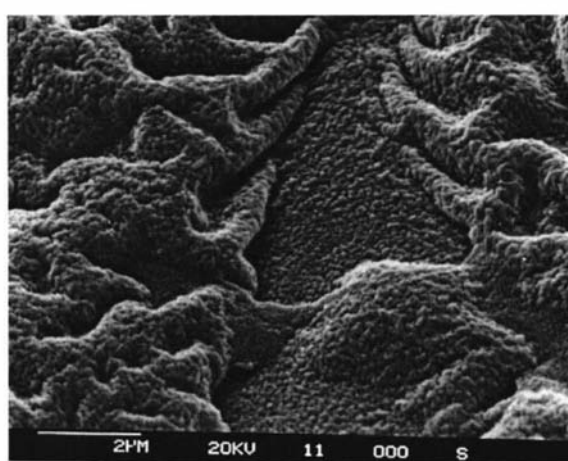
(a)



(b)



(c)



(d)

Fig. 7.45 SEM images of the solution and electrode side of the 1:20 TTh-Fc / EDOT copolymer : (a) 100 μm solution side; (b) 100 μm electrode side; (c) 2 μm solution side; (d) 2 μm electrode side.

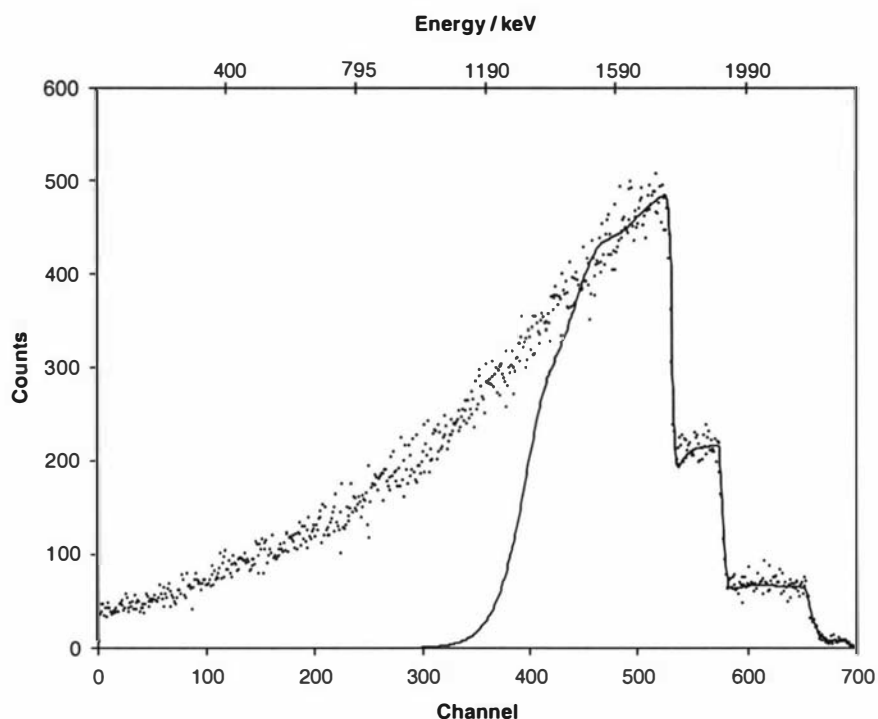


Fig. 7.46 RBS experimental (●) and simulated (—) spectra for the solution side of a TTh-Fc / EDOT copolymer (1:50) using a 2.5 MeV proton beam.

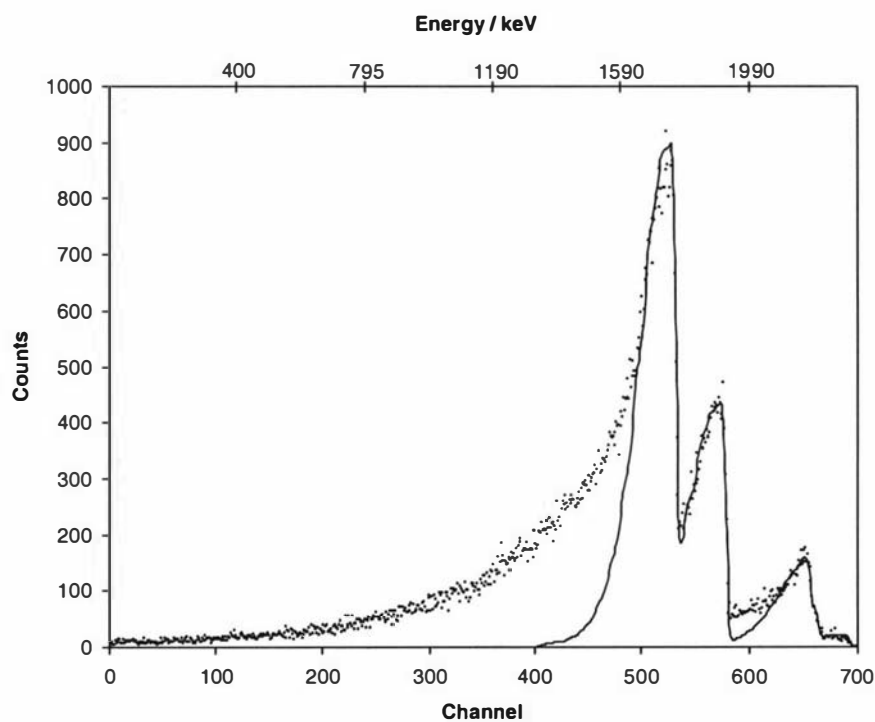
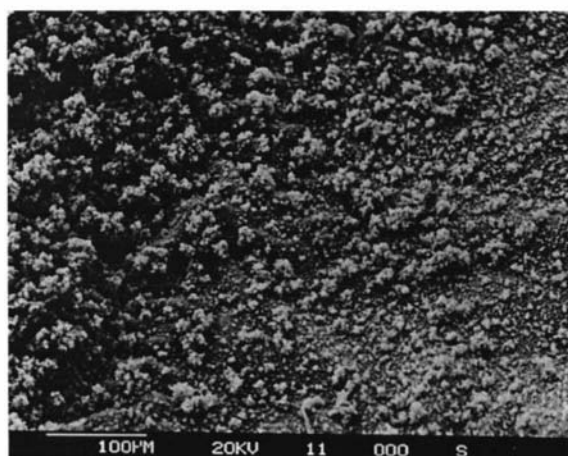
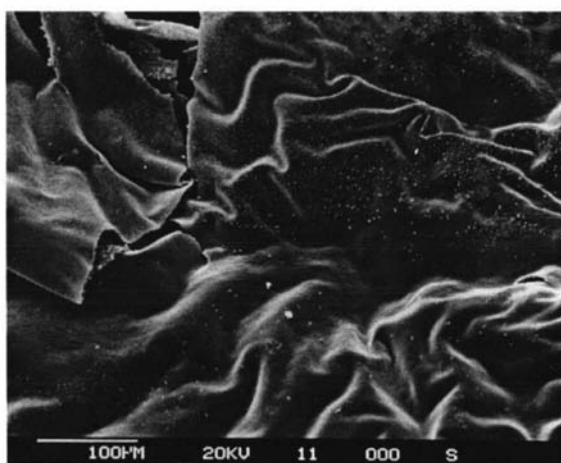


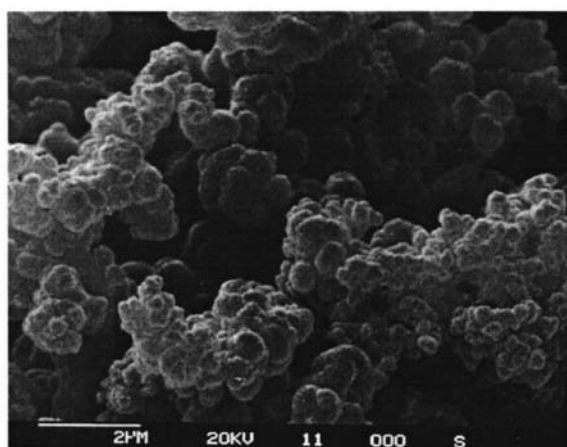
Fig. 7.47 RBS experimental (●) and simulated (—) spectra for the electrode side of a TTh-Fc / EDOT copolymer (1:50) using a 2.5 MeV proton beam.



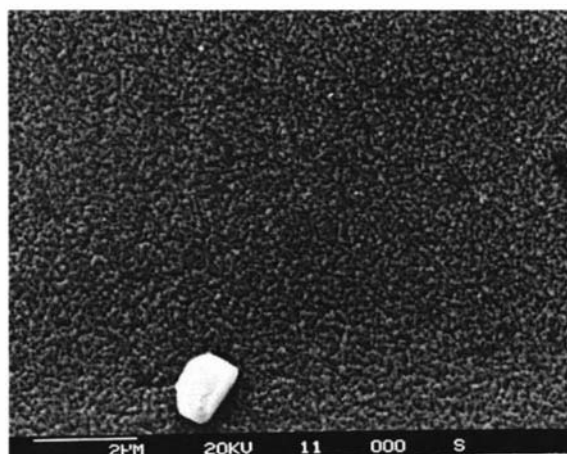
(a)



(b)



(c)



(d)

Fig. 7.48 SEM images of the solution and electrode side of the 1:50 TTh-Fc / EDOT copolymer : (a) 100 μm solution side; (b) 100 μm electrode side; (c) 2 μm solution side; (d) 2 μm electrode side.

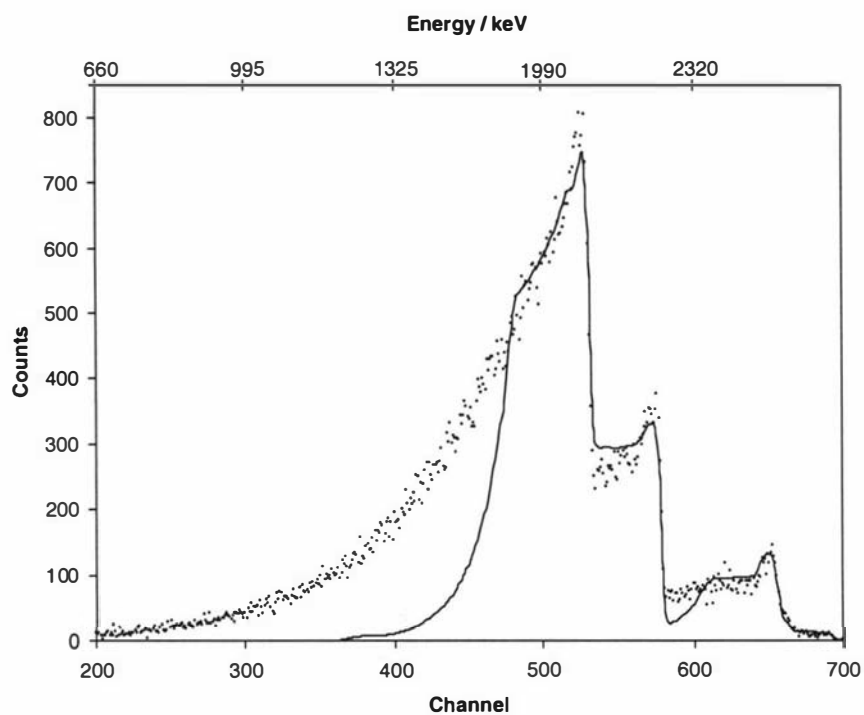
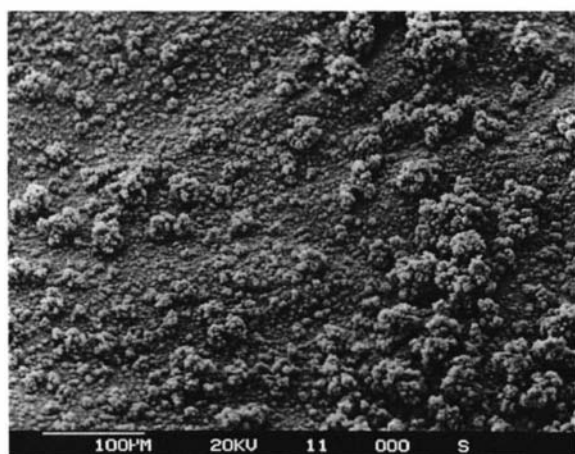
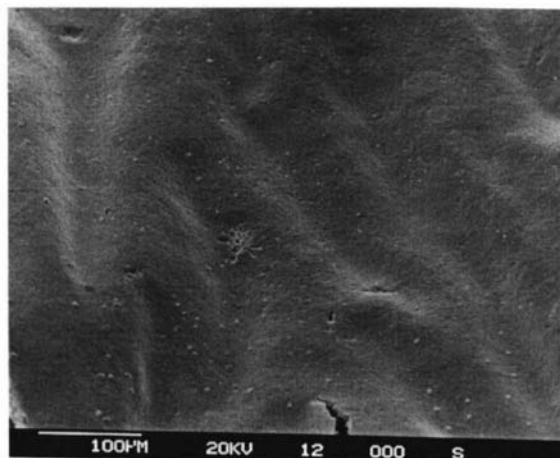


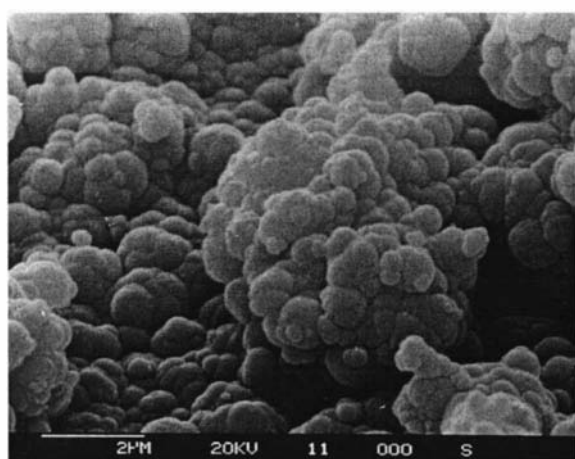
Fig. 7.49 RBS experimental (●) and simulated (—) spectra for the electrode side of a TTh-Fc / EDOT copolymer (1:100) using a 2.5 MeV proton beam.



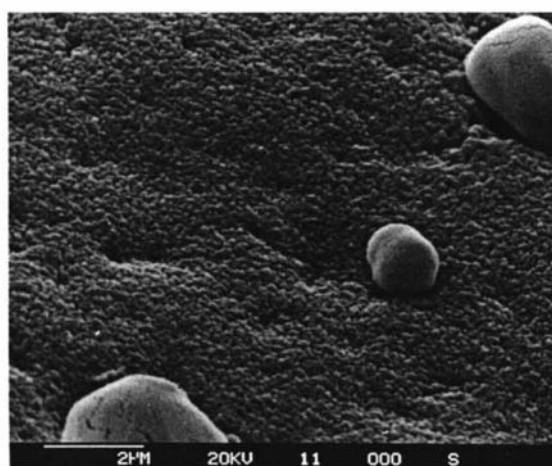
(a)



(b)



(c)



(d)

Fig. 7.50 SEM images of the solution and electrode side of the 1:100 TTh-Fc / EDOT copolymer : (a) 100 μm solution side; (b) 100 μm electrode side; (c) 2 μm solution side; (d) 2 μm electrode side.

Table 7.6 Layer thickness, roughness factors, and total analysed depth of each TTh-Fc / EDOT sample. Roughness factor values which have * have the roughness factor associated with the last simulated layer.

	Layer 1	Layer 2	Layer 3	Layer 4		
Monomer ratios (TTh-Fc / EDOT)	Thickness (μm)	Thickness (μm)	Thickness (μm)	Thickness (μm)	Roughness factor	Total thickness (μm)
1:10 solution side	1.93	6.46	12.64	12.64	0.81	38.77
1:10 electrode side	2.57	5.89			0.21*	8.46
1:20 solution side	14.16	6.27			0.58	20.43
1:50 solution side	6.52	4.38	10.38	10.38	0.70	21.28
1:50 electrode side	1.52	5.23			0.00*	6.75
1:100 electrode side	1.96	6.14	3.11		0.31*	11.21

Table 7.7 Listed are the EDOT to terthiophene-ferrocene monomer ratios and counter ion to terthiophene-ferrocene monomer ratios for each simulated layer. All ratios are quoted with respect to one terthiophene-ferrocene monomer.

	Layer 1		Layer 2		Layer 3		Layer 4	
Monomer ratio (TTh-Fc / EDOT)	EDOT (<i>m/n</i>)	Counter ion (<i>z/n</i>)	EDOT (<i>m/n</i>)	Counter ion (<i>z/n</i>)	EDOT (<i>m/n</i>)	Counter ion (<i>z/n</i>)	EDOT (<i>m/n</i>)	Counter ion (<i>z/n</i>)
1:10 solution side	4.1	3.6	3.1	2.3	4.1	3.6	4.3	1.3
1:10 electrode side	6.7	5.5	2.4	0.7				
1:20 solution side	6.9	6.3	6.8	0.8				
1:50 solution side	7.0	6.1	7.0	3.9	6.6	2.8		
1:50 electrode side	6.9	6.6	4.5	2.5				
1:100 electrode side	7.0	6.1	7.0	3.9	6.6	2.8		

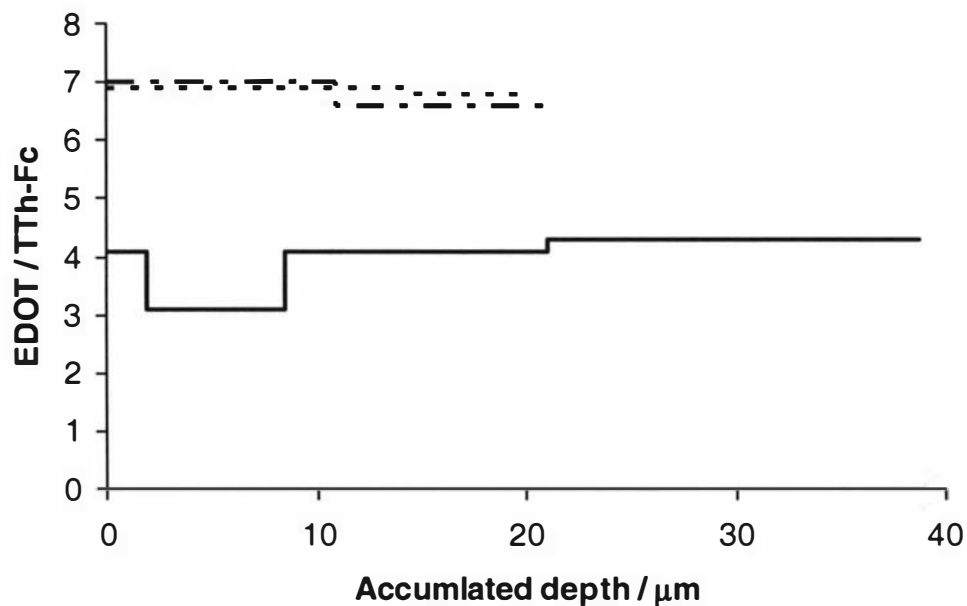


Fig 7.51 Plot of EDOT / TTh-Fc ratios changing with depth into the solution side of the copolymer, — 1:10, 1:20, — · — · 1:50.

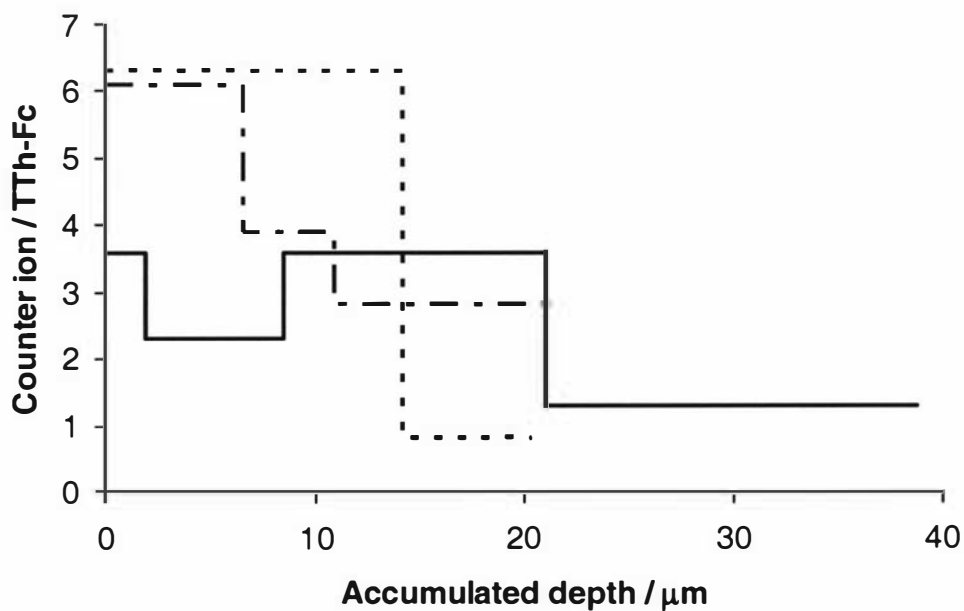


Fig 7.52 Plot of counter ion / TTh-Fc ratios changing with depth into the solution side of the EDOT / TTh-Fc copolymer, — 1:10, 1:20, — · — · 1:50.

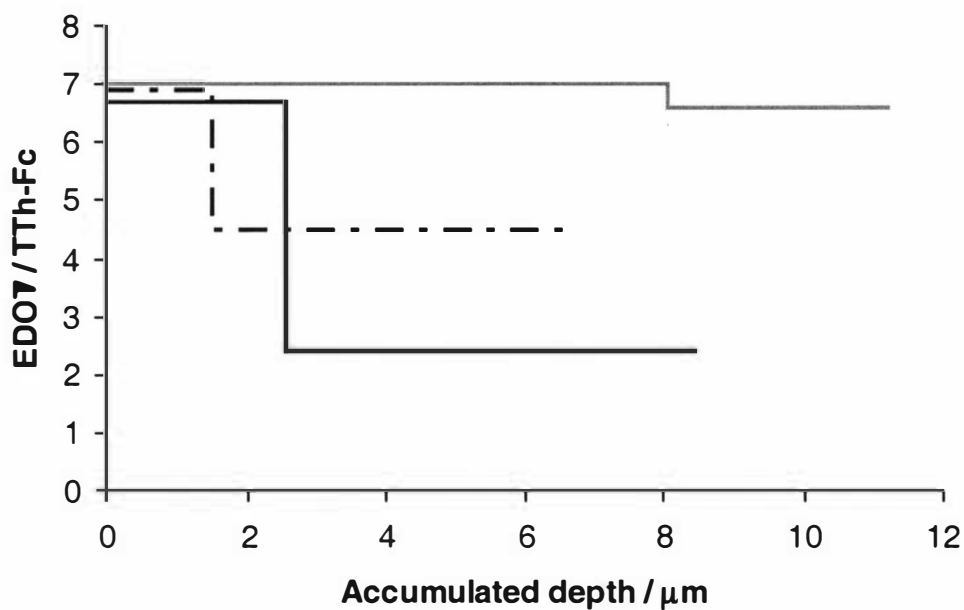


Fig 7.53 Plot of EDOT / TTh-Fc ratios changing with depth into the electrode side of the copolymer, — 1:10, — · — · 1:50, — 1:100.

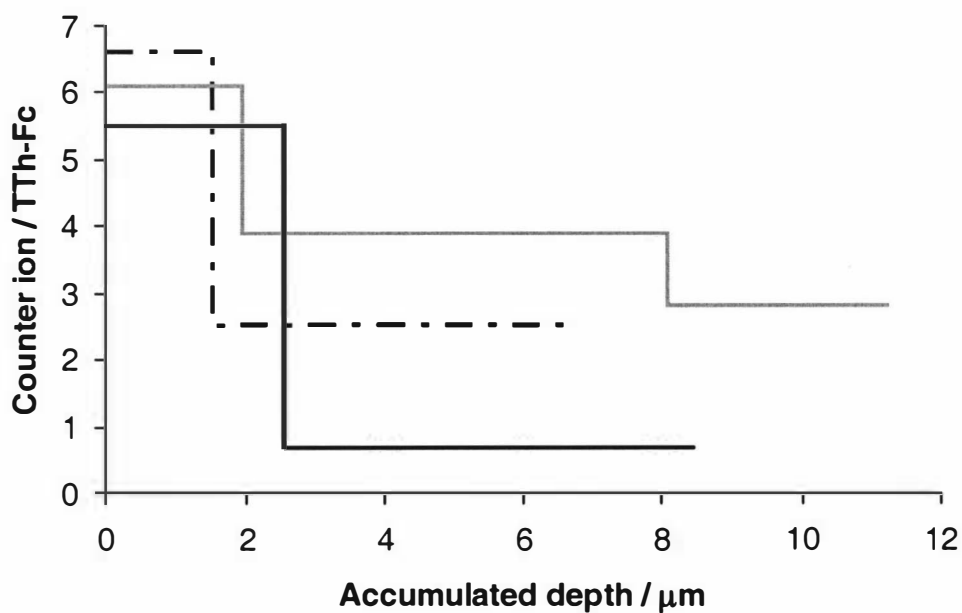


Fig 7.54 Plot of counter ion / TTh-Fc ratios changing with depth into the electrode side of the TTh-Fc / EDOT copolymer, — 1:10, — · — · 1:50, — 1:100.

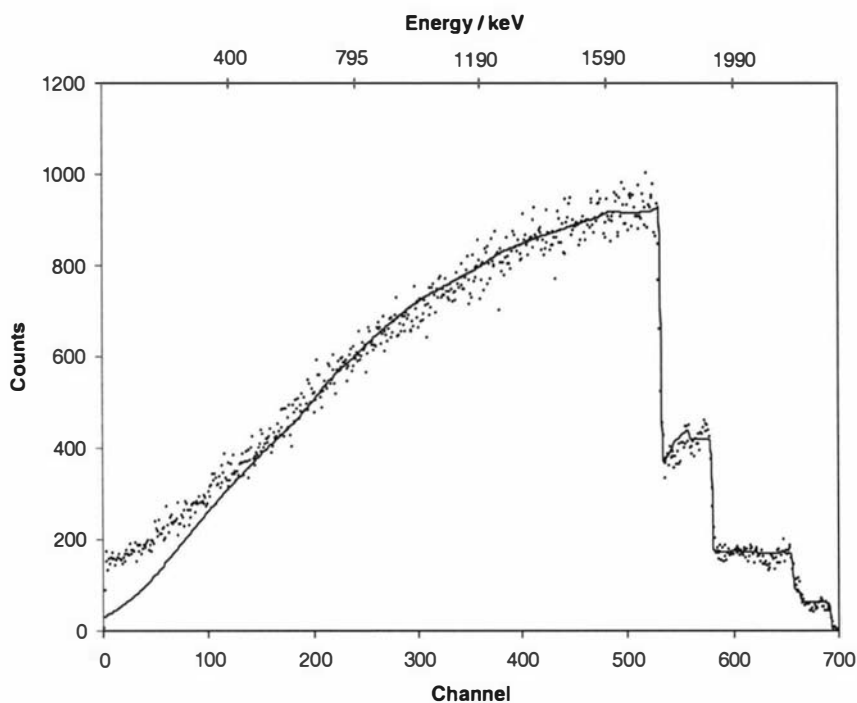


Fig. 7.55 RBS experimental (●) and simulated (—) spectra for the electrode side of a TTh-Fc / TTh-Por-TTh copolymer (2:1) using a 2.5 MeV proton beam.

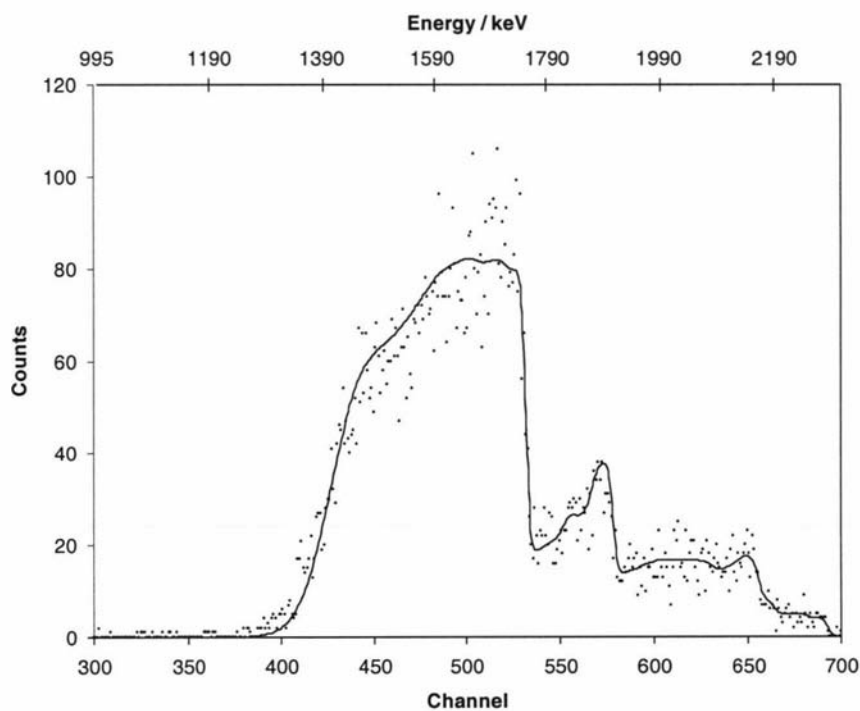
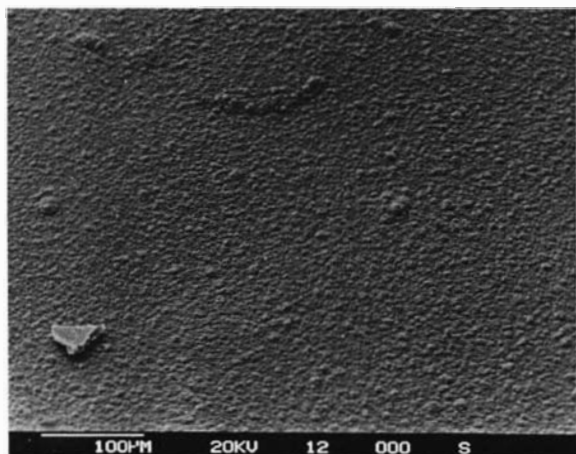
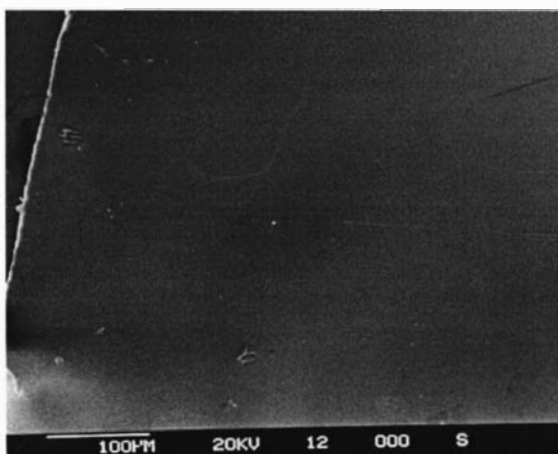


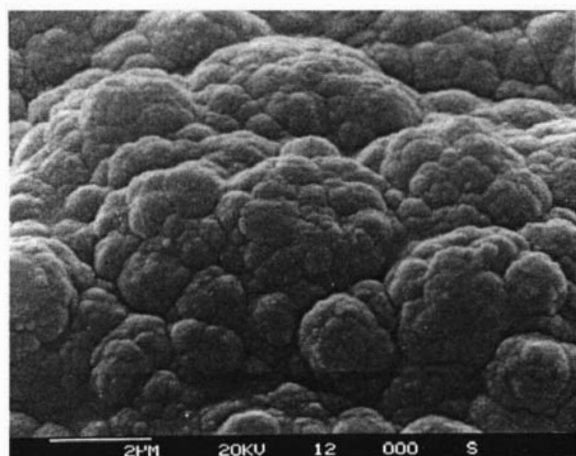
Fig. 7.56 RBS experimental (●) and simulated (—) spectra for the solution side of a TTh-Fc / TTh-Por-TTh copolymer (2:1) using a 2.5 MeV proton beam.



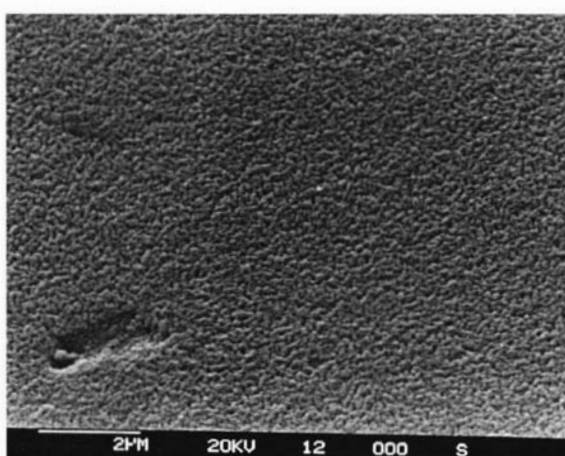
(a)



(b)



(c)



(d)

Fig. 7.57 SEM images of the solution and electrode side of the 2:1 TTh-Fc / TTh-Por-TTh copolymer : (a) 100 μm solution side; (b) 100 μm electrode side; (c) 2 μm solution side; (d) 2 μm electrode side.

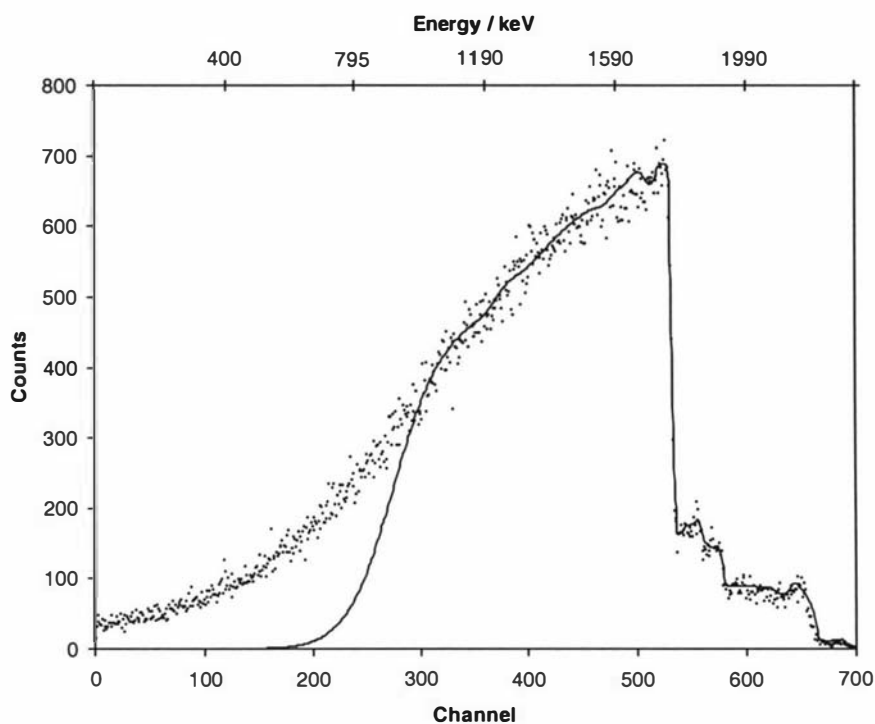


Fig. 7.58 RBS experimental (●) and simulated (—) spectra for the electrode side of a TTh-Fc / TTh-Por-TTh copolymer (1:5) using a 2.5 MeV proton beam.

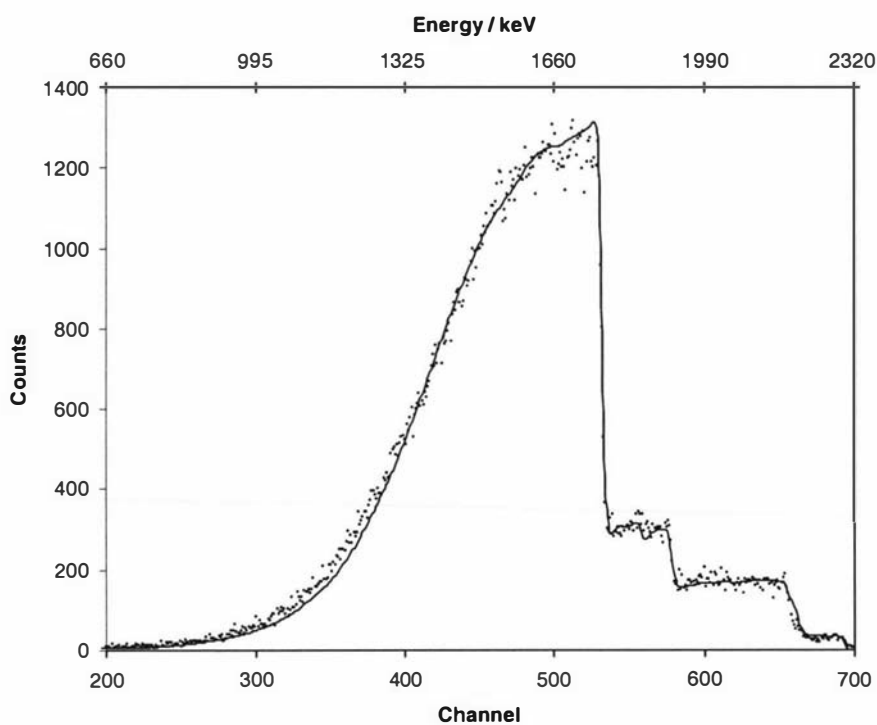
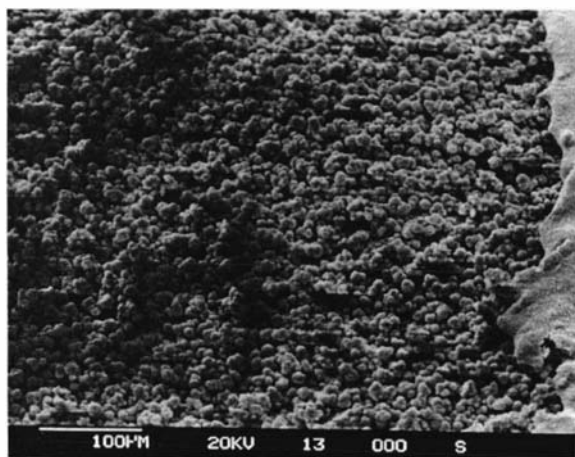
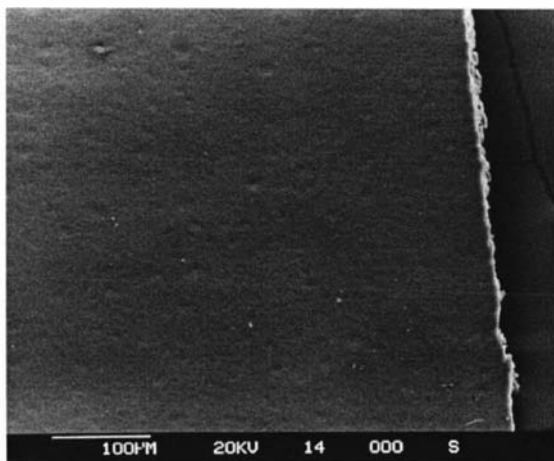


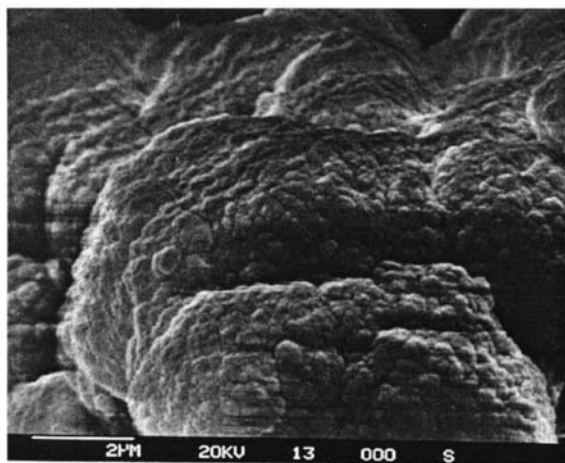
Fig. 7.59 RBS experimental (●) and simulated (—) spectra for the solution side of a TTh-Fc / TTh-Por-TTh copolymer (1:5) using a 2.5 MeV proton beam.



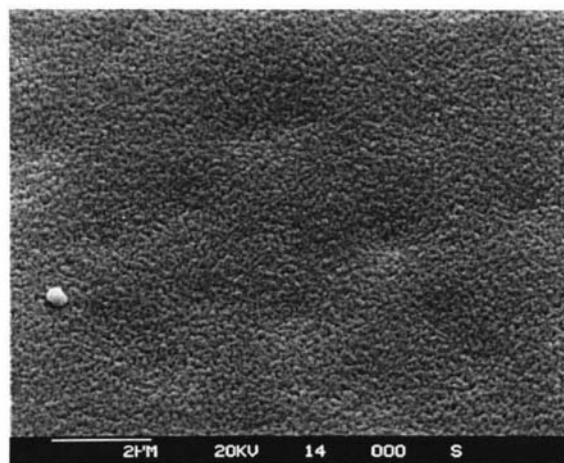
(a)



(b)



(c)



(d)

Fig. 7.60 SEM images of the solution and electrode side of the 1:5 TTh-Fc / TTh-Por-TTh copolymer : (a) 100 μm solution side; (b) 100 μm electrode side; (c) 2 μm solution side; (d) 2 μm electrode side.

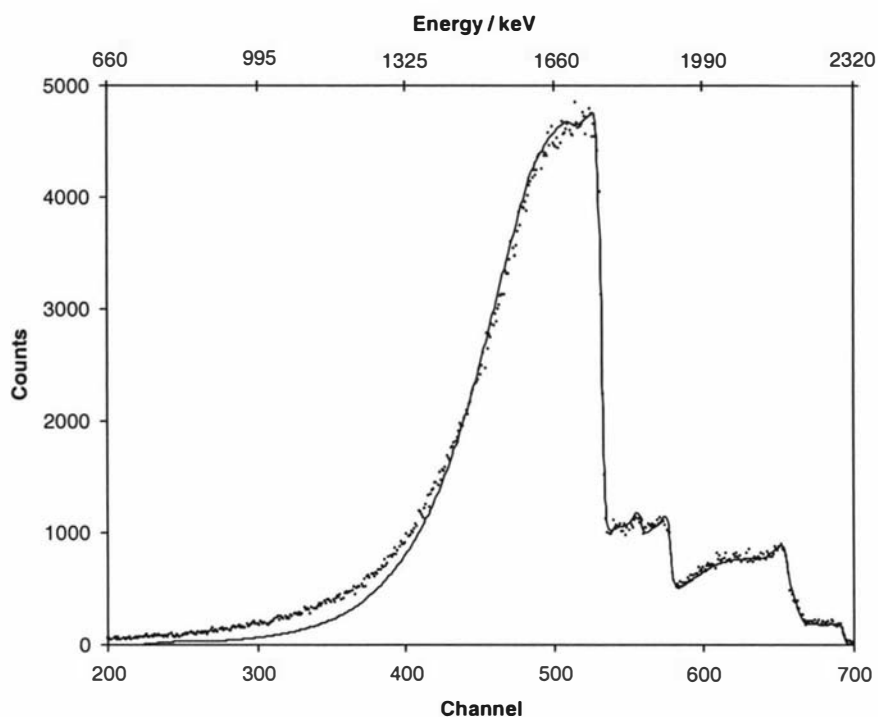


Fig. 7.61 RBS experimental (●) and simulated (—) spectra for the solution side of a TTh-Fc / TTh-Por-TTh copolymer (2:5) using a 2.5 MeV proton beam.

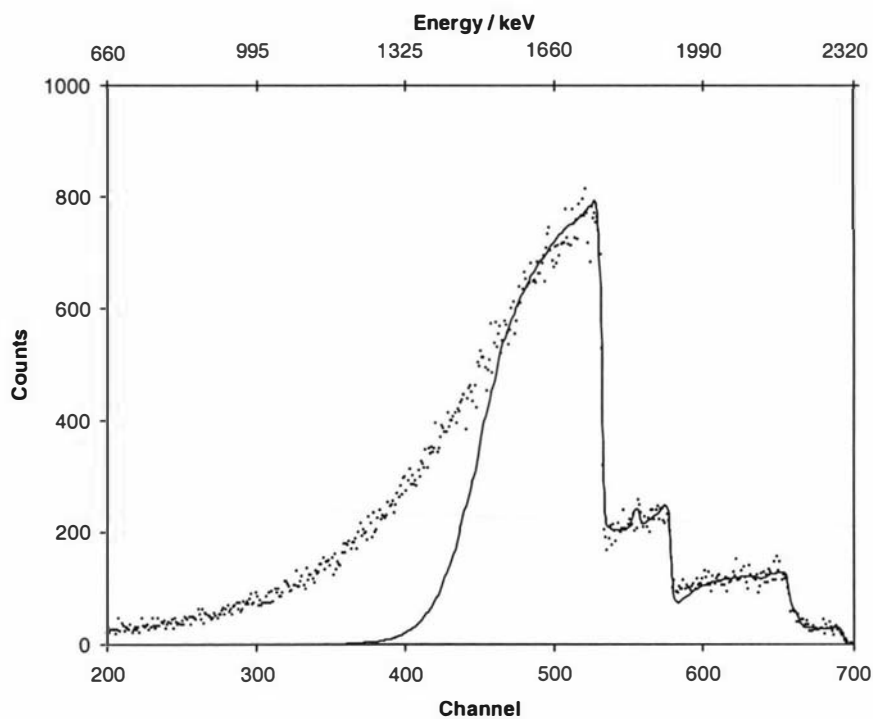
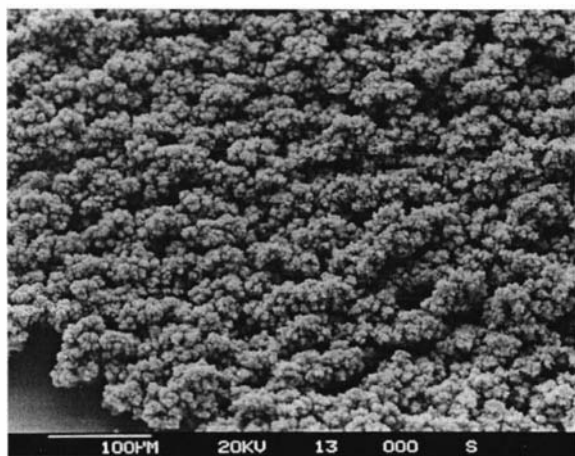
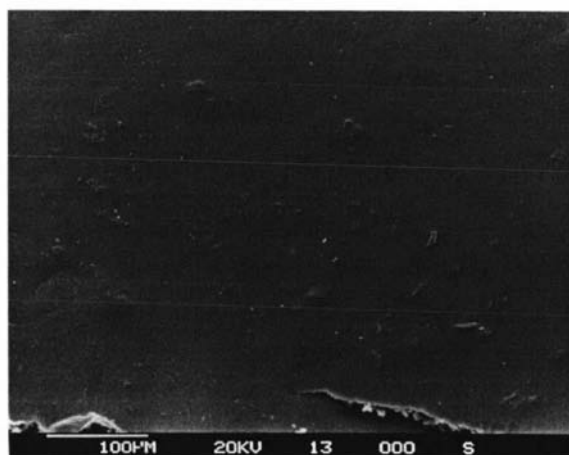


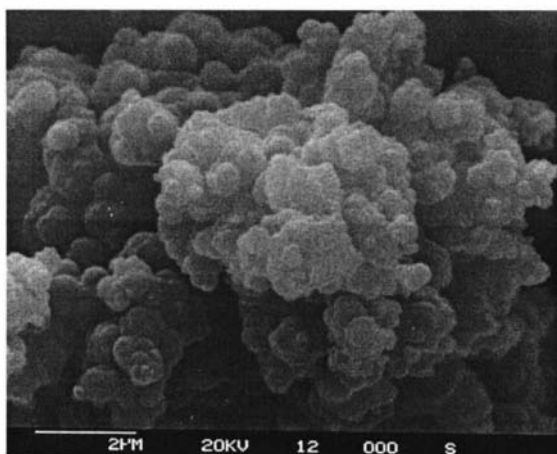
Fig. 7.62 RBS experimental (●) and simulated (—) spectra for the electrode side of a TTh-Fc / TTh-Por-TTh copolymer (2:5) using a 2.5 MeV proton beam.



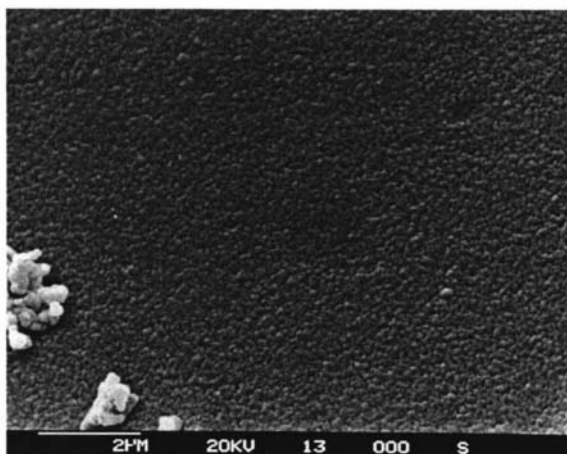
(a)



(b)



(c)



(d)

Fig. 7.63 SEM images of the solution and electrode side of the 2:5 TTh-Fc / TTh-Por-TTh copolymer : (a) 100 μm solution side; (b) 100 μm electrode side; (c) 2 μm solution side; (d) 2 μm electrode side.

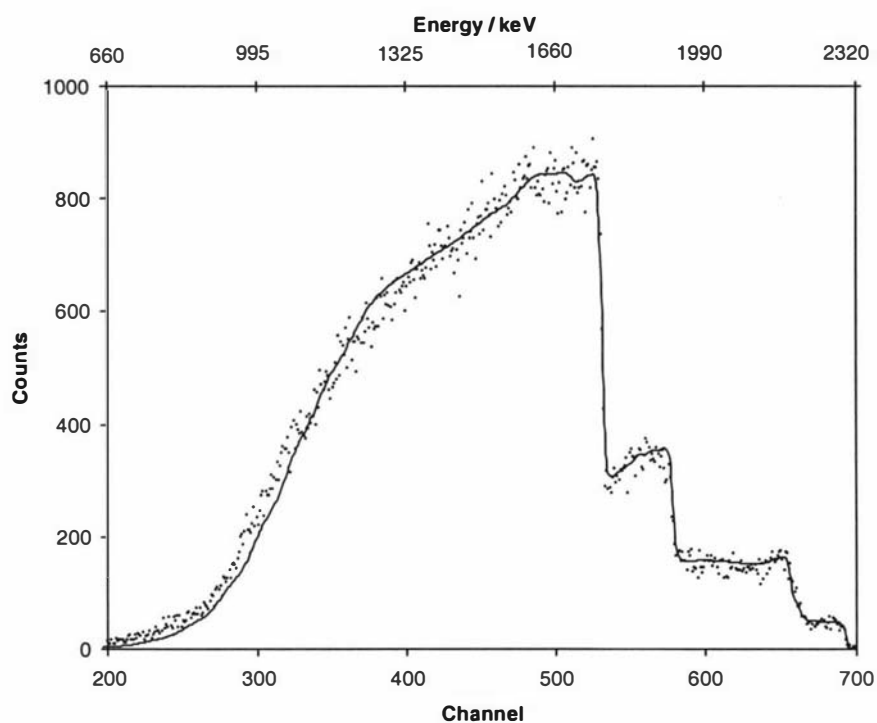


Fig. 7.64 RBS experimental (●) and simulated (—) spectra for the solution side of a TTh-Fc / TTh-Por-TTh copolymer (1:1) using a 2.5 MeV proton beam.

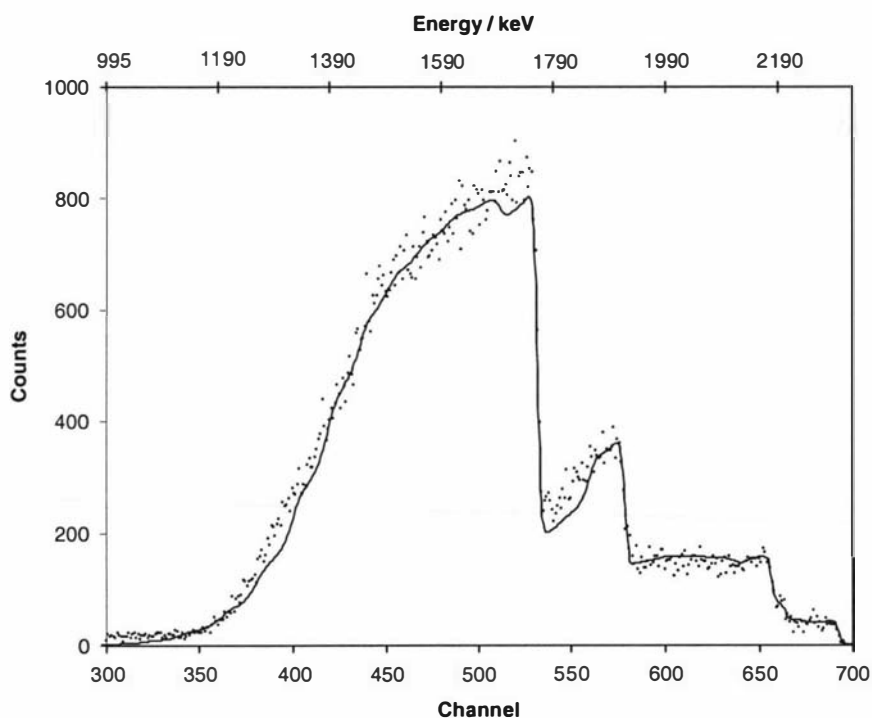
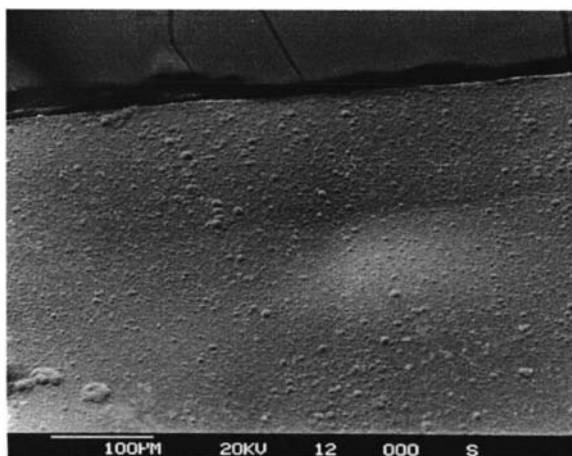
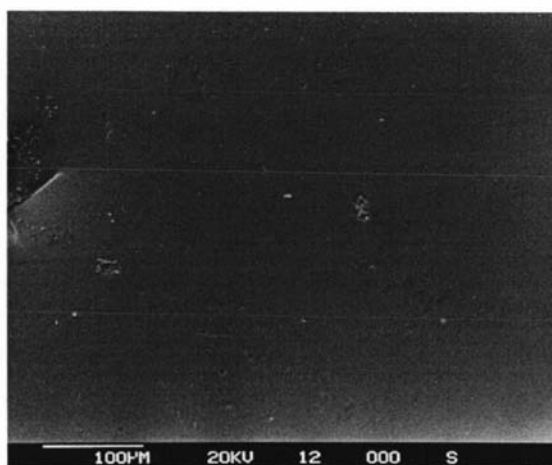


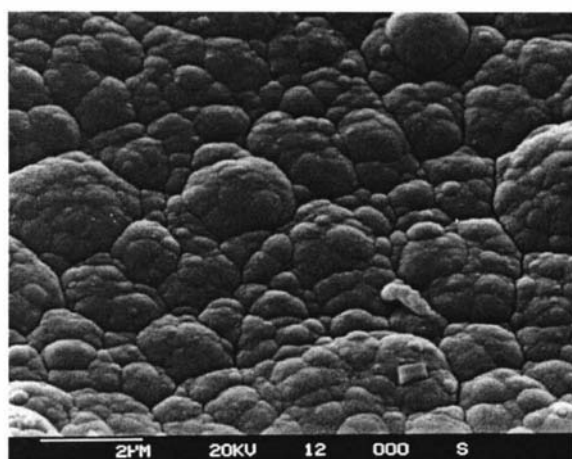
Fig. 7.65 RBS experimental (●) and simulated (—) spectra for the electrode side of a TTh-Fc / TTh-Por-TTh copolymer (1:1) using a 2.5 MeV proton beam.



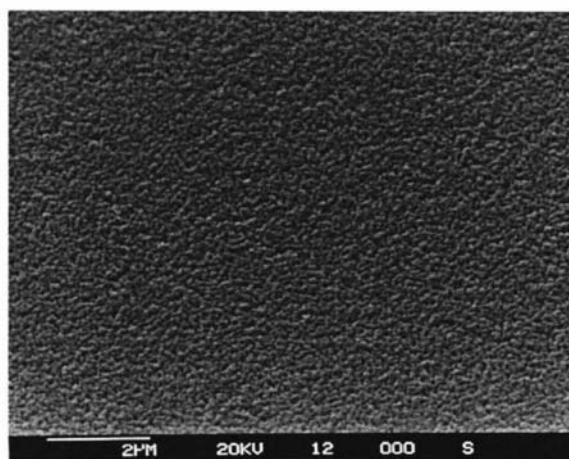
(a)



(b)



(c)



(d)

Fig. 7.66 SEM images of the solution and electrode side of the 1:1 TTh-Fc / TTh-Por-TTh copolymer : (a) 100 μm solution side; (b) 100 μm electrode side; (c) 2 μm solution side; (d) 2 μm electrode side.

Table 7.8 Layer thickness, roughness factors, and total analysed depth of each TTh-Fc / TTh-Por-TTh sample. Roughness factor values which have * have the roughness factor associated with the last simulated layer.

	Layer 1	Layer 2	Layer 3	Layer 4		
Monomer ratio (TTh-Fc / TTh-Por-TTh)	Thickness (μm)	Thickness (μm)	Thickness (μm)	Thickness (μm)	Roughness factor	Total thickness (μm)
5:10 solution side	1.77	2.41	11.90		0.76	16.08
5:10 electrode side	13.29	45.90			0.32*	59.19
5:1 solution side	0.91	1.90	2.16	15.18	0.50	20.15
5:1 electrode side	2.07	1.51	1.95	26.04	0.79*	31.57
5:2 solution side	0.93	2.30	2.70	8.98	0.56	14.91
5:2 electrode side	0.95	2.41	2.69	7.58	0.50*	13.63
1:1 solution side	1.03	2.31	2.88	24.67	0.69	30.89
1:1 electrode side	1.02	2.27	2.90	12.54	0.48*	18.73

Table 7.9 Listed are the bis terthiophene porphyrin to terthiophene-ferrocene monomer ratios and counter ion to terthiophene-ferrocene monomer ratios for each simulated layer. All ratios are quoted with respect to one terthiophene-ferrocene monomer.

	Layer 1		Layer 2		Layer 3		Layer 4	
Monomer ratio (TTh-Fc / TTh-Por-TTh)	TTh-Por-TTh (<i>m/n</i>)	Counter ion (<i>z/n</i>)	TTh-Por-TTh (<i>m/n</i>)	Counter ion (<i>z/n</i>)	TTh-Por-TTh (<i>m/n</i>)	Counter ion (<i>z/n</i>)	TTh-Por-TTh (<i>m/n</i>)	Counter ion (<i>z/n</i>)
2:1 solution side	0.11	1.92	0.11	1.92	0.08	1.32		
2:1 electrode side	0.11	2.04	0.11	2.04				
1:5 solution side	0.72	0.94	0.50	2.47	0.43	1.74	0.55	1.02
1:5 electrode side	1.10	1.98	0.37	1.51	0.28	0.90	0.84	1.42
2:5 solution side	0.27	1.94	0.34	2.13	0.32	1.52	0.34	1.31
2:5 electrode side	0.36	3.51	0.32	3.42	0.33	2.71	0.29	2.77
1:1 solution side	0.03	1.73	0.05	1.51	0.03	1.37	0.03	1.37
1:1 electrode side	0.03	1.45	0.08	2.40	0.04	1.33	0.01	1.42

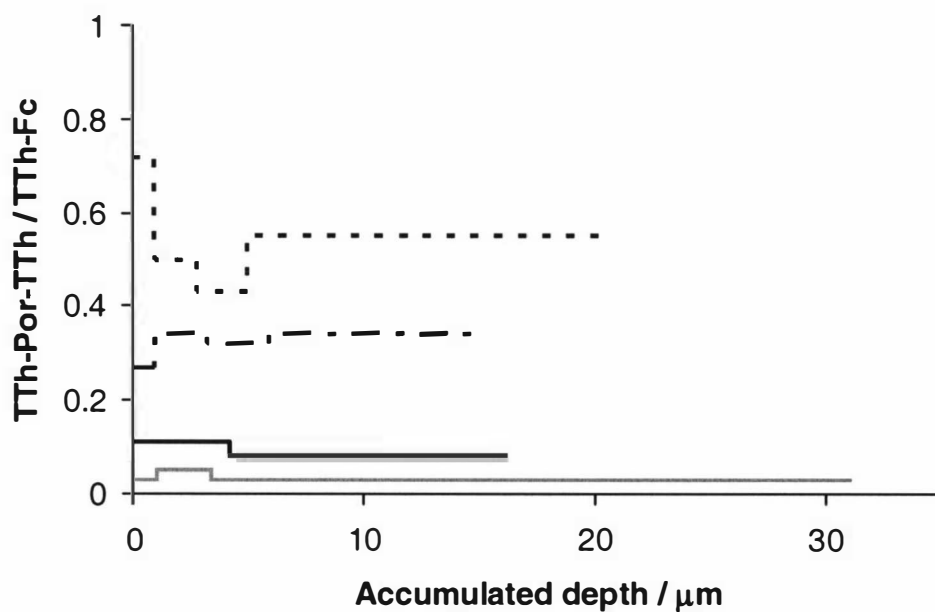


Fig 7.67 Plot of TTh-Por-TTh / TTh-Fc ratios changing with depth into the solution side of the TTh-Fc / TTh-Por-TTh copolymer, — 2:1, 1:5, — · — · 2:5, — 1:1.

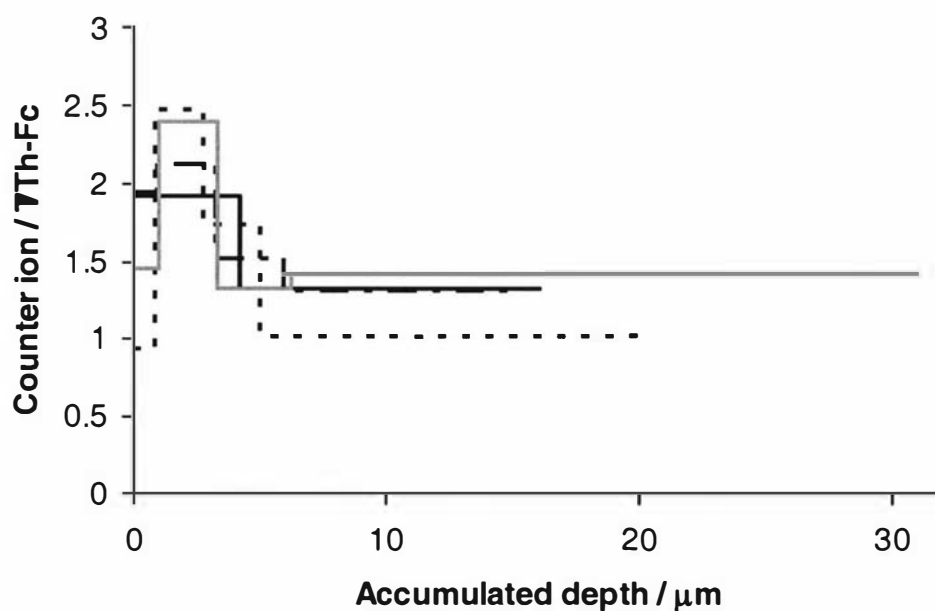


Fig 7.68 Plot of counter ion / TTh-Fc ratios changing with depth into the solution side of the TTh-Fc / TTh-Por-TTh copolymer, — 2:1, 1:5, — · — · 2:5, — 1:1.

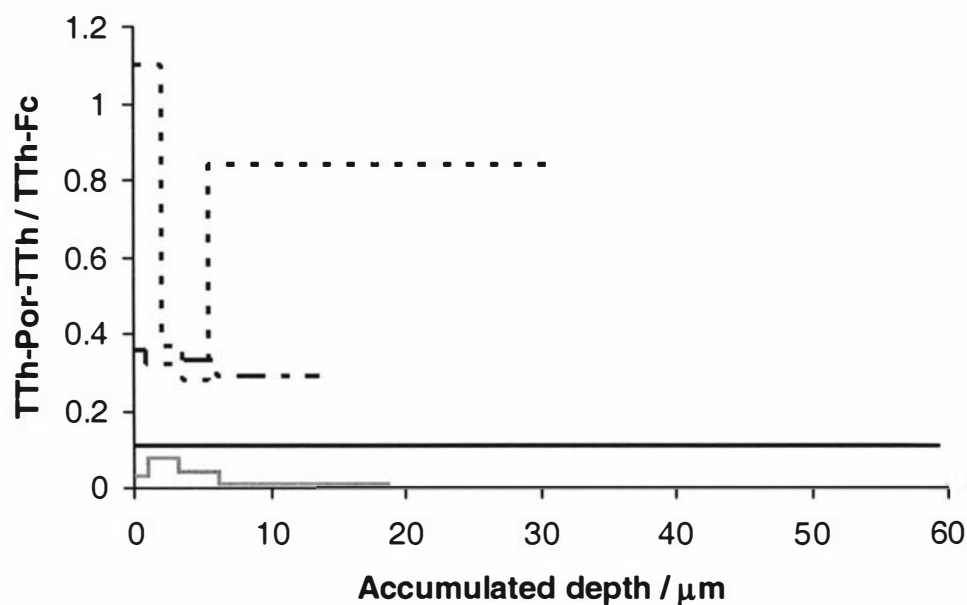


Fig 7.69 Plot of TTh-Por-TTh / TTh-Fc ratios changing with depth into the electrode side of the TTh-Fc / TTh-Por-TTh copolymer, — 2:1, 1:5, — · — · 2:5, — 1:1.

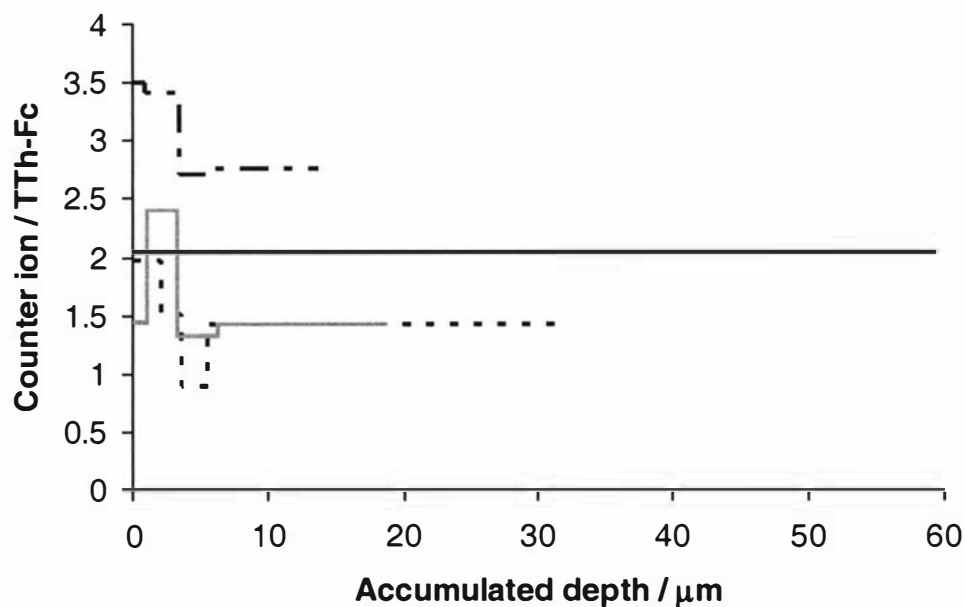


Fig 7.70 Plot of counter ion / TTh-Fc ratios changing with depth into the electrode side of the TTh-Fc / TTh-Por-TTh copolymers, — 2:1, 1:5, — · — · 2:5, — 1:1.

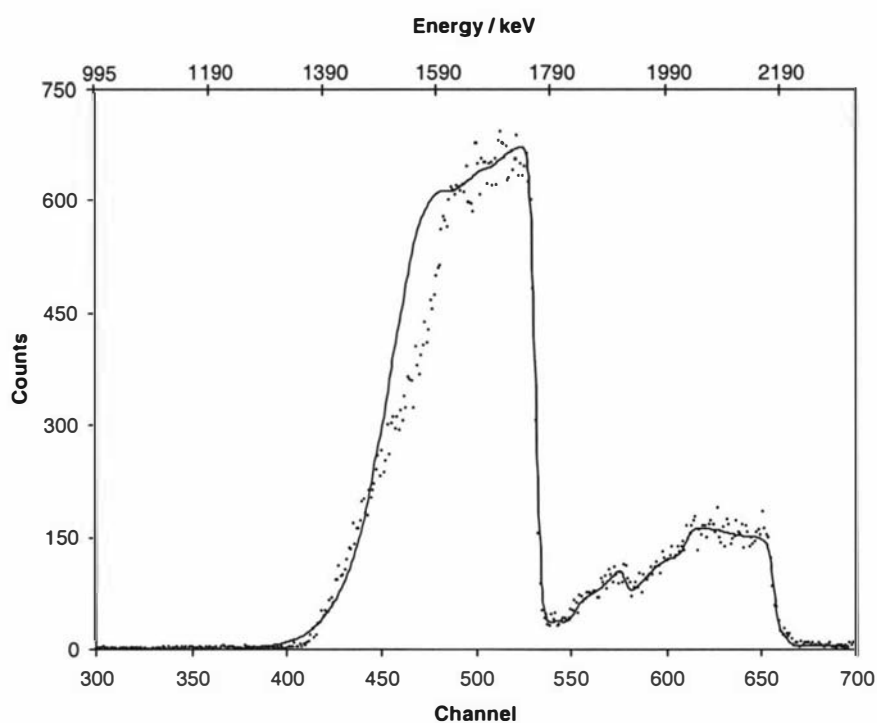


Fig. 7.71 RBS experimental (●) and simulated (—) spectra for the solution side of a TTh-Fc / Bridging TTh copolymer (1:10) using a 2.5 MeV proton beam.

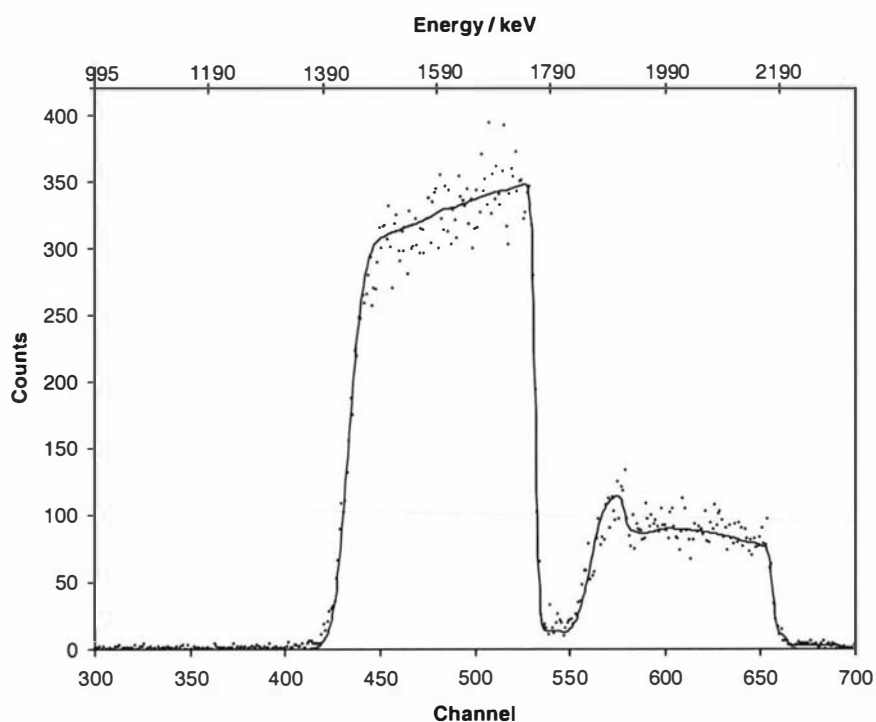
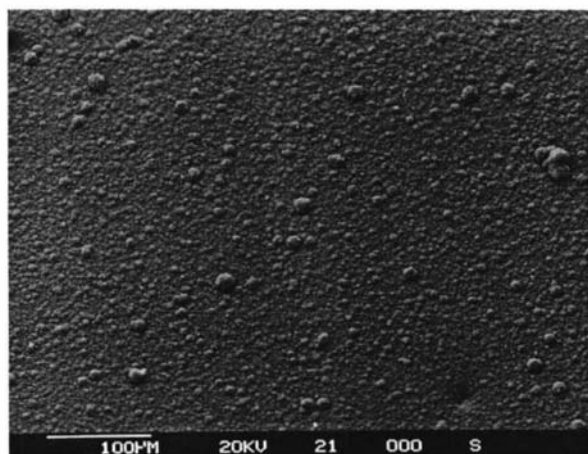
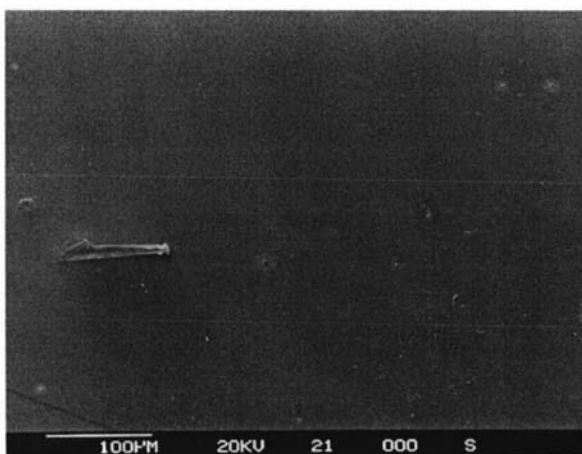


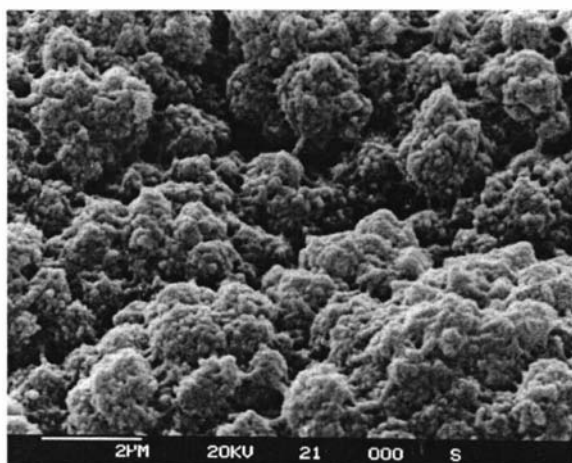
Fig. 7.72 RBS experimental (●) and simulated (—) spectra for the electrode side of a TTh-Fc / Bridging TTh copolymer (1:10) using a 2.5 MeV proton beam.



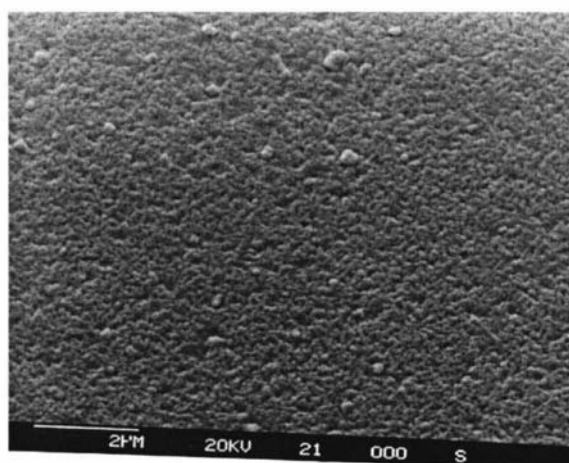
(a)



(b)



(c)



(d)

Fig. 7.73 SEM images of the solution and electrode side of the 1:10 TTh-Fc / Bridging TTh copolymer : (a) 100 μm solution side; (b) 100 μm electrode side; (c) 2 μm solution side; (d) 2 μm electrode side.

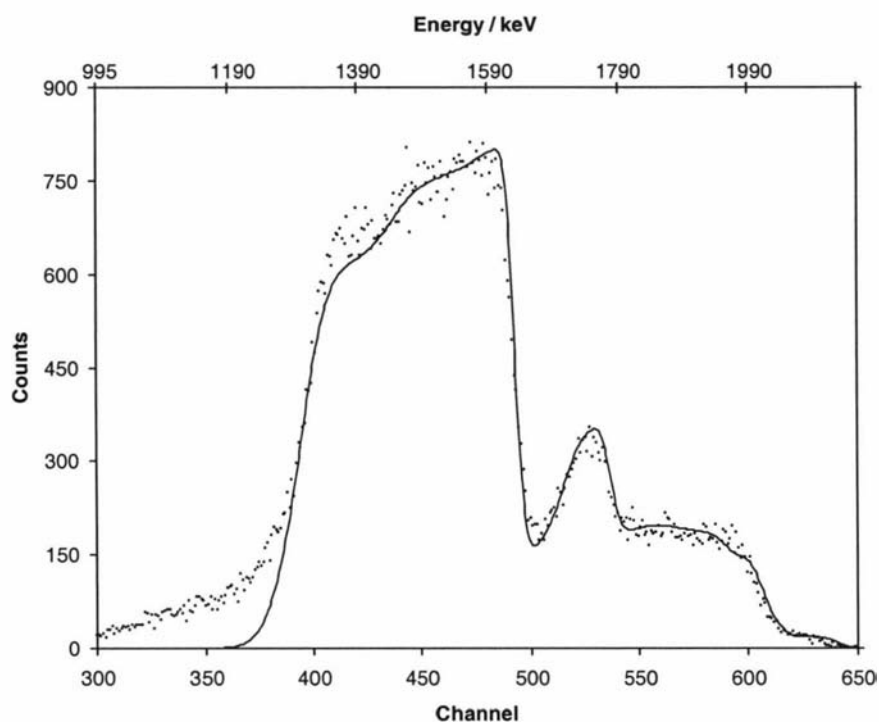


Fig. 7.74 RBS experimental (●) and simulated (—) spectra for the electrode side of a TTh-Fc / Bridging TTh copolymer (1:1) using a 2.5 MeV proton beam.

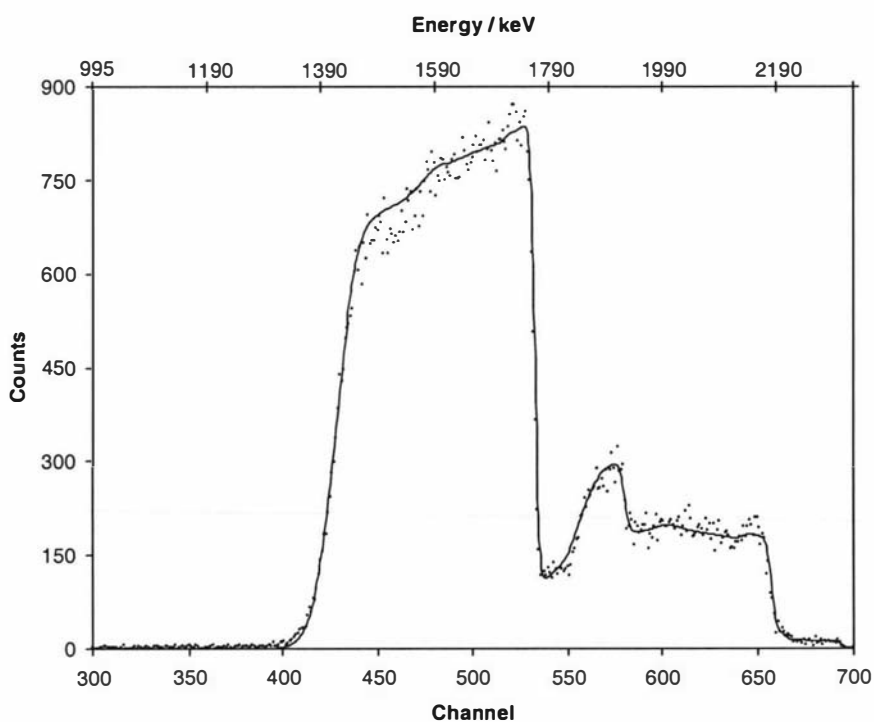
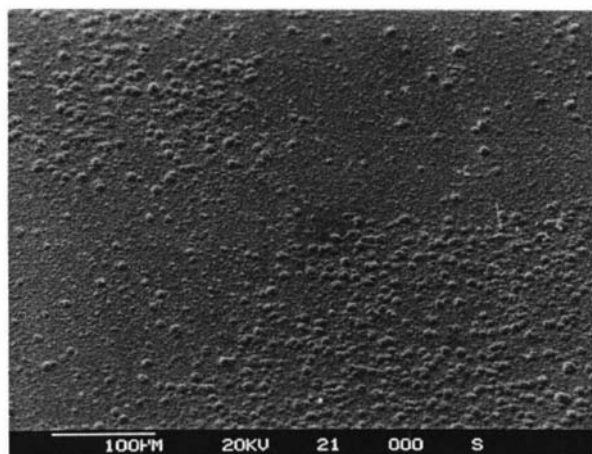


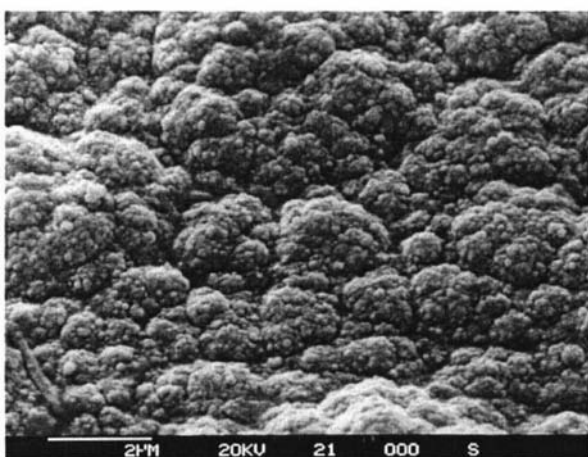
Fig. 7.75 RBS experimental (●) and simulated (—) spectra for the solution side of a TTh-Fc / Bridging TTh copolymer (1:1) using a 2.5 MeV proton beam.



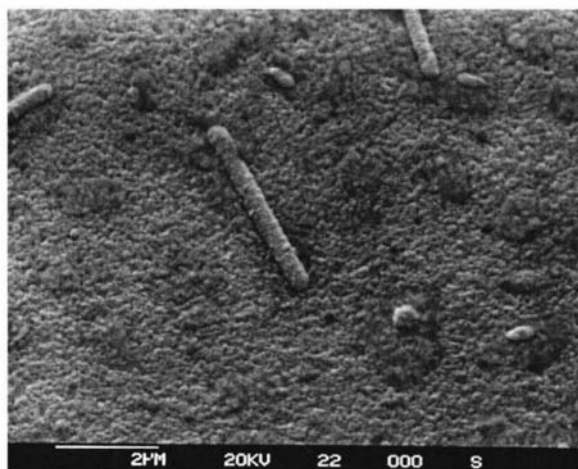
(a)



(b)



(c)



(d)

Fig. 7.76 SEM images of the solution and electrode side of the 1:1 TTh-Fc / Bridging TTh copolymer : (a) 100 μm solution side; (b) 100 μm electrode side; (c) 2 μm solution side; (d) 2 μm electrode side.

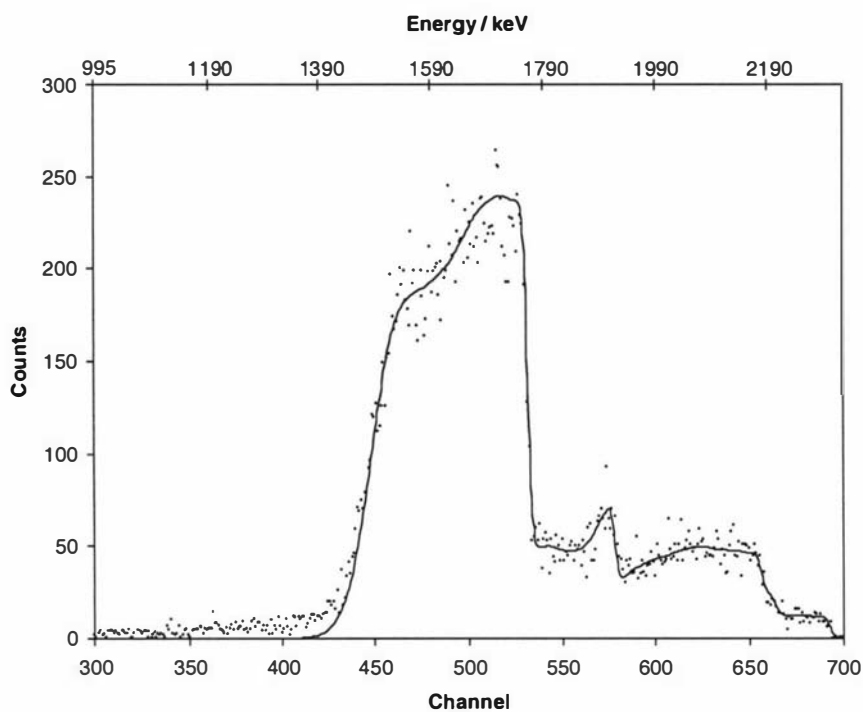


Fig. 7.77 RBS experimental (●) and simulated (—) spectra for the electrode side of a TTh-Fc / Bridging TTh copolymer (10:1) using a 2.5 MeV proton beam.

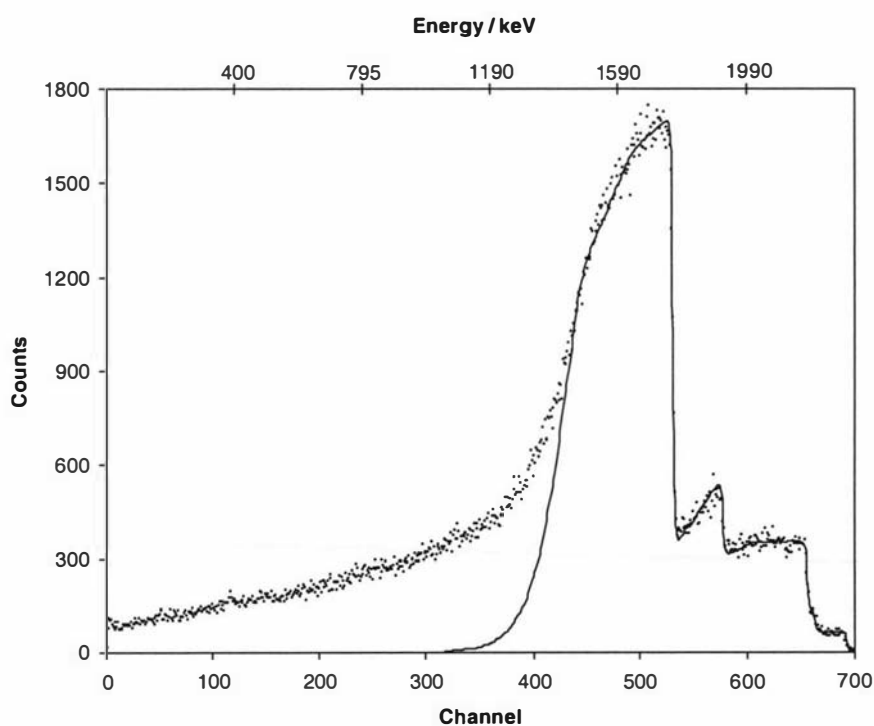
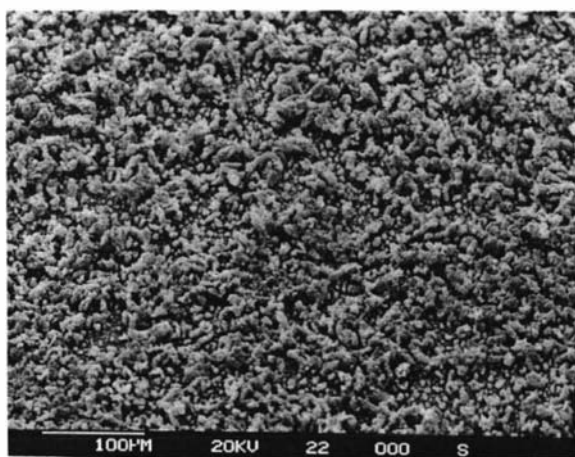
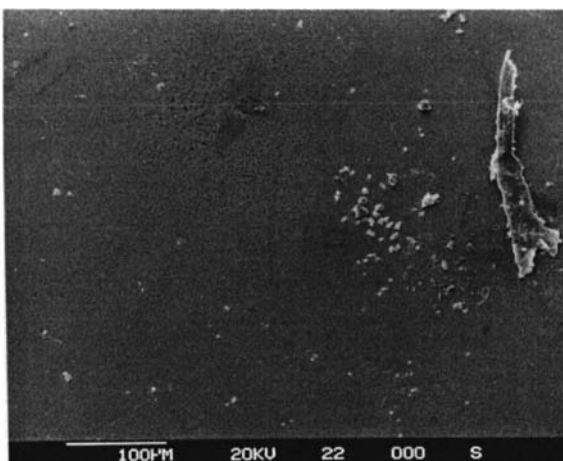


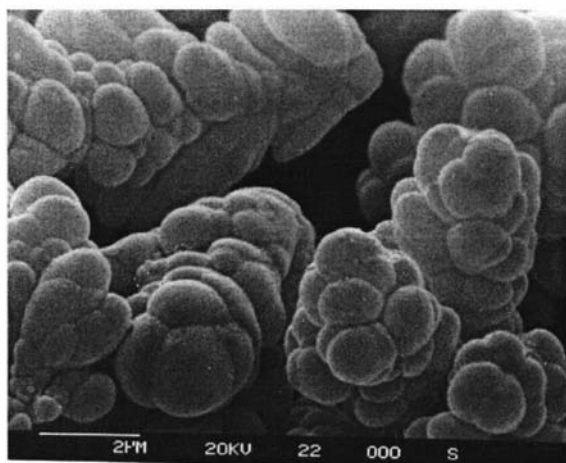
Fig. 7.78 RBS experimental (●) and simulated (—) spectra for the solution side of a TTh-Fc / Bridging TTh copolymer (10:1) using a 2.5 MeV proton beam.



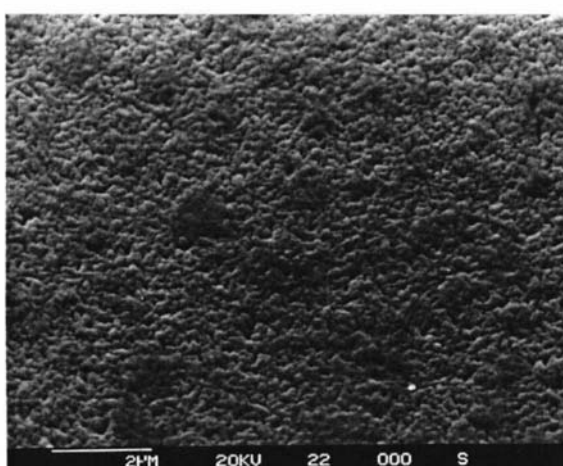
(a)



(b)



(c)



(d)

Fig. 7.79 SEM images of the solution and electrode side of the 10:1 TTh-Fc / Bridging TTh copolymer : (a) 100 μm solution side; (b) 100 μm electrode side; (c) 2 μm solution side; (d) 2 μm electrode side.

Table 7.10 Layer thickness, roughness factors, and total analysed depth of each TTh-Fc / Bridging TTh sample. Roughness factor values which have * have the roughness factor associated with the last simulated layer.

	Layer 1	Layer 2	Layer 3	Layer 4		
Monomer ratio (TTh-Fc / Bridging TTh)	Thickness (μm)	Thickness (μm)	Thickness (μm)	Thickness (μm)	Roughness factor	Total thickness (μm)
1:10 solution side	1.90	2.28	2.97	5.31	0.52	12.46
1:10 electrode side	1.36	1.36	4.45	7.45	0.90*	14.62
1:1 solution side	2.41	5.03	8.04		0.83	15.48
1:1 electrode side	0.75	2.52	4.27	8.86	0.81*	16.40
10:1 solution side	6.04	7.20	2.51	1.77	0.57	17.52
10:1 electrode side	1.77	2.52	2.85	6.07	0.75*	13.21

Table 7.11 Listed are the Bridging terthiophene to terthiophene-ferrocene monomer ratios and counter ion to terthiophene-ferrocene monomer ratios for each simulated layer. All ratios are quoted with respect to one terthiophene-ferrocene monomer.

	Layer 1		Layer 2		Layer 3		Layer 4	
Monomer ratio (TTh-Fc / Bridging TTh)	Bridging TTh (<i>m/n</i>)	Counter ion (<i>z/n</i>)	Bridging TTh (<i>m/n</i>)	Counter ion (<i>z/n</i>)	Bridging TTh (<i>m/n</i>)	Counter ion (<i>z/n</i>)	Bridging TTh (<i>m/n</i>)	Counter ion (<i>z/n</i>)
1:10 solution side	8.7	4.9	8.8	2.7	8.5	0.4	5.1	3.9
1:10 electrode side	9.2	5.2	9.3	2.9	8.5	1.8	8.8	1.8
1:1 solution side	1.1	7.0	1.6	4.7	2.3	3.8	2.2	3.2
1:1 electrode side	3.5	3.7	3.3	2.8	3.1	2.2		
10:1 solution side	0.1	2.0	0.2	1.6	0.2	1.9	0.2	1.6
10:1 electrode side	0.6	1.6	0.5	2.3	0.4	2.1	0.4	2.5

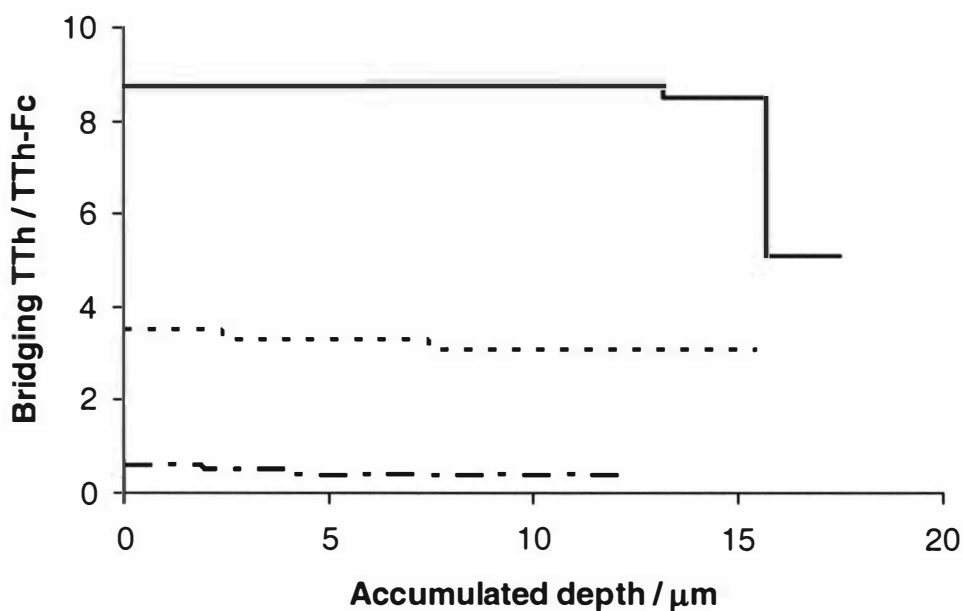


Fig 7.80 Plot of Bridging TTh / TTh-Fc ratios changing with depth into the solution side of the TTh-Fc / Bridging TTh copolymer, — · — · 10:1, 1:1, ——— 1:10.

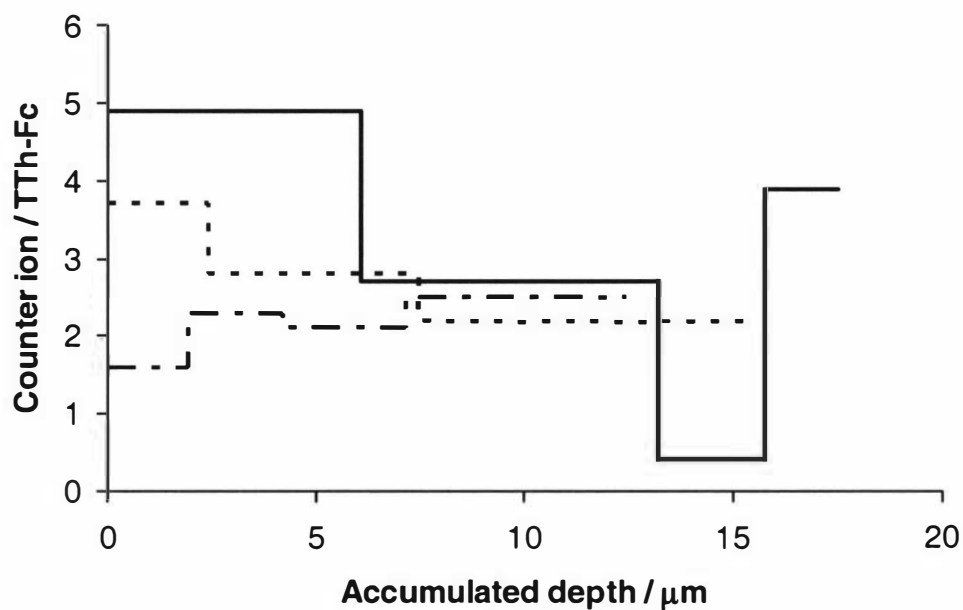


Fig 7.81 Plot of counter ion / TTh-Fc ratios changing with depth into the solution side of the TTh-Fc / Bridging TTh copolymer, — · — · 10:1, 1:1, ——— 1:10.

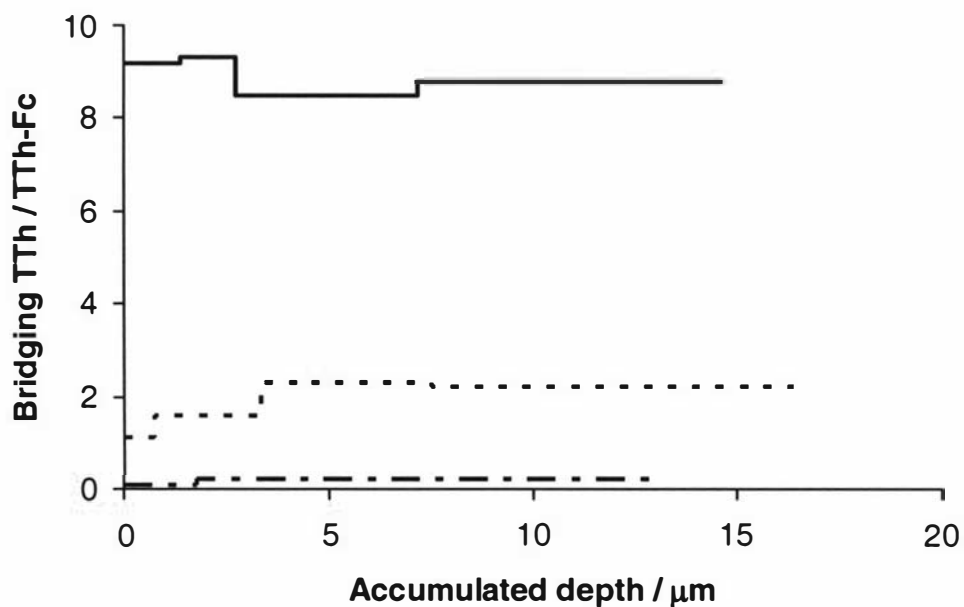


Fig 7.82 Plot of Bridging TTh / TTh-Fc ratios changing with depth into the electrode side of the TTh-Fc / Bridging TTh copolymer, — · — · 10:1, ······ 1:1, — 1:10.

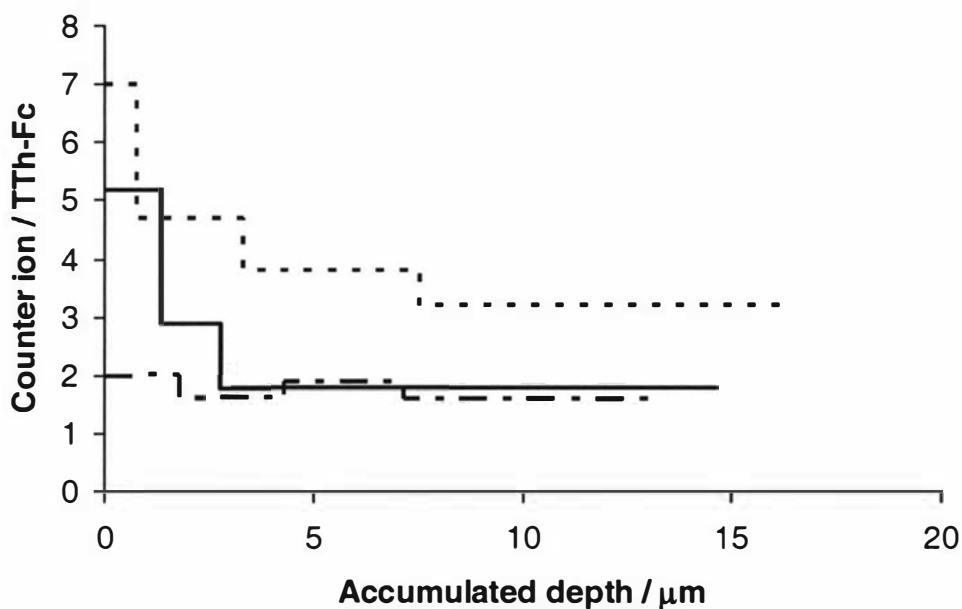


Fig 7.83 Plot of counter ion / TTh-Fc ratios changing with depth into the electrode side of the TTh-Fc / Bridging TTh copolymer, — · — · 10:1, ······ 1:1, — 1:10.

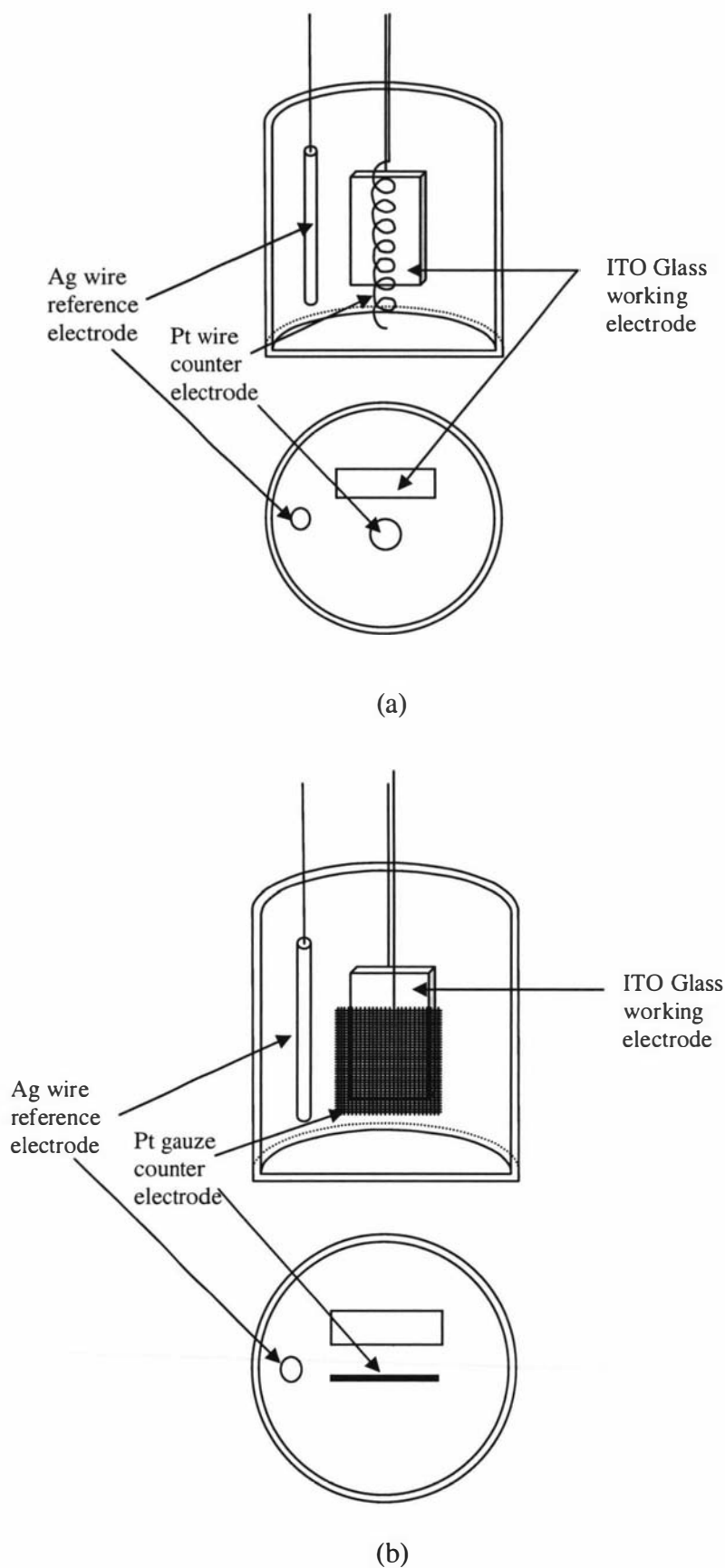


Fig. 7.84 Schematic diagrams of (a) the cell set up using Pt wire counter electrode, and (b) a Pt gauze counter electrode.

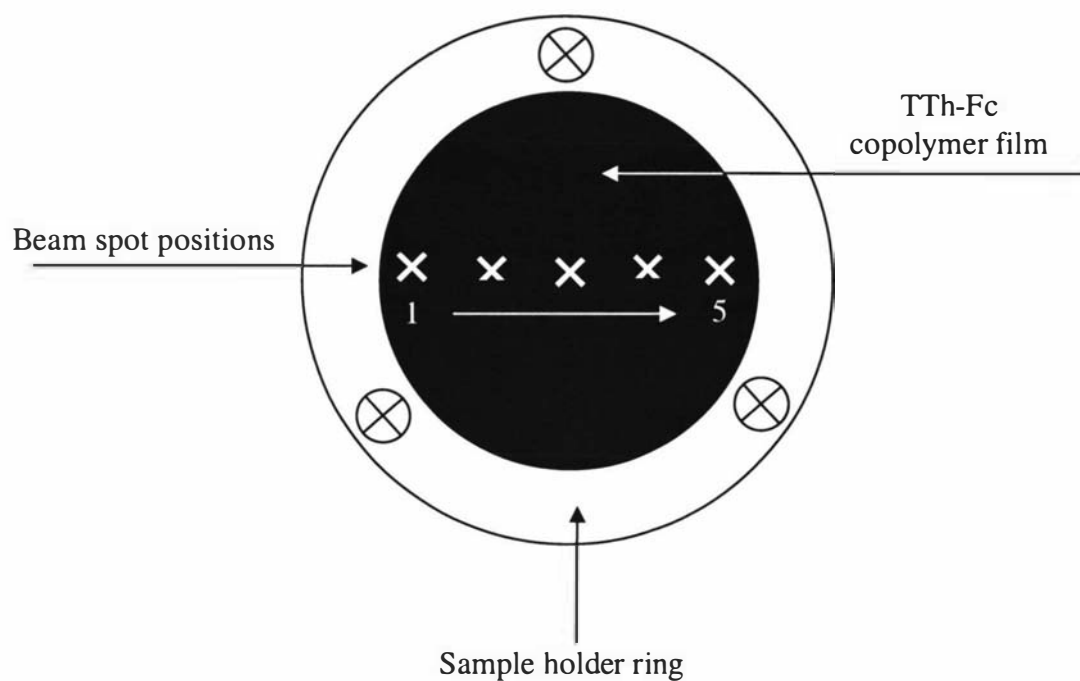


Fig. 7.85 Schematic diagram of the copolymer film held in the sample holder and the positions from where the five experimental RBS spectra were obtained from.

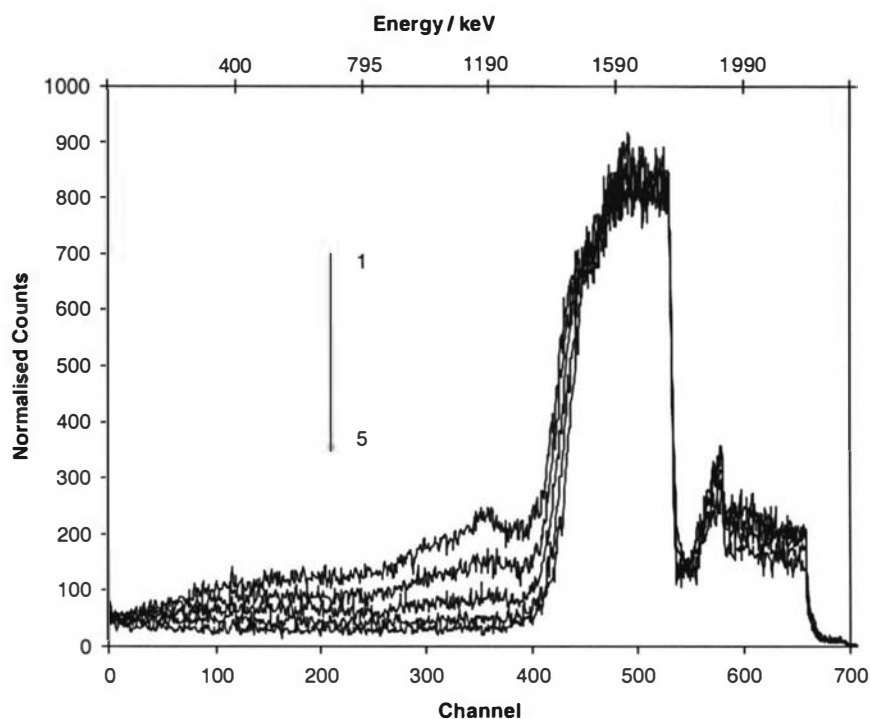


Fig. 7.86 Five overlaid experimental RBS spectra obtained from 1:10 TTh-Fc/Bridging TTh copolymer film using a Pt wire counter electrode.

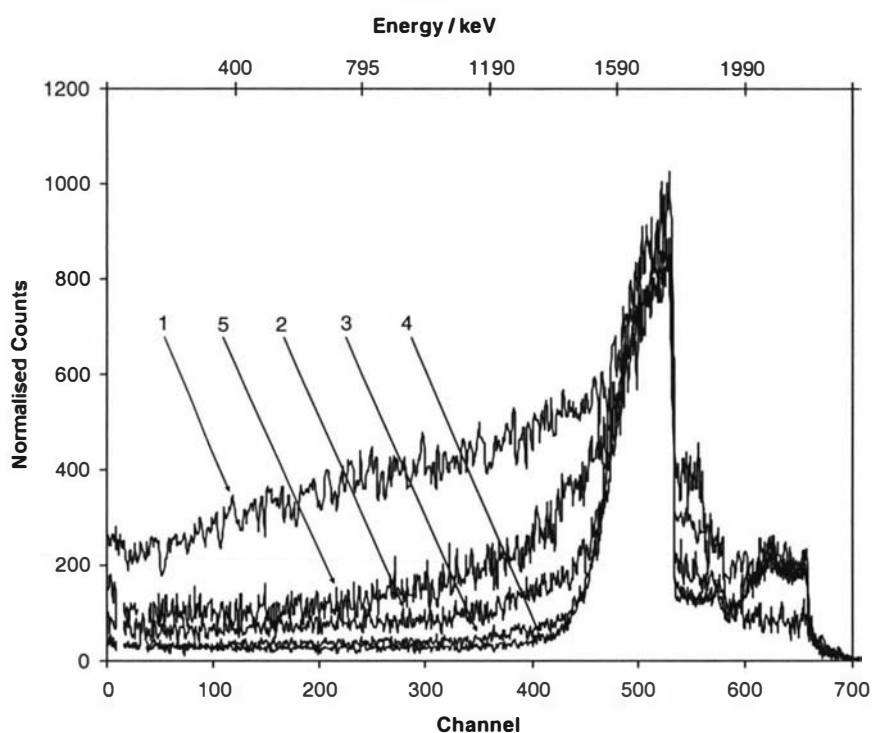


Fig. 7.87 Five overlaid experimental RBS spectra obtained from 1:10 TTh-Fc/Bridging TTh copolymer film using a Pt gauze counter electrode.

CHAPTER 8

Conclusions

IBA analysis was successfully adapted to interpret the RBS response for a number of organic soft material based conducting polymer films.

The first series of results arising from PIXE and RBS analysis of electrochemically deposited TTh-Por-TTh films on GC working electrodes. This formed the scoping study for this thesis (Chapter 3). Ion beam analysis has been used in the past to modify organic based materials particularly so in the case by bombardment with ions. The question of whether or not bombardment by $^4\text{He}^+$ results in chemical change has not been addressed in this work. However, stability was assessed in terms of the RBS response during ion bombardment consistent with no significant change in elemental composition of the film during analysis. In each case this response was invariant with time during ion beam bombardment. This is not inconsistent with either the samples not degrading or not chemically changing during ion bombardment, but this can not be conclusively proven using this technique. There also exists the possibility that when the samples are first subjected to the ion beam they instantly degrade or chemically change to a fixed extent but this was not thought likely.

The scoping study using the electrochemically deposited TTh-Por-TTh material showed that low concentration contaminants can be detected using PIXE analysis. These were detected throughout the measured depth of the samples and are thought to be associated with the reagents used in the synthesis of forming the TTh-Por-TTh monomers. More significantly, it was established that elemental information (e.g. presence of Zn) with depth into the sample material can be obtained by interpretation of the RBS spectra. A further important factor was established in this section of work relating to the presentation of the sample to the ion beam. Here the electrochemically deposited TTh-Por-TTh films were supported and remained on the GC during IBA

analysis. The RBS response for carbon was found to be a combination of that from TTh-Por-TTh material and that from the underlying GC substrate. There was no ability to distinguish between these two contributions. Further, it was deduced that an unexpected Al backscattering in both PIXE and RBS spectra arose from Al₂O₃ polishing material embedded in the GC electrode surface. As a consequence, to avoid this situation it was established that polymer films which were to be subjected to IBA studies should be removable from the working electrode substrate and free standing.

A series of six galvanostatically formed self-supporting PPy films were prepared, each with a different counter ion (Chapter 4). The aim of this was to attempt to use RBS to probe the oxidation state of conducting polymers as a function of depth, and to determine whether or not this varied with different counter ions.

It was established that the ion beam (to a total accumulated beam charge of 400 μC) did not degrade the RBS response, consistent with the earlier TTh-Por-TTh results.

PIXE analysis of the PPy films showed trace levels of a number of unexpected elements (e.g. K, Fe, and Cu). In contrast to the unexpected element found in the TTh-Por-TTh case, these contaminants were found to be confined to a thin surface layer on both sides of the film (30 nm). The proposed source of these unexpected elements is that they were incorporated during the handling and storage stages since they were confined to the outermost 30 nm of both side of the 30 μm thick films.

RBS analysis using a 1.5 MeV $^4\text{He}^+$ ion beam enabled profiling of the monomer to counter ion ratios to a depth ranging between 1.0 – 1.2 μm for all six PPy films. The monomer to counter ion ratio behaviour varied from film to film and also as a function of depth and ranged between 6:1 and 2:1. No non-polymer species were detected, such as K^+ or Na^+ , which might have formed cation-anion pairs within the film matrix (the anions being the film counter ions). This permitted the ability to propose that the average charge per pyrrole unit varied from 0.17 to 0.50 for the six films (PPy-NBS lowest, PPy-SB highest). This is based on the assumption that H^+ -anion pairing with the polymer films has not taken place (H^+ not being detectable by IBA).

These results suggest that RBS may well prove useful for surface elemental analysis and elemental depth profiling of organic films and polymers, but is likely to be of limited use at providing information for bulk soft organic materials since analysis was only possible to a maximum depth of 1.2 μm into the PPy samples. This is substantially less than the total film thicknesses which were typically at least 25 μm thick.

In addition, there was not strong agreement between the monomer to counter ion ratios near the surface of the PPy films deduced using $^4\text{He}^+$ 1.5 MeV RBS analysis and those found using bulk combustion analysis over the entire film thickness. This suggests that the surface composition differs from the bulk. Indeed, the likely performance of these conducting polymers may not be well reflected in exploring bulk properties alone, or conversely by the surface composition, this issue was not further addressed in this work.

The next section of work was to electrochemically form a series of free-standing TTh-Fc copolymer films (Chapter 5). A variety of solvents, counter ions, and working electrode substrates were used to establish the combination from which the optimal peelable films containing the TTh-Fc monomer could be reproducibly formed. The final system was one which employed DCM as the solvent, TBAP as the counter ion, and ITO coated glass as the working electrode. The copolymer monomers Py, bithiophene, EDOT, Bridging TTh, and TTh-Por-TTh were used to prepare a series of TTh-Fc based copolymers. The TTh-Fc to copolymer monomer solution concentration ratios were varied to prepare a range of copolymers of potentially different composition.

RBS analysis was attempted using a 1.5 MeV $^4\text{He}^+$ ion beam. Even though the energy was limited to 1.5 MeV, the TTh-Fc copolymer samples in the chamber were destroyed (as was visually observed). Due to this, a 2.1 MeV H^+ beam was used for the collection of RBS data with no sample degradation evident. However, an alternative data interpretation package, SIMNRA, was required for evaluation of these backscattered protons.

The combination of the comparatively complex samples with the requirement for the use of SIMNRA necessitated the development of a unique sample analysis protocol. Four successive models were developed before the final model was selected which enabled RBS interpretation (Chapter 7). In the first model SIMNRA was primed with calculated quantities of each element assumed to be present within the films according to the elemental makeup of the three components: the TTh-Fc monomer: the relevant copolymer monomer: and the counter ion (ClO_4^-). Then together with the first estimation of copolymer monomer to TTh-Fc, and counter ion to TTh-Fc ratios, these parameters determined the atom % for each element in the simulation and were successively optimised together with a sample thickness to fit the simulation to the experimental data. This first model was working on the assumption that there was one homogenous compositional layer as well. This did not appear to be the case, so a second model was designed.

The second model included two additional steps. The first was to increase the number of simulated layers which allows depths for elemental composition to alter with depth into the film. The second included 'roughness'; a SIMNRA parameter to allow for surface roughness of the sample. This assisted with the simulation of the low energy tail of the experimental RBS. These two new steps in the procedure, afforded better simulations than those from Model I, but were still not satisfactory.

Up until this point the two component species ratios had been changed manually, and then the overall percent values recalculated as needed, as variables for SIMNRA. This was not proving to result in model convergence, so a new approach was attempted. This involved priming SIMNRA with the elemental percent values, thickness, and roughness values from the best simulation obtained by Model II and then releasing the chemical restraints imposed by monomer and counter ion compositions and to attempt to fit the main features of the experimental RBS spectrum by eye. This approach provided a more ready means for identifying whether additional layers of varying compositions were required, and was superior to Model I and II.

Model III enabled evaluation of elemental atomic percents as a function of successive layers, and hence depth, into the sample. However, these compositions made no sense

from a chemical point of view. These atomic percent values were used to predict a theoretical polymer by consideration of the elemental composition of polymer building blocks (monomers and counter ions) and optimisation of monomer ratios and counter ion to monomer ratios. This optimisation was achieved using the 'Solver' routine in ExcelTM. This improved RBS interpretation, but did not adequately account for all features.

Model IV was developed to improve optimisation by the inclusion of additional parameters into the final optimisation. These included consideration of species thought to be entrained into the films: DCM, oxygen, water, carbon, and the cation $N(nBu)_4^+$. The inclusion of these parameters afforded improved optimisation and this last Model was used for all data interpretation (Chapter 7).

Several general features, limitations and conclusions could be drawn from the results obtained for the TTh-Fc copolymers. The following highlights the main features identified in Section 7.6.

All RBS responses could be operationally characterised as belonging to three types. Type 1 spectra were those where total film penetration with no low energy tail being observed, Type 2 spectra were those where total penetration was observed, however these spectra had a low energy tail, and Type 3 where the spectra where total film penetration did not occur and the were counts recorded and channel zero. It was not possible to adequately simulate all RBS spectra and this is viewed as a major limitation of the RBS technique when applied to organic materials.

An operational roughness factor was identified to assist interpretation (0 = rough, 1 = smooth). Roughness factors were evaluated for all RBS spectra. SEM images of the samples provided visual evidence for the degree of roughness observed from RBS spectra

Coral-like growth to varying degrees was observed in many of the SEM images on the solution sides of the TTh-Fc films, and it was found that when these were evident the RBS interpretation yielded a lower roughness factors than those not exhibiting coral-like growth.

Some films, such as the bithiophene copolymers, exhibited overlapping hemispherical growth to varying degrees, and their accompanying roughness factors reflected much smoother surfaces.

RBS spectra can provide an indication of thickness and surface roughness of a sample before any simulations are carried out. However, if only thickness and roughness information is required, then SEM would be a better technique to use than RBS. The advantage RBS offers is the opportunity to obtain low atomic number elemental depth profiling.

Correlation between the copolymer monomer to TTh-Fc ratios and the counter ion to TTh-Fc ratios in films and those in the polymerisation solution was not obtained. This suggests that the overall chemical makeup of these copolymer films is predominantly dominated by electrokinetic issues and not simply upon ratios of the monomers in the parent solutions.

In all cases the solution sides were rougher than the electrode sides of the copolymer films, and in some cases folding of the surface was observed. These features complicated interpretation of the RBS spectra.

In cases where total film penetration by the ion beam was observed (Type 1), one would expect the compositional layers arising from the RBS analysis of the solution and electrode sides to be identical but reversed in layer order. However, this was not established for any of the candidate films. This highlights a significant limitation of the RBS analysis of organic materials and is of great concern.

There is a significant limitation to RBS analysis when dealing with organic samples of unknown composition. It was established that simulation of RBS spectra without any elemental constraints would regularly fail to uniquely identify the real sample matrix. This is a severe limitation for the technique suggesting that it cannot be used as a general analytical technique for organic materials in the way that combustion elemental analysis is. However, in those cases where adequate and unambiguous interpretation is possible, as in the case of fixed elemental composition of monomer in

a polymer, RBS offers the possibility of providing depth profiling of low atomic number elements.

A further limitation found was that some SEM images showed mats of rod-like crystalline / fibrous structures on the electrode side surface which appear not to be copolymer film. This exogenous materials elemental composition will influence the first layer of the electrode side at least and roughness factors. Candidates for these surface species were proposed, however attempts to identify this material failed to yield meaningful results and consequently the nature of this material remains an unresolved issue of this study.

The modelled layers are relatively large in thickness given the often times substantial changes in successive species ratios. Consequently, while depth profiling is achieved it is significantly 'stair-cased' in terms of species ratios rather than smooth continuous trends.

Despite these limitations and the conclusions found from this work, if there is some level of prior chemical knowledge (for example, polymer building block composition), meaningful results for soft materials can be obtained from RBS. The greatest advantage that RBS offers is the possibility of obtaining low atomic number elemental composition information with depth into samples, which no other elemental techniques readily offer. However, further investigation into the concerns which have been raised in this work is required, before this technique could be used widely for the characterisation of soft organic materials, such as conducting polymers.

References

1. R. B. Kaner, A. G. MacDiarmid, *Sci. Am.*, 2 (1988) 258.
2. A. J. Epstein, *Mater. Res. Soc.*, 22 (6) (1997) 16.
3. J. Roncali, *Chem. Rev.*, 92 (1992) 711.
4. C. K. Chiang, C. R. Fincher, Y. W. Park, A. J. Heeger, E. J. Louis, S. C. Gau, A. G. MacDiarmid, *Phys. Lett. Rev.*, 39 (1977) 1098.
5. C. K. Chiang, M. A. Druy, S. C. Gau, A. J. Heeger, E. J. Louis, A. G. MacDiarmid, Y. W. Park, H. Shirakawa, *J. Am. Chem. Soc.*, 100 (3) (1997) 1013.
6. D. MacInnes, M. A. Dury, P. J. Nigrey, D. P. Nairns, A. G. MacDiarmid, A. J. Heeger, *J. Chem. Soc., Chem. Commun.*, (1981) 317.
7. P. J. Nigrey, A. G. MacDiarmid, A. J. Heeger, *J. Chem. Soc., Chem. Commun.*, (1979) 594.
8. A. J. Heeger, *Angew. Chem. Int. Ed. Eng.*, 40 (2001) 2591.
9. A. G. MacDiarmid, *Angew. Chem. Int. Ed. Eng.*, 40 (2001) 2581.
10. H. Shirakawa, *Angew. Chem. Int. Ed. Eng.*, 40 (2001) 2574.
11. A. J. Heeger, *Synth. Met.*, 125 (1) (2002) 23.
12. A. G. MacDiarmid, *Synth. Met.*, 125 (1) (2002) 11.

13. H. Shirakawa, *Synth. Met.*, 125 (1) (2002) 3
14. A. R. Hepburn, J. M. Maud, J. M. Marshall, *Met. Mater. (Inst. Mater.)*, 7(12) (1991) 747.
15. R. Baughman, L. W. Schacklette, “*Science and Applications of Conducting Polymers*”, IOP Publishing Ltd., Bristol, UK, (1990).
16. A. G. MacDiarmid, A. J. Epstein, “*Frontiers of Polymer Research*”, Plenum Publishing Corporation, New York (1991).
17. P. Novak, K. Miller, K. S. V. Santhanam, O. Haas, *Chem. Rev.*, 97 (1997) 207.
18. G. Barbero, M. C. Miras, R. Koetz, O. Haas, *Synth. Met.*, 55 (1993) 1539.
19. A. G. MacDiarmid, W. Zheng, *MRS Bulletin* 22 (1997) 24.
20. M. Mastragostino, A. M. Marinangeli, A. Corradini, S. Giacobbe, *Synth. Met.*, 28 (1989) C501.
21. J. C. Dubois, *Synth. Met.*, 28 (1989) C871.
22. J. Roncali, R. Garreau, D. Delabouglise, F. Garnier, M. Lemaire, *J. Chem. Soc., Chem. Commun.*, (1989) 679.
23. K. Kaneto, M. Kaneko, Y. Min, A. G. MacDiarmid, *Synth. Met.*, 71 (1995) 2211.
24. D. W. DeBerry, *J. Electrochem. Soc.*, 3 (1985) 1022.
25. Y. Furukawa, *J. Phys. Chem.*, 100 (39) (1996) 15644.

26. G. M. Spinks, P. C. Innis, T. W. Lewis, L. A. P. Kane-Maguire, G. G. Wallace, *Mater. Forum*, 24 (2000) 125.
27. A. Angeli, *Gazz. Chim. Ital.*, 46 (1916) 279.
28. S. Etemad, *Ann. Rev. Phys. Chem.*, 33 (1982) 443.
29. H. Shirakawa, S. Ikeda, *Polym. J.*, 2 (1971) 231.
30. Y. Ito, H. Shirakawa, S. Ikeda, *Polym. Sci., Polym. Chem.*, 12 (1974) 11.
31. K. Seeger, *Angew. Macromol. Chem.*, 109/10 (1982) 227.
32. H. Naarmann, "*Electronic Properties of Conjugated Polymers*", Springer-Varlaa, Solid State Sciences, 76 (1987).
33. P. Chandrasekhar, "*Conducting Polymers, Fundamentals and Applications*", Kluwer Academic Publishers, Massachusetts, USA (1999).
34. A. F. Diaz, *New Journal of Chemistry*, 12 (4) (1988) 171.
35. R. J. Waltman, *Can. J. Chem.*, 64 (1986) 76.
36. G. Tourillon, F. Garnier, *J. Electroanal. Chem.*, 135 (1982) 173.
37. R. J. Waltman, J. Bargon, A. F. Diaz, *J. Phys. Chem.*, 87 (1983) 1459.
38. T. Yamamoto, K. Sanechika, A. Yamamoto, *J. Poly. Sci., Polym. Lett. Ed.*, 18 (1980) 9.
39. G. Tourillon, F. Garnier, *J. Electroanal. Soc.*, 130 (1983) 2042.
40. A. G. MacDiarmid, *Polym. Prep. Am. Chem. Soc. Div. Polym. Chem.*, 25 (1984) 248.

41. E. Genies, C. Tsintavis, *J. Electroanal. Chem.*, 195 (1985) 109.
42. I. Rubenstein, E. Sabatini, J. Rishpan, *J. Electroanal. Chem.*, 134 (1987) 3078.
43. J. L. Bredas, R. R. Chance, R. Silbey, *Phys. Rev., Part B.*, B26(10) (1982) 5843.
44. B. R. Weinberger, E. Ehrenfreund, A. J. Heeger, A. G. MacDiarmid, *Mol. Cryst. Liq. Cryst.*, 72 (1981) 253.
45. J. L. Bredas, B. Themans, J. M. Andre, R. R. Chance, D. S. Boudreaux, R. Silbey, *J. de Physique Colloque*, C3, 44 (1983) 373.
46. A. R. Bishop, D. K. Campbell, K. Fesser, *Mol. Cryst. Liq. Cryst.*, 77 (1980) 253.
47. F. E. Okieimen, I. N. Uroghide, C. O. Oriakhi, *Eur. Polym. J.*, 26 (2) (1990) 233.
48. J. Lu, H. Liang, A. Li, Q. Cheng, *Eur. Polym. J.*, 40 (2) (2003) 397.
49. S. Poser, H. Fisher, M. Arnold, *Prog. in Polym. Sci.*, 23 (7) (1998) 1337.
50. G. Jiang, T. Wang, C. Horng, *Polym. Preprints (Am. Chem. Soc.)*, 37 (2) (1996) 352.
51. A. Charas, J. Morgado, L. Alcacer, J. Martinho, F. Cacialli, *Synth. Met.*, 135-136 (2003) 387.
52. A. Reiche, A. Weinkauff, B. Sandner, F. Rittig, G. Fleischer, *Electrochim. Acta*, 45 (8-9) (2000) 1327.

53. U. Geisier, M. Hallensleben, L. Toppare, *Synth. Met.*, 55 (2-3) (1993) 1483.
54. J. Pollino, L. Stubbs, M. Weck, *J. Am. Chem. Soc.*, 126 (2) (2004) 563.
55. T. Otsu, A. Kuriyama, *Polym. J.*, 34 (5) (2002) 124.
56. Irvin, S. Fallis, D. Stasko, A. Guenther, K. Davis, D. Kline, A. Paiz, *Polym. Mater. Sci. and Eng.*, 11-12 (2003) 86.
57. C. Schmitt, M. Lebienvenu, *J. Mater. Process. Tech.*, 134 (3) (2003) 303.
58. E. Sancaktar, *J. Adhes. Sci. Technol.*, 17 (9) (2003) 1265.
59. M. A. Gaynes, L. J. Matienzo, J. A. Zimmerman, D. Vanhart, *Mat. Res. Soc. Symp. Proceedings*, 445 (1997) 139.
60. G. Gadodia, V. Shrttukde, *Popul. Plast. Pack.*, 48 (12) (2003) 59.
61. H. K. Kim, M. S. Kim, K. Song, Y. H. Park, S. H. Kim, J. Joo, J. Y. Lee, *Synth. Met.*, 135-136 (2003) 105.
62. M. Saurin, S. P Armes, *J. Appl. Polym. Sci.*, 56 (1) (1995) 41.
63. R. Van de Leur, *Mater. World*, 1 (11) (1993) 607.
64. M. Sun, *Microelectronics*, 32 (3) (2001) 197.
65. E. A. Kim, S. Yoo, J. Kim, *Fiber. Polym.*, 4 (4) (2003) 215.
66. H. K. Kim, M. S. Kim, S. Y. Chun, Y. H. Park, S. Boong, Y. Jun, Y. K. Hong, J. Joo, S. H. Kim, *Mol. Cryst. Liq. Cryst.*, 405 (2003) 161.

67. H. H. Law, P. L. Rossiter, L. L. Koss, G. P. Simon, *J. Mater. Sci.*, 30 (10) (1995) 2648.
68. T. Otsubo, Y. Aso, K. Takimiya, *J. Mater. Chem.*, 12 (9) (2002) 2565.
69. M. K. Ram, C. Nicolini, *Recent Res. Dev. Phys. Chem.*, 4 (2) (2000) 219.
70. D. Kumar, R. C. Sharma, *Eur. Polym. J.*, 34 (8) (1998) 1053.
71. R. Dobay, G. Harsanyi, C. Gabor, *Anal. Chim. Acta*, 385 (1-3) (1999) 187.
72. Q. Fang, D. G. Chetwynd, J. Covington, *Sensor. Actuators, B: Chemical*, B84 (1) (2002) 66.
73. J. Janata, M. Josowicz, *Nat. Mater.*, 2 (1) (2003) 19.
74. T. M. Swager, *Am. Chem. Soc., Div. Polym. Chem.*, 44 (2) (2003) 444.
75. H. Karami, M. Mousavi, M. Shamsipur, *J. Power Sources*, 117 (1-2) (2003) 225.
76. Y. Lee, S. Kwang, S. H. Chang, *J. Power Sources*, 119-121 (2003) 321.
77. J. Sarrazin, M. Persin, M. Cretin, *Polym. Mem.*, 188 (2002) 1.
78. T. Sata, *Electrochim. Acta*, 37 (3) (1992) 555.
79. M. Shahinpoor, *Electrochim. Acta*, 48 (14-16) (2003) 2343.
80. J. D. Madden, R. A. Cush, T. S. Kanigon, J. Colin, I. W. Hunter, *Synth. Metals*, 113 (1-2) (2000) 185.
81. L. Bay, K. West, S. Skaarup, *Polymer*, 43 (12) (2002) 3527.

82. G. Spinks, G. G. Wallace, T. Lewis, L. S. Fitfield, L. Dia, R. H. Baughman, *Proceedings of SPIE*, 4234 (2001) 223.
83. K. L. Heitner, *J. Power Sources*, 89 (2) (2000) 128.
84. T. Tung, L. Chen, K. Ho, *Solid State Ionics*, 165 (1-4) (2003) 257.
85. F. Croce, S. Panero, S. Passerini, B. Scrosati, *Electrochim. Acta*, 39 (2) (1994) 255.
86. M. Nishizawa, I. Uchida, *Electrochim. Acta*, 44 (21-22) (1999) 3629.
87. V. N. Popok, V. B. Odzhaev, I. I. Azarko, I. P. Kozlov, D. V. Sviridov, V. Hnatowicz, J. Vacik, J. Cervena, *Nucl. Instrum. Meth. Phys. Res. B*, 166-167 (2000) 660.
88. C. Lui, Z. Zhu, Y. Jin, Y. Sun, M. Hou, Z. Wang, X. Chen, C. Zhang, J. Liu, B. Li, Y. Wang, *Nucl. Instrum. Meth. Phys. Res. B*, 166-167 (2000) 166.
89. K. Ueno, Y. Matsumoto, M. Nishimiya, M. Satou, , *Nucl. Instrum. Meth. Phys. Res. B*, B59-60 (1991) 1263.
90. V. B. Odzhaev, V. N. Popok, E. I. Kozlova, O. N. Jankoyskii, I. A. Karpovich, *Nucl. Instrum. Meth. Phys. Res. B*, 166-167 (2000) 655.
91. A. De Bonis, A. Bearzotti, G. Marletta, *Nucl. Instrum. Meth. Phys. Res. B*, 151 (1-4) (1999) 101.
92. T. Venkatesan, *Nucl. Instrum. Meth. Phys. Res. B*, B7-8 (2) (1985) 461.
93. E. Balanzat, N. Betz, S. Bouffard, *Nucl. Instrum. Meth. Phys. Res. B*, 105 (1-4) (1995) 46.

94. C. M. A. Brett and A. M. O. Brett, "*Electrochemistry Principles, Methods and Applications*", Oxford University Press Inc., New York (1993).
95. D. R. Crow, "*Principles and Applications of Electrochemistry*", Blackie Academic & Professional (1994).
96. Private communication with A. C. Partridge, I.R.L. (2001).
97. P. H. Rieger, "*Electrochemistry*", 2nd edition, Chapman and Hall Inc., (1994).
98. P.T. Kissinger and W.R. Heinman "*Laboratory Techniques in Electroanalytical Chemistry*", Marcel Dekker Inc., 2nd Edn. (1996).
99. E. Rutherford, "*The Scattering of α and β Particles by Matter and the Structure of the Atom*", *Phil. Mag.*, 21(6) (1911).
100. P. B. Moon, "*Ernest Rutherford and the atom*" Priory Press, London (1975).
101. R.D. Evens, "*The Atomic Nucleus*", Mc Graw-Hill, New York (1974).
102. A. Nurmela, V. Zazubovich, J. Raisanen, E. Rauhala, R. Lappalainen, *J. Applied Phys.*, 84 (4) (1998) 1796.
103. W. Chu, J. Mayer, M. Nicolet, "*Backscattering Spectrometry*", Academic Press, Boston (1978).
104. L. Feldman, J. Mayer, "*Fundamentals of surface and thin film analysis*", Prentice-Hall, Englewood Cliffs (1986).
105. A. Markwitz, *Nucl. Instrum. Meth. Phys. Res. B*, 161-163 (2000) 221.

106. J. Tesmer, M. Nastasi, J. Barbour, C. Maggiore, J. Mayer, "*Handbook of modern ion beam materials analysis*", Materials Research Society, Pittsburgh (1995).
107. J. R. Bird, J. S. Williams, "*Ion beams for materials analysis*", Academic Press, Sydney (1989).
108. RUMP software package handbook, Cornell University, 1996.
109. M. Mayer, *SIMNRA User's Guide*, Report IPP 9/113, Max-Planck-Institut für Plasmaphysik, Garching, Germany, 1997.
110. In house GNS software package, Bill Trompetter, 1998.
111. Private communication with A. Markwitz, GNS (2000).
112. Guelph PIXE software package handbook, Ontario, Canada, 2002.
113. T. Steckenreiter, E. Balanzat, H. Fuess, C. Trautmann, *Nucl. Instrum. Meth. Phys. Res. B*, 151(1-4) (1999) 161.
114. V. N. Popok, V. B. Odzhaev, I. P. Kozlov, I. I. Azarko, I. A. Karpovich, D. V. Sviridov, *Nucl. Instrum. Meth. Phys. Res. B*, 129(1) (1997) 60.
115. B. S. Elman, G. F. Blackburn, M. K. Thakur, D. J. Sandman, L. A. Samuelson, D. G. Kenneson, *Nucl. Instrum. Meth. Phys. Res. B*, 19-20 (2) (1987) 862.
116. L. Ruangchuay, A. Sirivat, J. Schwank, *Polym. Mater. Sci. and Eng.*, 86 (2002) 21.
117. P. Li, M. Thompson, *Anal. Chim. Acta*, 354 (2-3) (1997) 255.

118. M. J. Swann, A. Glidle, N. Gadegaard, L. Cui, J. R. Barker, J. M. Cooper, *Cond. Matter*, 276-278 (2000) 357.
119. B. Scrosati, *Phil. Mag. B: Phys. Cond. Matter*, 59 (1) (1989) 151.
120. M. P. De Long, A. W. Denier van der Gon, X. Crispin, W. Osikowicz, W. R. Salaneck, L. Groenendaal, *J. Chem. Phys.*, 118 (14) (2003) 6495.
121. A.C.Partridge, C. B. Milestone, C. O. Too, G. G. Wallace, *J. Membrane Sci.*, 152 (1) (1999) 152.
122. A. Kassim, A. Abdullah, M. Rahman, A. Zaki, Z. Zainal, A. Baker, S. Nita, H. Mahmud, *Res. J. Chem. and Enviro. Studies*, 5 (3) (2001) 33.
123. J. Chen, A. K. Burrell, G. E. Collis, D. L. Officer, G. F. Swiegers, C. O. Too, G. G. Wallace, *Electrochim. Acta*, 47 (17) (2002) 2715.
124. A. P. Chattaraj, I. N. Basumallick, *J. Power Sources*, 36(4) (1991) 557.
125. P. J. Skabara, D. M. Roberts, I. M Serebryakov, C. Pozo-Gonzalo, *Chem. Commun.*, 12 (2000) 1005.
126. P. J. Skabara, I. M. Serebryakov, D. M. Roberts, I. F. Perepichka, S. J. Coles, M. B. Hursthouse, *J. Org. Chem.*, 64 (1999) 6418.
127. O. Clot, M. O. Wolf, B. O. Patrick, *J. Am. Chem. Soc.*, 122(42) (2000) 10456.
128. C. Visy, J. Lukkari, J. Kankare, *Macromolecules*, 27 (1994) 3322.
129. K. J. Watson, P. S. Wolfe, S. T. Nguyen, J. Zhu, C. A. Mirkin, *Macromolecules*, 33 (2000) 4628.
130. T. Susumu, K. Masami, *J. Chem. Soc., Chem. Commun.*, 8 (1995) 815.

131. S. Dubey, B. Fabre, G. Marchand, J. F. Pilard, J. Simonet, *Electroanal. Chem.*, 477(2) (1999) 121.
132. Private communication with A. Markwitz, GNS (2003).

Appendix

RBS simulation data

Table A.1 RBS simulation data for TTh-Por-TTh spectrum in Chapter 3 (Fig. 3.10)

Layer number	Layer thickness (at/cm ²)	Elemental Composition												
		C	N	O	Al	Si	S	Cl	K	Mn	Fe	Cu	Zn	Br
1	550	2.000	0.800	0.900	0.400	0.005	0.150	0.100	0.040	0.003	0.007	0.006	0.004	0.002
2	550	2.000	0.400	0.400	0.200	–	0.040	0.008	–	–	0.004	0.002	–	–
3	500	2.000	0.200	0.100	0.130	–	0.010	0.010	–	–	0.002	–	–	–
4	500	2.000	0.050	0.100	0.100	–	0.020	–	–	–	0.001	–	–	–
5	500	2.000	–	–	0.070	–	0.005	–	–	–	–	–	–	–
6	500	2.000	–	–	0.050	–	0.005	–	–	–	–	–	–	–
7	500	2.000	–	–	0.045	–	0.005	–	–	–	–	–	–	–
8	500	2.000	–	–	0.035	–	0.005	–	–	–	–	–	–	–
9	500	2.000	–	–	0.025	–	0.005	–	–	–	–	–	–	–
10	6000	1.000	–	–	–	–	–	–	–	–	–	–	–	–

Table A.2 RBS simulation data for cycled TTh-Por-TTh spectrum in Chapter 3 (Fig. 3.11)

Elemental Composition														
Layer number	Layer thickness (at/cm ²)	C	N	O	Al	Si	S	Cl	Ar	K	Ca	Fe	Cu	Zn
1	500	1.200	0.200	0.200	0.100	0.005	0.021	0.020	0.009	0.002	0.001	0.004	0.001	0.002
2	500	1.200	0.040	0.080	0.040	–	0.005	0.005	–	–	–	0.002	–	–
3	500	1.200	0.020	0.020	0.028	–	0.001	0.001	–	–	–	0.002	–	–
4	500	1.200	0.045	0.050	0.023	–	0.001	–	–	–	–	–	–	–
5	500	1.200	0.035	–	0.015	–	0.001	–	–	–	–	–	–	–
6	500	1.200	0.030	–	0.010	–	0.001	–	–	–	–	–	–	–
7	1500	1.200	0.030	–	0.005	–	0.001	–	–	–	–	–	–	–
8	5000	1.000	–	–	–	–	–	–	–	–	–	–	–	–

Table A.3 RBS simulation data for the TTh-ZnPor-TTh sample from Chapter 3 (Fig. 3.13)

Elemental Composition													
Layer number	Layer thickness (at/cm ²)	C	N	O	Al	Si	S	Cl	Ar	K	Fe	Cu	Zn
1	450	1.200	0.210	0.300	0.120	0.010	0.020	0.020	0.010	0.004	0.003	0.001	0.012
2	450	1.200	0.110	0.150	0.050	–	0.003	0.003	–	–	0.002	0.001	0.001
3	450	1.200	0.090	0.110	0.040	–	0.001	0.008	–	–	0.004	0.002	0.001
4	450	1.200	0.045	–	0.031	–	0.001	–	–	–	–	–	–
5	450	1.200	0.035	–	0.030	–	0.001	–	–	–	–	–	–
6	450	1.200	0.030	–	0.025	–	0.001	–	–	–	–	–	–
7	450	1.200	0.030	–	0.020	–	0.001	–	–	–	–	–	–
8	450	1.200	0.030	–	0.018	–	0.001	–	–	–	–	–	–
9	450	1.200	0.030	–	0.015	–	0.001	–	–	–	–	–	–
10	450	1.200	0.030	–	0.010	–	0.001	–	–	–	–	–	–
11	5000	1.000	–	–	–	–	–	–	–	–	–	–	–

Table A.4 RBS simulation data for soaked TTh-Por-TTh spectrum in Chapter 3 (Fig. 3.12)

Elemental Composition															
Layer number	Layer thickness (at/cm ²)	C	N	O	Al	Si	S	Cl	Ar	K	Mn	Fe	Cu	Zn	Br
1	400	1.200	0.250	0.400	0.150	0.007	0.080	0.020	0.005	0.002	0.001	0.001	0.001	0.009	0.003
2	400	1.200	0.180	0.120	0.070	–	0.010	0.001	–	–	–	–	–	0.001	–
3	400	1.200	0.120	0.100	0.050	–	0.001	0.001	–	–	–	–	–	0.001	–
4	400	1.200	0.045	0.050	0.040	–	0.001	–	–	–	–	–	–	–	–
5	400	1.200	0.045	–	0.030	–	0.001	–	–	–	–	–	–	–	–
6	400	1.200	0.035	–	0.025	–	0.001	–	–	–	–	–	–	–	–
7	400	1.200	0.030	–	0.022	–	0.001	–	–	–	–	–	–	–	–
8	400	1.200	0.030	–	0.017	–	0.001	–	–	–	–	–	–	–	–
9	400	1.200	0.030	–	0.015	–	0.001	–	–	–	–	–	–	–	–
10	400	1.200	0.030	–	0.010	–	0.001	–	–	–	–	–	–	–	–
11	400	1.200	0.030	–	0.013	–	0.001	–	–	–	–	–	–	–	–
12	5000	1.000	–	–	–	–	–	–	–	–	–	–	–	–	–

Table A.5 RBS simulation data for the solution side PPy-DBS film from Chapter 4 (Fig. 4.12)

Elemental Composition													
Layer number	Layer thickness (at/cm ²)	C	N	O	Na	S	Cl	Ca	Ti	Cr	Mn	Co	Cu
1	150	150.0	24.0	14.0	3.0	3.0	2.8	1.4	0.5	0.2	0.1	1.0	0.1
2	1250	150.0	24.0	14.0	3.0	4.0	–	–	–	–	–	–	–
3	1250	150.0	20.0	13.0	4.0	3.0	–	–	–	–	–	–	–
4	1250	150.0	15.0	11.0	2.0	3.0	–	–	–	–	–	–	–
5	1250	150.0	15.0	12.0	2.0	3.0	–	–	–	–	–	–	–
6	1250	150.0	15.0	12.0	2.0	3.0	–	–	–	–	–	–	–

Table A.6 RBS simulation data for the solution side PPy-NBS film from Chapter 4 (Fig. 4.13)

Elemental Composition												
Layer number	Layer thickness (at/cm ²)	C	N	O	Na	S	Cl	K	Ca	Ti	Co	Cu
1	150	145.0	36.0	10.0	2.0	3.0	0.6	0.1	0.1	0.2	0.1	0.1
2	1375	145.0	36.0	10.0	2.0	3.0	–	–	–	–	–	–
3	1375	145.0	28.0	10.0	2.0	3.0	–	–	–	–	–	–
4	1375	145.0	24.0	10.0	2.0	3.0	–	–	–	–	–	–
5	1375	145.0	24.0	10.0	2.0	3.0	–	–	–	–	–	–
6	1375	145.0	24.0	10.0	2.0	3.0	–	–	–	–	–	–

Table A.7 RBS simulation data for the solution side PPy-HBS film from Chapter 4 (Fig. 4.14)

Elemental Composition															
Layer number	Layer thickness (at/cm ²)	C	N	O	Na	S	Ca	Sc	Cl	Ti	Cr	Mn	Fe	Co	Cu
1	150	100.0	26.0	20.0	2.8	3.5	0.3	0.2	0.6	0.3	0.4	0.3	0.1	0.7	0.1
2	1350	100.0	26.0	20.0	2.8	3.5	–	–	–	–	–	–	–	–	–
3	1350	100.0	28.0	14.0	2.8	3.2	–	–	–	–	–	–	–	–	–
4	1350	100.0	26.0	14.0	4.0	2.5	–	–	–	–	–	–	–	–	–
5	1350	100.0	26.0	14.0	3.0	2.8	–	–	–	–	–	–	–	–	–

Table A.8 RBS simulation data for the solution side PPy-MS film from Chapter 4 (Fig. 4.15)

Elemental Composition															
Layer number	Layer thickness (at/cm ²)	C	N	O	Na	S	Ca	Sc	Cl	Ti	Cr	Mn	Fe	Co	Cu
1	150	85.0	16.0	12.0	0.8	2.0	0.3	0.2	0.6	0.3	0.4	0.4	0.2	0.6	0.1
2	1350	85.0	16.0	12.0	0.8	2.0	–	–	–	–	–	–	–	–	–
3	1350	85.0	16.0	13.0	0.8	2.0	–	–	–	–	–	–	–	–	–
4	1350	85.0	16.0	16.0	1.6	2.0	–	–	–	–	–	–	–	–	–
5	1350	85.0	16.0	16.0	1.0	2.0	–	–	–	–	–	–	–	–	–

Table A.9 RBS simulation data for the solution side PPy-SB film from Chapter 4 (Fig. 4.16)

Elemental Composition										
Layer number	Layer thickness (at/cm ²)	C	N	O	Na	S	Ca	Cr	Fe	Co
1	150	85.0	20.0	21.0	0.9	3.1	2.0	0.1	0.1	0.1
2	1400	85.0	20.0	22.0	0.9	3.1	–	–	–	–
3	1400	85.0	19.0	18.0	0.8	3.1	–	–	–	–
4	1400	85.0	18.0	18.0	0.7	3.1	–	–	–	–
5	1400	85.0	18.0	18.0	0.7	3.1	–	–	–	–

Table A.10 RBS simulation data for the solution side PPy-PTS film from Chapter 4 (Fig. 4.17)

Elemental Composition														
Layer number	Layer thickness (at/cm ²)	C	N	O	Na	S	Ca	Sc	Cl	Ti	Cr	Mn	Co	Cu
1	150	85.0	24.0	20.0	2.0	4.0	0.2	0.2	1.8	0.2	0.2	0.1	0.6	0.5
2	1400	85.0	24.0	20.0	2.0	4.0	–	–	–	–	–	–	–	–
3	1400	85.0	24.0	16.0	2.0	3.5	–	–	–	–	–	–	–	–
4	1400	85.0	24.0	16.0	2.0	3.0	–	–	–	–	–	–	–	–
5	1400	85.0	24.0	16.0	2.0	3.5	–	–	–	–	–	–	–	–

Table A. 11 Parameters other than copolymer monomers and ClO₄⁻ used in the calculations of copolymer to TTh-Fc ratios and counter ion to TTh-Fc ratios.

Sample	Layer number	Parameters				
		CH ₂ Cl ₂	Bu ₄ N ⁺	H ₂ O	Oxygen	Carbon
1:10 TTh-Fc/ Py (electrode side)	1	0.044	—	—	—	—
	2	0.191	—	—	—	—
	3	0.017	—	—	—	—
1:20 TTh-Fc/ Py (solution side)	1	—	—	—	—	—
	2	0.163	—	—	—	—
	3	0.007	—	—	—	—
1:20 TTh-Fc/Py (electrode side)	1	0.226	—	—	—	—
	2	—	—	—	—	—
	3	—	—	—	—	—
1:50 TTh-Fc/Py (solution side)	1	0.175	—	—	—	—
	2	0.171	—	—	—	—
	3	0.057	—	—	—	—
1:50 TTh-Fc/Py (electrode side)	1	0.103	—	—	—	—
	2	0.112	—	—	—	—
	3	—	—	—	—	—
1:100 TTh-Fc/ Py (solution side)	1	0.136	—	—	—	—
	2	0.105	—	—	—	—
	3	—	—	—	—	—
1:100 TTh-Fc/ Py (electrode side)	1	0.071	—	—	—	—
	2	0.184	—	—	—	—
	3	0.065	—	—	—	—

Table A.11 continued

1:10 TTh-Fc/ bithiophene (solution side)	1	0.214	—	—	—	6.526
	2	0.187	—	—	—	5.171
	3	0.214	—	—	—	6.526
1:10 TTh-Fc/ bithiophene (electrode side)	1	—	—	—	—	1.484
	2	0.070	—	—	—	4.607
	3	0.086	—	—	—	7.634
1:20 TTh-Fc/ bithiophene (solution side)	1	0.075	—	—	1.075	0.149
	2	0.126	—	—	1.767	1.435
	3	0.180	—	—	1.957	2.687
1:20 TTh-Fc/ bithiophene (electrode side)	1	0.003	—	—	1.228	—
	2	—	—	—	—	1.099
	3	—	—	—	—	0.467
	4	0.075	—	—	1.222	1.305
	5	0.072	—	—	1.239	2.219
	6	0.066	—	—	0.879	2.463
1:50 TTh-Fc/ bithiophene (solution side)	1	0.003	—	—	2.979	1.694
	2	—	—	—	—	7.882
	3	0.025	—	—	—	3.055
	4	0.212	—	—	1.217	0.910
1:50 TTh-Fc/ bithiophene (electrode side)	1	—	—	—	—	—
	2	0.036	—	—	—	2.949
	3	—	—	—	—	2.413
1:100 TTh-Fc/ bithiophene (solution side)	1	0.126	—	—	—	0.932
	2	—	—	—	—	3.536
	3	—	—	—	—	1.893
1:100 TTh-Fc/ bithiophene (electrode side)	1	0.142	—	—	—	1.515
	2	—	—	—	1.041	2.831
	3	—	—	—	0.180	3.887

Table A.11 continued

1:10 TTh-Fc/ EDOT (solution side)	1	0.137	—	—	—	0.556
	2	0.263	—	—	—	2.346
	3	0.137	—	—	—	0.556
	4	0.333	—	—	—	0.811
1:10 TTh-Fc/ EDOT (electrode side)	1	0.098	—	—	—	1.563
	2	0.268	—	—	—	3.066
1:20 TTh-Fc/ EDOT (solution side)	1	0.089	—	—	—	1.468
	2	0.331	—	—	—	1.195
1:50 TTh-Fc/ EDOT (solution side)	1	0.078	—	—	—	1.647
	2	0.074	—	—	—	0.811
	3	0.031	—	—	—	1.534
1:50 TTh-Fc/ EDOT (electrode side)	1	0.053	—	—	—	1.460
	2	0.225	—	—	—	2.301
1:100 TTh-Fc/ EDOT (electrode side)	1	0.078	—	—	—	1.647
	2	0.074	—	—	—	0.811
	3	0.031	—	—	—	1.534
2:1 TTh-Fc/ TTh-Por-TTh (solution side)	1	—	—	—	33.100	—
	2	—	—	—	33.100	—
	3	1.151	—	1.147	1.566	0.029
2:1 TTh-Fc/ TTh-Por-TTh (electrode side)	1	—	—	—	197.357	1.410
	2	—	—	—	197.357	1.420
1:5 TTh-Fc/ TTh-Por-TTh (solution side)	1	5.696	—	12.892	—	—
	2	28.873	9.01	0.312	0.288	—
	3	15.947	4.792	0.325	1.117	—
	4	9.230	—	21.425	—	—

Table A.11 continued

1:5 TTh-Fc/ TTh-Por-TTh (electrode side)	1	0.564	—	—	—	—
	2	14.243	5.430	—	—	—
	3	0.616	5.267	1.677	2.444	—
	4	1.056	—	—	—	—
2:5 TTh-Fc/ TTh-Por-TTh (solution side)	1	3.184	1.988	—	—	—
	2	107.808	24.869	8.781	7.936	—
	3	16.505	4.407	1.096	1.913	—
	4	—	0.706	—	—	—
2:5 TTh-Fc/ TTh-Por-TTh (electrode side)	1	—	8.303	18.187	5.263	—
	2	67.993	19.019	27.848	27.283	—
	3	10.643	5.689	4.177	4.929	—
	4	16.640	—	3.626	—	—
1:1 TTh-Fc/ TTh-Por-TTh (solution side)	1	0.699	28.543	18.946	24.332	—
	2	22.664	16.967	86.327	16.186	—
	3	18.466	12.709	12.384	10.068	—
	4	18.466	12.709	12.384	10.068	—
1:1 TTh-Fc/ TTh-Por-TTh (electrode side)	1	13.862	14.441	35.274	23.455	—
	2	22.366	18.185	16.199	22.271	—
	3	9.004	5.085	5.287	6.218	—
	4	—	—	16.274	—	—
1:10 TTh-Fc/ Bridging TTh (solution side)	1	0.162	—	—	—	1.282
	2	0.241	—	—	—	1.248
	3	0.313	—	—	—	1.087
	4	0.168	—	—	—	5.784

Table A.11 continued

1:10 TTh-Fc/ Bridging TTh (electrode side)	1	0.171	—	—	—	2.302
	2	0.254	—	—	—	2.278
	3	0.263	—	—	—	1.335
	4	0.273	—	—	—	2.073
1:1 TTh-Fc/ Bridging TTh (solution side)	1	—	—	—	—	1.379
	2	0.009	—	—	—	1.978
	3	0.055	—	—	—	1.823
1:1 TTh-Fc/ Bridging TTh (electrode side)	1	0.012	—	—	—	11.739
	2	0.066	—	—	—	8.080
	3	0.205	—	—	—	1.264
	4	0.279	—	—	—	1.220
10:1 TTh-Fc/ Bridging TTh (solution side)	1	0.680	—	—	—	1.708
	2	0.354	—	—	—	7.375
	3	0.351	—	—	—	6.291
	4	0.829	—	—	—	8.813
10:1 TTh-Fc/ Bridging TTh (electrode side)	1	1.264	—	—	—	12.974
	2	0.531	—	—	—	6.696
	3	0.408	—	—	—	8.065
	4	0.622	—	—	—	7.089

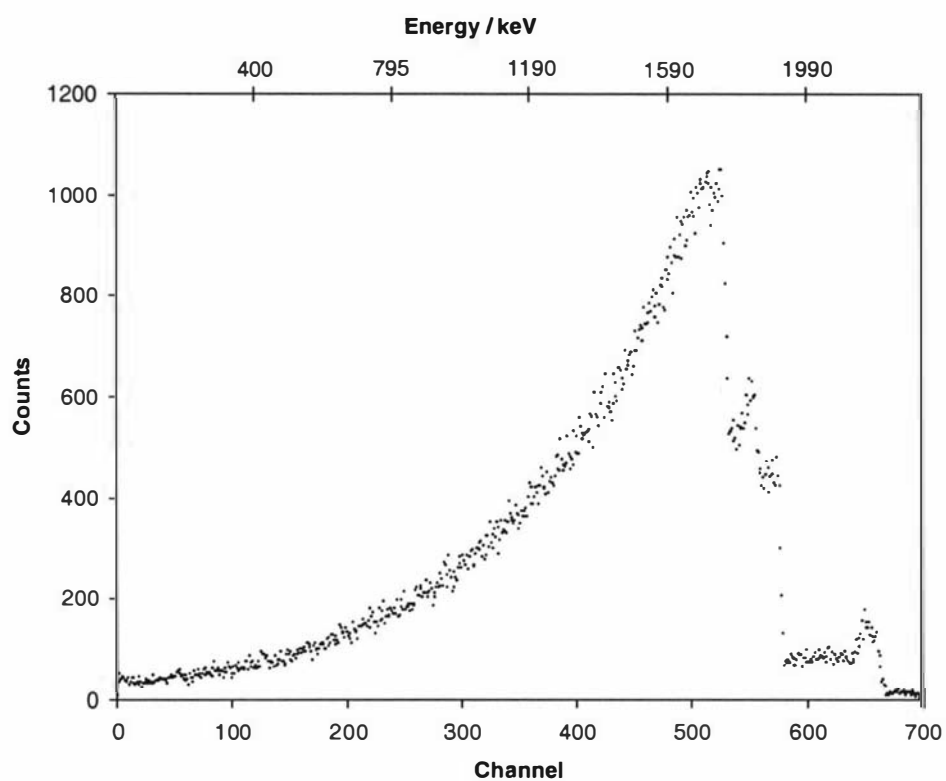


Fig. A.1 RBS experimental spectrum for the solution side of a TTh-Fc / Py copolymer (1:10) using a 2.5 MeV proton beam.

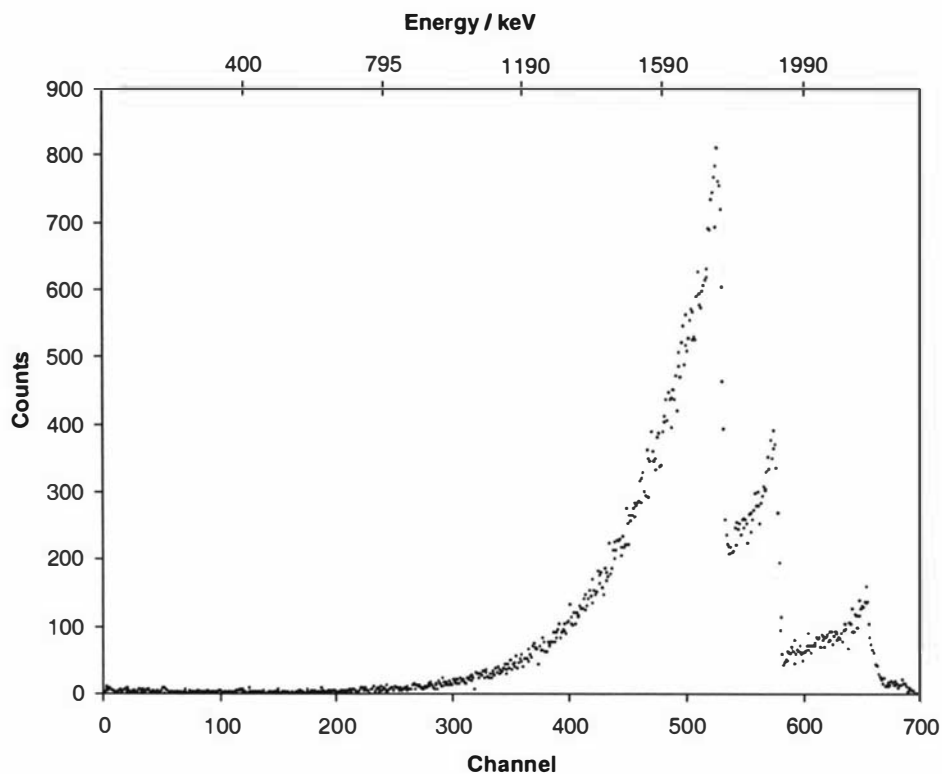


Fig. A.2 RBS experimental spectrum for the electrode side of a TTh-Fc / EDOT copolymer (1:20) using a 2.5 MeV proton beam.

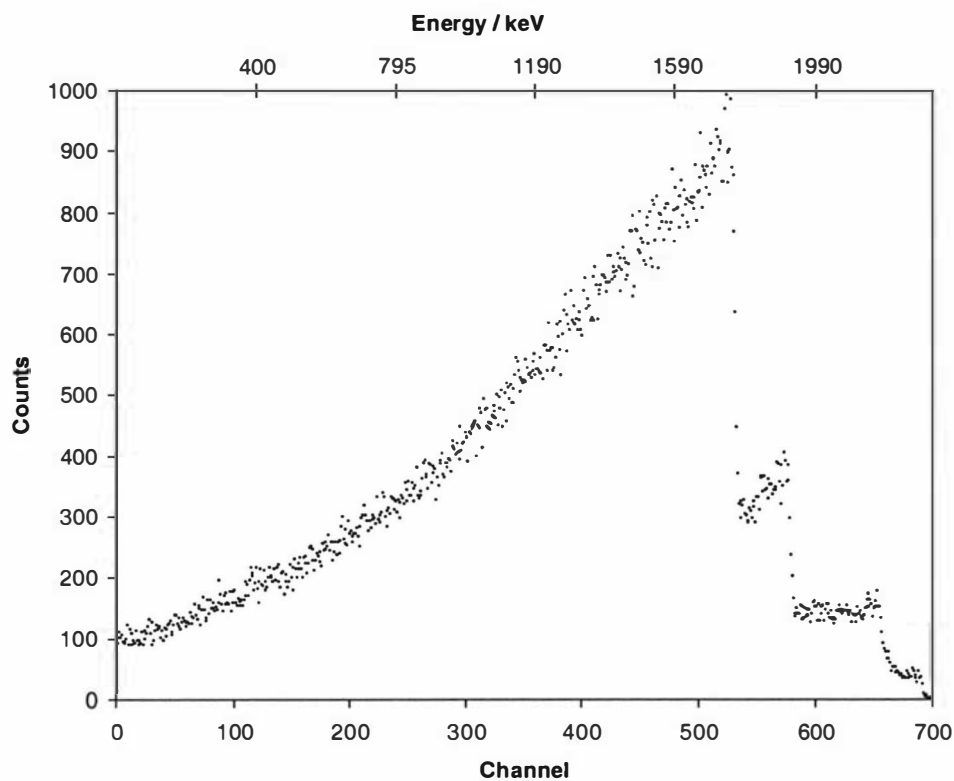


Fig. A.3 RBS experimental spectrum for the solution side of a TTh-Fc / EDOT copolymer (1:100) using a 2.5 MeV proton beam.

Table A.12 Un-simulated copolymer films and their spectrum type.

Film sample	Spectra type
1:10 TTh-Fc / Py (solution side)	3
1:20 TTh-Fc / EDOT (electrode side)	2
1:100 TTh-Fc / EDOT (solution side)	3

Table A.13 RBS simulation data for the electrode side 1:10 TTh-Fc / Py copolymer film from Chapter 7 (Fig. 7.9).

Elemental Composition								
Layer number	Layer thickness (at/cm ²)	H	C	N	O	S	Cl	Fe
1	13500	0.337	0.393	0.077	0.138	0.009	0.043	0.003
2	9500	0.357	0.353	0.067	0.138	0.009	0.073	0.003
3	6000	0.447	0.333	0.067	0.108	0.009	0.033	0.003

Table A.14 RBS simulation data for the solution side 1:20 TTh-Fc / Py copolymer film from Chapter 7 (Fig. 7.10).

Elemental Composition								
Layer number	Layer thickness (at/cm ²)	H	C	N	O	S	Cl	Fe
1	12500	0.347	0.363	0.092	0.148	0.009	0.038	0.003
2	6500	0.367	0.363	0.052	0.138	0.009	0.068	0.003
3	5000	0.457	0.318	0.052	0.128	0.009	0.033	0.003

Table A.15 RBS simulation data for the electrode side 1:20 TTh-Fc / Py copolymer film from Chapter 7 (Fig. 7.11).

Elemental Composition								
Layer number	Layer thickness (at/cm ²)	H	C	N	O	S	Cl	Fe
1	16000	0.268	0.408	0.067	0.178	0.006	0.071	0.002
2	6500	0.398	0.333	0.062	0.178	0.006	0.021	0.002
3	31000	0.423	0.328	0.072	0.143	0.006	0.026	0.002
4	30000	0.443	0.358	0.042	0.123	0.006	0.026	0.002

Table A.16 RBS simulation data for the solution side 1:50 TTh-Fc / Py copolymer film from Chapter 7 (Fig. 7.12).

Elemental Composition								
Layer number	Layer thickness (at/cm ²)	H	C	N	O	S	Cl	Fe
1	8000	0.331	0.348	0.087	0.153	0.006	0.073	0.002
2	4000	0.338	0.348	0.080	0.153	0.006	0.073	0.002
3	17000	0.341	0.351	0.092	0.153	0.006	0.053	0.002

Table A.17 RBS simulation data for the electrode side 1:50 TTh-Fc / Py copolymer film from Chapter 7 (Fig. 7.13).

Elemental Composition								
Layer number	Layer thickness (at/cm ²)	H	C	N	O	S	Cl	Fe
1	3000	0.341	0.393	0.062	0.142	0.006	0.054	0.002
2	11500	0.331	0.378	0.072	0.152	0.006	0.059	0.002
3	16500	0.406	0.363	0.066	0.128	0.006	0.029	0.002

Table A.18 RBS simulation data for the solution side 1:100 TTh-Fc / Py copolymer film from Chapter 7 (Fig. 7.14).

Elemental Composition								
Layer number	Layer thickness (at/cm ²)	H	C	N	O	S	Cl	Fe
1	13100	0.312	0.384	0.100	0.134	0.003	0.061	0.001
2	9000	0.315	0.393	0.065	0.165	0.003	0.058	0.001
3	3500	0.315	0.386	0.095	0.169	0.003	0.033	0.001

Table A.19 RBS simulation data for the electrode side 1:100 TTh-Fc / Py copolymer film from Chapter 7 (Fig. 7.15).

Elemental Composition								
Layer number	Layer thickness (at/cm ²)	H	C	N	O	S	Cl	Fe
1	3500	0.288	0.369	0.113	0.168	0.003	0.058	0.001
2	8000	0.279	0.389	0.102	0.158	0.003	0.068	0.001
3	12100	0.309	0.424	0.092	0.128	0.003	0.043	0.001

Table A.20 RBS simulation data for the solution side 1:10 TTh-Fc / bithiophene copolymer film from Chapter 7 (Fig. 7.24).

Elemental Composition							
Layer number	Layer thickness (at/cm ²)	H	C	O	S	Cl	Fe
1	39000	0.363	0.468	0.072	0.051	0.038	0.008
2	40000	0.384	0.448	0.072	0.051	0.038	0.008
3	37000	0.363	0.468	0.072	0.051	0.038	0.008

Table A.21 RBS simulation data for the electrode side 1:10 TTh-Fc / bithiophene copolymer film from Chapter 7 (Fig. 7.25).

Elemental Composition							
Layer number	Layer thickness (at/cm ²)	H	C	O	S	Cl	Fe
1	30000	0.438	0.374	0.097	0.051	0.020	0.020
2	10000	0.363	0.448	0.082	0.061	0.028	0.018
3	25000	0.323	0.488	0.082	0.061	0.028	0.018
4	25000	0.308	0.493	0.102	0.041	0.038	0.018
5	45000	0.329	0.442	0.112	0.061	0.038	0.018

Table A.22 RBS simulation data for the solution side 1:20 TTh-Fc / bithiophene copolymer film from Chapter 7 (Fig. 7.27).

Layer number	Layer thickness (at/cm ²)	Elemental Composition					
		H	C	O	S	Cl	Fe
1	45000	0.423	0.379	0.107	0.061	0.020	0.010
2	65000	0.366	0.431	0.112	0.061	0.020	0.010
3	65000	0.375	0.432	0.102	0.061	0.020	0.010

Table A.23 RBS simulation data for the electrode side 1:20 TTh-Fc / bithiophene copolymer film from Chapter 7 (Fig. 7.28).

Layer number	Layer thickness (at/cm ²)	Elemental Composition					
		H	C	O	S	Cl	Fe
1	10000	0.375	0.397	0.125	0.071	0.020	0.012
2	25000	0.415	0.392	0.092	0.071	0.020	0.010
3	10000	0.381	0.416	0.102	0.071	0.020	0.010
4	35000	0.341	0.456	0.102	0.071	0.020	0.010
5	35000	0.321	0.475	0.102	0.071	0.020	0.010
6	70000	0.378	0.444	0.097	0.051	0.020	0.010

Table A.24 RBS simulation data for the solution side 1:50 TTh-Fc / bithiophene copolymer film from Chapter 7 (Fig. 7.30).

Elemental Composition							
Layer number	Layer thickness (at/cm ²)	H	C	O	S	Cl	Fe
1	5000	0.263	0.506	0.115	0.091	0.016	0.010
2	5000	0.242	0.526	0.105	0.091	0.026	0.010
3	20000	0.372	0.436	0.095	0.061	0.026	0.010
4	52000	0.362	0.446	0.085	0.071	0.026	0.010

Table A.25 RBS simulation data for the electrode side 1:50 TTh-Fc / bithiophene copolymer film from Chapter 7 (Fig. 7.31).

Elemental Composition							
Layer number	Layer thickness (at/cm ²)	H	C	O	S	Cl	Fe
1	10000	0.302	0.466	0.098	0.101	0.026	0.007
2	50000	0.362	0.446	0.088	0.071	0.026	0.007
3	42000	0.382	0.436	0.078	0.071	0.026	0.007

Table A.26 RBS simulation data for the solution side 1:100 TTh-Fc / bithiophene copolymer film from Chapter 7 (Fig. 7.33).

Elemental Composition							
Layer number	Layer thickness (at/cm ²)	H	C	O	S	Cl	Fe
1	10000	0.337	0.445	0.095	0.081	0.036	0.006
2	15000	0.342	0.450	0.105	0.071	0.026	0.006
3	25000	0.337	0.445	0.105	0.081	0.026	0.006

Table A.27 RBS simulation data for the electrode side 1:100 TTh-Fc / bithiophene copolymer film from Chapter 7 (Fig. 7.34).

Elemental Composition							
Layer number	Layer thickness (at/cm ²)	H	C	O	S	Cl	Fe
1	10000	0.302	0.440	0.135	0.072	0.043	0.008
2	10000	0.382	0.410	0.125	0.059	0.016	0.008
3	19000	0.392	0.410	0.115	0.049	0.026	0.008

Table A.28 RBS simulation data for the solution side 1:10 TTh-Fc / EDOT copolymer film from Chapter 7 (Fig. 7.40).

Elemental Composition							
Layer number	Layer thickness (at/cm ²)	H	C	O	S	Cl	Fe
1	9000	0.358	0.383	0.162	0.051	0.039	0.007
2	30000	0.338	0.403	0.172	0.041	0.039	0.007
3	60000	0.368	0.383	0.153	0.051	0.038	0.007
4	85000	0.353	0.398	0.153	0.051	0.038	0.007

Table A.29 RBS simulation data for the electrode side 1:10 TTh-Fc / EDOT copolymer film from Chapter 7 (Fig. 7.41).

Elemental Composition							
Layer number	Layer thickness (at/cm ²)	H	C	O	S	Cl	Fe
1	12000	0.340	0.400	0.171	0.047	0.037	0.005
2	25000	0.380	0.400	0.151	0.027	0.037	0.005

Table A.30 RBS simulation data for the solution side 1:20 TTh-Fc / EDOT copolymer film from Chapter 7 (Fig. 7.43).

Elemental Composition							
Layer number	Layer thickness (at/cm ²)	H	C	O	S	Cl	Fe
1	65000	0.333	0.392	0.184	0.047	0.039	0.005
2	30000	0.363	0.392	0.154	0.047	0.039	0.005

Table A.31 RBS simulation data for the solution side 1:50 TTh-Fc / EDOT copolymer film from Chapter 7 (Fig. 7.45).

Elemental Composition							
Layer number	Layer thickness (at/cm ²)	H	C	O	S	Cl	Fe
1	30000	0.330	0.400	0.181	0.047	0.037	0.005
2	20000	0.320	0.385	0.211	0.052	0.027	0.005
3	50000	0.338	0.397	0.196	0.047	0.017	0.005

Table A.32 RBS simulation data for the electrode side 1:50 TTh-Fc / EDOT copolymer film from Chapter 7 (Fig. 7.46).

Elemental Composition							
Layer number	Layer thickness (at/cm ²)	H	C	O	S	Cl	Fe
1	7000	0.330	0.390	0.191	0.047	0.037	0.005
2	25000	0.350	0.390	0.181	0.037	0.037	0.005

Table A.33 RBS simulation data for the electrode side 1:100 TTh-Fc / EDOT copolymer film from Chapter 7 (Fig. 7.48).

Elemental Composition							
Layer number	Layer thickness (at/cm ²)	H	C	O	S	Cl	Fe
1	8000	0.238	0.407	0.244	0.084	0.022	0.005
2	28000	0.348	0.387	0.194	0.049	0.017	0.005
3	15000	0.338	0.397	0.204	0.039	0.017	0.005

Table A.34 RBS simulation data for the solution side 2:1 TTh-Fc / TTh-Por-TTh copolymer film from Chapter 7 (Fig. 7.54).

Elemental Composition								
Layer number	Layer thickness (at/cm ²)	H	C	N	O	S	Cl	Fe
1	8000	0.329	0.412	0.014	0.153	0.052	0.027	0.013
2	12000	0.403	0.400	0.011	0.096	0.033	0.040	0.015
3	62000	0.424	0.399	0.011	0.081	0.045	0.025	0.015

Table A.35 RBS simulation data for the electrode side 2:1 TTh-Fc/ TTh-Por-TTh copolymer film from Chapter 7 (Fig. 7.55).

Elemental Composition								
Layer number	Layer thickness (at/cm ²)	H	C	N	O	S	Cl	Fe
1	55000	0.265	0.465	0.008	0.157	0.054	0.031	0.020
2	190000	0.265	0.465	0.008	0.157	0.054	0.031	0.020

Table A.36 RBS simulation data for the solution side 1:5 TTh-Fc / TTh-Por-TTh copolymer film from Chapter 7 (Fig. 7.57).

Elemental Composition								
Layer number	Layer thickness (at/cm ²)	H	C	N	O	S	Cl	Fe
1	5000	0.422	0.432	0.024	0.055	0.021	0.039	0.021
2	10000	0.406	0.432	0.024	0.060	0.021	0.050	0.021
3	12000	0.443	0.415	0.021	0.045	0.021	0.048	0.021
4	83000	0.423	0.428	0.026	0.051	0.021	0.044	0.021

Table A.37 RBS simulation data for the electrode side 1:5 TTh-Fc / TTh-Por-TTh copolymer film from Chapter 7 (Fig. 7.58).

Elemental Composition								
Layer number	Layer thickness (at/cm ²)	H	C	N	O	S	Cl	Fe
1	12000	0.427	0.442	0.034	0.400	0.035	0.017	0.005
2	8000	0.397	0.442	0.034	0.050	0.035	0.037	0.005
3	12000	0.458	0.425	0.031	0.036	0.035	0.010	0.005
4	160000	0.474	0.419	0.016	0.031	0.035	0.020	0.005

Table A.38 RBS simulation data for the solution side 2:5 TTh-Fc / TTh-Por-TTh copolymer film from Chapter 7 (Fig. 7.60).

Elemental Composition								
Layer number	Layer thickness (at/cm ²)	H	C	N	O	S	Cl	Fe
1	5000	0.426	0.400	0.029	0.070	0.035	0.030	0.010
2	11000	0.369	0.435	0.026	0.070	0.030	0.060	0.010
3	14000	0.408	0.428	0.026	0.053	0.030	0.045	0.010
4	50000	0.423	0.416	0.026	0.051	0.030	0.044	0.010

Table A.39 RBS simulation data for the electrode side 2:5 TTh-Fc / TTh-Por-TTh copolymer film from Chapter 7 (Fig. 7.61).

Elemental Composition								
Layer number	Layer thickness (at/cm ²)	H	C	N	O	S	Cl	Fe
1	5000	0.401	0.385	0.034	0.115	0.030	0.025	0.010
2	11000	0.334	0.420	0.026	0.125	0.030	0.055	0.010
3	14000	0.413	0.388	0.031	0.088	0.030	0.040	0.010
4	40000	0.423	0.386	0.026	0.086	0.030	0.039	0.010

Table A.40 RBS simulation data for the solution side 1:1 TTh-Fc / TTh-Por-TTh copolymer film from Chapter 7 (Fig. 7.63).

Elemental Composition								
Layer number	Layer thickness (at/cm ²)	H	C	N	O	S	Cl	Fe
1	5000	0.385	0.397	0.006	0.123	0.048	0.025	0.016
2	10000	0.319	0.434	0.006	0.130	0.048	0.045	0.018
3	15000	0.427	0.398	0.011	0.078	0.040	0.030	0.016
4	130000	0.435	0.398	0.006	0.076	0.040	0.029	0.016

Table A.41 RBS simulation data for the electrode side 1:1 TTh-Fc / TTh-Por-TTh copolymer film from Chapter 7 (Fig. 7.64).

Elemental Composition								
Layer number	Layer thickness (at/cm ²)	H	C	N	O	S	Cl	Fe
1	5000	0.380	0.380	0.026	0.133	0.042	0.025	0.014
2	10000	0.319	0.419	0.026	0.135	0.042	0.045	0.014
3	15000	0.423	0.382	0.031	0.078	0.042	0.030	0.014
4	66000	0.433	0.380	0.026	0.076	0.042	0.029	0.014

Table A.42 RBS simulation data for the solution side 1:10 TTh-Fc / Bridging TTh copolymer film from Chapter 7 (Fig. 7.70).

Layer number	Layer thickness (at/cm ²)	Elemental Composition					
		H	C	O	S	Cl	Fe
1	10000	0.420	0.441	0.032	0.090	0.015	0.002
2	12000	0.420	0.441	0.032	0.090	0.015	0.002
3	16000	0.435	0.441	0.017	0.090	0.015	0.002
4	31000	0.455	0.431	0.037	0.061	0.015	0.002

Table A.43 RBS simulation data for the electrode side 1:10 TTh-Fc / Bridging TTh copolymer film from Chapter 7 (Fig. 7.71).

Layer number	Layer thickness (at/cm ²)	Elemental Composition					
		H	C	O	S	Cl	Fe
1	7000	0.400	0.461	0.032	0.090	0.015	0.002
2	7000	0.400	0.461	0.032	0.090	0.015	0.002
3	24000	0.435	0.445	0.012	0.090	0.016	0.002
4	39500	0.420	0.460	0.012	0.090	0.016	0.002

Table A.44 RBS simulation data for the solution side 1:1 TTh-Fc / Bridging TTh copolymer film from Chapter 7 (Fig. 7.73).

Elemental Composition							
Layer number	Layer thickness (at/cm ²)	H	C	O	S	Cl	Fe
1	4000	0.390	0.444	0.102	0.035	0.025	0.004
2	12000	0.346	0.456	0.102	0.065	0.026	0.006
3	20000	0.356	0.450	0.077	0.085	0.025	0.006
4	42000	0.365	0.451	0.068	0.085	0.025	0.006

Table A.45 RBS simulation data for the electrode side 1:1 TTh-Fc/ Bridging TTh copolymer film from Chapter 7 (Fig. 7.74).

Elemental Composition							
Layer number	Layer thickness (at/cm ²)	H	C	O	S	Cl	Fe
1	12000	0.378	0.461	0.057	0.090	0.010	0.004
2	27000	0.425	0.429	0.052	0.080	0.010	0.004
3	44500	0.444	0.429	0.033	0.080	0.010	0.004

Table A.46 RBS simulation data for the solution side 10:1 TTh-Fc/ Bridging TTh copolymer film from Chapter 7 (Fig. 7.76).

Elemental Composition							
Layer number	Layer thickness (at/cm ²)	H	C	O	S	Cl	Fe
1	8000	0.333	0.451	0.107	0.055	0.040	0.014
2	12000	0.365	0.444	0.092	0.055	0.030	0.014
3	13000	0.334	0.459	0.102	0.060	0.030	0.014
4	28000	0.344	0.459	0.093	0.060	0.030	0.014

Table A.47 RBS simulation data for the electrode side 10:1 TTh-Fc/ Bridging TTh copolymer film from Chapter 7 (Fig. 7.77).

Elemental Composition							
Layer number	Layer thickness (at/cm ²)	H	C	O	S	Cl	Fe
1	28000	0.354	0.459	0.072	0.073	0.030	0.012
2	33000	0.335	0.459	0.102	0.063	0.030	0.011
3	12000	0.365	0.444	0.092	0.058	0.030	0.011
4	8000	0.333	0.451	0.107	0.058	0.040	0.011